Control of Protein Binding at Interfaces: Gold Nanostructures and Affinity Peptide Labels

By

Nilan J. B. Kamathewatta
M.S., Sam Houston State University, 2014
B.Sc., University of Peradeniya, Sri Lanka, 2010

Submitted to the graduate degree program in Chemistry and the Graduate Faculty of the University of Kansas in partial fulfillment of the requirements for the degree of Doctor of Philosophy.

_____

Chair: Cindy L. Berrie

_____

Robert C. Dunn

_____

Yong Zeng

_____

James Blakemore

_____

Jennifer A. Roberts

Date Defended: 07 May 2020

The dissertation committee for Nilan J. B. Kamathewatta certifies that this is the approved version of the following dissertation:

Control of Protein Binding at Interfaces: Gold Nanostructures and Affinity Peptide Labels

Chair: Cindy L. Berrie

Date Approved: 14 May 2020

Abstract

Controlling protein adsorption at solid surfaces is critical for a large variety of applications such as biocatalysis, biomedicine, food safety, and environmental monitoring. The importance of controlling the orientation and conformation of the protein at the surface has been recognized as key to the successful implementation of such applications. Metal nanostructure platforms have potential applications not only in protein-based biosensing but also in electronics and energy harvesting applications. This works investigates the specificity and selectivity of proteins binding to metal surfaces for incorporation into metal nanostructure arrays for such applications. The specificity and selectivity of the coupling in this case is achieved through a genetically engineered peptide tag with a high affinity for a gold surface. Controlling the protein orientation on selected areas of surfaces is challenging due to the inability to control the selectivity and specificity of the desired molecules. This work mainly focuses on the utilization of affinity peptides to control the protein orientation on selected areas of metal-organic hybrid films.

Chapters 1 and 2 provide an introduction to the project and the methods employed. Investigations into the control of binding and orientations of a model protein (PutOX) at surfaces are described in *Chapters 3 and 4*. *Chapter 3* describes the utilization of an affinity peptide towards the selective immobilization of proteins on surfaces. Affinity peptides are specific sequences of amino acids that have a high affinity for a material, and in this study, we investigate gold affinity peptides. The specific attachment of functionally active PutOx via gold affinity peptide sequence (AuBP) to gold surfaces has been demonstrated using QCM, activity assays, temperature treatment, and AFM investigations of coverage and shape of individual molecules. The temperature treatment studies show that the peptide tagged protein shows higher stability on the surface than in the solution. *Chapter 4* reports the behavior of both wild type and PutOX-AuBP

enzymes on a variety of surfaces including TSG (template stripped gold), mica, Si(111), OTS-Si-SAM, Graphite, COOH-TSG-SAM, and OH-TSG-SAM. This part of the study addresses the effect of properties of the surface in the attachment of protein in the presence of affinity peptide tags to understand the binding specificity and selectivity when using the AuBP.

Once the selectivity and specificity of the gold binding peptide sequence towards the gold surface were demonstrated, methods to create Au nanostructures to bind the protein selectively on the metal nanostructures were required to create protein nanoarrays. Therefore, *Chapters 5-7* investigate the fabrication of gold nanostructures. The development of gold plating solutions for electroless deposition is described in *Chapter 5*. The approach we used is electroless deposition (ELD), which is a well-established process on silicon and other semiconductor surfaces to deposit metal films. This chapter further discusses the effects of plating components and how self-assembled monolayers are used to selectively deposit metal on Si surfaces. Here, the effect of plating solution components, pH, and deposition time was studied to develop mild plating solutions for fabrication of gold nanostructures in *Chapters 6 and 7*. Two different methods for gold nanostructure fabrication are explored in these Chapters. *Chapter 6* describes an AFM-based method for making gold nanowires using the combined techniques including self-assembled monolayer (SAM) resist formation, AFM nanoshaving, and electroless gold plating (whose deposition conditions were optimized in *Chapter 5*). Here, an OTS SAM on a silicon surface was utilized as a compelling molecular resist film for gold nanowire formation. The AFM nanoshaving was used to remove part of a molecular resist to expose the underlying silicon to facilitate gold nanostructure fabrication during ELD.

In *Chapter 7*, a combination of particle lithography (PL), self-assembly, and electroless deposition was used to develop large, periodic arrays of gold nanodots on the silicon surface. The

PL-based method addresses the limitations associated with the throughput of the AFM-based nanoshaving strategy discussed in *Chapter 6*. Here, the nanohole arrays are produced using a nanosphere mask and the formation of a self-assembled monolayer (SAM) film, and the nanohole array is then filled with metal via the ELD process. The metallic nanostructures developed using the PL provides the advantages of controllability of size and interparticle distance by changing the plating time and nanosphere diameter.

The combination of developed nanostructures and the affinity peptide-tagged proteins can be used to develop materials for the fabrication of nanoscale bionanodevices, which display a range of surface chemistries in the device. The developed nanoarrays could be useful towards plasmonic biosensing applications, with localized plasmonic resonance wavelength tunability, as well as platforms capable of sensitive electrochemical detection. Finally, this dissertation addresses several critical concepts for biomaterials research including orientation control of proteins, precise placement of nanostructures and nanoarrays, modification of the surface, ease of fabrication, and cost. In the future, this study will be extended to develop multiple metal nanoarrays of silver and gold on the same surface to study cell signaling pathways or coupled enzyme reactions using multiple affinity peptides, which specifically bind to different metals (*e.g.,* Au and Ag).

Acknowledgments

I would like to acknowledge my adviser, Dr. Cindy Berrie, for being an excellent mentor and a teacher throughout the last five and a half years. She always guided and encouraged me to be professional and do the right thing, even when the road got tough. I also much appreciate her patience, willingness to listen, and constant encouragement with a smiling face. Through all the support, she made graduate school an extraordinary place.

I am thankful to the members of the Berrie group, both past, and present, who have enriched my scientific endeavors. Also, I am grateful to Sasanka Ulapane and Jennifer Doolin for all the help they have done. Sasanka has been a great friend both in academic work and life outside. I thank members of the Berrie research group, Dr. Jenifer Tucker, Dr. Brad Neal, Dr. Christina Edwards, Dr. Monisola Okeowo, Yasmine Farhat, and Xavier Ortiz for the help throughout my studies. Also, I would like to acknowledge the undergraduate researchers Talisa Hughes, Patrick Connelly, and Sam Steuart, Tyler Nguyen, and Sarah Gress for helping me.

Also, I would like to express my gratitude to the collaborators, Mark Richter and Candan Tamerler for providing support. Also, I would like to express my appreciation to the Department of Chemistry and academic and non-academic staff of the department, including Liz Colmen, Susan Teague, Leal Ruben, Betsy Carlson, and Megan Belaire for helping me to finish the job efficiently. I also thank Sri Lankan community in Lawrence for all the help and beautiful memories.

I thank my High school, St Anthony's College, Kandy, for laying the background to become a chemist. Also, the University of Peradeniya and Sam Houston state university for providing me the support to finish my BSc and MSc in chemistry. Without all the support they have given, I will not be able to come this far. I thank my loving parents and brothers for their

continuous and unparalleled love, help, and support. I am thankful for their encouragement, moral support, personal attention, and care. Finally, I would like to thank my loving wife, Shanika Wanigasekara, for love and constant support for the past few years. She somehow has the patience to put up with me, and I will not be able to be where I am today without her. It has been incredible ten years with you and many more to go.

Table of Contents

List of Figures

List of Tables

Chapter 1: Introduction

The primary focus of this work is to utilize the selectivity and the specificity of affinity peptides to control the orientation of proteins on metal nanostructures as schematically shown in *Figure 1.1*. This dissertation discusses protein binding and metal nanostructure requirements. *Figure 1.2* provides a graphical outline of this dissertation. *Chapter 1* introduces the background information for the protein adsorption on surfaces and metal nanostructure fabrication. In *Chapter 2* of the thesis, all the materials, methods, and critical instruments utilized in this work are discussed in detail.

Chapters 3 and 4 introduce the concept of metal affinity peptides as a tool to control the orientation of protein on the surface. *Chapter 3* discusses the specific attachment of functionally active PutOx via AuBP to gold surfaces using a combination of QCM, activity assays, and AFM investigations of coverage and shape of individual molecules. *Chapter 4* discusses the behavior of PutOX and PutOX-AuBP enzymes on TSG, mica, Si(111), OTS-Si-SAM, Graphite, COOH-TSG-SAM, and OH-TSG-SAM.

Chapters 5-7 discuss the metal nanostructure fabrication process using electroless deposition. *Chapter 5* investigates the microscopic trends in electroless deposition for noble metal, gold, on Si surfaces, optimization of gold plating solutions for metal nanostructure formation, and investigation of the possibility of using self-assembled monolayers as a resist film for electroless deposition. *Chapter 6* explores the AFM-based technique combined with electroless deposition to fabricate gold nanowires on OTS-SAM modified surfaces. *Chapter 7* expands the applicability of the fabrication process through the use of particle lithography for gold nanosphere array fabrication on Si substrates using OTS monolayers as resist layers.

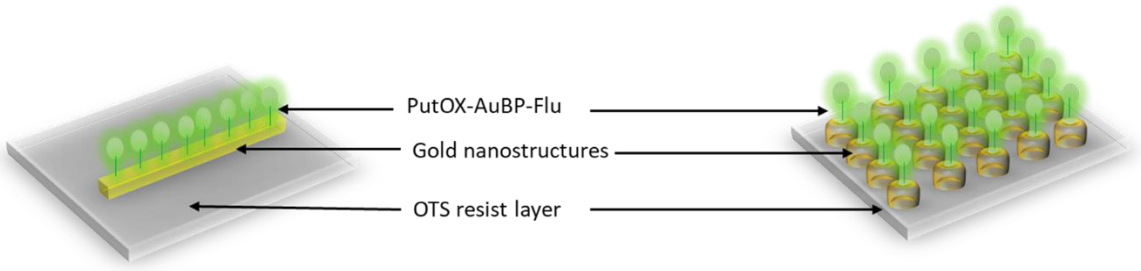

Figure 1. 1 *The selectivity and the specificity affinity peptides to control the orientation of protein on nanostructures.*

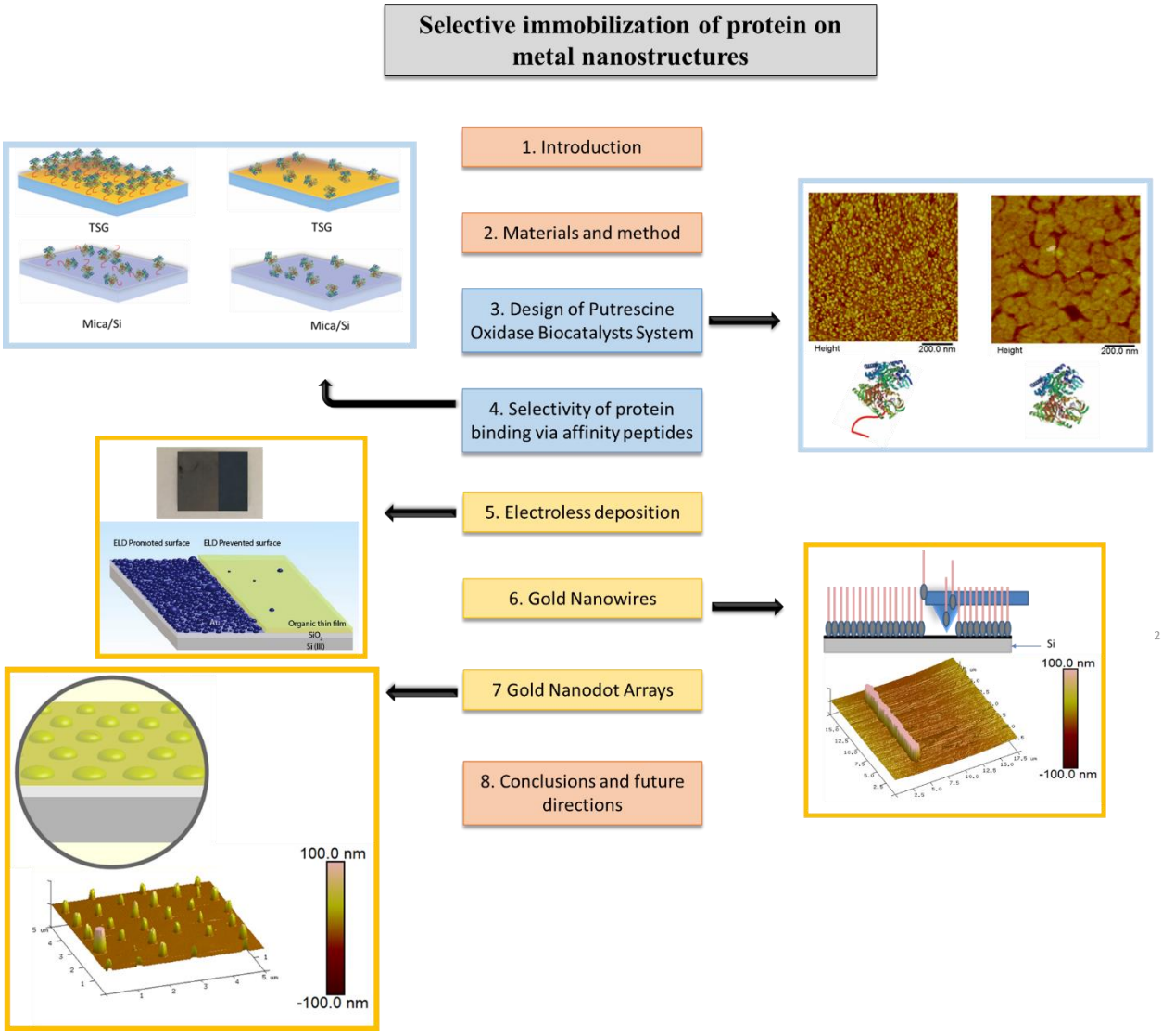

Figure 1. 2 *Graphical outline of the thesis. Chapter 3 discusses the designing of putrescine oxidase system. Chapter 4 is about selectivity and specificity of the AuBP tag. Chapter 5 discusses electroless silver deposition. Chapter 6 uses AFM-based nanoshaving combined with electroless deposition optimized in chapter 5. Chapter 7 combines nanosphere lithography and electroless deposition.*

1.1 Background: Protein Adsorption on Surfaces

Protein adsorption on surfaces has gained significant attention due to their importance in a broad range of fields. Creation of nanoscale protein arrays remains challenging due to the spatial demands of patterning, the difficulty of developing multiprotein arrays, and the difficulty of controlling protein-surface interactions to obtain desired activity. Protein adsorption onto surfaces is significant for a large variety of applications, including drug discovery,[1] sensing,[2] protein array formation,[3,4] disease identification,[5] protein purification,[6] and designing advanced materials.[7] To be successful in these applications, the control of protein orientation on surfaces is critical. If immobilization occurs successfully, the desired biological activity can be retained.

The adsorption of proteins on surfaces generally consists of multiple steps. The process can be either nonspecific or specific, depending on the properties of the surface and protein. Most nonspecific adsorption occurs via hydrogen bonding, van der Waals interactions, and electrostatic interactions.[3] Specific interactions occur between specific functional groups on the surface and others on the protein. Proteins interact differently on different types of surfaces. During the process of adsorption, both the properties of the surface and the protein play important roles. Protein molecules are composed of amino acids, forming large, complex 3D structures. Proteins are prone to unfolding, aggregation, etc, and therefore protein solutions must be properly prepared and stored. Due to the complex nature of proteins, individual molecules can form multiple interactions with both surfaces and neighboring molecules. Protein-protein interactions often lead to dimeric or trimeric structures of protein, which lead to even more complex interactions once introduced to the surface.[8,9]

Once a solution of protein is introduced to the surface, protein may adsorb in different orientations and may diffuse on the surface. There is an equilibrium between surface bound and

solution phase protein. At equilibrium, both adsorption and desorption are occurring at equal rates. Researchers have seen molecule rearrangement after adsorption to the surfaces.[10,11] This can lead to conformational changes, which result in irreversible binding of the protein on to the surface.[11] In addition to this, protein-surface interactions are affected by the pH of the solution, the isoelectric point of the protein, and the ionic strength of the solution. Studying the protein surface interactions in terms of competitive interactions, affinity, binding strength, conformation, orientation, kinetics, dynamics, and concentration will lead to understanding the fundamental aspects for these applications. In the studies reported here, we focus on the utilization of gold affinity peptides to control the orientation of protein molecules on gold surfaces.

1.1.1 Controlling Protein Orientation on Surfaces

As discussed in the previous section, controlling the protein adsorption on surfaces plays a significant role in a wide variety of applications. The methods of protein adsorption are direct adsorption, thiol coupling,[12,13] amine coupling,[14,15] binding through histidine tags,[16] complementary DNA strands,[17,18] affinity peptides[19,20], and affinity proteins.[16,21,22]

Direct adsorption of proteins onto surfaces is based on non-specific interactions, and sometimes leads to protein denaturation. Nonspecific adsorption, typically weak relative to other types of binding) can preserve the native structure, but weak interactions to the surface can result in the desorption of molecules during the applications. Covalent interactions such as chemical crosslinking, utilization of reducing agents, and enzyme crosslinking will provide strong interactions to the surface but may alter the three-dimensional structure of the protein. Due to this, the potential loss of bioactivity of molecules may happen. Previous studies have shown that on hydrophobic surfaces, proteins shows conformational changes, clustering, nonuniform adsorption,

and mobility towards the step edges during the immobilization.[10,11,23,24] This indicates that the properties of the surfaces, such as functionality, charge, and morphology, play a major role in the stability of the immobilized protein.

SAM can allow for control of the surface functionality and tuning the protein surface interactions, and for that reason, a variety of SAM surfaces have been used to study protein immobilization.[25–28] Researchers have shown that hydrophilicity and steric repulsion capability make these monolayers resistive to protein binding.[4] Recent studies have shown that protein resistivity can be obtained by manipulating the surface charge since the Coulomb interactions play a significant role in binding events.[4,29,30]

1.1.2 Current Issues Associated with Controlling Protein Orientation on Surfaces

Biological systems typically integrate multicomponent self-assembly for complex tasks requiring the precise function of many components in tandem. There is a growing interest in harnessing such self-assembly of materials for hybrid nanodevice function, but functional assembly of multicomponent systems at the nanoscale remains a significant challenge.[19,31] Two critical considerations that accompany incorporation of biomolecules into solid supports are the maintenance of functional integrity of the biomolecule when surface-immobilized and the precise placement and orientation of the biomolecule in a manner that allows control over its interactions with the interface directly and with other components in the assembly. These factors are essential for the construction of complex nanostructured materials and devices such as protein arrays, biosensors, and biochips.

For proteomic and biosensing applications, patterns of biomolecules on surfaces were developed using lithographic and self-assembly techniques. In most studies, thiol[12] molecules have

been utilized as the linker between surface and biomolecule. Generally, these linkers are unstable and lacking selectivity towards a specific material. Most commonly, the attachment strategies are based on the carboxyl and amine functional groups available in both protein and surface. The numerous amines and carboxyl groups that are exposed on the surface of proteins provide many potential binding sites when coupling through these functional groups to the surface. Therefore it is difficult to control the orientation of protein on the surface.[32,33]

1.1.3 Affinity Peptide to Control Protein Surface Interactions

The aforementioned problems can be overcome by the use of surface recognition peptides, which have been derived from cell surface displays and peptide phage display libraries.[19,34–37] These peptides have shown excellent selectivity for particular surfaces, which can potentially be used in protein immobilization. However, there have been relatively few reports which have investigated the binding of these peptide tagged proteins on the nanoscale. Since the assembly is directed by the peptide sequence, the problems associated with the altering of proteins during surface binding can be overcome. There are several affinity peptides developed for material binding over a wide range of surfaces. The properties of these peptides have been critically examined in studies of surface functionalization, self-assembly, and formation of various nanostructures. They were also demonstrated to be efficient surface linkers as fusion partners to other biomolecules.[36,38] The mechanism of binding for such peptides is not well understood at the molecular level but likely is a result of accumulation of multiple hydrogen bonding, van der Waals and electrostatic interactions. Using such peptides with high affinity could facilitate biological friendly attachment of proteins via built-in linkers without altering the protein structure.

The affinity peptides have specific sequences of amino acids that recognize specific inorganic surfaces. During last few decades, the combination of affinity peptides with the proteins has been utilized in different applications. Some of the frequently used affinity peptides are gold affinity peptides,[34,39] silicon affinity peptides,[19,40] and silver affinity peptides.[20,41] There are several reports regarding silicon binding peptides utilized in cancer recognition applications.[40] This method has shown promising bioactivity in comparison to traditional approaches. Also, recent studies have shown that binding proteins onto surfaces via affinity peptides shows preserved fluorescence activity on gold surfaces more than the native type proteins.[42]

Most of the AFM, QCM, CV, and SPR studies have been done to investigate the self-assembly, activity, role of surface charge, and adsorption kinetics of the affinity peptides.[39–41] There are significantly fewer studies that show the utilization of affinity peptide tags to immobilize proteins on the surface. Previous studies show the utilization of affinity peptides to bind GFP and DsRed proteins via AuBP sequence without compromising bioactivity.[45]

1.1.4 Protein System of Interest: Putrescine Oxidase

Here, we have engineered a fusion protein consisting of putrescine oxidase (PutOx) and a gold binding peptide (AuBP). Putrescine oxidase is a member of the amine oxidase family of proteins that use a Flavin cofactor to oxidize substrates to produce electroactive hydrogen peroxide.[46,47] The hydrogen peroxide can be reduced at an electrode surface producing an electrical current, thus providing a sensitive method for detecting the presence of the oxidase substrate. Flavin oxidases have been used in a variety of biosensing applications and the putrescine oxidase it selected here as a model redox active enzyme for surface immobilization.[48] The gold binding peptide used in this study binds with high selectivity and affinity, and it has enabled self-assembly

of the PutOx protein onto gold surfaces, including gold nanoparticles. The PutOx-AuBP self-assembled onto the gold surfaces, binding with significantly higher affinity than the native PutOx enzyme and remained functionally active on the surface. The AFM analysis demonstrates that the protein orientation on the Au surface is significantly different than the wild type when the AuBP tag is incorporated. This could potentially be used as a promising approach for protein assembly in multicomponent systems.

In this part of the study, wildtype and affinity peptide tagged PutOx enzymes were utilized on different surfaces to determine the specificity and selectivity of the tag (see *Chapters 3 and 4*). Both proteins were adsorbed onto hydrophilic, hydrophobic and SAM surfaces to investigate differences in adsorption. The ability to assemble proteins for nanoscale devices requires specific recognition of the patterning material with low background absorption on the rest of the surface. Therefore, investigation of how the absorption varies with the material is critical for the design of such devices. The AFM investigation of the different surfaces shows that the adsorption of molecules occurs differently to gold when the peptide sequence is attached, and with greater affinity. Hydrophobic surfaces also show significant denaturation and aggregation of the protein. Hydrophilic surfaces including mica, carboxyl, and hydroxyl-terminated SAM surfaces do not show extensive denaturation and result in minimal nonspecific binding. These may be ideal candidates for resist layers when immobilizing proteins on patterned gold surfaces at the nanoscale. Additionally, these results investigate the specificity and selectivity of the AuBP tag in controlling protein-surface interactions with a variety of materials.

1.2 Background: Nanostructures of Gold via Electroless Deposition

Controlling the orientation of proteins on metal nanostructures is very important for nanoscale applications. As technology advances, nanoscale fabrication will continue to gain significant attention. Nanostructures of metal and biomolecules are applicable in the fields of electronics, storage, sensing, catalysis, and cancer treatment. Some of the standard methods of fabricating nanostructures on surfaces are molecular self-assembly,[49,50] dip-pen lithography, nanoshaving,[51,52] e-beam lithography,[53,54] photolithography[55] and particle lithography.[56–58]

Molecular self-assembly is the most straight forward method of fabricating novel multicomponent structures onto surfaces. This is a naturally occurring phenomenon that is common in biological systems. The assembly is mediated by hydrogen bonding, ionic interactions, hydrophobic interactions, van der Waals interactions, and covalent bonding. Researchers have utilized the self-assembly process to fabricate peptides,[59] proteins,[60] lipids,[61] and small organic molecules[62,63] onto the surface. From the self-assembly process, nanofiber proteins, bionanotubes, nanometer-thick coatings on surfaces, nanowires, bio-optical structures have been developed, which will give potential benefits in biological applications.[64]

Recently, nanoscale fabrication based on scanning probe techniques has been explored. Researchers have shown that these techniques have the capability of fabricating features with few nanometers of resolution.[52,65] After 1999 when the dip pen lithography was introduced, there have been several advancements in the field.[66,67] DPN can be used to introduce DNA,[68] polymers,[69] small organic molecules,[70] proteins,[71] peptides,[69] colloidal nanoparticles[72] and metal ions[73] in an arrayed manner to the surface. Overall, the DPN process has been used in fabricating biological nanoarrays and templated hierarchical assembly of materials.[65,67] Nowadays, the available

techniques have been expanded to include cantilever-free nanolithography, which enables the use of this technique in a wide variety of fields.

Atomic Force Microscopy (AFM) also can be used for the direct manipulation of surfaces on the nanoscale. AFM has been used recently as a lithographic tool in which the material surface is modified by the AFM probe tip.[51,52,74] AFM-nanoshaving utilizes the AFM tip to manipulate the surface of interest. AFM techniques have been utilized in making two-dimensional patterns within inorganic, organic, or biological materials; and build 3D biological assemblies on the surface instead of just being utilized for topographical imaging.

Photolithography has been used to manufacture microscale structures on the surface. This method highly depends on the diffraction limit of light, and it is very difficult to get to the nanoscale dimentions.[55] With the advancement of technology, nanostructures with tens-of-nanometers resolution have been developed using photolithography; however, this process is very expensive. Electron beam lithography (E-beam) uses a focused beam of an electron to make patterns on the surface, which is coated with a resist film. This method is capable of creating structures with sub-10 nm resolution, and it is capable of direct patterning on a substrate with a high degree of automation.[54] However, after considering nanoscale applications, low throughput and high cost make this less attractive in many applications.

Compared to the methods described above, particle lithography (PL) provides a simple approach to produce arrayed structures on the surface. This method is an inexpensive fabrication tool for producing homogenous and regular arrays with different sizes. PL enables the formation of arrays of metals,[75] SAMs,[76] proteins,[77] polymers,[78] and nanoparticles[79] on the surface. Recent advancements show that this method is capable of forming multicomponent arrays on the surface in combination with other techniques.[80,81] Fischer et al. in 1981 reported the first ordered

monolayer of colloidal spheres on a glass surface.[82] In the 1990s, Hulteen and Van Duyne developed nanodot structures that have close-packed structures.[80] Further, Van Duyne's group intensely studied the plasmon resonance properties of metallic patterns to produce biosensing applications.[81]

1.2.1 Electroless Metal Deposition

Chapter 5 investigates the optimization of plating conditions for obtaining thin gold metallic films on Si surfaces while preventing deposition on the resistive monolayer of OTS developed on Si. Due to the rapid development of electronics, semiconductors, magnetic materials, biomedical, and nanofabrication industries,[83–89] metal deposition on surfaces has recently gained significant attention. Electroless deposition (ELD) is one of the simplest methods of metal deposition and can be used to deposit different metals on the surface.

In the electroless deposition, no external current or potential is required and there is more control in comparison to other methods, such as electroplating. When using a Si surface, no reducing agent is needed due to the silicon itself serves as the reducing agent in the presence of HF or NH_4F (etching agent). Electroless plating can transform non-conductive materials into conductive materials. In the method of metal electroless deposition, solutions of metal ion are used with an etching agent with other additives to directly deposit metal on the surface. Most of the industrial electroless metal plating are carried out this way because it is a rapid process to obtain uniform coating.[90,91]

The first electroless deposition on a Si surface was reported by Silverman and Benn in 1958, using an alkaline solution of $KAu(CN)_2$ to deposit Au on a silicon surface.[92] Since the silicon surfaces have a native oxide layer, an etching agent is required to remove the oxide layer. D'Asaro

et al. showed that addition of HF into the plating solution Removed the oxide layer and prevents the layer from reforming on semiconductor surfaces. Nagahara and coworkers studied the effect of HF solution in the electroless deposition of metals on silicon surfaces.[93] When the HF concentration of the plating solution increases, the metal deposition rate increased only for Au, Cu, and Pd. For Al and Sn, the deposition rate was independent of HF concentration.[93] They have observed all the metal ions deposited in this manner have poor adhesion to the silicon surface. The quantitative evaluation of adhesion of gold thin films on to Si surfaces has shown that, most of the time, gold adheres poorly onto the Si surface while carrying out the electroless deposition. Introducing an adhesion layer, such as a seed layer of Ag, prior to electroless deposition has resulted in stronger adhesion of the gold onto Si.[94]

Several studies of gold electroless deposition on Si(111) and Si(100) interfaces show that during the initial metal growth there is diffusion of Si atoms to the Au layers. Au on Si forms four different surface structure types.[95] Warrant et al., using AFM and XRD studies, found that Au deposition occurs epitaxially on Si(111) with Au(111) plane parallel to the substrate, sometimes referred to as Volmer Weber growth.[96] For a given exposure time, they observed a linear relationship between Au concentration on Si surface and in the aqueous solution.

1.2.2 Critical Components of a Plating Solution

Most electroless plating solutions consist of a metal ion source, an etching agent, accelerators, buffers, and chelating agents. A majority of the studies in the literature use complex mixtures suitable for industrial scale and higher concentrations of components.[97–100] For gold electroless deposition as metal ion source including $HAuCl_4$, $AuCl_3$, $NaAuCl_4$ and $NaAu(SO_3)_2$ have been used. As the surface etching agent HF and NH_4F have been utilized. Previous works

show that in the presence of organic molecules in the plating solution, such as polyvinylpyrrolidone (PVP),[101,102] trisodium citrate ($Na_3C_6H_5O_7$),[103] citric acid ($H_3C_6H_5O_7$),[104] ascorbic acid ($C_6H_8O_6$)[97,98] tend to play multiple roles.

Utilization of simple plating solutions with low concentrations will help to gain more control over the coating process in nanoscale fabrication. If not, rapid nucleation of the metal will lead to nonuniform metal growth on the surface. For the nanoscale fabrication, only two essential components can be used for carrying out the electroless deposition, a metal ion source, an etching agent. Researchers have used Ag, Au, Cu, Fe, Ni, Co, and Pt as metal ions for the electroless deposition since they have wide range of applications in electronics, plasmonics, catalysis, and biosensing. Most of these studies have not discussed the role of each component added to the plating solutions.

1.2.3 Our focus: To Develop Mild Plating Solutions

There are only very few studies regarding the combined techniques of electroless deposition with organic thin films to generate metal nanostructures.[74] The development of such plating solutions that allow metal to deposit on silicon exposed areas while preventing metal deposition on organic thin film resist layer. This will provide a model platform for investigation of novel applications. Some of the applications of interest are high technology electronics, optoelectronic devices, and platforms to study biological systems. In this work we develop and optimize a mild plating solution that plates metallic gold on bare silicon substrates and prevents any metal deposition over areas protected by organosilane monolayers. To achieve this, we studied the effect of change in concentration of metal ions, ammonium fluoride, citric acid, trisodiumcitrate, PVP, pH, and deposition time for the electroless deposition of gold on the Si(111)

surface. RMS roughness, surface coverage, and particle diameter variations will be compared with the change of the above parameters. To demonstrate the ability of the monolayer to protect the surface from metal deposition, deposition on bare Si(111) and OTS coated Si(111) were compared order to assess the effectiveness of the OTs layer as a resist coating under the deposition conditions. Also, the stability of the plating solutions was tested using UV-Visible spectroscopy. We confirmed electroless deposition was limited to only trace amounts on the OTS modified surfaces by AFM images, whereas unmodified surfaces were fully covered with metal (see *Chapter 5*).

1.2.4 Existing Methods of Nanostructure Fabrication

Basically, nanofabrication strategies can be categorized as top-down or bottom-up approaches. Also, there are some new techniques that utilize the combination of the above two approaches. The top-down approach is the most frequent technique used in semiconductor industries. The top-down approach requires a high-cost operation, applicable only for planer surfaces and mostly incompatible for the biological samples. Bottom-up approaches, such as self-assembly and soft lithography, are inexpensive, easy to carry out and offer scalability. However, most of the time they lack control over the shape and positioning of structures. Today, researchers now use hybrid techniques such as nanoimprint lithography,[105,106] edge lithography,[107] and stencil lithography,[108] which reduce fabrication cost and increases flexibility in the design of nanopatterns.

By using various metals, there are several studies regarding the development of periodic nanostructures on surfaces. Some of the techniques that are utilized to form nanoarrays on surfaces are photolithography (PL),[55] e-beam lithography,[54] nanoimprint lithography (NIL), dip-pen lithography (DPL),[67] stencil lithography,[108] and nanosphere lithography (NSL).[80] Most of these

techniques involve the development of resistive organic films and metal deposition in a periodic manner.

Photolithography utilizes a light source to pattern or damage the resist coating. The exposed areas can be further manipulated to control metal deposition. This method is limited by the diffraction of light and its high-cost instrumentation. Electron beam lithography uses a similar technique by using an electron beam instead of a light source. This method is limited by the electron-electron repulsion but capable of making patterns with sub 10 nm resolution. To obtain large template arrays, nanoimprint lithography can be used. This method utilizes a mold or stamp to pattern the surface. Dip pen lithography uses a coated AFM tip by dipping the tip on a solution of desired metal. When the tip is scanned on the surface, the species of interest can graft to the surface. This method has less capability of giving uniform and consistent coating. Stencil lithography uses a stencil to transfer features from a thin sheet on to an underlying substrate. This method has numerous advantages, such as surface adaptability, scalability, and reusability.

1.2.5 Metallic Nanowire Fabrication via Self-Assembly, AFM-nanoshaving, and Electroless Deposition on Si(111) Surfaces

Materials composed of nanostructures are one of the most intense fields in research due to having a vast range of practical applications. Fabrication of metal nanowires is useful in the areas of biosensing, solar cells, batteries, transparent electronics, nanoelectronics, biomedicine, and biological cell manipulation. [83–89] For most of the above applications, the production of nanowires is done in solution or arrays are formed on surfaces. Since the properties of nanostructures can be altered by changing the physical properties such as size and shape, there are applications in a vast variety of fields. Atoms at the interface have modified surface energy and reactivity. Also, the

preparation of metallic structures with reduced dimensions such as metal colloids, quantum dot structures, nanorods, and nanowires are in high demand due to their large range of applicability.

The AFM cantilever can be used in two ways to carry out the nanoshaving: static[74] and dynamic plowing.[109] The contact mode AFM is used in static plowing to selectively remove a part of resist layer developed on surface.[74] Though this technique has advantages such as low-cost and low-effort technique, there are drawbacks such as developing edge irregularities, damaging the tip after multiple uses and the dependency on the stiffness of the sample while shaving. In the dynamic plowing lithography, the surface is modified using the oscillating tip in the mode of tapping. When considering harder surfaces, such as OTS, it is difficult to modify with the dynamic plowing lithography.

One of the important steps in static plowing lithography is to determine a good resist layer which is compatible for the metal deposition technique. The most common resist layers are either polymeric material or self-assembled monolayers.[76] Most importantly, the formed resist layer should be well-packed and should have minimum defect sites. The thin polymer coating can be obtained on the surface by spin coating. This method sometimes leads to multiple layers and also a nonuniform coating on the surface due to having less controllability. Using self-assembled monolayers as the resist layers has gained more attention due to having a single molecular thick uniform layer, which can be easily removed by AFM nanoshaving. This study used silane SAM on silicon surfaces since silanes are capable of forming a uniform and well-arranged monolayer on silicon surfaces, which can act as a resistive layer for the electroless deposition of gold metal on AFM nanoshaved areas. Optimized plating solutions consist of metal source, etching agent, and chelating agent was utilized to deposit metals on nanopatterns to obtain nanowires of gold.

To be used in high technology applications, the nanostructures should be precisely positioned on surfaces. To be useful for electronics application, the aspect ratio, surface morphology deposition rate of metal and the adhesion onto the surface should be closely controlled. Here we report a top-down approach using tip-based nanofabrication. This method used a tip in contact with the surface to alter the surface by mechanically, thermally or electronically. These techniques can be categorized into STM-based and AFM-based models. Here, a combination of AFM nanoshaving and electroless deposition was utilized to create metal nanowires with different sizes and shapes (See *Chapter 6*). Octadecyltrichlorosilane (OTS) SAMs developed on silicon surface were used as the organic monolayer, and part of the surface was removed using AFM nanoshaving. By changing the parameters' shape and the size of the nanoshaved area can be changed. Finally, utilizing the redox chemistry between desired metal ions and exposed silicon, metal nanowires can be obtained.

1.2.6 Periodic Gold Nanodot Array Fabrication on Si(111) Surfaces by Using Self Assembly, Particle Lithography and Electroless Deposition

Periodic arrays of nanostructures developed on surfaces have applications in storage devices,[110,111] electronic components,[112] and biosensing devices.[113110,113–120] Previously mentioned AFM-based nanoshaving with the combination of electroless deposition was able to give controlled size, shape, and positioning of nanostructures on OTS-Si modified surfaces. But this technique does not have the ability to make periodic nanostructures on the entire surface, and also the throughput of the fabrication is very low. In this study, we develop periodic gold nanodot arrays by using the combination of particle lithography, self-assembly, and electroless deposition techniques. This method is cost-effective and shows great controllability oversize and spatial

distribution. This method can be expanded to prepare large scale arrays with different metals on organic thin film modified surfaces.

Nanosphere lithography is a technique that drop casts spheres onto a surface to develop nanosized features that are hexagonally packed or similar patterns.[80] This method is capable of forming nanostructures that are regularly spaced on the surface with different sizes. NSL is a two-step process that started with mask preparation and followed by nanostructure formation. In the initial step, the spheres were introduced to a cleaned hydrophilic surface to obtain uniformly distributed spheres on the surface. Drying of the surface leads to the self-organization of spheres, which arrange in the hexagonally packed system. Next, the surface is exposed to metal or organic molecules using various techniques to get the patterned surface. Removal of nanosphere masks will give the patterned surface with desired features. Researchers have shown that this method is capable of forming metal nanopatterns, self-assembled monolayers, proteins, polymers, and nanoparticles. There are recent reports regarding the sequential deposition of two metal vapors through two different particle templates to develop binary nanopatterns. Also, with the combination of microcontact printing and particle lithography, multicomponent systems have been designed in one step.

During this study, particle lithography was used to develop nanodot arrays of gold on silicon surfaces (see *Chapter 7*). This method consists of three steps. First, the nanosphere was packed on cleaned Si surface by drop-casting the colloidal solution. Second, the octadecyltrichlorosilane (OTS) monolayer was introduced to the surface to obtain the self-assemby on the areas that have exposed Si. Following, the nanospheres were removed by sonication or other methods to obtain nanoholes. Third, selective metal deposition was performed to obtain gold nanoarrays. This method shows the remarkable capability of obtaining metal nanostructures for

the metals that demonstrate spontaneity in redox chemistry with Si, including Ag, Au, Cu, Ni, Pb, Cd, Fe, and Pt.[83] Our studies have demonstrated the capability of tuning height and the spacing of the nanostructures by changing plating time and the sizes of the spheres respectively. Our method has advantages such as simplicity without any expensive equipment, reproducibility, capability of patterning a broad range of materials, and controllability of feature size and spatial distribution.

1.3 Thesis Summary and Overview.

In this work, we have shown the specific interaction of PutOx through gold affinity peptide on to Au surfaces by AFM analysis, QCM, and activity analysis. Also, a comparison of wildtype and the AuBP tagged proteins on different surfaces has been performed to demonstrate the material selectivity and specificity of these proteins towards the Au surfaces. Among the surfaces studied, hydroxyl-terminated SAM surfaces were selected as the most protein resistive surface, which can be utilized as a mask for gold nanostructure development. Finally, gold nanowires and nanodot arrays on OTS modified Si surfaces were developed using AFM based nanoshaving and particle lithography-based techniques respectively to study the specific binding of proteins via affinity peptide tags.

The first half of the study highlighted the controlling of the orientation of the protein on gold surfaces via affinity peptide sequences. This was carried out by using both wild-type, and AuBP tagged proteins to compare the dimensions and coverage on different surfaces. The difference in height of proteins bound to the Au surface suggests that there is a significant role played by the affinity peptide during the binding event. Also, to determine the material selectivity, AFM analysis of proteins was carried out on hydrophilic and hydrophobic surfaces. In the second half of this study, the metal plating solutions were developed to produce thin gold films on Si

surfaces while using OTS monolayer as a resist for electroless metal deposition. This study was extended to create nanowires of gold on Si-OTS surfaces by using AFM nanoshaving and electroless deposition. Further, to obtain arrayed gold features on the Si-OTS modified surfaces, nanosphere lithography was utilized with the combination of electroless metal plating.

In this study, we address the importance of affinity peptides towards the controlling orientation of the biomolecules at the interface to obtain the desired activity. Also, we develop nanoscale structures with controllable size, shape, and spacing, which can apply to the fields of biosensing, electronics, and storage materials. Most of the methods and instrumentation that were utilized are relatively inexpensive, and we hope our research will be useful in large areas of studies.

1.4 References

(1) Veerapandian, M.; Yun, K. Study of Atomic Force Microscopy in Pharmaceutical and Biopharmaceutical Interactions - A Mini Review. *Curr. Pharm. Anal.* **2009**, *5* (3), 256–268. https://doi.org/10.2174/157341209788922020.

(2) Kost, J. Proteins at Interfaces II: Fundamentals and Applications. *J. Control. Release* **1997**, *45* (1), 1–113. https://doi.org/10.1080/01932699708943757.

(3) Kenseth, J. R.; Harnisch, J. A.; Jones, V. W.; Porter, M. D. Investigation of Approaches for the Fabrication of Protein Patterns by Scanning Probe Lithography. *Langmuir* **2001**, *17* (13), 4105–4112. https://doi.org/10.1021/la0100744.

(4) Zhou, D.; Wang, X.; Birch, L.; Rayment, T.; Abell, C. AFM Study on Protein Immobilization on Charged Surfaces at the Nanoscale: Toward the Fabrication of Three-Dimensional Protein Nanostructures. *Langmuir* **2003**, *19* (25), 10557–10562. https://doi.org/10.1021/la035491q.

(5) McCabe, R. P.; Haspel, M. V.; Pomato, N.; Thompson, E.; Hanna, M. G.; Lamm, D. L.; Smith, K. O. A Diagnostic-Prognostic Test for Bladder Cancer Using a Monoclonal Antibody-Based Enzyme-Linked Immunoassay for Detection of Urinary Fibrin(Ogen) Degradation Products. *Cancer Res.* **1984**, *44*, 5886–5893.

(6) Kim, J. -S; Raines, R. T. Ribonuclease S-peptide as a Carrier in Fusion Proteins. *Protein Sci.* **1993**, *2* (3), 348–356. https://doi.org/10.1002/pro.5560020307.

(7) Mrksich, M. Using Self-Assembled Monolayers to Understand the Biomaterials Interface. *Curr. Opin. Colloid Interface Sci.* **1997**, *2* (1), 83–88. https://doi.org/10.1016/s1359-0294(97)80012-x.

(8) Haynes, C. A.; Norde, W. Globular Proteins at Solid/Liquid Interfaces. *Colloids Surfaces B Biointerfaces* **1994**, *2* (6), 517–566. https://doi.org/10.1016/0927-7765(94)80066-9.

(9) Kost, J. Protein at Interfaces II. Fundamentals and Applications. *J. Control. Release* **1997**, *45* (1), 1–113. https://doi.org/10.1016/S0168-3659(97)90013-4.

(10) Marchin, K. L.; Phung, S.; Berrie, C. L. Evidence for Fibrinogen Mobility on Hydrophobic Surfaces. *e-Journal Surf. Sci. Nanotechnol.* **2005**, *3*, 173–178. https://doi.org/10.1380/ejssnt.2005.173.

(11) Marchin, K. L.; Berrie, C. L. Conformational Changes in the Plasma Protein Fibrinogen upon Adsorption to Graphite and Mica Investigated by Atomic Force Microscopy. *Langmuir* **2003**, *19* (23), 9883–9888. https://doi.org/10.1021/la035127r.

(12) Ba, O. M.; Hindie, M.; Marmey, P.; Gallet, O.; Anselme, K.; Ponche, A.; Duncan, A. C. Protein Covalent Immobilization via Its Scarce Thiol versus Abundant Amine Groups: Effect on Orientation, Cell Binding Domain Exposure and Conformational Liability. *Colloids Surfaces B Biointerfaces* **2015**, *134*, 73–80. https://doi.org/10.1016/j.colsurfb.2015.06.009.

(13) Karyakin, A. A.; Presnova, G. V.; Rubtsova, M. Y.; Egorov, A. M. Oriented Immobilization of Antibodies onto the Gold Surfaces via Their Native Thiol Groups. *Anal. Chem.* **2000**, *72* (16), 3805–3811. https://doi.org/10.1021/ac9907890.

(14) Wong, L. S.; Khan, F.; Micklefield, J. Selective Covalent Protein Immobilization: Strategies and Applications. *Chem. Rev.* **2009**, *109* (9), 4025–4053. https://doi.org/10.1021/cr8004668.

(15) Rusmini, F.; Zhong, Z.; Feijen, J. Protein Immobilization Strategies for Protein Biochips. *Biomacromolecules* **2007**, *8* (6), 1775–1789. https://doi.org/10.1021/bm061197b.

(16) Takahashi, S.; Kishi, K.; Hiraga, R.; Hayashi, K.; Mamada, Y.; Oshige, M.; Katsura, S. A New Method for Immobilization of His-Tagged Proteins with the Application of Low-Frequency AC Electric Field. *Sensors (Switzerland)* **2018**, *18* (3), 11–15. https://doi.org/10.3390/s18030784.

(17) Palla, K. S.; Hurlburt, T. J.; Buyanin, A. M.; Somorjai, G. A.; Francis, M. B. Site-Selective Oxidative Coupling Reactions for the Attachment of Enzymes to Glass Surfaces through DNA-Directed Immobilization. *J. Am. Chem. Soc.* **2017**, *139* (5), 1967–1974. https://doi.org/10.1021/jacs.6b11716.

(18) Ngo, T. A.; Dinh, H.; Nguyen, T. M.; Liew, F. F.; Nakata, E.; Morii, T. Protein Adaptors Assemble Functional Proteins on DNA Scaffolds. *Chem. Commun.* **2019**, *55* (83), 12428–12446. https://doi.org/10.1039/c9cc04661e.

(19) Hnilova, M.; So, C. R.; Oren, E. E.; Wilson, B. R.; Kacar, T.; Tamerler, C.; Sarikaya, M. Peptide-Directed Co-Assembly of Nanoprobes on Multimaterial Patterned Solid Surfaces. *Soft Matter* **2012**, *8* (16), 4327–4334. https://doi.org/10.1039/c2sm06426j.

(20) Eckhardt, S.; Brunetto, P. S.; Gagnon, J.; Priebe, M.; Giese, B.; Fromm, K. M. Nanobio Silver: Its Interactions with Peptides and Bacteria, and Its Uses in Medicine. *Chem. Rev.* **2013**, *113* (7), 4708–4754. https://doi.org/10.1021/cr300288v.

(21) Faccio, G. From Protein Features to Sensing Surfaces. *Sensors (Switzerland)* **2018**, *18* (4), 1–17. https://doi.org/10.3390/s18041204.

(22) Kang, J. H.; Choi, H. J.; Hwang, S. Y.; Han, S. H.; Jeon, J. Y.; Lee, E. K. Improving Immunobinding Using Oriented Immobilization of an Oxidized Antibody. *J. Chromatogr. A* **2007**, *1161* (1–2), 9–14. https://doi.org/10.1016/j.chroma.2007.05.023.

(23) Cullen, D. C.; Lowe, C. R. AFM Studies of Protein Adsorption: Time-Resolved Protein Adsorption to Highly Oriented Pyrolytic Graphite. *Journal of Colloid and Interface Science*. 1994, pp 102–108. https://doi.org/10.1006/jcis.1994.1276.

(24) McAllister, C.; Karymov, M. A.; Kawano, Y.; Lushnikov, A. Y.; Mikheikin, A.; Uversky, V. N.; Lyubchenko, Y. L. Protein Interactions and Misfolding Analyzed by AFM Force Spectroscopy. *J. Mol. Biol.* **2005**, *354* (5), 1028–1042. https://doi.org/10.1016/j.jmb.2005.10.012.

(25) Fenter, P.; Eisenberger, P.; Li, J.; Camillone, N.; Bernasek, S.; Scoles, G.; Ramanarayanan, T. A.; Liang, K. S. Structure of CH 3 (CH 2) 17 SH Self-Assembled on the Ag(111) Surface: An Incommensurate Monolayer. *Langmuir* **1991**, *7* (10), 2013–2016. https://doi.org/10.1021/la00058a008.

(26) Luk, Y. Y.; Kato, M.; Mrksich, M. Self-Assembled Monolayers of Alkanethiolates Presenting Mannitol Groups Are Inert to Protein Adsorption and Cell Attachment. *Langmuir* **2000**, *16* (24), 9604–9608. https://doi.org/10.1021/la0004653.

(27) Li, L.; Chen, S.; Zheng, J.; Ratner, B. D.; Jiang, S. Protein Adsorption on Oligo(Ethylene Glycol)-Terminated Alkanethiolate Self-Assembled Monolayers: The Molecular Basis for Nonfouling Behavior. *J. Phys. Chem. B* **2005**, *109* (7), 2934–2941. https://doi.org/10.1021/jp0473321.

(28) Kankate, L.; Werner, U.; Turchanin, A.; Gölzhäuser, A.; Großmann, H.; Tampé, R. Protein Resistant Oligo(Ethylene Glycol) Terminated Self-Assembled Monolayers of Thiols on Gold by Vapor Deposition in Vacuum. *Biointerphases* **2010**, *5* (2), 30–36. https://doi.org/10.1116/1.3407483.

(29) Donatan, S.; Sarikaya, M.; Tamerler, C.; Urgen, M. Effect of Solid Surface Charge on the Binding Behaviour of a Metal-Binding Peptide. *J. R. Soc. Interface* **2012**, *9* (75), 2688–

2695. https://doi.org/10.1098/rsif.2012.0060.
(30) Scopelliti, P. E.; Borgonovo, A.; Indrieri, M.; Giorgetti, L.; Bongiorno, G.; Carbone, R.; Podestà, A.; Milani, P. The Effect of Surface Nanometre-Scale Morphology on Protein Adsorption. *PLoS One* **2010**, *5* (7), 1–9. https://doi.org/10.1371/journal.pone.0011862.
(31) Sarikaya, M.; Tamerler, C.; Jen, A. K.; Schulten, K.; Baneyx, F. Molecular Biomimetics-Nanotechnology through Biology. *Nat. Mater.* **2003**, *2*, 577–585.
(32) Maduraiveeran, G.; Sasidharan, M.; Ganesan, V. Electrochemical Sensor and Biosensor Platforms Based on Advanced Nanomaterials for Biological and Biomedical Applications. *Biosens. Bioelectron.* **2018**, *103*, 113–129. https://doi.org/10.1016/j.bios.2017.12.031.
(33) Erol, O.; Uyan, I.; Hatip, M.; Yilmaz, C. Recent Advances in Bioactive 1D and 2D Carbon Nanomaterials for Biomedical Applications. *Nanomedicine Nanotechnology, Biol. Med.* **2018**, *14* (7), 2433–2454. https://doi.org/10.1016/j.nano.2017.03.021.
(34) So, C. R.; Tamerler, C.; Sarikaya, M. Adsorption, Diffusion, and Self-Assembly of an Engineered Goldbinding Peptide on Au(111) Investigated by Atomic Force Microscopy. *Angew. Chemie - Int. Ed.* **2009**, *48* (28), 5174–5177. https://doi.org/10.1002/anie.200805259.
(35) Wittrup, K. D. Protein Engineering by Cell-Surface Display. *Curr. Opin. Biotechnol.* **2001**, *12* (4), 395–399. https://doi.org/10.1016/S0958-1669(00)00233-0.
(36) Evans, J. S.; Samudrala, R.; Walsh, T. R.; Oren, E. E.; Tamerler, C. Molecular Design of Inorganic-Binding Polypeptides. *MRS Bull.* **2008**, *33* (5), 514–518. https://doi.org/10.1557/mrs2008.103.
(37) Tamerler, C.; Sarikaya, M. Molecular Biomimetics: Genetic Synthesis, Assembly, and Formation of Materials Using Peptides. *MRS Bull.* **2008**, *33* (5), 504–512. https://doi.org/10.1557/mrs2008.102.
(38) Tamerler, C.; Duman, M.; Oren, E. E.; Gungormus, M.; Xiong, X.; Kacar, T.; Parviz, B. A.; Sarikaya, M. Materials Specificity and Directed Assembly of a Gold-Binding Peptide. *Small* **2006**, *2* (11), 1372–1378. https://doi.org/10.1002/smll.200600070.
(39) Tamerler, C.; Oren, E. E.; Duman, M.; Venkatasubramanian, E.; Sarikaya, M. Adsorption Kinetics of an Engineered Gold Binding Peptide by Surface Plasmon Resonance Spectroscopy and a Quartz Crystal Microbalance. *Langmuir* **2006**, *22* (18), 7712–7718. https://doi.org/10.1021/la0606897.
(40) Ramakrishnan, S. K.; Jebors, S.; Martin, M.; Cloitre, T.; Agarwal, V.; Mehdi, A.; Martinez, J.; Subra, G.; Gergely, C. Engineered Adhesion Peptides for Improved Silicon Adsorption. *Langmuir* **2015**, *31* (43), 11868–11874. https://doi.org/10.1021/acs.langmuir.5b02857.
(41) Naik, R. R.; Jones, S. E.; Murray, C. J.; McAuliffe, J. C.; Vaia, R. A.; Stone, M. O. Peptide Templates for Nanoparticle Synthesis Derived from Polymerase Chain Reaction-Driven Phage Display. *Adv. Funct. Mater.* **2004**, *14* (1), 25–30. https://doi.org/10.1002/adfm.200304501.
(42) Hnilova, M.; Liu, X.; Yuca, E.; Jia, C.; Wilson, B.; Karatas, A. Y.; Gresswell, C.; Ohuchi, F.; Kitamura, K.; Tamerler, C. Multifunctional Protein-Enabled Patterning on Arrayed Ferroelectric Materials. *ACS Appl. Mater. Interfaces* **2012**, *4* (4), 1865–1871. https://doi.org/10.1021/am300177t.
(43) Zareie, H. M.; Sarikaya, M. Assembly of Gold-Binding Proteins for Biomolecular Recognition. *Austin J. Biosens. Bioelectron.* **2015**, *1* (1), 1–4.
(44) Hnilova, M.; Khatayevich, D.; Carlson, A.; Oren, E. E.; Gresswell, C.; Zheng, S.; Ohuchi, F.; Sarikaya, M.; Tamerler, C. Single-Step Fabrication of Patterned Gold Film Array by an

Engineered Multi-Functional Peptide. *J. Colloid Interface Sci.* **2012**, *365* (1), 97–102. https://doi.org/10.1016/j.jcis.2011.09.006.

(45) Hnilova, M.; Karaca, B. T.; Park, J.; Jia, C.; Wilson, B. R.; Sarikaya, M.; Tamerler, C. Fabrication of Hierarchical Hybrid Structures Using Bio-Enabled Layer-by-Layer Self-Assembly. *Biotechnol. Bioeng.* **2012**, *109* (5), 1120–1130. https://doi.org/10.1002/bit.24405.

(46) Kopacz, M. M.; Rovida, S.; Van Duijn, E.; Fraaije, M. W.; Mattevi, A. Structure-Based Redesign of Cofactor Binding in Putrescine Oxidase. *Biochemistry* **2011**, *50* (19), 4209–4217. https://doi.org/10.1021/bi200372u.

(47) Kopacz, M. M.; Heuts, D. P. H. M.; Fraaije, M. W. Kinetic Mechanism of Putrescine Oxidase from Rhodococcus Erythropolis. *FEBS J.* **2014**, *281* (19), 4384–4393. https://doi.org/10.1111/febs.12945.

(48) Moonen, M. J. H.; Fraaije, M. W.; Rietjens, I. M. C. M.; Laane, C.; Van Berkel, W. J. H. Flavoenzyme-Catalyzed Oxygenations and Oxidations of Phenolic Compounds. *Adv. Synth. Catal.* **2002**, *344* (10), 1023–1035. https://doi.org/10.1002/1615-4169(200212)344:10<1023::AID-ADSC1023>3.0.CO;2-T.

(49) Ulapane, S. B.; Kamathewatta, N. J. B.; Ashberry, H. M.; Berrie, C. L. Controlled Electroless Deposition of Noble Metals on Silicon Substrates Using Self-Assembled Monolayers as Molecular Resists to Generate Nanopatterned Surfaces for Electronics and Plasmonics. *ACS Appl. Nano Mater.* **2019**, *2* (12), 7114–7125. https://doi.org/10.1021/acsanm.9b01641.

(50) Brzoska, J. B.; Azouz, I. Ben; Rondelez, F. Silanization of Solid Substrates: A Step toward Reproducibility. *Langmuir* **1994**, *10* (11), 4367–4373. https://doi.org/10.1021/la00023a072.

(51) Headrick, J. E.; Armstrong, M.; Cratty, J.; Hammond, S.; Sheriff, B. A.; Berrie, C. L. Nanoscale Patterning of Alkyl Monolayers on Silicon Using the Atomic Force Microscope. *Langmuir* **2005**, *21* (9), 4117–4122. https://doi.org/10.1021/la0481905.

(52) Xu, S.; Liu, G. Nanometer-Scale Fabrication by Simultaneous Nanoshaving and Molecular Self-Assembly. *Langmuir* **2002**, *13* (2), 127–129. https://doi.org/10.1021/la962029f.

(53) Chen, Y. Nanofabrication by Electron Beam Lithography and Its Applications: A Review. *Microelectron. Eng.* **2015**, *135*, 57–72. https://doi.org/10.1016/j.mee.2015.02.042.

(54) Tseng, A. A.; Chen, K.; Chen, C. D.; Ma, K. J. Electron Beam Lithography in Nanoscale Fabrication: Recent Development. *IEEE Trans. Electron. Packag. Manuf.* **2003**, *26* (2), 141–149. https://doi.org/10.1109/TEPM.2003.817714.

(55) Doan, N. M.; Qiang, L.; Li, Z.; Vaddiraju, S.; Bishop, G. W.; Rusling, J. F.; Papadimitrakopoulos, F. Low-Cost Photolithographic Fabrication of Nanowires and Microfilters for Advanced Bioassay Devices. *Sensors (Switzerland)* **2015**, *15* (3), 6091–6104. https://doi.org/10.3390/s150306091.

(56) Garno, J. C.; Amro, N. A.; Wadu-mesthrige, K.; Liu, G.-Y. Production of Periodic Arrays of Protein Nanostructures Using Particle Lithography. *Langmuir* **2002**, *18* (21), 8186–8192. https://doi.org/10.1021/la020518b.

(57) Saner, C. K.; Lu, L.; Zhang, D.; Garno, J. C. Chemical Approaches for Nanoscale Patterning Based on Particle Lithography with Proteins and Organic Thin Films. *Nanotechnol Rev* **2015**, *4* (2), 129–143. https://doi.org/10.1515/ntrev-2015-0002.

(58) Li, J.; Lusker, K. L.; Yu, J.; Garno, J. C. Engineering the Spatial Selectivity of Surfaces at the Nanoscale Using Particle Lithography Combined with Vapor Deposition of

Organosilanes. *ACS Nano* **2009**, *3* (7), 2023–2035.
(59) So, C. R.; Hayamizu, Y.; Yazici, H.; Gresswell, C.; Khatayevich, D.; Tamerler, C.; Sarikaya, M. Controlling Self-Assembly of Engineered Peptides on Graphite by Rational Mutation. *ACS Nano* **2012**, *6* (2), 1648–1656. https://doi.org/10.1021/nn204631x.
(60) Jung, Y.; Jeong, M. L.; Jung, H.; Bong, H. C. Self-Directed and Self-Oriented Immobilization of Antibody by Protein G-DNA Conjugate. *Anal. Chem.* **2007**, *79* (17), 6534–6541. https://doi.org/10.1021/ac070484i.
(61) Tabaei, S. R.; Jackman, J. A.; Kim, S. O.; Zhdanov, V. P.; Cho, N. J. Solvent-Assisted Lipid Self-Assembly at Hydrophilic Surfaces: Factors Influencing the Formation of Supported Membranes. *Langmuir* **2015**, *31* (10), 3125–3134. https://doi.org/10.1021/la5048497.
(62) Tamada, K.; Hara, M.; Sasabe, H.; Knoll, W. Surface Phase Behavior of n -Alkanethiol Self-Assembled Monolayers Adsorbed on Au(111): An Atomic Force Microscope Study. *Langmuir* **1997**, *13* (6), 1558–1566. https://doi.org/10.1021/la950630s.
(63) Maoz, R.; Matlis, S.; DiMasi, E.; Ocko, B. M.; Sagiv, J. Self-Replicating Amphiphilic Monolayers. *Nature* **1996**, *384* (6605), 150–153. https://doi.org/10.1038/384150a0.
(64) Zhang, S. Fabrication of Novel Biomaterials through Molecular Self-Assembly. *Nat. Biotechnol.* **2003**, *21* (10), 1171–1178. https://doi.org/10.1038/nbt874.
(65) Ginger, D. S.; Zhang, H.; Mirkin, C. A. The Evolution of Dip-Pen Nanolithography. *Angew. Chemie - Int. Ed.* **2004**, *43* (1), 30–45. https://doi.org/10.1002/anie.200300608.
(66) Salaita, K.; Wang, Y.; Mirkin, C. A. Applications of Dip-Pen Nanolithography. *Nat. Nanotechnol.* **2007**, *2* (1), 145–155.
(67) Liu, G.; Hirtz, M.; Fuchs, H.; Zheng, Z. Development of Dip-Pen Nanolithography (DPN) and Its Derivatives. *Small* **2019**, *15* (21), 1–9. https://doi.org/10.1002/smll.201900564.
(68) Demers, L. M. Direct Patterning of Modified Oligonucleotides on Metals and Insulators by Dip-Pen Nanolithography. *Science (80-.).* **2002**, *296* (5574), 1836–1838. https://doi.org/10.1126/science.1071480.
(69) Nyamjav, D.; Ivanisevic, A. Properties of Polyelectrolyte Templates Generated by Dip-Pen Nanolithography and Microcontact Printing. *Chem. Mater.* **2004**, *16* (25), 5216–5219. https://doi.org/10.1021/cm049179t.
(70) Zhang, Y.; Salaita, K.; Lim, J. H.; Mirkin, C. A. Electrochemical Whittling of Organic Nanostructures. *Nano Lett.* **2002**, *2* (12), 1389–1392. https://doi.org/10.1021/nl0202298.
(71) Lee, K. B.; Lim, J. H.; Mirkin, C. A. Protein Nanostructures Formed via Direct-Write Dip-Pen Nanolithography. *J. Am. Chem. Soc.* **2003**, *125* (19), 5588–5589. https://doi.org/10.1021/ja034236p.
(72) Gundiah, G.; John, N. S.; Thomas, P. J.; Kulkarni, G. U.; Rao, C. N. R.; Heun, S. Dip-Pen Nanolithography with Magnetic Fe2O3 Nanocrystals. *Appl. Phys. Lett.* **2004**, *84* (26), 5341–5343. https://doi.org/10.1063/1.1766399.
(73) Ding, L.; Li, Y.; Chu, H.; Li, X.; Liu, J. Creation of Cadmium Sulfide Nanostructures Using AFM Dip-Pen Nanolithography. *J. Phys. Chem. B* **2005**, *109* (47), 22337–22340. https://doi.org/10.1021/jp053389r.
(74) Porter, L. A.; Ribbe, A. E.; Buriak, J. M. Metallic Nanostructures via Static Plowing Lithography. *Nano Lett.* **2003**, *3* (8), 1043–1047. https://doi.org/10.1021/nl034328c.
(75) Haynes, C. L.; McFarland, A. D.; Smith, M. T.; Hulteen, J. C.; Van Duyne, R. P. Angle-Resolved Nanosphere Lithography: Manipulation of Nanoparticle Size, Shape, and Interparticle Spacing. *J. Phys. Chem. B* **2002**, *106* (8), 1898–1902. https://doi.org/10.1021/jp013570+.

(76) Li, J. R.; Garno, J. C. Nanostructures of Octadecyltrisiloxane Self-Assembled Monolayers Produced on Au(111) Using Particle Lithography. *ACS Appl. Mater. Interfaces* **2009**, *1* (4), 969–976. https://doi.org/10.1021/am900118x.

(77) Taylor, Z. R.; Keay, J. C.; Sanchez, E. S.; Johnson, M. B.; Schmidtke, D. W. Independently Controlling Protein Dot Size and Spacing in Particle Lithography. *Langmuir* **2012**, *28* (25), 9656–9663. https://doi.org/10.1021/la300806m.

(78) Mornet, S.; Brétagnol, F.; Mannelli, I.; Valsesia, A.; Sirghi, L.; Colpo, P.; Rossi, F. Large-Scale Fabrication of Bi-Functional Nanostructured Polymer Surfaces for Selective Biomolecular Adhesion. *Small* **2008**, *4* (11), 1919–1924. https://doi.org/10.1002/smll.200701162.

(79) Chan, Y. H.; Chen, J.; Wark, S. E.; Skiles, S. L.; Son, D. H.; Batteas, J. D. Using Patterned Arrays of Metal Nanoparticles to Probe Plasmon Enhanced Luminescence of CdSe Quantum Dots. *ACS Nano* **2009**, *3* (7), 1735–1744. https://doi.org/10.1021/nn900317n.

(80) Hulteen, J. C.; Van Duyne, R. P. "Nanosphere Lithography: A Materials General Fabrication Process for Periodic Particle Array Surfaces. *J. Vac. Sci. Technol.* **1995**, *13* (3), 1553–1558.

(81) Jensen, T. R.; Schatz, G. C.; Van Duyne, R. P. Nanosphere Lithography: Surface Plasmon Resonance Spectrum of a Periodic Array of Silver Nanoparticles by Ultraviolet - Visible Extinction Spectroscopy and Electrodynamic Modeling. *J. Phys. Chem. B* **1999**, *103* (13), 2394–2401. https://doi.org/10.1021/jp984406y.

(82) Fischer, U. C.; Zingsheim, H. P. Submicroscopic Pattern Replication with Visible Light. *J. Vac. Sci. Technol.* **1981**, *19* (4), 881–885.

(83) Shacham-Diamand, Y.; Osaka, T.; Okinaka, Y.; Sugiyama, A.; Dubin, V. 30 Years of Electroless Plating for Semiconductor and Polymer Micro-Systems. *Microelectron. Eng.* **2015**, *132*, 35–45. https://doi.org/10.1016/j.mee.2014.09.003.

(84) Lahiri, A.; Kobayashi, S. Electroless Deposition of Gold on Silicon and Its Potential Applications : Review. *Surf. Eng.* **2015**, *32* (5), 321–337. https://doi.org/10.1179/1743294415Y.0000000060.

(85) Gray, J. E.; Norton, P. R.; Alnouno, R.; Marolda, C. L.; Valvano, M. A.; Griffiths, K. Biological Efficacy of Electroless-Deposited Silver on Plasma Activated Polyurethane. *Biomaterials* **2003**, *24* (16), 2759–2765. https://doi.org/10.1016/S0142-9612(03)00057-7.

(86) Osaka, T. Co-Based Soft Magnetic Films Produced by Electroless Deposition. *J. Electrochem. Soc.* **2006**, *139* (5), 1311. https://doi.org/10.1149/1.2069402.

(87) Porter, L. A.; Choi, H. C.; Ribbe, A. E.; Buriak, J. M. Controlled Electroless Deposition of Noble Metal Nanoparticle Films on Germanium Surfaces. *Nano Lett.* **2002**, *2* (10), 1067–1071. https://doi.org/10.1021/nl025677u.

(88) Khoperia, T. N. Electroless Deposition in Nanotechnology and ULSI. *Microelectron. Eng.* **2003**, *69*, 384–390. https://doi.org/10.1016/S0167-9317(03)00325-3.

(89) Osaka, T.; Takano, N.; Yokoshima, T. Microfabrication of Electro- and Electroless-Deposition and Its Application in the Electronic Field. *Surf. Coatings Technol.* **2003**, *169–170*, 1–7. https://doi.org/10.1016/S0257-8972(03)00037-9.

(90) Shacham-Diamand, Y.; Osaka, T.; Okinaka, Y.; Sugiyama, A.; Dubin, V. 30 Years of Electroless Plating for Semiconductor and Polymer Micro-Systems. *Microelectron. Eng.* **2015**, *132*, 35–45. https://doi.org/10.1016/j.mee.2014.09.003.

(91) Ali, H. O.; Christie, I. R. A. A Review of Electroless Gold Deposition Processes. *Circuit World*. 1985, pp 10–16. https://doi.org/10.1108/eb043759.

(92) Silverman, S. J.; Benn, D. R. Junction Delineation in Silicon by Gold Chemiplating. *J. Electrochem. Soc* **1958**, *105*, 170–172.
(93) Nagahara, L. A.; Ohmori, T.; Hashimoto, K.; Fujishima, A. Effects of HF Solution in the Electroless Deposition Process on Silicon Surfaces. *J. Vac. Sci. Technol. A Vacuum, Surfaces, Film.* **1993**, *11* (4), 763–767. https://doi.org/10.1116/1.578344.
(94) Jing, F.; Tong, H.; Kong, L.; Wang, C. Electroless Gold Deposition on Silicon(100) Wafer Based on a Seed Layer of Silver. *Appl. Phys. A* **2005**, *80*, 597–600. https://doi.org/10.1007/s00339-003-2236-z.
(95) Plass, R.; Marks, D. Submonolayer Au on Si (111) Phase Diagram. **1997**, *380*, 497–506.
(96) Warren, S.; Reitzle, A.; Kazimirov, A.; Ziegler, J. C.; Bunk, O.; Cao, L. X.; Renner, F. U.; Kolb, D. M.; Bedzyk, M. J.; Zegenhagen, J. A Structure Study of the Electroless Deposition of Au on Si(111):H. *Surf. Sci.* **2002**, *496* (3), 287–298. https://doi.org/10.1016/S0039-6028(01)01589-8.
(97) Sullivan, A. M.; Kohl, P. A. The Autocatalytic Deposition of Gold in Nonalkaline, Gold Thiosulfate Electroless Bath. *J. Electrochem. Soc.* **1995**, *142* (7), 2250–2255. https://doi.org/10.1149/1.2044282.
(98) Kato, M.; Yazawa, Y.; Okinaka, Y. Electroless Gold Plating Bath Using Ascorbic Acid as Reducing Agent - Recent Improvements. *Lancet* **1979**, *1* (8116), 615.
(99) Osaka, T.; Okinaka, Y.; Sasano, J.; Kato, M. Development of New Electrolytic and Electroless Gold Plating Processes for Electronics Applications. *Science and Technology of Advanced Materials*. 2006, pp 425–437. https://doi.org/10.1016/j.stam.2006.05.003.
(100) Ali, H. O.; Christie, I. R. A. A Review of Electroless Gold Deposition Processes. *Circuit World* **1984**, *17* (4), 118–127. https://doi.org/10.1108/eb043759.
(101) Lin, J. Y.; Hsueh, Y. L.; Huang, J. J. The Concentration Effect of Capping Agent for Synthesis of Silver Nanowire by Using the Polyol Method. *J. Solid State Chem.* **2014**, *214*, 2–6. https://doi.org/10.1016/j.jssc.2013.12.017.
(102) Kittler, S.; Greulich, C.; Köller, M.; Epple, M. Synthesis of PVP-Coated Silver Nanoparticles and Their Biological Activity towards Human Mesenchymal Stem Cells. *Mater. Sci. Eng. Technol.* **2009**, *40* (4), 258–264. https://doi.org/10.1002/mawe.200800437.
(103) Kumar, S.; Gandhi, K. S.; Kumar, R. Modeling of Formation of Gold Nanoparticles by Citrate Method. *Ind. Eng. Chem. Res.* **2007**, *46* (10), 3128–3136. https://doi.org/10.1021/ie060672j.
(104) Kilin, D. S.; Prezhdo, O. V.; Xia, Y. Shape-Controlled Synthesis of Silver Nanoparticles: Ab Initio Study of Preferential Surface Coordination with Citric Acid. *Chem. Phys. Lett.* **2008**, *458* (1–3), 113–116. https://doi.org/10.1016/j.cplett.2008.04.046.
(105) Mårtensson, T.; Carlberg, P.; Borgström, M.; Montelius, L.; Seifert, W.; Samuelson, L. Nanowire Arrays Defined by Nanoimprint Lithography. *Nano Lett.* **2004**, *4* (4), 699–702. https://doi.org/10.1021/nl035100s.
(106) Maurer, J. H. M.; Reiser, B.; Kanelidis, I.; Kraus, T. Templated Self-Assembly of Ultrathin Gold Nanowires by Nanoimprinting for Transparent Flexible Electronics. **2016**, 10–14. https://doi.org/10.1021/acs.nanolett.5b04319.
(107) McLellan, J. M.; Geissler, M.; Xia, Y. Edge Spreading Lithography and Its Application to the Fabrication of Mesoscopic Gold and Silver Rings. *J. Am. Chem. Soc.* **2004**, *126* (35), 10830–10831. https://doi.org/10.1021/ja0470766.
(108) Vazquez-Mena, O.; Sannomiya, T.; Villanueva, L. G.; Voros, J.; Brugger, J. Metallic Nanodot Arrays by Stencil Lithography for Plasmonic Biosensing Applications. *ACS Nano*

2011, *5* (2), 844–853. https://doi.org/10.1021/nn1019253.

(109) Cappella, B.; Sturm, H.; Weidner, S. M. Breaking Polymer Chains by Dynamic Plowing Lithography. *Polymer (Guildf).* **2002**, *43* (16), 4461–4466. https://doi.org/10.1016/S0032-3861(02)00285-9.

(110) Aricò, A. S.; Bruce, P.; Scrosati, B.; Tarascon, J.; Schalkwijk, W. V. A. N.; Picardie, U. De; Verne, J.; Umr-, C. Nanostructured Materials for Advanced Energy Conversion and Storage Devices. *Nature* **2005**, *4*, 366–377.

(111) Saini, D.; Chauhan, R. P.; Kumar, S. Effects of Annealing on Structural and Magnetic Properties of Template Synthesized Cobalt Nanowires Useful as Data Storage and Nano Devices. *J. Mater. Sci. Mater. Electron.* **2014**, *25* (1), 124–127. https://doi.org/10.1007/s10854-013-1560-0.

(112) Kim, H.; Park, S.; Hinsberg, W. D. Block Copolymer Based Nanostructures : Materials , Processes , and Applications to Electronics. *Chem. Rev.* **2010**, *110* (1), 146–177.

(113) Kim, S. A.; Byun, K. M.; Kim, K.; Jang, S. M.; Ma, K.; Oh, Y.; Kim, D.; Kim, S. G.; Shuler, M. L.; Kim, S. J. Surface-Enhanced Localized Surface Plasmon Resonance Biosensing of Avian Influenza DNA Hybridization Using Subwavelength Metallic Nanoarrays. *Nanotechnology* **2011**, *22* (28), 289501 (1pp). https://doi.org/10.1088/0957-4484/22/28/289501.

(114) Barth, J. V; Costantini, G.; Kern, K. Engineering Atomic and Molecular Nanostructures at Surfaces. *Nature*. September 28, 2005, pp 671–679. https://doi.org/10.1038/nature04166.

(115) Vogel, E. M. Technology and Metrology of New Electronic Materials and Devices. *Nature* **2007**, *2*, 25–32.

(116) Jeon, J. H.; Joo, H.-Y.; Kim, Y.-M.; Lee, D. H.; Kim, J.-S.; Kim, Y. S.; Choi, T.; Park, B. H. Selector-Free Resistive Switching Memory Cell Based on BiFeO3 Nano-Island Showing High Resistance Ratio and Nonlinearity Factor. *Sci. Rep.* **2016**, *6* (1), 1–10. https://doi.org/10.1038/srep23299.

(117) Hong, A. J.; Liu, C.; Wang, Y.; Kim, J.; Xiu, F.; Ji, S.; Zou, J.; Nealey, P. F.; Wang, K. L. Metal Nanodot Memory by Self-Assembled Block Copolymer Lift-Off. *Nano Lett.* **2010**, *10*, 224–229. https://doi.org/10.1021/nl903340a.

(118) Tracey, J. I.; Carroll, D. M. O. Short-Wavelength Lasing-Spasing and Random Spasing with Deeply Subwavelength Thin-Film Gain Media. *Adv. Funct. Mater.* **2018**, *28* (39), 1–9. https://doi.org/10.1002/adfm.201802630.

(119) Fabris, L.; Dante, M.; Braun, G.; Lee, S. J.; Reich, N. O.; Moskovits, M.; Nguyen, T.; Bazan, G. C. A Heterogeneous PNA-Based SERS Method for DNA Detection. *J. Am. Ceram. Soc.* **2007**, *129*, 6086–6087. https://doi.org/10.1021/ja0705184.

(120) Zhang, J.; Atay, T.; Nurmikko, A. V. Optical Detection of Brain Cell Activity Using Plasmonic Gold Nanoparticles. *Nano Lett.* **2009**, *9* (2), 519–524.

Chapter 2: Materials and Methods Employed

2.1 Summary

This chapter introduces the techniques and the methodologies employed to carry out this project. The overall goal of this study was to selectively immobilize proteins tagged with a gold affinity peptide, on gold nanostructures fabricated on Si-OTS surfaces. To study the orientation of proteins on gold surfaces, atomic force microscopy (AFM) was used. In addition, ellipsometry, goniometry, UV-Visible spectrometry, vacuum evaporation and fluorescence imaging techniques were used to characterize the surfaces. Modifications to the surfaces were carried out using self-assembled monolayer formation, gold evaporation on mica, template stripping of gold, and electroless deposition of gold on Si surfaces. These techniques are all briefly discussed in this chapter.

Section 2.2 describes substrate preparation for a variety of different substrates used in the nanoscale fabrication and protein adsorption studies. This includes preparation of gold (evaporated, flame annealed, and template stripped), Si, mica, and graphite. The surface modification via self-assembly process is explained in section 2.3. Self-assembled monolayer (SAM) formation is a one of the major processes used in this thesis, which has applications in different fields including nanoelectronic devices, sensor arrays, supercapacitors, catalysts, rechargeable power sources etc.[1] General methodologies for SAM formation on Si and Au surfaces are discussed briefly in Section 2.3. To characterize films, ellipsometry, goniometry, and AFM have been used (Section 2.4-2.6). Ellipsometry measures the monolayer thickness of thin organic films on a reflective surface (Section 2.4). Goniometry measures the contact angle, which provides information about the hydrophilicity/hydrophobicity of a surface (Section 2.5). AFM can be used to characterize a number of surface properties including topography and the Section 2.6 discusses

the different modes of AFM utilized in this study (tapping mode and contact mode). The tapping mode AFM was primarily employed in the protein adsorption studies, while contact mode was used in AFM nanoshaving, and characterization of substrates.

An introduction to UV-Vis spectrometry can be found in Section 2.7, which was used for the gold nanoparticle characterization in solution phase. Based on the absorbance of light, information regarding size and shape of the nanoparticle formed can be determined.

Electroless deposition of Au on silicon surfaces is discussed in Section 2.8. Here, significant modifications have been made to the industrial plating solutions to obtain thin metal films on silicon surfaces which will be useful for nanoscale applications. These methods are used in *Chapters 5 and 6,* which describe the processes relevant for Au nanowire and nanodot array fabrication using ELD. Section 2.9 describes the general methodology used in protein adsorption studies onto different surfaces and these methods are used with minor changes in adsorption time in *Chapter 3-4* for protein binding studies.

2.2 Surface Preparation

For carrying out nanoscale studies such as metal nanostructure development or protein binding, either cleaning or preparation of the surface has to be done to avoid contamination. Preparation of surfaces must be done carefully since contamination can cause difficulties in proper film formation as well as in interpretation of topography data. For the AFM studies, flat and uniform surfaces are preferred. For each surface, the preparation procedure for producing flat, clean surfaces differs. The surfaces used are gold evaporated on mica, template stripped gold on glass, commercially available gold films on silicon (Platypus Technologies, referred to as “Platypus gold”), mica, silicon, and graphite. Gold and silicon surfaces can be further modified to

obtain different functionality via self-assembly monolayer (SAM) formation. On gold surfaces, SAMs of alkanethiols can be easily formed, and they are well known in literature.[2–4] By doing this, the functionality can be tuned in such a way to build a biologically friendly environment for protein attachment. Also, silicon surfaces can be modified to obtain more stable silane SAMs.[5–7] More importantly, silanes can be modified by using surface chemical reactions to obtain different functionalities.[8] For the purpose of studying protein-surface interactions and orientation, atomically flat surfaces are needed. Mica (hydrophilic), Graphite (hydrophobic), and silicon (hydrophilic) surfaces are atomically flat and they can be utilized to study protein surface interactions without further modification beyond cleavage or cleaning. Most of the commercially available gold surfaces are not atomically smooth and the use of template stripping allows larger domains of uniform Au(111) terraces to be exposed for investigation.[9–11] The preparation strategies for each surface utilized are described below.

2.2.1 Gold Evaporation on to Mica Surfaces

In our lab, we commonly use four different types of gold substrates: commercially available thin film gold on silicon (Platypus gold)[12], in-house thermally evaporated gold, hydrogen flame annealed gold, and template-stripped gold (TSG). These gold films have different characteristics such as thickness, grain size, and optical properties. These will be discussed within each section of the surface preparation.

Mica is atomically flat and can be easily used to evaporate gold epitaxially without an adhesion layer, unlike other surfaces such as silicon and glass. For evaporation, freshly cleaved mica was used to prevent dust and organic matter interference. The instrument utilized was an

Edwards Auto 306 Vacuum Evaporator and the major compartments are shown below (*Figure 2.1).*[13]

First, freshly cleaved mica was mounted on a sample plate via solvent cleaned (ethanol) metal bars and screws. The sample plate was secured into the rotating axel allowing sample rotation during evaporation for uniform film deposition. A tungsten wire basket was used to hold the piece of gold shot (cleaned by rinsing with chloroform and methanol). Next, the sample holder was covered by the shutter to prevent the deposition of the surface contamination layer from the evaporation source on to the mica substrate as it is initially heated. The evaporation chamber contains a bell jar mounted to the evaporator using rubber gaskets and vacuum grease. Before starting any evaporation, the bell jar, rubber gaskets, and sample holder should be cleaned well using ethanol (both inside and outside). Then the bell jar and rubber gaskets must be inserted using a minimum amount of grease on either side of the rubber gasket. Before the vacuum pump is turned on, the cooling lines for the diffusion pump are switched on, and liquid nitrogen was added to the cold trap above the diffusion pump to reduce the back streaming of the pump oil in to the evaporation chamber. Once the chamber was sealed, it was pumped down to ~10^{-6} torr while monitoring using a Penning gauge. Next, the chamber was heated by a quartz lamp mounted inside the chamber, controlled by a temperature controller, until the pressure can be maintained at 1-4 × 10^{-6} Torr at the desired temperature. The coating temperature was set to 200-220 ˚C, and the temperature controller, monitoring a thermocouple inside the chamber, turned the lamp turned on and off to keep the temperature to a set value. When the temperature and pressure inside the evaporation chamber reach the desired values, gold coating on to mica/glass was started. The tungsten basket inside the chamber was heated through resistive heating, running current through the basket, until the desired evaporation rate was reached and then the sample shutter was removed

to start coating. The pressure in the chamber during evaporation was slightly higher during the evaporation, due the evaporation. The current was controlled to maintain an evaporation rate of 0.5-1 Å/s[11], monitored by Quartz Crystal Microbalance (QCM) which located near the rotating sample holder. The rate of evaporation and the substrate temperature strongly influence the grain size and roughness of the evaporated surface. Slow evaporation rates lead to larger flat Au(111) grains, which is required for AFM investigations. Once the desired film thickness was reached, the shutter over the evaporation source was closed and the thickness from the QCM was recorded. It should be noted here, that the QCM is not located in exactly the same position in the chamber as the substrate, so the thickness of gold evaporated onto the sample will not be exactly the same as that read by the QCM, but AFM measurements in our lab have indicated that it is close (with ~10-15%) and the thicknesses for these experiments are not critical, so no further calibration has been carried out. Then, the current was gradually decreased and switched off (this may take 10-15 minutes). The substrates were held at the evaporation temperature for annealing for 3 hours after the evaporation to improve film quality. Then, the heater lamp is turned off, and the system was cooled for 30 to 45 minutes until reached room temperature. Finally, water supply for the cooling system is turned off and the evaporator is switched off and vented before the samples are removed.

These samples were characterized using visual inspection, goniometry, and the AFM to determine the grain size and roughness of the surface (see *Table 2.1*). *Figure 2.2* shows representative AFM image of gold surfaces following different preparation methods along with the cross-sectional profiles. The initially prepared gold on mica surface contains relatively small Au grains with significant height variations (*Figure 2.2a*) which can be improved through the methods described below.

2.2.2 Flame Annealing of Evaporated Gold on Mica

From the root mean square average of height deviation (Rq image roughness) and grain sizes obtained from the initial thermally evaporated gold via AFM, it can be concluded that the sizes of the grains are not ideal for imaging the conformations of proteins on the surface (which requires large, flat terraces). To obtain larger grain sizes and smaller roughness values, flame annealing[11,14] was carried out using a flame of Hydrogen (H_2) gas. Gold on mica pieces (roughly 10 × 10 cm) were kept on a thick sheet of mica (flat surface). Then the hydrogen gas flame was prepared by using a gas tank, regulator, flashback arrestor and quartz tube with a taper to a very small aperture. The Quartz tube was connected to the gas tank (with a back-flash arrestor) with a very small nitrogen flow and the flame was ignited with a striker under dark conditions to visualize the flame clearly (the hydrogen flame is quite difficult to see under ambient light). Initially, the flame was yellow in color and was allowed to sit a few minutes to become blue with orange rim (this may be due to having junk and organic matters trapped inside the tube and surroundings). Then the flame was adjusted to 3-4 cm long before start annealing. An increase of temperature allows gold atoms to diffuse on the surface and to move to voids. This will increase the grain size and decrease the roughness of the surface. Initially, the flame was scanned on the mica surface a few minutes to desorb contaminants before the annealing procedure. Then the gold/mica sample was placed on the freshly cleaned mica, and the flame was raster scanned across the surface for 30 seconds. This was done with the flame at 30˚angle with respect to the surface at a distance of a few centimeters away from the surface to avoid overheating of the sample. Finally, the flame was turned off, and the sample was kept in a desiccator after cooling. A representative AFM image of an evaporated gold film following flame annealing is shown in *Figure 2.2B* and *Table 2.1* contains

all the characterization data. The annealed surfaces have lower surface roughness and higher grain sizes than the unannealed surfaces (see *Table 2.1*).

2.2.3 TSG surface formation

Freshly cleaved mica surfaces are atomically smooth over larger areas, have comparable lattice parameters to Au(111), and are contamination free upon initial exposure.[15] This leads to epitaxial growth of large Au(111) grains on mica. As growth proceeds, strain builds in the film creating defects and increasing roughness. Therefore, the first few layers are the flattest layers that can be obtained. The template stripping process exposes the gold that was initially deposited at the mica interface. So the process of template stripping allows the exposure of the large Au(111) grains that formed at the initial interface.[10,16,17]

The process for template stripping is shown in *Figure 2.3*. Glass cover slides were cut into approximately 1.0 × 1.0 cm^2 pieces by using a scribe and then washed with acetone and distilled water. To glue the glass onto the exposed gold surface, epoxy kit (EPO-TEK 377) parts A and B from Epoxy Technology were used. For this, equal volumes of epoxy part A and B were obtained to glass pipette, added to a sample vial and vortexed for roughly 1 to 2 minutes. The gold coated mica samples were cut to small pieces (~1 cm^2) and a small drop of the epoxy mixture was applied using Q-tip on to a gold side. Then the glass piece was placed on top of that using a tweezer, to press it against a mica surface until a thin layer of epoxy spread through the surface and all the gas bubbles are gone.

Prepared samples were kept in the oven at 80 ˚C for 4-24 hours. After the desired time interval, samples were cooled and taken out (see *Figure 2.3*). These samples can be stored until needed and are cleaved immediately before use. Samples were mechanically cleaved using a

tweezer by pressing the sample and gently peeling off the mica from glass which allows the exposure of atomically flat gold layer. In some occasions, when peeling, mica pieces adhere to the the gold surface due to incomplete cleavage. This can be overcome by placing a piece of scotch tape on top of the area with remaining mica and peeling it off quickly. Images of a typical templated stripped gold sample are shown in *Figure 2.2* and the roughness, grain sizes, contact angles are shown in *Table 2.1*. The data shows that the roughness of TSG is smaller than the flame annealed and the evaporated gold. The average grain size of the TSG is higher than that of the evaporated Au and lower than the FA-Au.

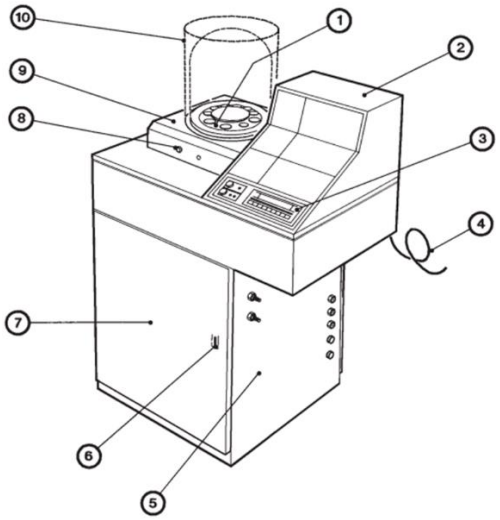

Figure 2. 1: *Edwards Auto 306 Vacuum Evaporator. 1. Base plate, 2. Control cabinet, 3. Auto 306 controller, 4. Electrical supply cable, 5. Service panel, 6. Front door lock, 7. Front door, 8. Needle valve, 9. Front baseplate cover, and 10. bell jar and implosion guard*

.

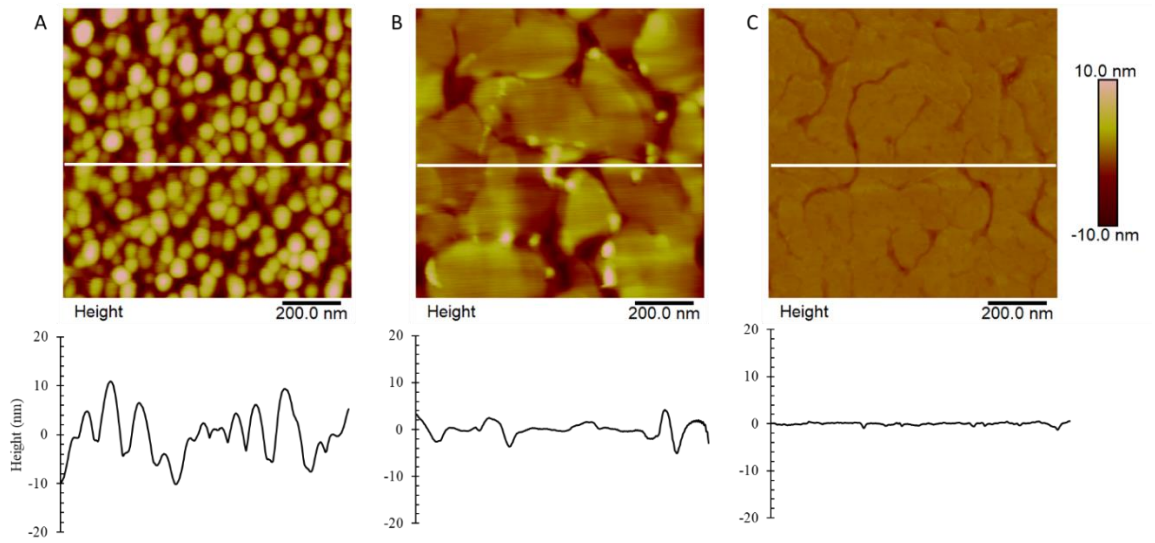

Figure 2. 2: *The AFM images of A. Evaporated, B. Flame annealed, and C. Template stripped gold surfaces. The white line on the surface is where the cross-section was taken. The representative cross-section of each image is shown under each image. The images are 1.0 µm × 1.0 µm in size and representative height scales are shown next to image.*

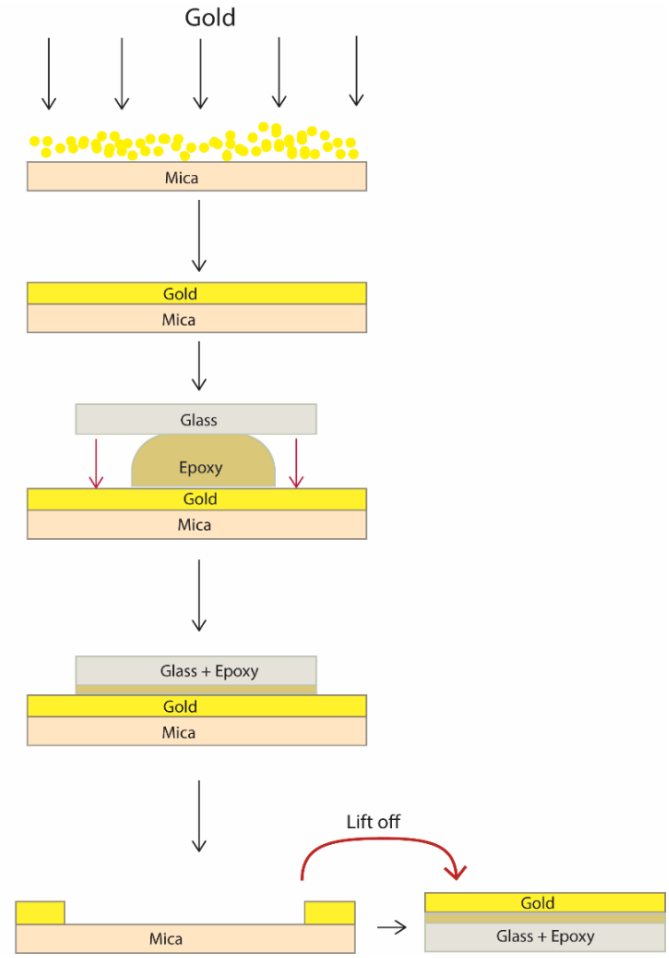

***Figure 2. 3**: The process of template stripping from the evaporated gold on to mica.*

***Table 2. 1:** The typical contact angle, Rq roughness and the grain sizes for different types of gold surfaces prepared in lab.*

Type of Au Surface	**Contact angle (°)**	**Rq roughness over 1.0×1.0 µm^2 (nm)**	**Grain size (nm)**
Evaporated	40-60	4.1	40-90
Flame annealed	40-60	2.1	200-600
Template stripped	40-60	0.9	100-500

2.2.4 Si(111) Surface Preparation

Si wafers were purchased from Virginia Semiconductor, Inc. and were cut approximately into 1.0×1.0 cm pieces using a diamond tipped scribe. Then, the pieces were washed with DI water to remove any particles and dried with a stream of nitrogen. Piranha solution was made by adding (3:7 ratio of) 30% H_2O_2 and concentrated H_2SO_4 to a beaker inside a fume hood. *Piranha solution is extremely corrosive and reacts violently with organic compounds. It must be handled with appropriate personal protective clothing and must not be stored in closed containers*. Then the solution was boiled, and the dried Si samples were added into the solution for 25-20 minutes. For all the operations inside the solution, piranha resistant tweezers (Teflon) were used. Then the samples were taken out, washed with DI water and dried under stream of nitrogen gas. To dispose of the used piranha solution, sodium bisulfite was added until bubbling was reduced, and sodium bicarbonate was added until pH reaches neutral. Cleanliness of the samples was checked by using contact angle measurements and AFM imaging.

The average contact angle of piranha cleaned silicon surface was 0-5°, AFM images and cross-sectional profile is shown in *Figure 2.4*. The Rq roughness of the surface over $1.0 \times 1.0\ \mu m^2$ was 0.061±0.003 nm. This indicates the silicon surfaces are uniform and flat, which can be used to study nanoparticle growth, protein adsorption, orientation and dimension analysis. Once the cleaning was completed, samples were used for electroless deposition, protein binding or monolayer formation.

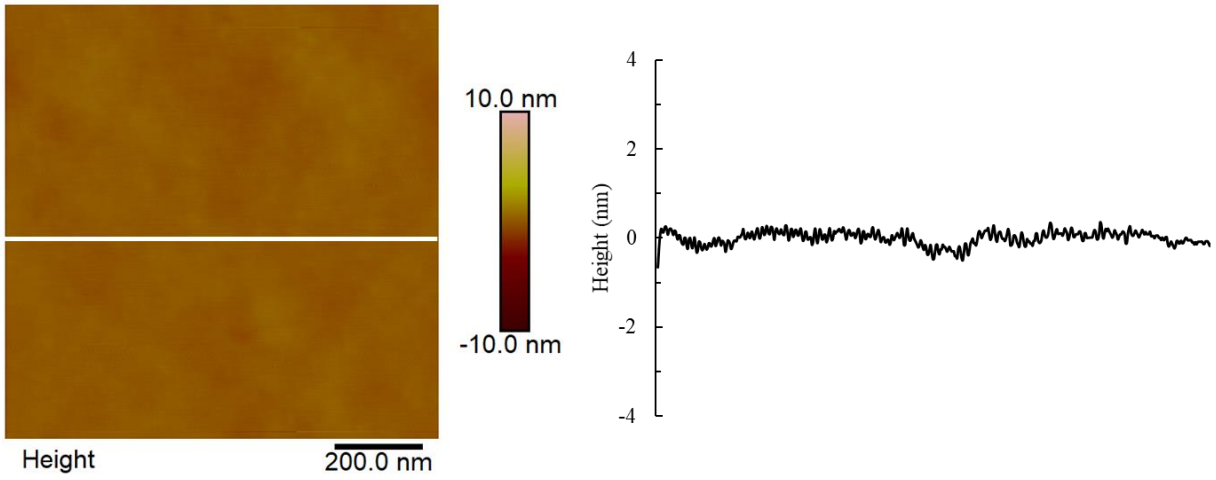

Figure 2. 4: *The AFM topography image of bare Si(111) surface with the cross-sectional profile. The white line on the surface is where the cross-section was taken. Size of the image is 1.0 ×1.0 µm2 and the relevant height scale is shown next to the figure.*

2.2.5 Graphite Surface Preparation

Graphite surfaces are used as models for hydrophobic surfaces which are atomically flat and can be utilized to study the orientation and dimensions of adsorbed protein molecules.[18,19] Graphite is composed of six-membered fused carbon rings.[20] Grade ZYH-HOPG (highly oriented pyrolytic graphite) graphite samples were obtained from Bruker and freshly cleaved before use. The freshly cleaved surface had large contact angles, indicating the hydrophobic nature of the surface. *Figure 5* shows the AFM topography image and the cross-sectional profile of a 2.0×2.0 μm^2 area of a freshly cleaved graphite surface. The Rq roughness of 0.154±0.003 nm over 2×2 μm^2 area indicates the smoothness of the surface and the AFM image height scale indicates the uniform nature of the surface. The characteristic step edge of the graphite surface is 0.34±0.08 nm, and it represents the height of a single layer of a graphite sheet (*See Figure 2.5*). These surfaces are beneficial to study the hydrophobic interactions of proteins on surfaces and to observe the unfolding and aggregation of protein molecules when they are not compatible. Arrows show step edges of the different sheets in *Figure 2.5* below.

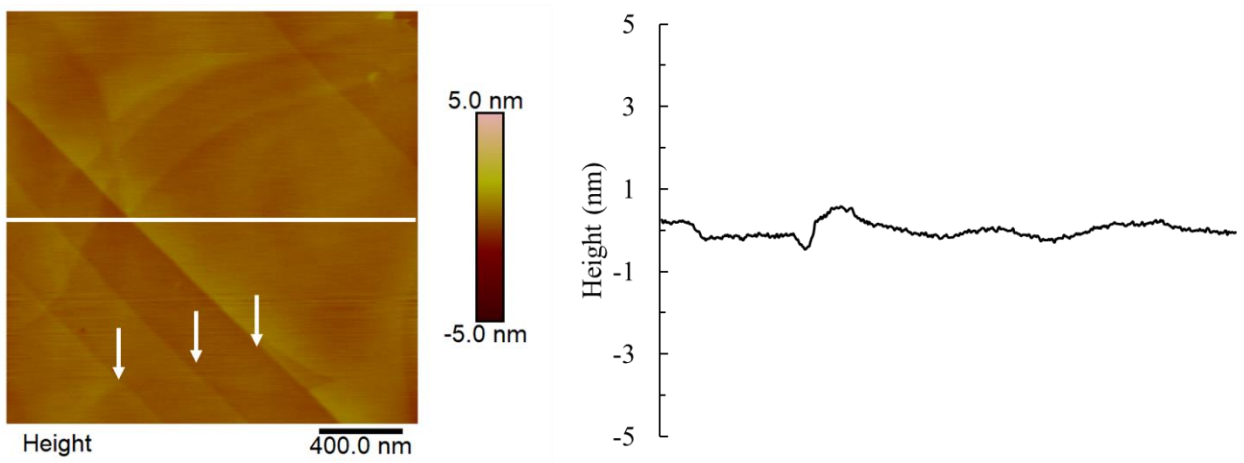

Figure 2. 5: *The AFM topography image of freshly cleaved graphite surface with the cross-sectional profile (right). The white line on the surface is where the cross-section was taken. Size of the image is 2.0 ×2.0 µm² and the relevant height scale is shown next to the figure.*

2.2.6 Mica Surface Preparation

As a model for an atomically flat hydrophilic surface, mica was used. Size 3 V1 Ruby Muscovite Mica was obtained from Lawrence & Co. As mentioned earlier, Mica can be used to determine the different orientation of protein molecules that are bound nonspecifically to a surface. Freshly cleaved mica has a contact angle of <10° indicating the hydrophilic nature of the surface. AFM images (see *Figure 2.6*) indicate the smoothness of surface from the height scale and also from the Rq roughness of 0.081±0.003 nm over are of 1.0 ×1.0 µm^2 area. The surfaces were cut into 1.0×1.0 cm^2 pieces and cleaved before the protein adsorption studies.

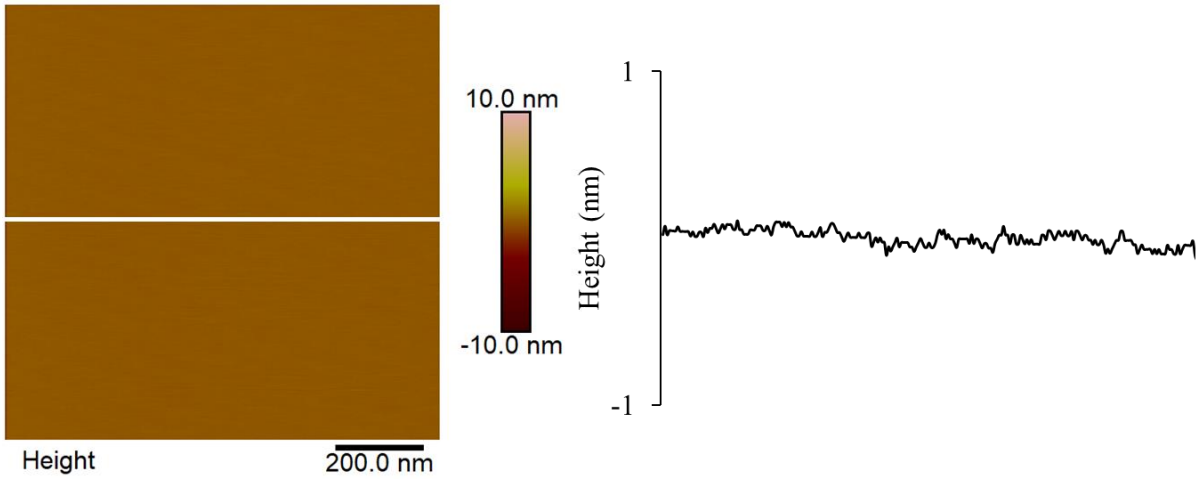

Figure 2. 6: *The AFM topography image of freshly cleaved mica surface with the cross-sectional profile (right). The white line on the surface is where the cross-section was taken. Size of the image is 1.0 ×1.0 µm^2 and the relevant height scale is shown next to the figure.*

2.3 Self Assembled Monolayers

Self-assembled monolayers are single molecule thick, closely-packed arrays of molecules on a surface. They are formed spontaneously by the immersion of suitable substrate in a solution of the molecule of interest.[21,22] There are different types of self-assembly (SA) such as organosiliane on hydroxylated surfaces,[6] thiols onto Cu, Ag and Au, and carboxylic acids on Al_2O_3 and Ag.[23–26] The bond between surface and the SA molecule can be either covalent (Si-O bonds) or ionic (metal carboxylate assembly). There are a lot of applications in the fields of electronics, biosensing, and fabrication industry.[27,28] A key feature of self-assembly is the ability to vary the terminal functional group on the molecule to obtain different surface properties for different applications. By changing the terminal functional group, a surface can be modified to be hydrophilic or hydrophobic.[29]

2.3.1 Self Assembly Monolayer Formation on Silicon Surfaces

Silane molecules were used for SAM formation on the Si(111) surface. 1.0 ×1.0 cm^2 pieces were cut from silicon wafers and piranha cleaned (see Section 2.1.4) before the formation of monolayers. A 2.5 mM solution of desired the silane was prepared in toluene. Then the silane solution was divided equally into glass vials. The cleaned silicon samples were introduced to the vials and closed. Next, the vials were sealed with Parafilm and kept in a desiccator for 20-24 hours. The next day, samples were taken out and washed with toluene and sonicated in toluene for 30 minutes. Samples were taken out and washed using toluene, chloroform, acetone, and ethanol respectively. Samples were stored in clean vials after drying with a stream of N_2 gas. The OTS monolayers on Si have the contact angle of 108.9 ± 0.6 ˚and the thickness of 28.9 ± 1.4 Å. These values are close to the values found in literature 112 ˚and 26.2 Å.[30,31]

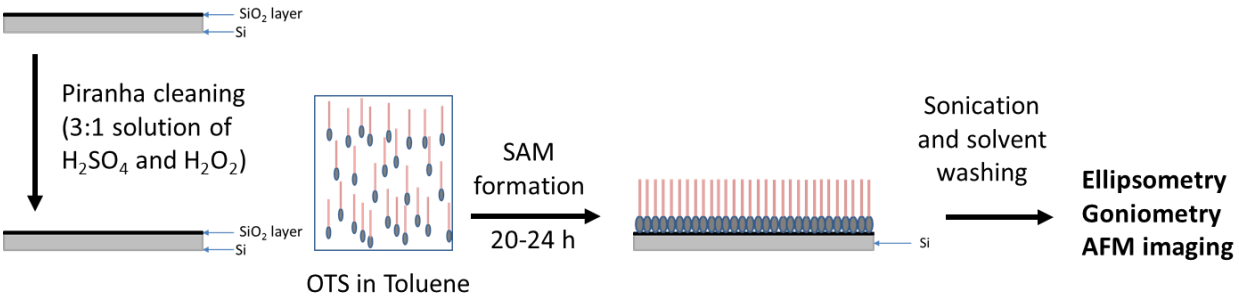

Figure 2. 7: *Process outline for the OTS monolayer formation.*

In this study Octadecyltrichlorosilane (OTS) was used for the formation of SAM on silicon surface. In order to carry out metal deposition using an organic resist layer, it is very important to have a monolayer that covers the entire surface with a minimum number of defect sites. The mechanism of silane monolayer formation is well known.[32,33] *Figure 2.8* illustrates the mechanism of monolayer formation over the native oxide layer on Si in the presence of a small amount of

water. This spontaneous process occurs on silica, glass and other metal oxide substrates. The reaction starts by hydrolysis of chlorides bonded to the Si head group of the OTS molecules, followed by a condensation reaction that forms a siloxane bridge between surface Si atoms and OTS molecules. There can be cross-reaction between OTS molecules, which leads to formation of a polymeric structure on silicon surface. This arrangement results in a well-packed monolayer with a high amount of intermolecular interactions.[32,33]

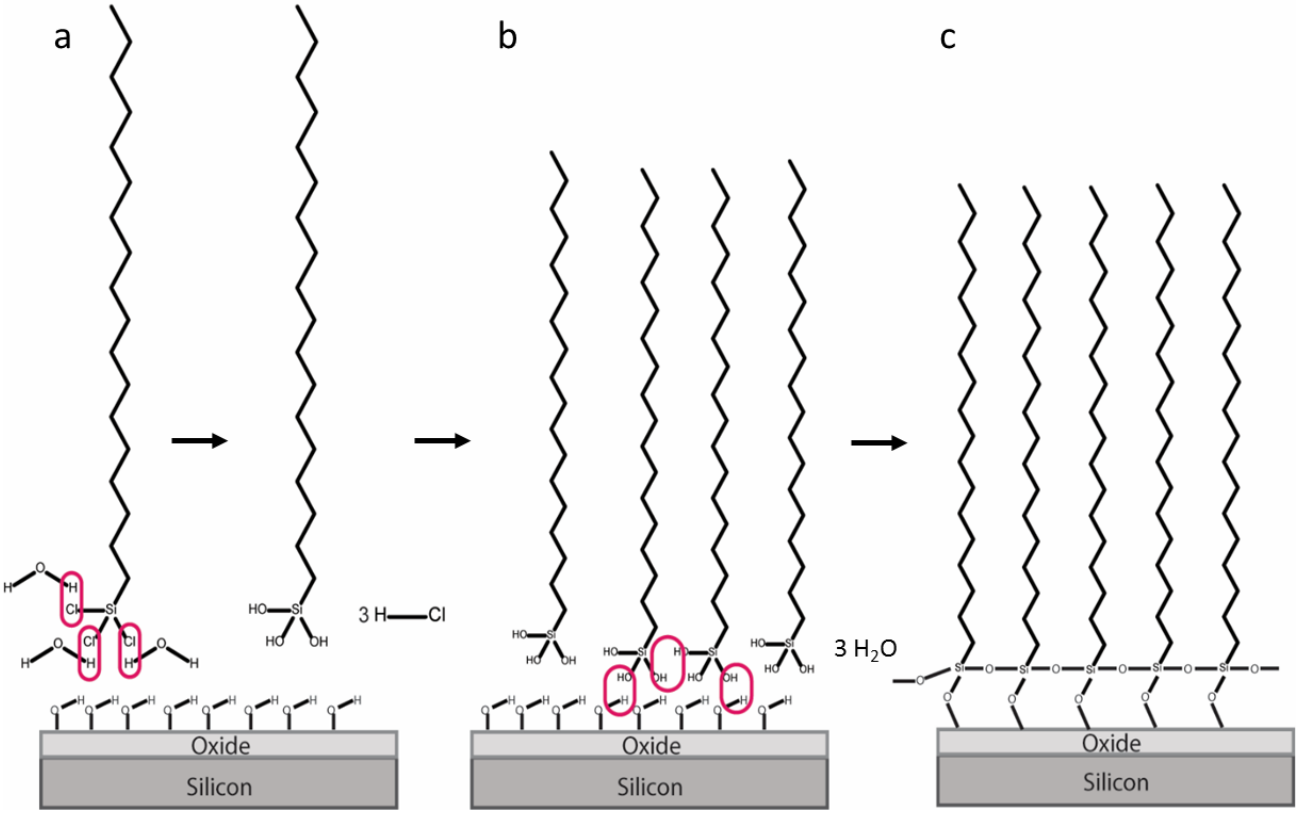

Figure 2. 8: *The mechanism of OTS monolayer formation on silicon surface. a. Hydrolysis of Cl groups on OTS, b. Condensation of OH groups and c. Forming array of polymer on surface.*

2.3.2 The Formation of Self Assembled Monolayers on Gold Surfaces

The *Figure 2.9* below shows the method outline for the SAM formation. For thiol monolayer formation, gold on mica, template stripped gold (TSG), or platypus gold can be utilized.[25,34] First samples were cut into 1.0 ×1.0 cm^2 and either cleaned using piranha solution or solvent rinsing (chloroform, acetone, and ethanol respectively). The samples were kept in the 1-5 mM thiol in ethanol solution for 2-24 hours. In our studies, 0.1-5.0 mM solutions of 11-mercapto-1-undecanol or 11-mercaptoundecanoic acid were made in ethanol. Then, the samples were taken out and rinsed with the toluene, chloroform, acetone, and ethanol sequence to remove the nonspecifically adsorbed molecules. The procedure was changed for the carboxyl and amine terminated thiol solutions by adding 2% (by volume) trifluoroacetic acid (TFA) solution to prevent multilayer formation.[35,36] TFA forms hydrogen bonds with the COOH and NH_2 functional groups to prevent multilayer formation. The monolayers were characterized using ellipsometry goniometry and AFM imaging. The thiol monolayers have to be utilized soon after preparation since the S-Au bond at the interface is subject to oxidation over time, making them less robust than the silane monolayers.[37]

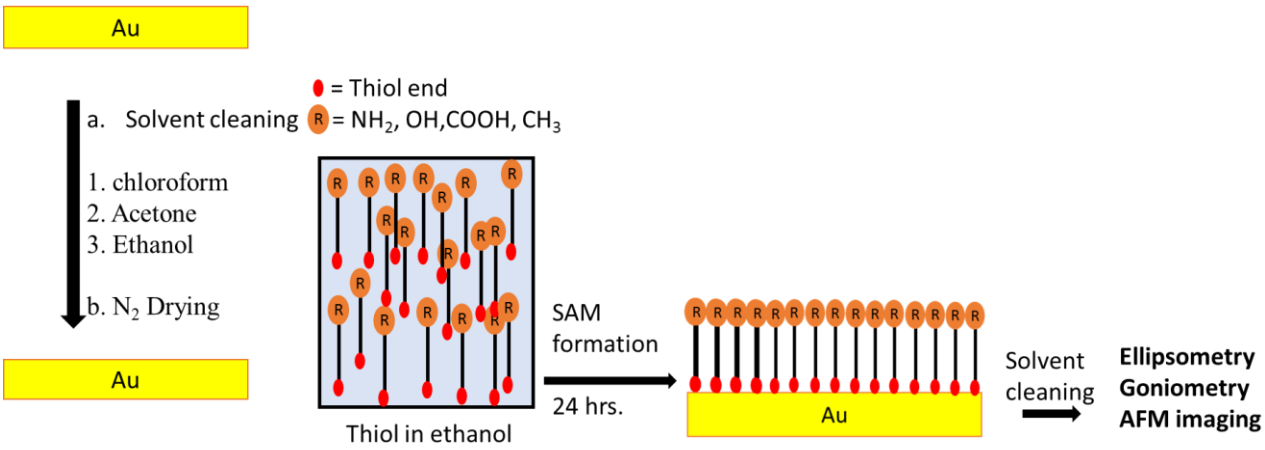

Figure 2. 9: *Process outline for the thiol SAM formation. This process includes the cleaning of surface, introducing the cleaned surface to a desired thiol molecule in ethanol, SAM formation for 24 hours and solvent cleaning before characterization.*

2.4 Goniometry (Contact Angle)

Goniometry measures the contact angle between a liquid droplet and a solid surface. Here in our lab, we use Milli-Q water to measure the contact angle. This measures the surface free energy and can be directly related to the hydrophilicity or the hydrophobicity of the surfaces.[38] Contact angle changes with respect to the bare surface are a good indication of proper monolayer formation and surface functionalization. High water contact angle values (above 90°) indicate a hydrophobic of the surface, and low contact angles (0 -30°) indicate hydrophilic surfaces. Example schematic representations of the shapes of the water droplets on hydrophilic and hydrophobic surfaces are shown in *Figure 2.10* below. More importantly, the exposed terminal functional group determines the contact angle of a substrate, and this tells about the differences of the relative energies of the liquid-air, solid–air, and the solid-liquid interfaces. Young's equation relates the contact angle (θ) and the interfacial energies of the droplet of liquid on the surface according to the equation 1.[39]

$$\gamma_{S-G} = \gamma_{S-L}\gamma_{L-G}cos\theta \qquad (1)$$

Where $\gamma_{S\text{-}G}$ is the solid-gas interface energy, $\gamma_{S\text{-}L}$ is the solid-liquid interface energy, and the $\gamma_{L\text{-}G}$ is the liquid-gas interface energy.

To measure the contact angle, a droplet of Milli-Q water was added placed on the level sample using micro-syringe attached to the goniometer. Then the contact angle of the droplet was measured from the surface-water interface. The measurements were taken from both sides of the droplet and averaged to get the actual reading. The same procedure was followed three times to get the average value. Overall, the contact angle is very sensitive to the terminal functional group, and therefore changes if the packed density changes exposing different functional groups at the interface. In addition, there are other factors contribute to the contact angle. Contact angle is also

changed by surface roughness, surfaces with nanoscale roughness often demonstrating very high contact angles (termed superhydrophobic surfaces). Roughness is one of the factors that will alter the contact angle, and this will result in higher standard deviation for contact angles.

The contact angle values obtained for the OTS-SAM, TSG-SAM-OH on Au and TSG-SAM-OH on Au are 108.9 ± 0.6 °, 32.2°±2.0°, and 30.0°±2.3°. The OTS monolayer had a high contact angle which indicates the surface is hydrophobic and the COOH and OH SAMs are hydrophilic in nature since they have low contact angles.

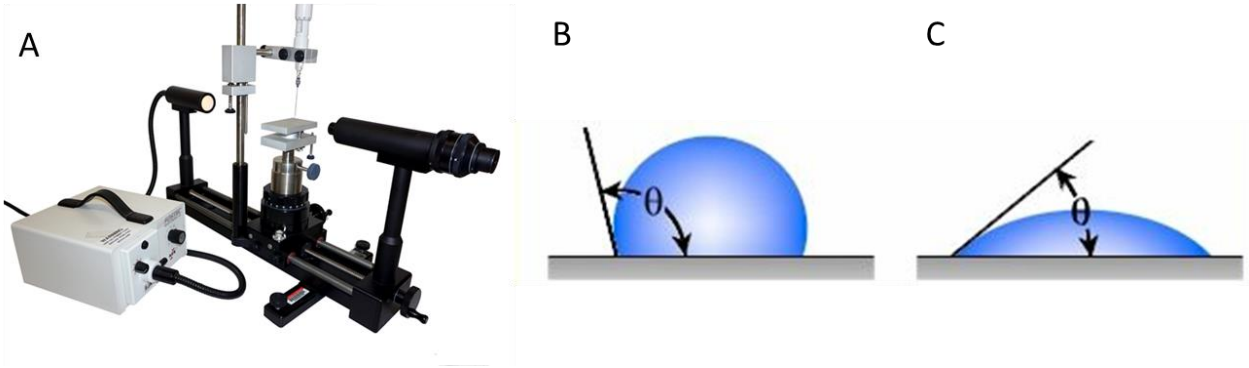

Figure 2. 10: *Goniometry. A. Goniometer with the light source, adjustable stage and a syringe attachment, B. contact angle of hydrophobic and C. hydrophilic surfaces.*

2.5 Ellipsometry

Ellipsometry measures the thickness of molecules/layers of molecules on a surface. Other than thickness measurements, surface roughness, dielectric constant, and crystalline structures can be determined from the ellipsometry.[40–42] A simple schematic of an ellipsometer is shown in *Figure 2.11* below along with the components along the laser path. Laser light source (He-Ne laser 632.8 nm) passes through the rotating polarizer and quarter wave plate to give elliptically polarized light directed towards the sample surface at an angle of 70^{o} (θ). The sample is set on the sample stage and should be highly reflective to obtain reliable values. The elliptically polarized light

travels through the organic thin film and then reaches the interface and reflects towards the detector by passing through the organic thin film again. This phenomenon will change the amplitude and the phase of the s and p components of the polarized light. The polarization of the reflected light is measured and detected by passing it through another polarizer. The equation 2 below explains the complex reflectivity ratio, ρ,

$$\rho = \frac{R_P}{R_S} = tan\,\Psi \times e^{i\Delta} \qquad (2)$$

Where, ρ is the complex reflectivity ratio, R_p is the normalized amplitude of the p polarized light while R_s is the normalized amplitude for the s polarized light, tan Ψ is the amplitude ratio of the reflection, Δ is the shift of phase upon reflection.[43] The Ψ and Δ change with the thickness of the film that the light travels through. This is an indirect method and above values combined with a known index of refraction for the desired thin film surfaces will allow the thickness of thin film on the surface to be determined. Ellipsometry is a very sensitive technique used to measure thicknesses for ultrathin (sub-nanometer) monolayer films. To take the measurements, an Auto EL III ellipsometer from Rudolph Research, was utilized and calibration was carried out using cleaned calibration standard over 5 spots of surface. Then the measurements were taken from the sample over five spots.

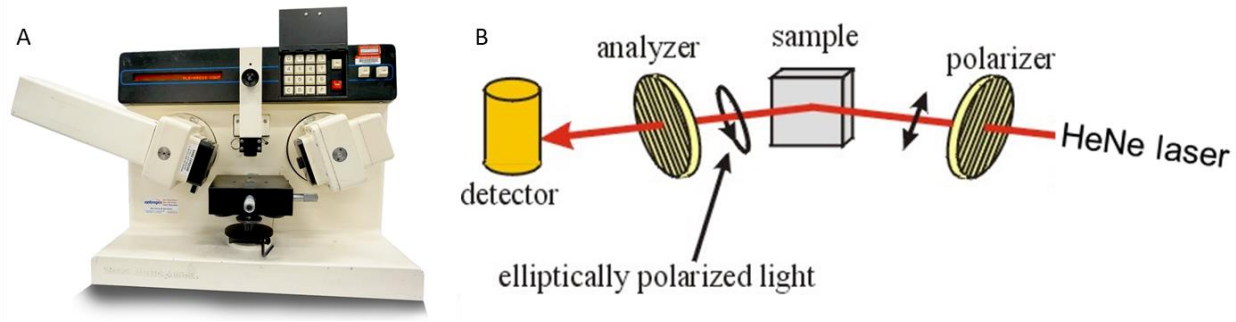

Figure 2. 11: *A. Ellipsometer with its components and B. shows the internal setup with HeNe laser, polarizer, quarter-wave plate, sample surface, reflected light, analyzer, and detector.*

2.6 Atomic Force Microscopy (AFM)

AFM can be used in a variety of studies, including surface topography, friction, surface potential, and conductivity. Due to this ability, AFM techniques are utilized in the fields of electronics, nanofabrication, cell migration studies, protein immobilization, polymer chemistry, and electromagnetic studies.[44–48] In addition, there are combined surface analysis techniques such as AFM-MS[49] and AFM-FTIR,[50] which enhance the applicability in a variety of fields. Overall AFM is a very powerful technique, and it is capable of analyzing features in the nanoscale.[46] In this study, AFM was used to obtain images of the topography of different surfaces including protein molecules (*Chapters 3-4*) and electrolessly deposited metal nanostructures (*Chapters 5-7*).

A schematic of a general AFM system is shown in *Figure 2.12* below. The AFM works by scanning a sharp tip on a cantilever that is moved back and forth on a surface. When a surface contains topographic features, the tip deflects vertically. The deflection of the tip can be monitored, amplified and recorded by aligning a laser on the back of the tip, which is also aligned to the center of a four-quadrant position-sensitive photodiode detector. The deflection can be monitored as the tip encounters any changes in height while scanning. When the laser light hits different positions on photodetector it creates different voltages and the differences in voltage in quadrants indicate the position of the deflected laser which results in a change in the voltage applied to the piezo electric scanner to maintain constant deflection through a feedback loop on the photodetector signal. The computer interface analyzes the differences and creates the surface image. In our studies, multimode Nanoscope IIIA and Nano E scanning probe microscopes (Digital Instruments, CA) were utilized for the data collection.

When the sample is imaged, the tip moves in x and y directions which is controlled by a piezoelectric scanner. There are two ways of utilizing the piezoelectric units. Some instruments

have a piezoelectric device attached to the tip to scan across the sample. Others have the piezoelectric device coupled to the sample stage and stage moves while the tip is stationary. In these studies, our lab utilizes second type of AFM systems which has the piezoelectric unit on the sample stage. The sample size for the AFM experiment vary upon the type of instrument used. In our lab, typical size of a sample is ~1.0×1.0 cm and mounted to a puck via sticky tabs. These samples are kept on the sample stage while the tip holder with the AFM cantilever goes on top of the sample stage.

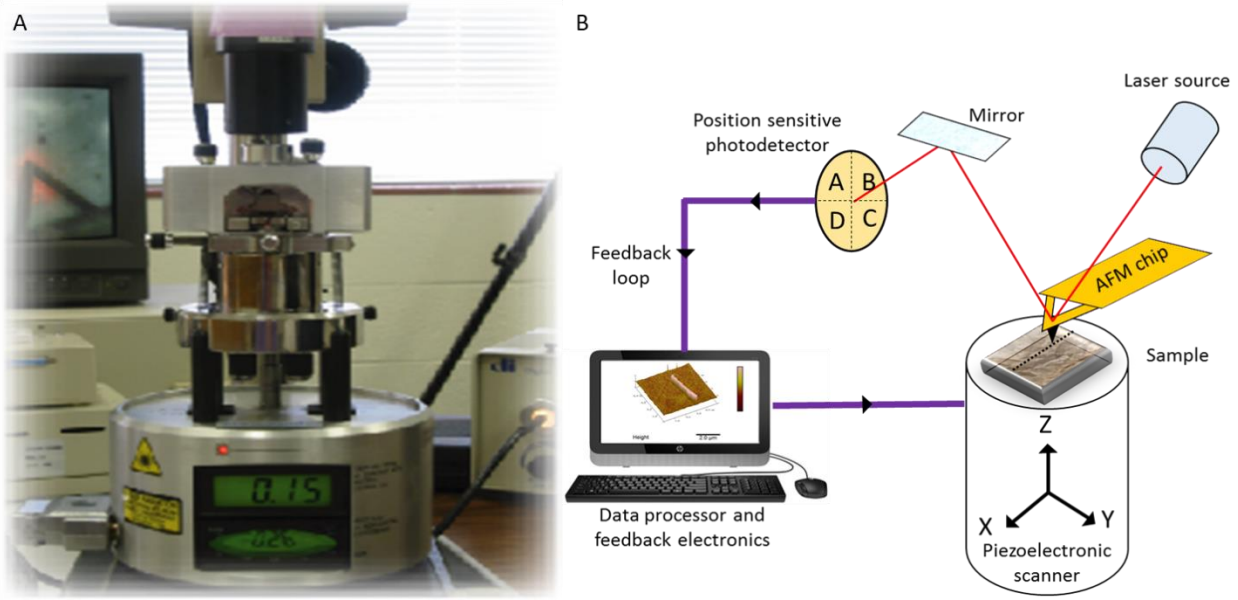

Figure 2. 12: *The multimode scanning probe microscope, B. Overall layout of the AFM system with mounted sample on piezoelectric device.*

Throughout the studies, different types of AFM tips have been utilized, for different applications. Non-conductive silicon nitride cantilevers, with spring constants of 0.12 to 0.06 N/m, were used from Bruker (Camarillo, CA) for carrying out contact mode AFM images. For tapping mode images, diamond-like carbon coating (DLC) tap 300 probes (spring constant 40 N/m and

resonance frequency of 300 kHz) were used from Budget sensors. All the AFM images were analyzed using NanoScope Analysis 1.5 software from Bruker Corporation (Billerica, MA)

2.6.1 Contact Mode AFM

In contact mode, the AFM probe tip constantly comes in contact with the surface while is scans the sample surface. The changes in sample topography induces the vertical deflection of the cantilever. The result is topographical map of the surface. The data is presented as false color maps which have color scales corresponding to different height scales. In the images presented in this thesis, the lower areas are dark in color while the higher features are light in color. In contact mode, the surface and tip come in to contact with each other, and this enables the analyses of strongly adsorbed features only. If there is loosely bound molecules or features, it will be often be moved across the surface by the force of the AFM tip. This is one of the drawbacks of the contact mode AFM. The *Figure 2.13* below shows the AFM images before and after electroless deposition of gold on silicon surfaces.

In this dissertation, contact mode AFM was utilized to characterize surfaces with AFM nano-shaved features, metal deposited on surfaces, and to determine the cleanliness of surfaces (see *Figure 2.13*). *Figure 2.13A* shows an image of bare Si surface after piranha cleaning. It shows consistent color through the surface indicating uniformness of the surface. *Figure 2.13B* shows an image with metal deposited using electroless deposition on cleaned silicon surface. The bright spots on the surface are adhered metal indicating strong interaction with the surface when imaging with the contact mode.

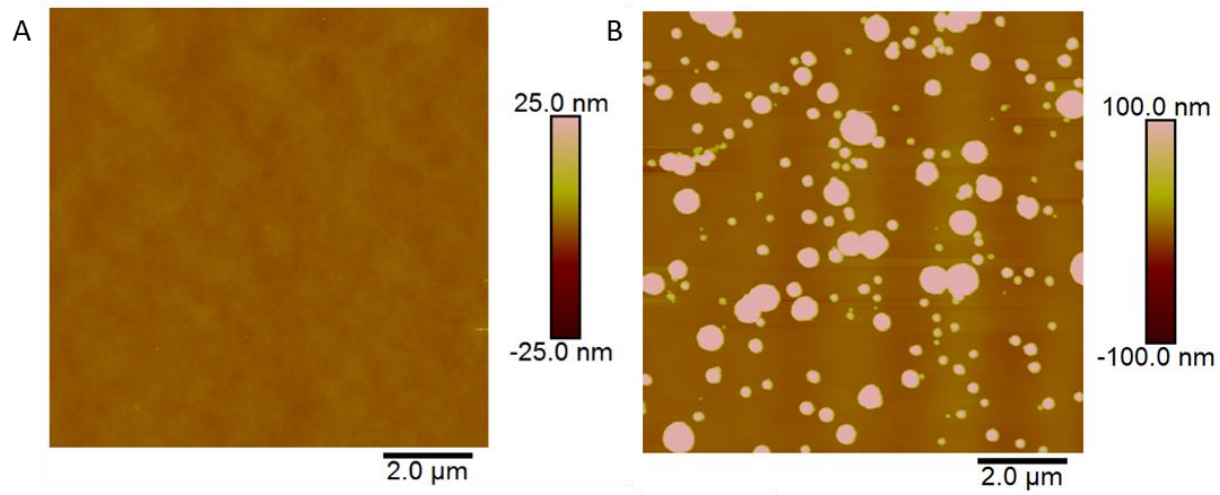

Figure 2. 13: *AFM images of A. Bare silicon surface, B. After electroless deposition. Image before the metal deposition shows uniform surface with no features and image after deposition shows bright spots which indicates gold features developed on the surface.*

2.6.2 Tapping Mode AFM

When analyzing the soft samples such as protein on surfaces, the force applied by the AFM tip in contact mode can deform or drag around the molecules. Therefore, it is not possible to observe the features properly and sometimes even will not be able to image them at all. In tapping mode, the problem of having high lateral force on the features is avoided because the tip touches the surface only intermittently. Since the lateral force does not drag across, the sample features are not altered or moved. The tapping mode tips have different properties than the tips used in the contact mode. The tip used in tapping mode is tuned to a value close to its resonance frequency. When the scanning starts, the cantilever oscillated while moving across the surface and touching the surface at the downward oscillation minimum. The change in amplitude of this oscillation is monitored while the tip scans the surface. When the tip encounters features on the surface, the amplitude is dampened, and this produces a topographical image of the surface and the substances adsorbed to it.

Figure 2.14a. shows isolated protein (putrescine oxidase) molecules on gold surface captured via tapping mode AFM. The central dark area in image 2.14b was imaged in contact mode, and no protein molecules were observed. Then, a larger image was taken in the same region of the surface, showing that the protein molecules are distributed all over the surface, except in the areas that were previously imaged in contact mode (center of *Figure 2.14b*). This demonstrated that the contact mode imaging can alter the surface and is not appropriate for imaging of soft samples such as proteins adsorbed to the surface.

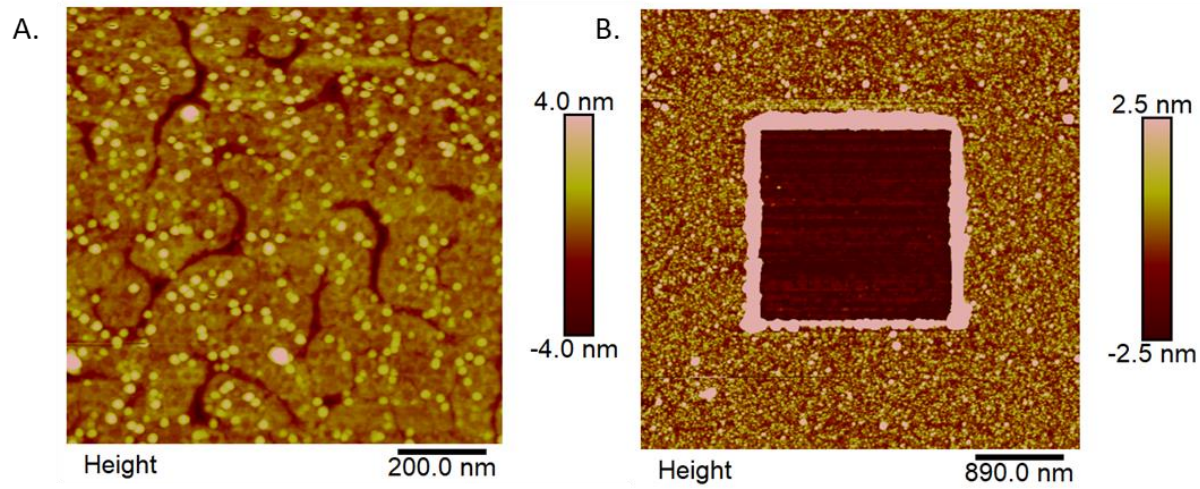

Figure 2. 14: *AFM images of A. Protein molecules observed under tapping mode AFM and B. Combination of contact and tapping mode that shows importance of tapping mode when soft sample imaging.*

2.7 UV-Visible Spectroscopy

Ultraviolet-Visible spectroscopy (UV-Vis) measures the change in intensity of light when transmitted through a solution of interest. Most commonly UV-Vis spectrometry is utilized in quantifying substances by determining how much light absorbed by a chemical of interest.[51] This is done by measuring the intensity of light that passing through by a sample with respect to suitable blank sample. This can be done on different type of samples such as liquids, solids, and thin films in the form of absorbance/transmittance or reflection measurements. Also, this can be used as a

qualitative tool to determine unknown substances.[52–54] A typical spectrometer consist of a light source, a monochromator (to select wavelength), a sample/sample stage and a detector (see *Figure 2.15* below).[51]

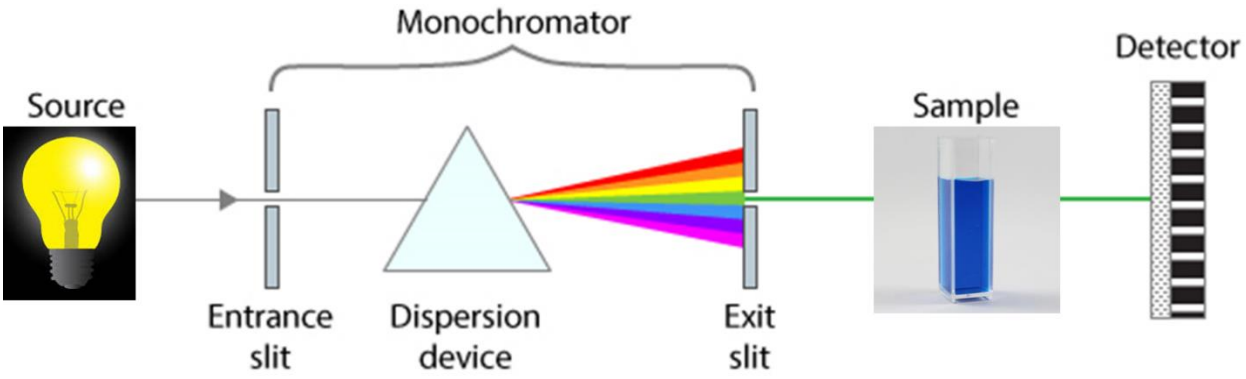

Figure 2. 15: *Schematic of UV-Visible spectrometer setup.*

In this work, transmittance UV-VIS spectroscopy setup was utilized to determine whether the plating solutions for electroless deposition were stable over time, and whether solution phase gold nanoparticle formation was occurring. For this, Ocean optics USB-ISS-UV-Vis-2 spectrometer was utilized with quartz cuvettes in the transmittance mode. The studied plating solutions consist of NH_4F, $HAuCl_4 \cdot 3H_2O$, PVP, Sodium Citrate, and Citric acid. Measurements were taken for the solution combinations of gold/NH_4F, gold/NH_4F/citric acid, gold/NH_4F/sodium citrate, and gold/NH_4F/PVP with respect to time after mixing. *Figure 2.16* shows the UV-Vis spectrum of 0.10 M $HAuCl_4$ (yellow in color) which shows two characteristic peaks with peak maxima at ~225 nm and ~295 nm. Detailed investigation of the solutions is discussed in *Chapter 5* in this dissertation.

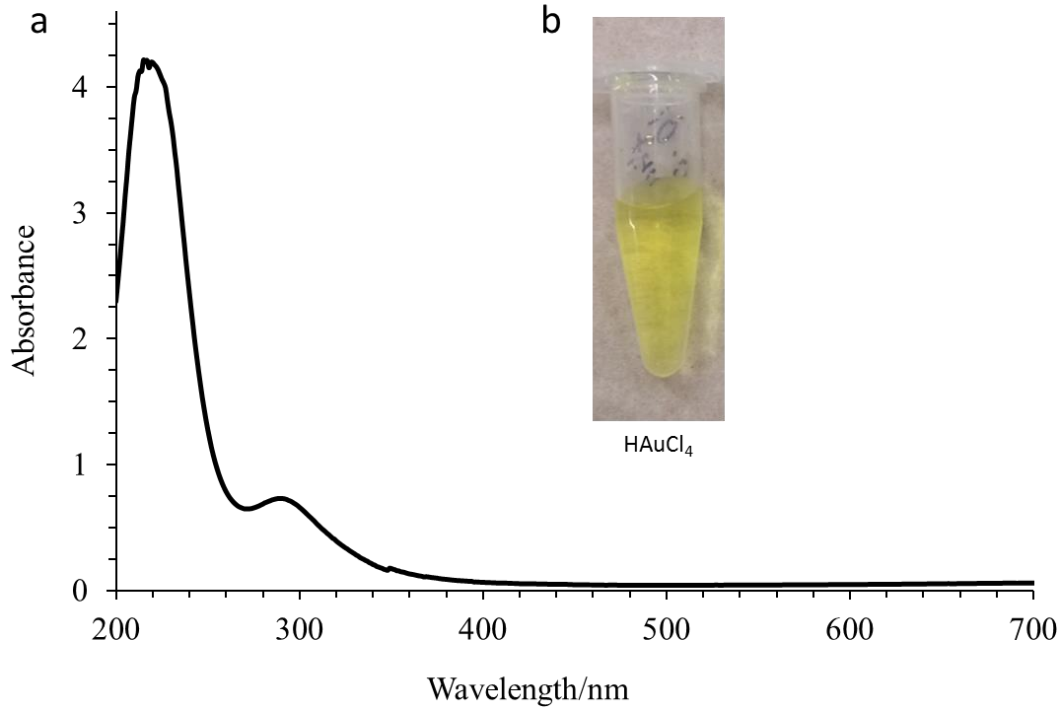

Figure 2. 16: *a. The UV-Vis spectra of $HAuCl_4$ solution (0.100 M) and b. the color of the solution.*

2.8 Electroless Deposition of Gold to Obtain Gold Nanostructures

In electroless deposition (ELD), no external current or potential required and this method have more control over the other methods like electroplating.[55] When using Si surfaces no reducing agent is needed due to sacrificing the substrate silicon as the reducing agent in the presence of HF or NH_4F.[56] Electroless plating can make non-conducting materials into conducting materials. ELD has been carried out for a variety of metals including Au, Cu, Ag, Pt, Cu, Co, Ni, and Fe on a variety of surfaces including silicon, polymer materials, and some ceramic materials.[57]

To carry out the electroless deposition, a solution of metal ions should be introduced to the desired surface along with additives. For silicon surfaces, an etching agent is added to the plating solution since the native oxide layer must be removed to access the underlying silicon to start the metal deposition. Most studies utilize HF as oxide etching agent, but NH_4F has also been used as

mild etching agent.[56] *Figure 2.17* shows the step by step schematic of the electroless deposition process on clean silicon surface.

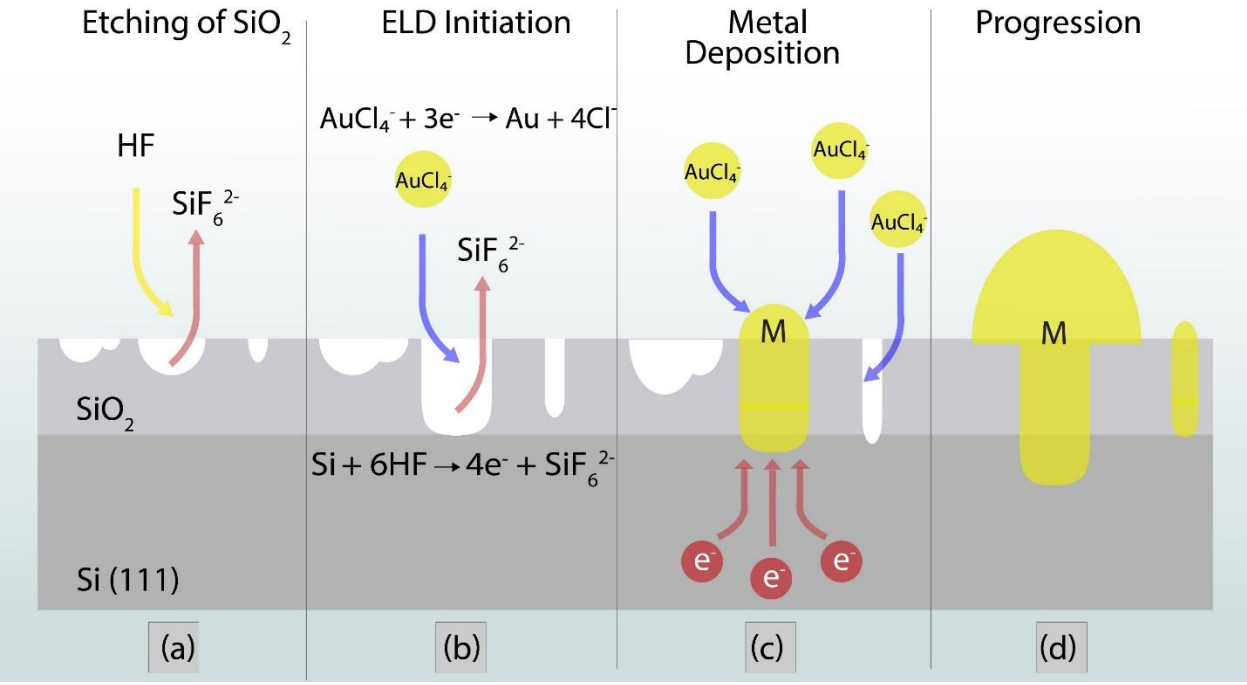

Figure 2. 17: *Step by step progression of electroless deposition of gold. a. etching of oxide layer, b. initiation of gold deposition by accepting electrons from oxidizing silicon, c. nucleation and d. progression.*

The electroless deposition process is a spontaneously driven process due to the redox potential difference between metal ion and the silicon surface. The anodic and cathodic half-reactions are shown in equations below (reactions 1-3). The reaction 1 has the potential of -1.24 V and reaction 2 has a potential of 0.994 V yielding potential of +2.23 V. This gives favorable free energy change under standard conditionsfor the gold deposition.

$$Si(s) + 6NH_4F(aq) \rightarrow (NH_4)_2SiF_6(aq) + 4NH_4^+(aq) + 4e \qquad E = -1.24\,V \qquad (1)$$

$$AuCl_4^-(aq) + 3e \rightarrow Au(s) + 4Cl^-(aq) \qquad E = 0.994V \qquad (2)$$

$$3Si(s) + 18NH_4F(aq) + 4AuCl_4^-(aq) \rightarrow 3(NH_4)_2SiF_6(aq) + 12NH_4^+(aq) + 4Au(s) + 16Cl^- \qquad (3)$$

Also, additives such as citric acid and PVP can be introduced to the solution as metal chelating agents. In this study, two different plating solutions have been developed. The first,

solution contains NH_4F and $HAuCl_4 \cdot 3H_2O$ and the second solution contains NH_4F, sodium citrate, and $HAuCl_4 \cdot 3H_2O$.

The pH of all the plating solutions were measured using standard pH papers before carrying out the metal deposition. The electroless deposition carried out by placing a drop of (100 µL) plating solution on to the piranha cleaned silicon surface. Then the surface was washed with DI water after allowing to deposit predetermined time and dried off with stream of N_2 gas. The AFM images were collected using contact mode AFM from two different samples using four different spots. Rq or the root mean square average height and the average particle diameter over 10.0 × 10.0 μm^2 were calculated using NanoScope analysis 1.5 software. All the plating solution contents, concentrations, plating time and the pH are shown in *Chapter 5*.

2.9 Protein Adsorption on to Surfaces

There is a critical need to control the protein adsorption and orientation on surfaces to obtain desired activity. These are important for application such as biocatalysis, biomedicine[58,59], food safety, and environmental monitoring.[60–62] Some of the approaches to control the orientation are to use covalent and noncovalent coupling with variety of functional groups.[63–66]

In this study, the approach of affinity peptide tag immobilization is used to study the orientation of protein. Here proteins were adsorbed onto different surfaces to determine the best platform which will give selective adsorption for specific types of proteins. The protein used was wild type putrescine oxidase (PutOx), and putresine oxidase with a gold binding peptide tag (PutOX-AuBP). This allows the effect of the metal binding peptide to be investigated. The proteins were dissolved in buffer solutions at pH 7.4 or 8.0 to prevent the denaturing and observe

the maximum activity. For the putrescene oxidase studies, 10 mM pH 8.0 Potassium phosphate monobasic/sodium hydroxide buffer solution was utilized.

For protein adsorption, surfaces were conditioned with 1.0 mL of Milli-Q water (resistivity > 18.2 MΩ-cm). Then, surfaces were conditioned with 1.0 mL of desired buffer solution. After that, 100 µL of protein solution was introduced and incubated at ambient temperature for predetermined time. Soon after that, the surface with protein was washed off with the same buffer solution to remove any nonspecifically bound protein molecules followed by washing with Milli-Q water to prevent salt crystal formation from the buffer salts while drying the surface. After drying the surface with N_2(g), AFM images were taken using Nanoscope IIIA multimode AFM system in tapping mode using scan rates of 1 Hz (see *Figure 2.18*). The concentration of protein used was altered to obtain desired amount of protein on the surface. Detailed descriptions of the experimental conditions can be found in *Chapter 3 and 4.*

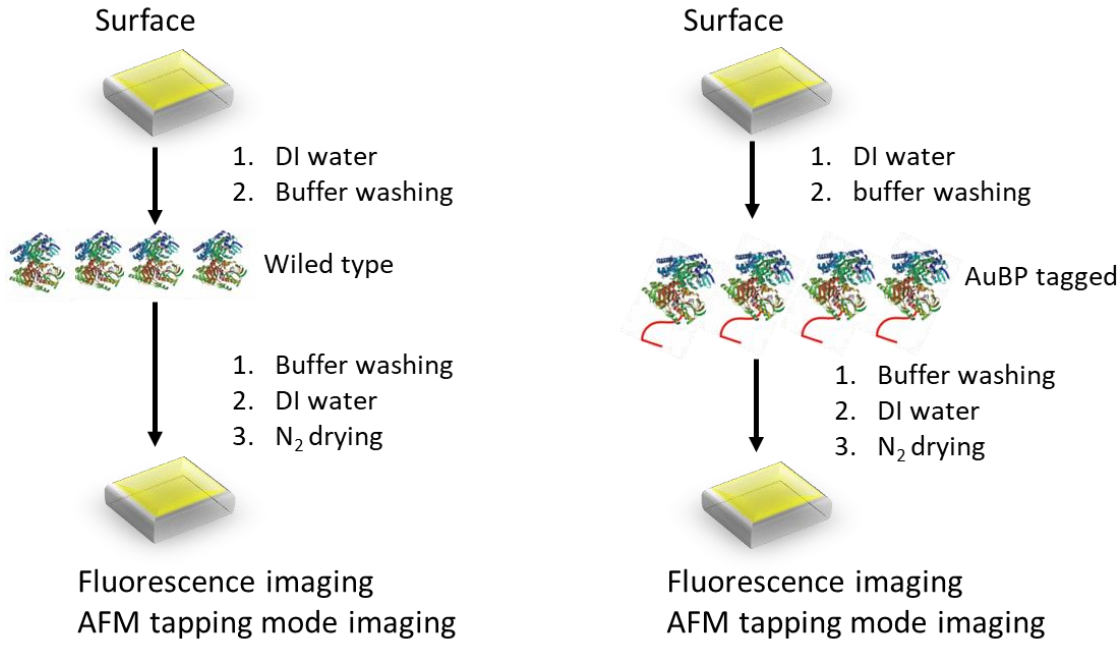

Figure 2. 18: *General approach for protein adsorption on to different surfaces. This method was used for all the proteins that were studied with slight changes.*

2.10 Conclusion

This chapter provides a brief introduction to the methods employed to study the protein adsorption and nanostructure development. The protein adsorption protocol described in the section 2.10 was used in the *Chapter 3 and 4* with slight changes to study the selectivity, specificity, and orientation of proteins. Self-assembly process and electroless deposition discussed in Sections 2.3 and 2.8 were used in *Chapters 5, 6 and 7* to produce metal-organic hybrid nanostructures. The AFM techniques are the most common techniques used in this study and appear throughout the thesis. Many of these methods are readily available in previously published work and we recommend "An Introduction to Ultrathin Organic Films by Abraham Ulman as a good source for the more information regarding the techniques described here.[67]

2.11 References

(1) Chaki, N. K.; Aslam, M.; Sharma, J.; Vijayamohanan, K. Applications of Self-Assembled Monolayers in Materials Chemistry. *J. Chem. Sci.* **2001**, *113*, 659–670.

(2) E. Laibinis, P.; M. Whitesides, G.; L. Allara, D.; Tai Tao, Y.; N. Parikh, A.; G. Nuzzo, R. Comparison of the Structures and Wetting Properties of Self-Assembled Monolayers of n-Alkanethiols on the Coinage Metal Surfaces, Copper, Silver, and Gold. *J. Am. Chem. Soc.* **2002**, *113* (19), 7152–7167. https://doi.org/10.1021/ja00019a011.

(3) Christopher Love, J.; A. Estroff, L.; K. Kriebel, J.; G. Nuzzo, R.; M. Whitesides, G. Self-Assembled Monolayers of Thiolates on Metals as a Form of Nanotechnology. *Chem. Rev.* **2005**, *105* (4), 1103–1170. https://doi.org/10.1021/cr0300789.

(4) Vericat, C.; Vela, M. E.; Benitez, G.; Carro, P.; Salvarezza, R. C. Self-Assembled Monolayers of Thiols and Dithiols on Gold: New Challenges for a Well-Known System. *Chem. Soc. Rev.* **2010**, *39* (5), 1805–1834. https://doi.org/10.1039/b907301a.

(5) Lessel, M.; Bäumchen, O.; Klos, M.; Hähl, H.; Fetzer, R.; Paulus, M.; Seemann, R.; Jacobs, K. Self-Assembled Silane Monolayers: An Efficient Step-by-Step Recipe for High-Quality, Low Energy Surfaces. *Surf. Interface Anal.* **2015**, *47* (5), 557–564. https://doi.org/10.1002/sia.5729.

(6) Wang, M.; Liechti, K. M.; Wang, Q.; White, J. M. Self-Assembled Silane Monolayers: Fabrication with Nanoscale Uniformity. *Langmuir* **2005**, *21* (5), 1848–1857. https://doi.org/10.1021/la048483y.

(7) Sierra, H.; Cordova, M.; Chen, C.-S. J.; Rajadhyaksha, M. Confocal Imaging–Guided Laser Ablation of Basal Cell Carcinomas: An Ex Vivo Study. *J. Invest. Dermatol.* **2015**, *135* (2), 612–615. https://doi.org/10.1038/jid.2014.371.

(8) Zeira, A.; Chowdhury, D.; Maoz, R.; Sagiv, J. Contact Electrochemical Replication of Hydrophilic−Hydrophobic Monolayer Patterns. *ACS Nano* **2008**, *2* (12), 2554–2568. https://doi.org/10.1021/nn8005174.

(9) Vogel, N.; Zieleniecki, J.; Köper, I. As Flat as It Gets: Ultrasmooth Surfaces from Template-Stripping Procedures. *Nanoscale* **2012**, *4* (13), 3820–3832. https://doi.org/10.1039/c2nr30434a.

(10) Hegner, M.; Wagner, P.; Semenza, G. Ultralarge Atomically Flat Template-Stripped Au Surfaces for Scanning Probe Microscopy. *Surf. Sci.* **1993**, *291* (1–2), 39–46. https://doi.org/10.1016/0039-6028(93)91474-4.

(11) Nogues, C.; Wanunu, M. A Rapid Approach to Reproducible, Atomically Flat Gold Films on Mica. *Surf. Sci.* **2004**, *573* (3), L383–L389. https://doi.org/10.1016/j.susc.2004.10.019.

(12) Gold Coated Silicon Wafers And Chips.

(13) AUTO 306 Vacuum Coater with Turbomolecular Pumping System.

(14) Maver, U.; Planinšek, O.; Jamnik, J.; Hassanien, A. I.; Gaberšček, M. Preparation of Atomically Flat Gold Substrates for AFM Measurements. *Acta Chim. Slov.* **2012**, *59* (1), 212–219.

(15) Ostendorf, F.; Schmitz, C.; Hirth, S.; Kühnle, A.; Kolodziej, J. J.; Reichling, M. How Flat Is an Air-Cleaved Mica Surface? *Nanotechnology* **2008**, *19* (30), 305705 (6pp). https://doi.org/10.1088/0957-4484/19/30/305705.

(16) Lee, S.; Ragan, R.; Bae, S.-S.; Kim, S.; Medeiros-Ribeiro, G.; Blackstock, J. J.; Stewart, D. R. Scanning Tunneling Microscopy of Template-Stripped Au Surfaces and Highly Ordered Self-Assembled Monolayers. *Langmuir* **2008**, *24* (12), 5984–5987.

https://doi.org/10.1021/la800265q.
(17) Vogel, N.; Zieleniecki, J.; Köper, I. As Flat as It Gets: Ultrasmooth Surfaces from Template-Stripping Procedures. *Nanoscale* **2012**, *4* (13), 3820–3832. https://doi.org/10.1039/c2nr30434a.
(18) Marchin, K. L.; Berrie, C. L. Conformational Changes in the Plasma Protein Fibrinogen upon Adsorption to Graphite and Mica Investigated by Atomic Force Microscopy. *Langmuir* **2003**, *19* (23), 9883–9888. https://doi.org/10.1021/la035127r.
(19) V. Dubrovin, E.; A. Barinov, N.; E. Schäffer, T.; V. Klinov, D. In Situ Single-Molecule AFM Investigation of Surface-Induced Fibrinogen Unfolding on Graphite. *Langmuir* **2019**, *35* (30), 9732–9739. https://doi.org/10.1021/acs.langmuir.9b01178.
(20) Rooksby, H.; E., S. Structure of Graphite. *Nature* **1947**, *159*, 638–639.
(21) Bigelow, W. C.; Pickett, D. L.; Zisman, W. A. Oleophobic Monolayers. I. Films Adsorbed from Solution in Non-Polar Liquids. *J. Colloid Sci.* **1946**, *1* (6), 513–538. https://doi.org/10.1016/0095-8522(46)90059-1.
(22) A., Z. W. Relation of the Equilibrium Contact Angle to Liquid and Solid Constitution; 1964; pp 1–51. https://doi.org/10.1021/ba-1964-0043.ch001.
(23) Sung, M. M.; Sung, K.; Kim, C. G.; Lee, S. S.; Kim, Y. Self-Assembled Monolayers of Alkanethiols on Oxidized Copper Surfaces. *J. Phys. Chem. B* **2000**, *104* (10), 2273–2277. https://doi.org/10.1021/jp992995h.
(24) Lang, P.; Mekhalif, Z.; Rat, B.; Garnier, F. Self-Assembled Alkylthiols Monolayers onto Platinum; Influence of the Adsorbed Oxygen. *J. Electroanal. Chem.* **1998**, *441* (1–2), 83–93. https://doi.org/10.1016/S0022-0728(97)00421-X.
(25) Cohen-Atiya, M.; Mandler, D. Studying Thiol Adsorption on Au, Ag and Hg Surfaces by Potentiometric Measurements. *J. Electroanal. Chem.* **2003**, *550–551*, 267–276. https://doi.org/10.1016/S0022-0728(02)01145-2.
(26) Megias-Alguacil, D.; Tervoort, E.; Cattin, C.; Gauckler, L. J. Contact Angle and Adsorption Behavior of Carboxylic Acids on α-Al2O3 Surfaces. *J. Colloid Interface Sci.* **2011**, *353* (2), 512–518. https://doi.org/10.1016/j.jcis.2010.09.087.
(27) Fendler, J. H. Chemical Self-Assembly for Electronic Applications. *Chem. Mater.* **2001**, *13* (10), 3196–3210. https://doi.org/10.1021/cm010165m.
(28) Ariga, K.; Nishikawa, M.; Mori, T.; Takeya, J.; Shrestha, L. K.; Hill, J. P. Self-Assembly as a Key Player for Materials Nanoarchitectonics. *Sci. Technol. Adv. Mater.* **2019**, *20* (1), 51–95. https://doi.org/10.1080/14686996.2018.1553108.
(29) Mahapatro, A.; Johnson, D. M.; Patel, D. N.; Feldman, M. D.; Ayon, A. A.; Agrawal, C. M. Surface Modification of Functional Self-Assembled Monolayers on 316L Stainless Steel via Lipase Catalysis. *Langmuir* **2006**, *22* (3), 901–905. https://doi.org/10.1021/la052817h.
(30) Wasserman, S. R.; Whitesides, G. M.; Tidswell, I. M.; Ocko, B. M.; Pershan, P. S.; Axe, J. D. The Structure of Self-Assembled Monolayers of Alkylsiloxanes on Silicon: A Comparison of Results from Ellipsometry and Low-Angle X-Ray Reflectivity. *J. Am. Chem. Soc.* **1989**, *111* (15), 5852–5861. https://doi.org/10.1021/ja00197a054.
(31) Prunici, P.; Hess, P. Ellipsometric in Situ Measurement of Oxidation Kinetics and Thickness of (C2–C20) Alkylsilyl (Sub)Monolayers. *J. Appl. Phys.* **2008**, *103* (2), 024312. https://doi.org/10.1063/1.2832439.
(32) Brzoska, J. B.; Azouz, I. Ben; Rondelez, F. Silanization of Solid Substrates: A Step toward Reproducibility. *Langmuir* **1994**, *10* (11), 4367–4373. https://doi.org/10.1021/la00023a072.

(33) Xiao, X.; Hu, J.; Charych, D. H.; Salmeron, M. Chain Length Dependence of the Frictional Properties of Alkylsilane Molecules Self-Assembled on Mica Studied by Atomic Force Microscopy. *Langmuir* **1996**, *12* (2), 235–237. https://doi.org/10.1021/la950771u.

(34) Porter, M. D.; Bright, T. B.; Allara, D. L.; Chidsey, C. E. Spontaneously Organized Molecular Assemblies. 4. Structural Characterization of n-Alkyl Thiol Monolayers on Gold by Optical Ellipsometry, Infrared Spectroscopy, and Electrochemistry. *J. Am. Chem. Soc.* **1987**, *109* (12), 3559–3568. https://doi.org/10.1021/ja00246a011.

(35) Wang, H.; Chen, S.; Li, L.; Jiang, S. Improved Method for the Preparation of Carboxylic Acid and Amine Terminated Self-Assembled Monolayers of Alkanethiolates. *Langmuir* **2005**, *21* (7), 2633–2636. https://doi.org/10.1021/la046810w.

(36) Jadhav, S. A. Self-Assembled Monolayers (SAMs) of Carboxylic Acids: An Overview. *Cent. Eur. J. Chem.* **2011**, *9* (3), 369–378. https://doi.org/10.2478/s11532-011-0024-8.

(37) Schoenfisch, M. H.; Pemberton, J. E. Air Stability of Alkanethiol Self-Assembled Monolayers on Silver and Gold Surfaces. *J. Am. Chem. Soc.* **1998**, *120* (18), 4502–5413. https://doi.org/10.1021/ja974301t.

(38) Janssen, D.; De Palma, R.; Verlaak, S.; Heremans, P.; Dehaen, W. Static Solvent Contact Angle Measurements, Surface Free Energy and Wettability Determination of Various Self-Assembled Monolayers on Silicon Dioxide. *Thin Solid Films* **2006**, *515* (4), 1433–1438. https://doi.org/10.1016/j.tsf.2006.04.006.

(39) Adam, N. K. Use of the Term "Young's Equation" for Contact Angles. *Nature* **1957**, *180* (4590), 625–633.

(40) Cardona, M.; Rönnow, D.; Santos, P. V. Ellipsometric Investigations of Piezo-Optical Effects. *Thin Solid Films* **1998**, *313–314*, 10–17. https://doi.org/10.1016/S0040-6090(97)00763-3.

(41) Vedam, K. Spectroscopic Ellipsometry: A Historical Overview. *Thin Solid Films* **1998**, *313–314*, 1–9. https://doi.org/10.1016/S0040-6090(97)00762-1.

(42) Collins, R. W.; Kim, Y. T. Ellipsometry for Thin-Film and Surface Analysis. *Anal. Chem.* **1990**, *62* (17), 887–900. https://doi.org/10.1021/ac00216a721.

(43) Schweizer, T. Handbook of Ellipsometry. *Appl. Rheol.* **2005**, *15* (1), 10–11. https://doi.org/10.1515/arh-2005-0022.

(44) Last, J. A.; Russell, P.; Nealey, P. F.; Murphy, C. J. The Applications of Atomic Force Microscopy to Vision Science. *Investig. Ophthalmol. Vis. Sci.* **2010**, *51* (12), 6083–6094. https://doi.org/10.1167/iovs.10-5470.

(45) Vahabi, S.; Nazemi Salman, B.; Javanmard, A. Atomic Force Microscopy Application in Biological Research: A Review Study. *Iran. J. Med. Sci.* **2013**, *38* (2), 76–83.

(46) Giessibl, F. J. Advances in Atomic Force Microscopy. *Rev. Mod. Phys.* **2003**, *75* (3), 949–983. https://doi.org/10.1103/RevModPhys.75.949.

(47) Marrese, M.; Guarino, V.; Ambrosio, L. Atomic Force Microscopy: A Powerful Tool to Address Scaffold Design in Tissue Engineering. *J. Funct. Biomater.* **2017**, *8* (1), 7. https://doi.org/10.3390/jfb8010007.

(48) Cullen, D. C.; Lowe, C. R. AFM Studies of Protein Adsorption: 1. Time-Resolved Protein Adsorption to Highly Oriented Pyrolytic Graphite. *Journal of Colloid and Interface Science*. 1994, pp 102–108. https://doi.org/10.1006/jcis.1994.1276.

(49) Somnath, S.; Jesse, S.; Van Berkel, G. J.; Kalinin, S. V.; Ovchinnikova, O. S. Improved Spatial Resolution for Spot Sampling in Thermal Desorption Atomic Force Microscopy-Mass Spectrometry: Via Rapid Heating Functions. *Nanoscale* **2017**, *9* (17), 5708–5717.

https://doi.org/10.1039/c6nr09675a.
(50) Boerio, F. J.; Starr, M. J. AFM/FTIR: A New Technique for Materials Characterization. *J. Adhes.* **2008**, *84* (10), 872–895. https://doi.org/https://doi.org/10.1080/00218460802445308.
(51) Owen, T. *Fundamentals of UV-Visible Spectroscopy*; Hewlett-Packard, 1996.
(52) Bosch Ojeda, C.; Sanchez Rojas, F. Recent Applications in Derivative Ultraviolet/Visible Absorption Spectrophotometry: 2009-2011. A Review. *Microchem. J.* **2013**, *106*, 1–16. https://doi.org/10.1016/j.microc.2012.05.012.
(53) Famili, A.; Baldy, W. J.; Palkar, S. A. UV-Visible Spectroscopy for Quantification of Drop-on-Demand Inkjet Performance. *Ind. Eng. Chem. Res.* **2011**, *50* (17), 9829–9833. https://doi.org/10.1021/ie1023673.
(54) Baldock, B. L.; Hutchison, J. E. UV-Visible Spectroscopy-Based Quantification of Unlabeled DNA Bound to Gold Nanoparticles. *Anal. Chem.* **2016**, *88* (24), 12072–12080. https://doi.org/10.1021/acs.analchem.6b02640.
(55) Ali, H. O.; Christie, I. R. A. A Review of Electroless Gold Deposition Processes. *Circuit World*. 1985, pp 10–16. https://doi.org/10.1108/eb043759.
(56) Chen, W. W. pdf.; Sun, X. H.; Wang, S. D.; Lee, S. T.; Teo, B. K. Etching Behavior of Silicon Nanowires with HF and NH4F and Surface Characterization by Attenuated Total Reflection Fourier Transform Infrared Spectroscopy: Similarities and Differences between One-Dimensional and Two-Dimensional Silicon Surfaces. *J. Phys. Chem. B* **2005**, *109* (21), 10871–10879. https://doi.org/10.1021/jp0443411.
(57) Shacham-Diamand, Y.; Osaka, T.; Okinaka, Y.; Sugiyama, A.; Dubin, V. 30 Years of Electroless Plating for Semiconductor and Polymer Micro-Systems. *Microelectron. Eng.* **2015**, *132*, 35–45. https://doi.org/10.1016/j.mee.2014.09.003.
(58) Maduraiveeran, G.; Sasidharan, M.; Ganesan, V. Biosensors and Bioelectronics Electrochemical Sensor and Biosensor Platforms Based on Advanced Nanomaterials for Biological and Biomedical Applications. *Biosens. Bioelectron.* **2018**, *103* (October 2017), 113–129. https://doi.org/10.1016/j.bios.2017.12.031.
(59) Erol, O.; Uyan, I.; Hatip, M.; Yilmaz, C. Recent Advances in Bioactive 1D and 2D Carbon Nanomaterials for Biomedical Applications. *Nanomedicine Nanotechnology, Biol. Med.* **2018**, *14* (7), 2433–2454. https://doi.org/10.1016/j.nano.2017.03.021.
(60) Justino, C.; Duarte, A.; Rocha-Santos, T. Recent Progress in Biosensors for Environmental Monitoring: A Review. *Sensors* **2017**, *17* (12), 1–25. https://doi.org/10.3390/s17122918.
(61) Lang, Q.; Han, L.; Hou, C.; Wang, F.; Liu, A. A Sensitive Acetylcholinesterase Biosensor Based on Gold Nanorods Modified Electrode for Detection of Organophosphate Pesticide. *Talanta* **2016**, *156–157*, 34–41. https://doi.org/10.1016/j.talanta.2016.05.002.
(62) Soh, N.; Tokuda, T.; Watanabe, T.; Mishima, K. A Surface Plasmon Resonance Immunosensor for Detecting a Dioxin Precursor Using a Gold Binding Polypeptide. **2003**, *60*, 733–745. https://doi.org/10.1016/S0039-9140(03)00139-5.
(63) Hitaishi, V.; Clement, R.; Bourassin, N.; Baaden, M.; de Poulpiquet, A.; Sacquin-Mora, S.; Ciaccafava, A.; Lojou, E. Controlling Redox Enzyme Orientation at Planar Electrodes. *Catalysts* **2018**, *8* (5), 192. https://doi.org/10.3390/catal8050192.
(64) Johnson, D. L.; Martin, L. L. Controlling Protein Orientation at Interfaces Using Histidine Tags: An Alternative to Ni/NTA. *J. Am. Chem. Soc.* **2005**, *127* (7), 2018–2019. https://doi.org/10.1021/ja045084g.
(65) Lin, W.; Insley, T.; Tuttle, M. D.; Zhu, L.; Berthold, D. A.; Král, P.; Rienstra, C. M.;

Murphy, C. J. Control of Protein Orientation on Gold Nanoparticles. *J. Phys. Chem.* **2015**, *119* (36), 21035–21043. https://doi.org/10.1021/acs.jpcc.5b07701.

(66) Wasserberg, D.; Cabanas-Danés, J.; Prangsma, J.; O'Mahony, S.; Cazade, P. A.; Tromp, E.; Blum, C.; Thompson, D.; Huskens, J.; Subramaniam, V.; et al. Controlling Protein Surface Orientation by Strategic Placement of Oligo-Histidine Tags. *ACS Nano* **2017**, *11* (9), 9068–9083. https://doi.org/10.1021/acsnano.7b03717.

(67) Ulman, A. *An Introduction to Ultrathin Organic Films*; Elsevier, 1991. https://doi.org/10.1016/C2009-0-22306-3.

Chapter 3: Design of Self-Immobilized Putrescine Oxidase Biocatalysts System Using a Metal Binding Peptide

This project is carried out with the collaboration of Dwight O. Deay III,[1] Rachel T. Lietz,[2] Steve Seibold,[1] James Meyer,[2] Brandon Tomas,[1,2] Banu Taktak Karaca,[2] Mark Richter,[1] and Candan Tamerler[2,3] ([1]Department of Molecular Biosciences; [2]Department of Mechanical Engineering; [3]Bioengineering Research Center (BERC) & Bioengineering Program). The tentative title of the manuscript is "Investigation of the Selectivity of binding of Putrescine Oxidase through Genetically Engineered Gold Binding Peptide Tags." Some of the data presented here collected by Tyler Nguyen and Talisa Hughes, who worked as undergraduate students in Berrie Lab. The expression, protein purification, protein adsorption kinetics on nanoparticles and QCM studies were done by Dwight O. Deay III from the [1]Department of Molecular Biosciences, University of Kansas and the protein activity studies are done by Rachel T. Lietz from the [2]Department of Mechanical Engineering, University of Kansas.

3.1 Abstract

Flavin oxidases are valuable biocatalysts for the oxidative synthesis of a wide range of compounds, while at the same time reducing oxygen to hydrogen peroxide. Compared to other redox enzymes, their ability to use molecular oxygen as an electron acceptor offers a relatively simple system which does not require a dissociable coenzyme. As such, they are attractive targets for adaptation as cost effective biosensor elements. Their functional immobilization on surfaces offers unique opportunities to expand their utilization for a wide range of applications. Genetically engineered peptides have been demonstrated as enablers of the functional assembly of biomolecules at solid materials interfaces. Once identified as having a high affinity for the material

of interest, these peptides can provide a single step bio-assembly process with orientation control, a critical parameter for functional immobilization of the enzymes. In this study, for the first time, we explored bio-assembly of a putrescine oxidase enzyme using a gold binding peptide tag. The enzyme was genetically engineered to incorporate a gold binding peptide using a spacer sequence with an expectation of effective display of the peptide tag to interact with the gold surface. We characterized the fusion enzyme using multiple characterization techniques including protein electrophoresis, enzyme activity, microscopic and spectroscopic methods. Surface binding was selective for gold and the enzyme retained catalytic activity when immobilized. Atomic force microscopy images show significant differences in height of the molecules when immobilized through the peptide tag compared to immobilization by adsorption of the native enzyme, indicating differences in orientation of the bound enzyme when attached via the affinity tag. The temperature treatment studies show that the peptide tagged protein shows higher stability on the surface than in solution.

3.2 Introduction

Nature has provided a versatile array of enzymes responsible for a wide variety of selective redox reactions. Oxidative enzymes have emerged as desirable for a range of applications due to their high degree of selectivity relative to other chemocatalysts.[1–3] This feature is highly valued by industry as the use of oxidative enzymes in organic synthesis can minimize by-product formation and circumvent the need for protection and deprotection steps.

Flavin-dependent oxidase enzymes in particular have been used extensively to generate compounds of interest to the pharmaceutical, chemical and agrochemical industries as well as for

biosensing applications.[4–9] These enzymes contain a flavin adenine mononucleotide (FMN) or dinucleotide (FAD) which is tightly associated with the enzyme and, in some cases covalently bound.[1] Flavoprotein oxidases can catalyze two-electron oxidations of a wide range of compounds such as amines and alcohols, at the same time reducing molecular oxygen to hydrogen peroxide. Their ability to rely on the reductive activation of molecular oxygen as an electron acceptor to regenerate the oxidized enzyme-bound flavin provides a simpler and less expensive system compared to other redox enzymes that require a constant supply of a dissociable coenzyme (NAD(P)H/NADH). Flavin oxidases that produce hydrogen peroxide are especially useful as the recognition element for biosensors since the hydrogen peroxide product is electroactive.[2–6]

The best studied flavin oxidase is glucose oxidase which has been applied for many years in the textile industry and for diagnostic application [7–9]. Glucose oxidase catalyzes sugar oxidation coupled to the reduction of FAD to $FADH_2$ and to hydrogen peroxide production. Another flavin-containing enzyme is putrescine oxidase (PutOx, E.C 1.4.3.10) which is capable of degrading polyamines. PutOx is a homodimeric protein and unique among flavin-containing enzymes since the isolated enzyme appears to include only one non-covalently bound FAD per dimeric protein.[10–12] Recently, PutOx has been utilized as a diagnostic tool for the detection of biogenic amines such as putrescine and cadaverine[13–17] in body fluids as increased levels of these biogenic amines reflect tumor growth rates and thus can be used as tumor biomarkers. [18,19] PutOx is also used to monitor food freshness by detecting polyamines in spoiling food.[14–20] The physiological and toxicological effects of several biogenic amines have been reported in a wide range of food products and are a potential public health concern. These include but are not limited to putrescine, histamine, cadaverine, spermine and agmatine. The consumption of foods containing high levels of biogenic amines has been associated with poisoning cases and health hazards; biogenic amines formed in

food can cause serious allergic reactions that may lead to difficulty in breathing, itching, rash, vomiting, fever, and hypertension.[21,22] Consequently, there has been an increasing effort in developing sensors that allow monitoring of these compounds and relate the outcomes to the freshness of food products.[23] For instance, Inaba *et al* have developed an electrochemical biosensor based on two oxygen electrodes utilizing a combination of putrescine oxidase and agmatinase to determine squid freshness .[14] Boka *et al* also developed a biosensor based on an enzyme modified carbon electrode for rapid determination of putrescine in food products with a detection limit of 0.01-0.25 mM.[13]

Biological systems typically integrate multicomponent self-assembly for complex tasks requiring precise function of many components in tandem. There is a growing interest in harnessing such self-assembly of materials for hybrid bionanodevice function, but functional assembly of multicomponent systems at the nanoscale remains a significant challenge.[24–30] Two critical considerations that accompany incorporation of biomolecules into solid supports are 1) maintenance of functional integrity of the biomolecule when surface-immobilized, and 2) precise placement and orientation of the biomolecule in a manner that allows control over its interaction not only with the interface directly but also with other components in the assembly.[31,32] These factors are essential for the construction of complex nanostructured materials and devices such as protein arrays, biosensors, and biochips.[29,30,32]

Self-assembled monolayers (SAM) that can be patterned using lithographic methods have been used extensively to create surface arrays of proteins for proteomic or biosensing applications.[33–35] Linkers that are most often used to immobilize proteins are silanes and thiols that bind at one end to the inorganic materials surface via silanol or thiol moieties and have a functional group at the other end (*e.g.* amine, carboxyl) for protein binding.[36–38] Although widely used, these

linkers have a number of disadvantages including instability, lack of material selectivity or multilayer coverage. More importantly, attachment to surface groups on the protein is dependent on the availability and location of those groups. It is, therefore, difficult to control the orientation of the protein on the surface, which is often heterogeneous due to the attachment of the linker to one or more different groups on the protein. This can result in a mixture of active, inactive, or partially active proteins on the surface. Different immobilization techniques have been employed for putrescine biosensors. Enzyme electrodes were constructed by covalently binding the enzyme onto modified carbon or platinum surfaces by crosslinking with glutaraldehyde.[13,17,18] Recently a great deal of effort has been made to fabricate biosensors based on direct electron transfer between the catalytic site of enzyme and electrode. This phenomenon is highly difficult in the case of PutOx, since the FAD cofactor is deeply embedded within the protein.[10,11] It is, however, feasible to create electron bridges between a conductive surface and a redox component within the enzyme, and this strategy is being actively pursued but again this requires control over the surface orientation of the protein.

The use of surface-recognition peptides as an alternative to chemical coupling methods as surface specific bio-linkers is gaining considerable traction[39,40] The peptides are selected from combinatorial peptide phage or cell surface display libraries. The peptide-mediated surface functionalization provides much greater control over the assembly process in a self-directed manner, removing the uncertainty of orientation that accompanies a hit-and-miss attachment approach. The dissociation constant values for surface-recognition peptides vary within the nM to mM range [41–43] and can be tuned for selective material binding over a wide range of surfaces.[44] The properties of these peptides have been critically examined in studies of surface

functionalization, self-assembly, and formation of various nanostructures.[34,35] They were also demonstrated to be efficient surface linkers as fusion partners to other biomolecules.[45–47]

In the present work, we designed a self-immobilized biocatalyst system by focusing on a recently discovered putrescine oxidase from actinomycete *Rhodococcus erthropolis.* The enzyme ($PutOx_{Rh}$) displays a low level of sequence identity to other family members, but the structure of the flavin-binding region is highly conserved. $PutOx_{Rh}$ exhibits a high catalytic activity and high specificity toward putrescine as substrate (k_{cat} of 26.4 s^{-1} and K_M of 8.2 μM).[10] The enzyme is a homodimer of ~100 kDa subunits.[11] Flavin oxidases have been used in a variety of biosensing applications [13–15,48–50] and the putrescine oxidase has been selected here as a model redox active enzyme for surface immobilization studies.[10,13,15] The most promising way to achieve direct electron transfer to a metal surface can be fusion of PutOx enzyme with inorganic binding peptide, which is highly specific for several types of metal surfaces either flat or with structured nanoscale topography. [48,51–55] In our prior work, we have demonstrated that the gold binding peptide alone binds to gold surfaces with high selectivity and affinity.[39,40] Building upon the prior art, we engineered a fusion protein consisting of the $PutOx_{Rh}$ and a C-terminal gold binding peptide (AuBP). In this work, we have studied its self-immobilization onto a variety of gold surfaces and demonstrated that the PutOx-AuBP self-immobilized onto the gold surfaces, binding with a significantly higher affinity than the native PutOx enzyme lacking the AuBP. Furthermore, the immobilized enzyme remained functionally active on the surface. A detailed investigation of the enzyme binding using atomic force microscopy demonstrated that the protein shape and orientation at the surface are significantly altered on the gold surface upon the incorporation of the AuBP. The use of PutOx engineered with a peptide tag offers a precise assembly while securing

the enzyme function in a single step and can be adapted easily as a promising strategy for designing immobilized enzyme biocatalysts in multicomponent systems.

3.3 Materials and Methods

DNA ligase and Dpn1 were purchased from Thermo Fisher. *E.coli* XL-10 Gold and BL21 (DE3) competent cells were purchased from Agilent Technologies. TEV was prepared as described.[56] NuPAGE gel, 12% Bis-Tris, Life Technologies, stained with InstantBlue from Expedeon. Gold-citrate nanoparticles were obtained Nanopartz™. All other reagents were of the highest grade available. Standard pH 8.0 phosphate buffer was obtained from Fisher scientific (10 mM Potassium phosphate monobasic/sodium hydroxide). Ruby muscovite mica was purchased from Lawrence Mica Company (New York). It was freshly cleaved before use. Milli-Q water (resistivity> 18.2 MΩ-cm) was used to rinse surfaces before and after protein incubation.

Template stripped gold surfaces were prepared by thermal evaporation of gold (Alfa Aesar, 99.999%) on mica at a rate of ~1-3 Å/sec in an Edwards Auto 306 thermal evaporator while heating to a temperature of ~200℃ with a quartz lamp. Template stripping was carried out as described previously.[57] Briefly, the samples were glued to a clean glass surface using Epo-Tek 3377 epoxy (Epoxy Technology) and cured at 80℃ for for 16 to 24 hours. The pieces were mechanically cleaved at the gold/mica interface immediately prior to use to expose a flat Au(111) surface with relatively large grains.

3.3.1 Expression Vector Construction

Construction of expression vectors for the production of PutOx-AuBP was performed using inverse PCR on the pTBMalE plasmid[58] encoding the putrecine oxidase (PutOx) gene from *Rhodococcus erythropolis* together with His6-maltose-binding protein (His6-MBP). Inverse PCR

primers targeted to either the N or C terminus of the PutOx gene were produced with 5' overhangs each encoding half of the cyclic AuBP peptide (cpgWALRRSIRRQSYgpc) plus linker (PGGG) sequence.[12,39,41] For the production of the N terminal construct, primer annealing sites were chosen to delete the 6xHis-MBP, and TEV cut site coding regions thereby generating an ORF coding for PutOx-AuBP. The annealing site of primers for C terminal insertion was selected to leave these sequences intact with the intention of removing them by TEV protease cleavage after expression. The primers used are shown in *Table 3.1*. Primers were phosphorylated on their 5' termini with polynucleotide kinase prior to PCR. PCR products were purified using a Qiagen PCR cleanup kit, ligated with DNA ligase, digested with Dpn1 and transformed into 50 µL of XL-10 Gold cells. Transformants were selected on 100 µg/mL ampicillin LB agar plates. DNA from transformant colonies was purified using a Qiagen miniprep kit, sequenced and transformed into BL21 (DE3) pRARE cells for expression.

Table 3. 1: *Mutagenic inverse PCR primers used to create PutOx-AuBP and 6xhis-MBP-TEV-PutOx-AuBP encoding expression vectors from a 6xHis-MBP-TEV-PutOx encoding pTBMalE plasmid.*

Primer name	**Sequence**
C-terminal, AuBP primer A	5’-act tcg tcg gag agc cca tcc agg aca gcc gcc gcc cgg ggc cttg ctg cgg gcg atg a-3'
C-terminal AuBP Primer B	5'-atc cga cgg cag agc tac ggg ccc tgt tga cat tgg aag tgg ata acg -3'
N-terminal AuBP primer A	5’-act tcg tcg cag agc cca tcc agg aca gcc gcc gcc cgg cat atg tat atc tcc ttc tta aa-3’
N-terminal AuBP Primer B	5'-ata cgc cga caa agt tat gga cct tgt gtg cct aca ctc cag aga ga-3'

3.3.2 Protein Expression and Purification

BL21 DE3 pRARE transformant starter cultures were grown in 25 mL LB containing 200 µg/mL carbenicillin at 30 ^{o}C overnight. Large scale protein expression was performed the next day at 20 ^{o}C in 1 L of enhanced LB medium (200 µg/mL carbenicillin, 50 g low salt LB mix, 10 mM $MgCl_2$, 0.8 % (V/V) glycerol, 89 mM sodium phosphate, pH 7.4). Cells were grown to an OD_{600} of 0.6 at 350 rpm shaking speed before the addition of 100 µM IPTG and 0.5 % (V/V) glycerol. Expression was allowed to continue for 24 hours before cells were chilled to 4 ^{o}C and harvested by centrifugation at 2744 rcf for 10 min. Cell pellets were resuspended in 100 mL lysis buffer (50 mM Tris-HCl, pH 8.0, 300 mM NaCl, 10 mM imidazole) and frozen overnight at -80 ^{o}C. Cells suspensions were thawed and sonicated in an ice water bath using a Branson model 400 sonifier (2 sec on, 10 s off at 30% amplitude for 10 min). The lysate was clarified by centrifugation at 20,000 rcf for 1 hr. The soluble fraction was gently mixed with 5 mL of Qiagen Superflow Ni-NTA resin equilibrated with lysis buffer. The resin slurry was loaded onto a 1.6 cm x 30 cm (biorad) column and washed with 20 column volumes of lysis buffer followed by 20 column volumes of lysis buffer containing 20 mM imidazole. The protein was eluted with 1.5 column volumes of lysis buffer containing 250 mM imidazole-HCl.

The Ni-NTA column eluate was subjected to gel filtration on Sephadex G50 equilibrated with TEV protease buffer (10 mM Tris-HCl, pH 7.5, 100 mM NaCl, 100 □M EDTA, and 2 mM DTT). TEV protease was added to a 1:20 (TEV: protein) molar ratio. The cleavage reactions were sterile filtered, and cleavage was allowed to proceed for 48 hr at 25 ^{o}C. Following gel filtration on Sephadex G50 equilibrated with TBS (20 mM Tris-HCl, pH 7.5, 140 mM NaCl), the protein was applied to the Ni-NTA column. The tag-less protein that was collected in the flow-through was >99% pure as judged by SDS-PAGE (*Figure 3.1*). The protein was concentrated to ~40

mg/mL by ultrafiltration (Amicon Ultra-15 concentrator) and loaded onto a 1.6 x 60 cm Superdex PG200 column at a flow rate of 1.25 mL/min. Peak fractions containing the PutOx-AuBP dimer were pooled, glycerol added to 20 % (v/v), and the sample flash frozen in liquid nitrogen and stored at -80 ^{o}C.

3.3.3 Gold Nanoparticle Binding Assay

Au-citrate nanoparticles were concentrated to 5 mg/mL by centrifugation at 200 rcf for 48 hr and resuspended in 100 mL H_2O. 25 µL of PutOx and PutOx-AuBP at 10 mg/mL in 200 µM sodium phosphate buffer, pH 7.4, were each combined with a 25 µL sample of the concentrated nanoparticles and allowed to incubate at room temperature overnight. Samples were then diluted with 900 µL of the sodium phosphate buffer and pelleted by centrifugation at 200 rcf for 48 hr. 900 µL of supernatant was carefully removed with a pipet and the pellet resuspended in 50-100 µL of residual buffer. The protein/nanoparticle suspension was assayed for volume specific putrescine oxidation activity using the Amplex Red/Horseradish Peroxidase (HRP) assay method using 200 µM putrescine-HCl as the substrate. After the assay, 900 µL of phosphate washing buffer was added to the suspension and the particles again collected by centrifugation. This cycle of washing the particles followed by volumetric specific activity determination was repeated 8 times.

3.3.4 Quartz Crystal Microbalance Determination of Binding Constants

PutOx and PutOx-AuBP stocks were prepared for QCM-D analysis by gel filtration into 140 mM NaCl, 10 mM sodium phosphate, pH 7.4, followed by centrifugation at 21,000 rcf for 10 min and filtration through a 0.1 µm filter (Millipore, UltraFree-MC, type VV). The concentrations

of protein samples were adjusted with freshly degassed buffer and filtered through 0.2 µm Millipore filters. Amorphous gold QCM-D sensors (Q-sense) were rigorously cleaned, mounted in flow cells, and equilibrated with the same phosphate buffer for 2 hr. Only sensors achieving baseline stability (< 0.5 Hz/hr drift) were used for data collection. Protein solutions were passed over the equilibrated sensors at 200 µL/min. For each concentration, side-by-side replicates were collected for both PutOx and PutOx-AuBP.

3.3.5: AFM imaging of protein on Gold and Mica

To study the material specificity of the proteins, template stripped gold surfaces and mica surfaces were used as substrates for protein adsorption. The surfaces were cleaned with pH adjusted (pH = 8.0) doubly distilled water for 45 seconds and conditioned with pH 8.0 phosphate buffer (10 mM potassium phosphate monobasic/sodium hydroxide) for 45 seconds. The protein concentrations were adjusted to 10 ppm with the phosphate buffer. 100 µL of each protein sample was applied to the template stripped gold surfaces and mica surfaces and allowed to incubate for 2 hours. The surfaces were then washed with pH 8.0 phosphate buffer for 45 seconds and washed under a stream of pH adjusted MilliQ water (pH=8.0) for 45 seconds and dried under a stream of nitrogen. The surfaces were imaged via tapping mode AFM *(Digital Instruments, NanoScope IIIa)*. Diamond-like carbon coated tips (TAP300DLC, *f=300 kHz, k = 40 N/m)* were used for imaging in tapping mode. Typical scan rates were 1–3 Hz with a scan size of 1 µm×1µm.

To determine the dimensions of single molecules, samples were prepared with low protein coverage. Protein solutions containing 1 ppm PutOx-AuBP were allowed to adsorb for 15 minutes on template stripped gold surfaces followed by rinsing with buffer and water as described above. To isolate the unlabelled PutOx molecules on template stripped gold surfaces, a 10 ppm solution

of protein was incubated on the surface for 2 hours. For mica samples, 10 ppm solutions were used with 2 hours of incubation. To measure the dimensions of individual molecules Bruker-NanoScope analysis 1.5 software was used, and from each sample, 50 molecules were analyzed (n=50 for each protein). The average length and the width were measured at full width at half maximum (FWHM) the and the average height was measured with respect to the flat surface.

3.3.6 Determination of the Thermal Stability and the Activity of the Protein

The TSG, surfaces were conditioned with pH (8.0) adjusted Milli-Q water and conditioned with pH = 8.0 phosphate buffer solution before the protein adsorption. Then, 100 µL of 5.0 µg/mL solution the gold binding peptide tagged putrescine oxidase enzymes was adsorbed for 30 minutes under ambient conditions. Next, surfaces were washed with pH 8.0 phosphate buffer and followed by washing with pH adjusted Milli-Q water to remove any leftover phosphate crystals. After drying with the stream of N_2, surfaces were imaged with Nanoscope IIIA Multimode AFM system in tapping mode with typical scan rates of 1 Hz. Next, surfaces were incubated for 1 hour under different temperatures (30, 55, 65, 75, 85, and 95 °C) with phosphate buffer solution. Then, surfaces were cooled to room temperature and washed with pH 8.0 phosphate buffer followed by distilled water. After drying with the stream of N_2, surfaces were imaged with Nanoscope IIIA Multimode AFM system in tapping mode.

3.4 Results and discussion

The binding and orientation of proteins at interfaces are critical for a variety of applications including biosensing and biocatalysis. In this work, the QCM and nanoparticle binding assays suggest that significant differences arise in the binding of the PutOx enzyme on gold surfaces, due

to the incorporation of a relatively small peptide tag. Typically, these peptides are developed through biocombinatorial approaches including phage display to identify peptides with high affinity for a surface. Genetically engineered peptide sequences have been developed for a variety of materials including gold, silver, platinum, silica, and graphite. They have been shown to allow the direction of protein binding at the microscale, however little is known about the control of the orientation of the assembled proteins. Here, the binding of the PutOx has been specifically studied with and without the peptide tag, AuBP, to investigate the role of the peptide tag in the binding process.

3.4.1: Fusion protein constructs

The previously characterized gold binding peptide AuBP2[39,41]was chosen for this study due to its demonstrated high specificity and high affinity for binding to gold surfaces. The peptide was cyclized by incorporating flanking cysteinyl residues together with a short linker sequence attaching the peptide to the C-terminus of the protein. The oxidase partner for this construct, putrescine oxidase (PutOx), was chosen because it could be readily produced in a soluble, recombinant form when a maltose binding protein (MBP) solubility tag was incorporated into the N-terminus, plus a high resolution structure of the enzyme is available for computational analysis of constructs.[11] Preliminary experiments also indicated that PutOx retains >95 % of its bound FAD upon purification following over-expression. Fusion proteins were engineered into the pMAL-4 vector such that they contained the AuBP on either the N- or the C-terminal end of the MBP-PutOx. When placed on the N-terminus of MBP-PutOx, attempts to recover the fusion protein from the soluble fraction, either by DEAE-cellulose or ammonium sulfate precipitation, resulted in irreversible aggregation of the protein. For this reason, work with the N-terminally labeled

construct was abandoned. In contrast, when the AuBP was placed on the C-terminus of MBP-PutOx (*Figure 3.1A*) the fusion protein remained soluble during purification (*Figure 3.1B*) and retained 100 % of its catalytic function when compared to the wild type enzyme (not shown). A sequence coding for the TEV protease was introduced either 3´ (for N-terminal insertion) or 5' (for C-terminal insertion) to the poly-linker insertion sites. This allowed the 6HisMBP tag to be cleaved from the protein following purification (*Figure 3.1D*). Several methods were subsequently employed to examine the contribution of the AuBP to selective interaction with gold surfaces.

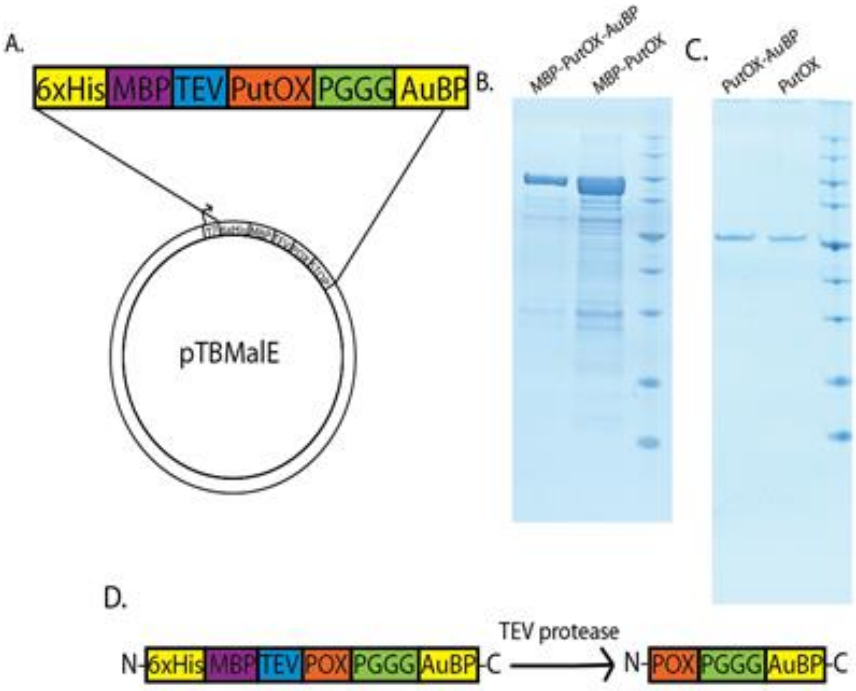

Figure 3. 1: *(A) Fusion protein construct in pTBMaIE vector. (B) SDS-page gel of as expressed fusion construct with protein ladder (right lane). (C) SDS-page gel of protein after affinity column purification and cleavage of MBP. (D) TEV protease expected cleavage site.*

The expression of the folded, functional, active protein with the peptide tag on the C-terminal end of the protein was demonstrated, while expression with the tag on the N-terminal end of the protein did not allow recovery of folded, active protein.

3.4.2 PutOx-AuBP attachment to gold nanoparticles

The PutOx-AuBP or PutOx was incubated for 2 hr with 15 nm diameter citrate-coated gold nanoparticles and then subjected to multiple washes with phosphate buffer. A representative experiment is shown in *Figure 3.2*. The PutOx-AuBP is expected to replace the citrate on the particle surface. To wash, the particles were subjected to a low centrifugal force over 48 hr to prevent particle aggregation upon sedimentation and multiple washes were needed to completely remove the bulk excess of enzyme. At the end of each wash, the catalytic activity of the particles was measured using the Amplex red assay that measures the H_2O_2 generated upon putrescine oxidation.[59,60] The results indicated essentially complete loss of activity due to any non-specifically bound PutOx at the end of 8 washing cycles whereas the particles treated with the PutOx-AuBP construct retained a significant amount of active enzyme after the washing cycles, indicating tight binding only in the presence of the AuBP.

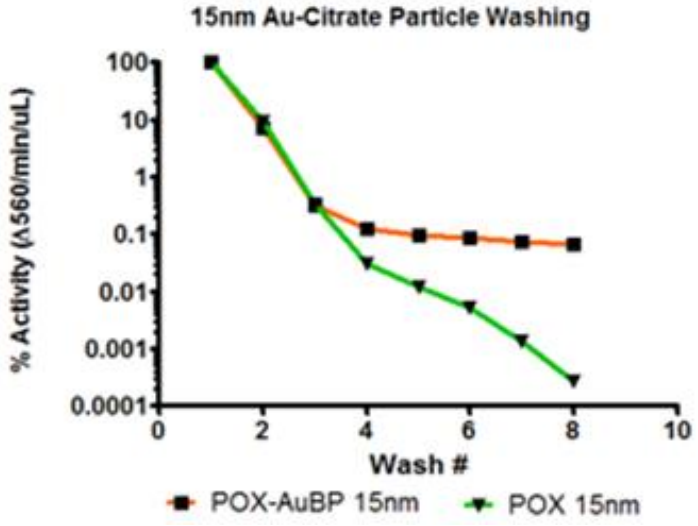

Figure 3. 2: *15 nm diameter gold particles were incubated with wild type putrescene oxidase (Green triangles) or PutOx-AuBP (red squares) followed by successive wash cycles. Putrescene oxidase activity decreases in both cases, but more activity is retained in the case of the PutOx-AuBP. Activity is normalized to initial activity of protein bound particles.*

The binding of the protein to gold nanoparticles and their stability under a series of washing steps showed that while both the native PutOx and the PutOx-AuBP bound to the gold nanoparticles and desorbed after washing steps, the PutOx-AuBP retained significantly more activity on the particles over time than did the PutOx. This is likely due to the higher affinity of the PutOx-AuBP for the gold, as well as the increased stability of the PutOx-AuBP on the surface due to differences in binding.

3.4.3 QCM binding curves for the PutOx-AuBP fusion protein

The interaction between both PutOx-AuBP and PutOx and the gold surface were investigated using a quartz crystal microbalance. The proteins were introduced at different concentrations in a small flow cell at a constant flow rate of 200 µL/min and the frequency recorded during adsorption to the gold surface. Response curves are shown for two different concentrations (20 nM and 100 nM) of PutOx-AuBP compared to 100 nM PutOx lacking the gold binding tag (*Figure 3.3A*). Adsorption data were fit to a single exponential to obtain maximum equilibrium frequency shift (Δf) values over a range of concentrations (*Figure 3.3B*). Little if any desorption occurred following several hours of washing in the absence of enzyme, indicating very tight binding. Estimates of the dissociation constant for binding of PutOx-AuBP were obtained from a Langmuir fit of the kinetic data (20.2 ± 9.6 nM) as well as from a non-linear regression analysis (20.0 ± 7.1 nM) of the data shown in *Figure 3.3B.*

The difference in affinity for the gold was confirmed by QCM studies which showed much stronger binding of the PutOx-AuBP to the gold than the PutOx. Analysis of the PutOx-AuBP/Au interaction indicated that the K_d for the interaction is approximately 20 nM. This is critical if these

types of peptides are to be used for immobilization of the protein in applications such as biosensing which require stable long-term immobilization of the protein at the interface.

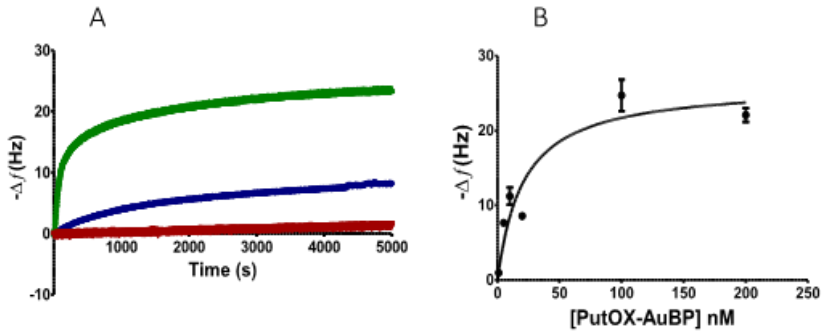

Figure 3. 3: *(A) QCM response curves (change in frequency vs time) for binding of PutOx (red) and PutOx-AuBP (blue, at 20 nM, green, at 100 nM). B: Concentration dependence for PutOX-AuBP binding.*

3.4.4 Protein Coverage and Orientation -AFM

The QCM and nanoparticle washing experiments indicated that the PutOx-AuBP bound considerably more tightly to gold surfaces than the enzyme lacking the AuBP tag. To probe this binding further, the PutOx and PutOx-AuBP were introduced to template-stripped gold surfaces and mica surfaces. AFM images were collected of the films after protein adsorption for 2 hours at a concentration of 10 μg/mL. The images were collected in tapping mode after washing with both buffer and Milli-Q water (*Figure 3.4*). In *Figure 3.4A,* the image shows the PutOx-AuBP on Au(111). This surface has a high coverage of protein molecules compared to the very low coverage indicated in the image of the PutOx (*Figure 3.4C*). This is consistent with the PutOx-AuBP molecules adsorbing to the surface via the AuBP tag. In contrast, on mica, the adsorption of the PutOx-AuBP and the PutOx under conditions identical to those for binding to the gold surface are relatively low and indistinguishable from one another. The coverage is identical, and the distribution of the two different protein molecules is similar on the mica surface indicating that the interaction with the mica surface is not affected by the presence of the AuBP.

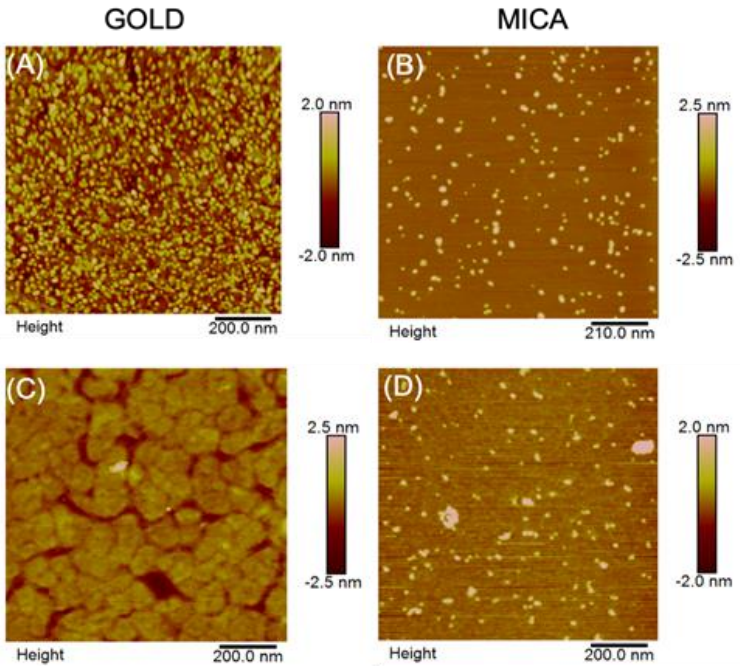

Figure 3. 4: *AFM images of PutOx on Au(111) (A,C) and mica (B,D) surfaces. (A) PutOx-AuBP on Au(111) (B) PutOx-AuBP on mica (C) PutOx on Au(111), (D) PutOx on mica.*

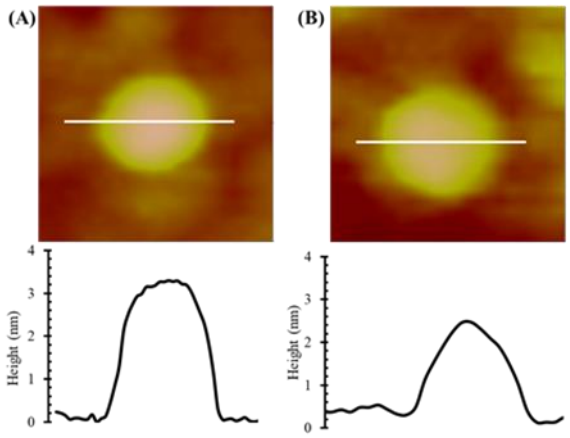

Figure 3. 5**:** AFM images of individual molecules on the Au(111) surface along with cross-sectional cuts through the molecules along the indicated line in the image. (A) PutOx-AuBP (B) PutOx.

Under low coverage conditions, AFM images of individual molecules can be analyzed to determine the single molecule dimensions of the protein. *Figure 3.5* shows representative images and cross-sections through the PutOx and the PutOx-AuBP molecules bound to gold. For each sample, 50 molecules were analyzed to determine the length, width (FWHM) and height of the

molecules. The dimensions are reported in *Table 3.2.* While there is little change in the length and width of the PutOx and the PutOx-AuBP, there is a significant increase in the height of the PutOx-AuBP molecules on Au compared to the PutOx. The dimensions reported here have not been deconvoluted for the tip shape, but images were recorded with the same tip under similar imaging conditions to allow direct comparison. When a similar analysis is carried out for the individual molecules on the mica surface, there is no significant difference in any of the three dimensions, again suggesting that the adsorption of the PutOx to mica is not affected by the presence of the AuBP tag, but the adsorption to gold is significantly modified. The approximately 1 nm increase in height observed on the Au surface of bound PutOx-AuBP is significant and likely comes from a difference in how the protein is interacting with the surface. This suggests that the presence of the AuBP holds the protein away from the surface in a more vertical orientation. The significant increase in coverage of the PutOx-AuBP on Au is consistent with this difference in interaction as well as the tighter binding observed between the PutOx-AuBP and the Au in the QCM data.

Table 3. 2: *AFM measured dimensions of PutOx-AuBP and PutOx on Au(111). Error bars represent 95% confidence limits based on the analysis of n=50 molecules.*

	PutOX-AuBP	**PutOX**
Length (nm)	20.0 ± 0.4	19.5 ± 0.4
Width (nm)	17.8 ± 0.3	17.3 ± 0.3
Height (nm)	3.2 ± 0.1	2.31 ± 0.06

In contrast, when similar experiments were carried out on mica surfaces, there was no change in coverage or dimensions of the protein when the AFM experiments were carried out. This confirms that the differences seen between the PutOx and PutOx-AuBP binding on the gold surface are in fact due to the specific interaction between the peptide tag and the gold surface.

Similar experiments have been conducted on other surfaces as well and will be the subject of a future manuscript (See *Chapter 4*).

The fact that the binding through the AuBP tag results in significant differences in not only the protein coverage, but also the shape and orientation suggests that binding through these genetically engineered peptide tags may provide strong benefits in protein assembly at interfaces over other methods for peptide attachment, including nonspecific interactions (both covalent and noncovalent coupling) which lack the precise control of orientation and materials specificity desired. Facile, self-assembly of complex multicomponent systems necessitates material specificity as well as orientational control that binding through the engineered peptide tags affords.

3.4.5 Thermal Stability and the Activity of the Protein

When the temperature of increases the amount of protein remaining on the surface decreases. To explain this following equilibrium can be considered.

$$Protein_{Surface\ bound} \leftrightarrow Protein_{solution}$$

When incubating with the buffer some of the protein molecules are desorbed and there will be above-mentioned equilibrium. At higher temperatures other than unfolding and aggregation of molecules shifting the equilibrium towards right-hand side will lead to more molecules desorbing from the surface (See *Figure 3.6*).

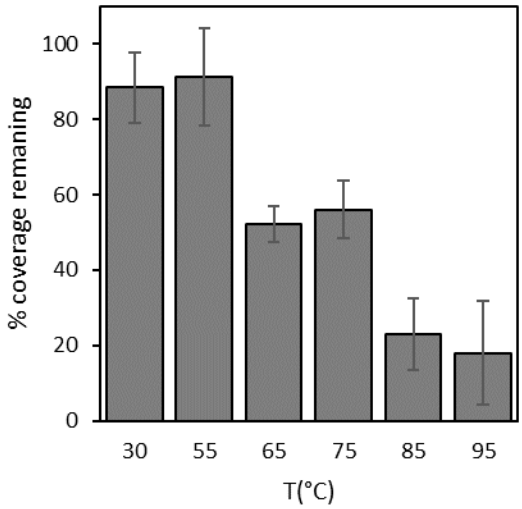

Figure 3. 6: *Percent surface coverage remaining with the temperature.*

At lower temperatures, (from 30 to 65 °C) the height decreases, but the length and width probably not have change enough to be detected (convoluted with tip). This is due to initiating multiple interactions with the surface while increasing the temperature. At higher temperatures (85 and 95 °C) dimensions of the molecules increase bigger due to unfolding and aggregation of molecules. At temperatures above 65-75 °C, clustering and aggregation are observed which leads to increases in all three dimensions (See *Figure 3.7*).

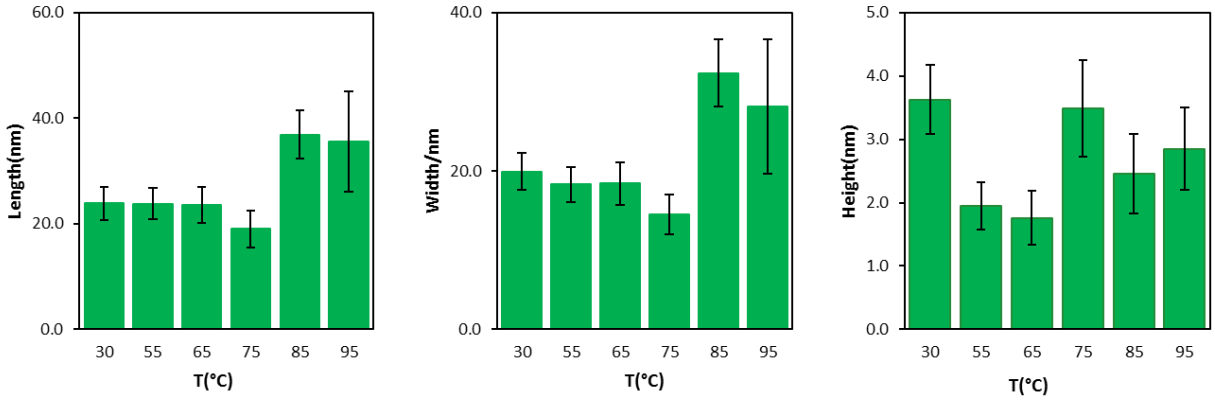

Figure 3. 7**:** The change of protein dimensions with the change in incubation temperature.

The AFM topography images for the selected temperatures are shown in *Figure 3.8*. The AFM images shows that until around 55 °C protein molecules have the expected shape and it consistent with the activity studies which have been carried out using the Horseradish peroxidase (HRP) assay HRP assay. The AFM images shows higher amount of protein molecules on the surface until 55˚C and further increment of temperature tend to unfolding and desorbing molecules from the surface. The activity data imply that in solution, the activity goes down with the increasing temperature. However, on surface, the activity of the protein increases while increasing the incubation temperature (up to 50 ˚C) and then loses the activity. This may be due to the stabilization of protein on the surface due to the restricted motion of the hinge region of the protein when bound through the nearby peptide tag. (*see Figure 3.9*).

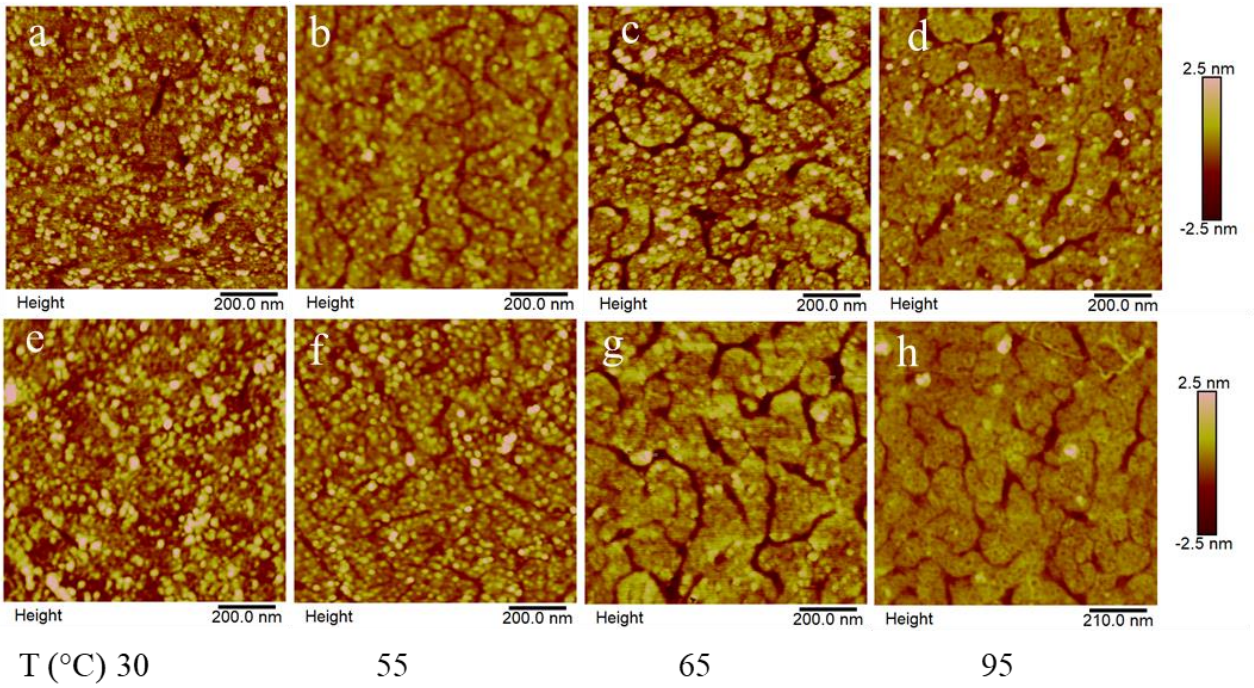

Figure 3. 8: *AFM images for before (a, b, c and d) and after temperature treatment at e. 30, f. 55, g. 75, and h. 95 °C for 1 hour.*

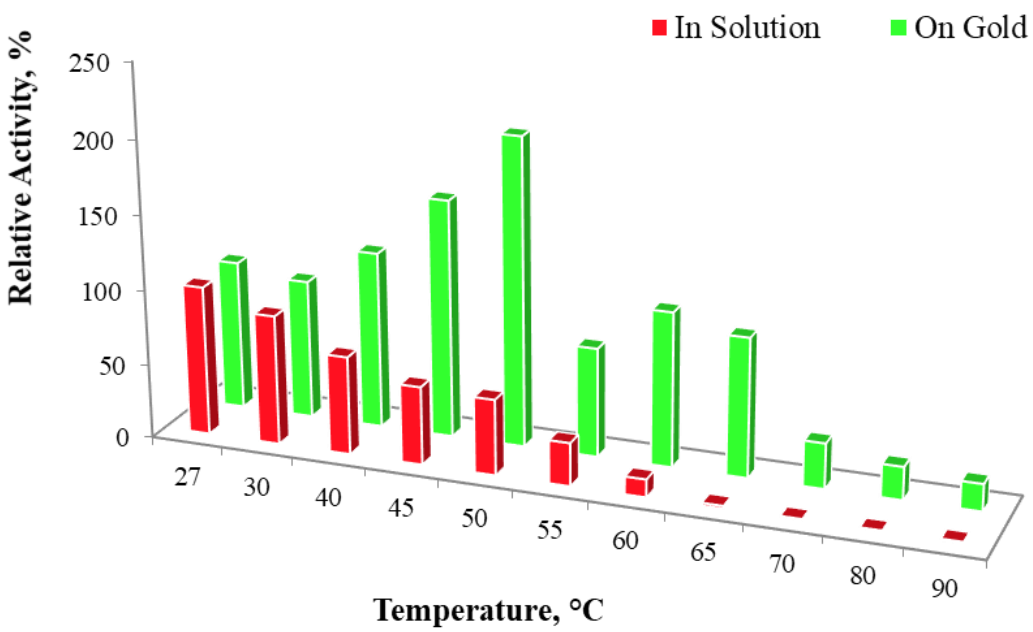

Figure 3. 9: *The relative activities obtained from HRP assay for the PutOx-AuBP in solution and on surface for different temperatures.*

3.5 Conclusion

The specific attachment of functionally active PutOx via AuBP to gold surfaces has been demonstrated using a combination of QCM, activity assays, and AFM investigations of coverage and shape of individual molecules. The increase in coverage as well as the difference in single molecule dimensions show that the binding to the gold surface is mediated by a specific interaction with the AuBP, which results in a more stably bound, functionally active protein at the interface with a different shape than enzyme bound nonspecifically without the AuBP. This highlights the critical role of controlling specific interfacial interactions when self-assembling proteins at interfaces for an expanding list of applications of hybrid nanodevices based on proteins.

3.6. Reference

(1) Torres Pazmiño, D. E.; Winkler, M.; Glieder, A.; Fraaije, M. W. Monooxygenases as Biocatalysts: Classification, Mechanistic Aspects and Biotechnological Applications. *J. Biotechnol.* **2010**, *146* (1), 9–24. https://doi.org/10.1016/j.jbiotec.2010.01.021.

(2) Ceccoli, R. D.; Bianchi, D. A.; Rial, D. V. Flavoprotein Monooxygenases for Oxidative Biocatalysis: Recombinant Expression in Microbial Hosts and Applications. *Front. Microbiol.* **2014**, *5* (FEB), 1–14. https://doi.org/10.3389/fmicb.2014.00025.

(3) Dong, J. J.; Fernández-Fueyo, E.; Hollmann, F.; Paul, C. E.; Pesic, M.; Schmidt, S.; Wang, Y.; Younes, S.; Zhang, W. Biocatalytic Oxidation Reactions: A Chemist's Perspective. *Angew. Chemie - Int. Ed.* **2018**, *57* (30), 9238–9261. https://doi.org/10.1002/anie.201800343.

(4) Montersino, S.; Tischler, D.; Gassner, G. T.; Van Berkel, W. J. H. Catalytic and Structural Features of Flavoprotein Hydroxylases and Epoxidases. *Adv. Synth. Catal.* **2011**, *353* (13), 2301–2319. https://doi.org/10.1002/adsc.201100384.

(5) Moonen, M. J. H.; Fraaije, M. W.; Rietjens, I. M. C. M.; Laane, C.; Van Berkel, W. J. H. Flavoenzyme-Catalyzed Oxygenations and Oxidations of Phenolic Compounds. *Adv. Synth. Catal.* **2002**, *344* (10), 1023–1035. https://doi.org/10.1002/1615-4169(200212)344:10<1023::AID-ADSC1023>3.0.CO;2-T.

(6) Ullrich, R.; Hofrichter, M. Enzymatic Hydroxylation of Aromatic Compounds. *Cell. Mol. Life Sci.* **2007**, *64* (3), 271–293. https://doi.org/10.1007/s00018-007-6362-1.

(7) Bankar, S. B.; Bule, M. V.; Singhal, R. S.; Ananthanarayan, L. Glucose Oxidase - An Overview. *Biotechnol. Adv.* **2009**, *27* (4), 489–501. https://doi.org/10.1016/j.biotechadv.2009.04.003.

(8) Tzanov, T.; Costa, S. A.; Gübitz, G. M.; Cavaco-Paulo, A. Hydrogen Peroxide Generation with Immobilized Glucose Oxidase for Textile Bleaching. *J. Biotechnol.* **2002**, *93* (1), 87–94. https://doi.org/10.1016/S0168-1656(01)00386-8.

(9) Wilson, R.; Turner, A. P. F. Glucose Oxidase: An Ideal Enzyme. *Biosens. Bioelectron.* **1992**, *7* (3), 165–185. https://doi.org/10.1016/0956-5663(92)87013-F.

(10) Kopacz, M. M.; Heuts, D. P. H. M.; Fraaije, M. W. Kinetic Mechanism of Putrescine Oxidase from Rhodococcus Erythropolis. *FEBS J.* **2014**, *281* (19), 4384–4393. https://doi.org/10.1111/febs.12945.

(11) Kopacz, M. M.; Rovida, S.; Van Duijn, E.; Fraaije, M. W.; Mattevi, A. Structure-Based Redesign of Cofactor Binding in Putrescine Oxidase. *Biochemistry* **2011**, *50* (19), 4209–4217. https://doi.org/10.1021/bi200372u.

(12) Van Hellemond, E. W.; Van Dijk, M.; Heuts, D. P. H. M.; Janssen, D. B.; Fraaije, M. W. Discovery and Characterization of a Putrescine Oxidase from Rhodococcus Erythropolis NCIMB 11540. *Appl. Microbiol. Biotechnol.* **2008**, *78* (3), 455–463. https://doi.org/10.1007/s00253-007-1310-4.

(13) Bóka, B.; Adányi, N.; Szamos, J.; Virág, D.; Kiss, A. Putrescine Biosensor Based on Putrescine Oxidase from Kocuria Rosea. *Enzyme Microb. Technol.* **2012**, *51* (5), 258–262. https://doi.org/10.1016/j.enzmictec.2012.07.006.

(14) Inaba, Y.; Tokishita, S.; Hamada-Sato, N.; Kobayashi, T.; Imada, C.; Yamagata, H.; Watanabe, E. Development of Agmatine Sensor Using the Combination of Putrescine Oxidase and Agmatinase for Squid Freshness. *Biosens. Bioelectron.* **2004**, *20* (4), 833–840. https://doi.org/10.1016/j.bios.2004.03.022.

(15) Lee, J. I.; Jang, J. H.; Yu, M. J.; Kim, Y. W. Construction of a Bifunctional Enzyme Fusion for the Combined Determination of Biogenic Amines in Foods. *J. Agric. Food Chem.* **2013**, *61* (38), 9118–9124. https://doi.org/10.1021/jf403044m.

(16) Nagy, L.; Nagy, G.; Gyurcsányi, R. E.; Neuman, M. R.; Lindner, E. Development and Study of an Amperometric Biosensor for the in Vitro Measurement of Low Concentration of Putrescine in Blood. *J. Biochem. Biophys. Methods* **2002**, *53* (1–3), 165–175. https://doi.org/10.1016/S0165-022X(02)00105-7.

(17) Rochette, J. F.; Sacher, E.; Meunier, M.; Luong, J. H. T. A Mediatorless Biosensor for Putrescine Using Multiwalled Carbon Nanotubes. *Anal. Biochem.* **2005**, *336* (2), 305–311. https://doi.org/10.1016/j.ab.2004.10.027.

(18) Casero, R. A.; Marton, L. J. Targeting Polyamine Metabolism and Function in Cancer and Other Hyperproliferative Diseases. *Nat. Rev. Drug Discov.* **2007**, *6* (5), 373–390. https://doi.org/10.1038/nrd2243.

(19) Liu, R.; Lin, X.; Li, Z.; Li, Q.; Bi, K. Quantitative Metabolomics for Investigating the Value of Polyamines in the Early Diagnosis and Therapy of Colorectal Cancer. *Oncotarget* **2018**, *9* (4), 4583–4592. https://doi.org/10.18632/oncotarget.22885.

(20) Kalač, P.; Krausová, P. A Review of Dietary Polyamines: Formation, Implications for Growth and Health and Occurrence in Foods. *Food Chem.* **2005**, *90* (1–2), 219–230. https://doi.org/10.1016/j.foodchem.2004.03.044.

(21) Bardócz, S. Polyamines in Food and Their Consequences for Food Quality and Human Health. *Trends Food Sci. Technol.* **1995**, *6* (10), 341–346. https://doi.org/10.1016/S0924-2244(00)89169-4.

(22) Kalač, P. Health Effects and Occurrence of Dietary Polyamines: A Review for the Period 2005-Mid 2013. *Food Chem.* **2014**, *161*, 27–39. https://doi.org/10.1016/j.foodchem.2014.03.102.

(23) Reverté, L.; Prieto-Simón, B.; Campàs, M. New Advances in Electrochemical Biosensors for the Detection of Toxins: Nanomaterials, Magnetic Beads and Microfluidics Systems. A Review. *Anal. Chim. Acta* **2016**, *908*, 8–21. https://doi.org/10.1016/j.aca.2015.11.050.

(24) Muguruma, H.; Iwasa, H.; Hidaka, H.; Hiratsuka, A.; Uzawa, H. Mediatorless Direct Electron Transfer between Flavin Adenine Dinucleotide-Dependent Glucose Dehydrogenase and Single-Walled Carbon Nanotubes. *ACS Catal.* **2017**, *7* (1), 725–734. https://doi.org/10.1021/acscatal.6b02470.

(25) Sarikaya, M.; Tamerler, C.; Schwartz, D. T.; Baneyx, F. Materials Assembly and Formation Using Engineered Polypeptides. *Annu. Rev. Mater. Res.* **2004**, *34*, 373–408. https://doi.org/10.1146/annurev.matsci.34.040203.121025.

(26) Schulz, C.; Kittl, R.; Ludwig, R.; Gorton, L. Direct Electron Transfer from the FAD Cofactor of Cellobiose Dehydrogenase to Electrodes. *ACS Catal.* **2016**, *6* (2), 555–563. https://doi.org/10.1021/acscatal.5b01854.

(27) So, C. R.; III, J. L. K.; Oren, E. E.; Zareie, H.; Tamerler, C.; Evans, J. S.; Sarikaya, M. Molecular Recognition And. *ACS Nano* **2009**, *3* (6), 1525–1531.

(28) Tamerler, C.; Sarikaya, M. Molecular Biomimetics: Genetic Synthesis, Assembly, and Formation of Materials Using Peptides. *MRS Bull.* **2008**, *33* (5), 504–512. https://doi.org/10.1557/mrs2008.102.

(29) Willner, I. Biomaterials for Sensors, Fuel Cells,and Circuitry. *Science (80-.).* **2002**, *298*, 2407–2409.

(30) Willner, I.; Willner, B. Biomolecule-Based Nanomaterials and Nanostructures. *Nano Lett.*

2010, *10*, 3805–3815. https://doi.org/10.1021/nl102083j.

(31) Tamerler, C.; Duman, M.; Oren, E. E.; Gungormus, M.; Xiong, X.; Kacar, T.; Parviz, B. A.; Sarikaya, M. Materials Specificity and Directed Assembly of a Gold-Binding Peptide. *Small* **2006**, *2* (11), 1372–1378. https://doi.org/10.1002/smll.200600070.

(32) Woodbury, R. G.; Wendin, C.; Clendenning, J.; Melendez, J.; Elkind, J.; Bartholomew, D.; Brown, S.; Furlong, C. E. Construction of Biosensors Using a Gold-Binding Polypeptide and a Miniature Integrated Surface Plasmon Resonance Sensor. *Biosens. Bioelectron.* **1998**, *13* (10), 1117–1126. https://doi.org/10.1016/S0956-5663(98)00060-8.

(33) Haussmann, A.; Milde, P.; Erler, C.; Eng, L. M. Ferroelectric Lithography: Bottom-up Assembly and Electrical Performance of a Single Metallic Nanowire. *Nano Lett.* **2009**, *9* (2), 763–768. https://doi.org/10.1021/n18033784.

(34) Hnilova, M.; Khatayevich, D.; Carlson, A.; Oren, E. E.; Gresswell, C.; Zheng, S.; Ohuchi, F.; Sarikaya, M.; Tamerler, C. Single-Step Fabrication of Patterned Gold Film Array by an Engineered Multi-Functional Peptide. *J. Colloid Interface Sci.* **2012**, *365* (1), 97–102. https://doi.org/10.1016/j.jcis.2011.09.006.

(35) Kacar, T.; Zin, M. T.; So, C.; Wilson, B.; Ma, H.; Gul-Karaguler, N.; Jen, A. K. Y.; Sarikaya, M.; Tamerler, C. Directed Self-Immobilization of Alkaline Phosphatase on Micro-Patterned Substrates via Genetically Fused Metal-Binding Peptide. *Biotechnol. Bioeng.* **2009**, *103* (4), 696–705. https://doi.org/10.1002/bit.22282.

(36) Fenter, P.; Eisenberger, P.; Li, J.; Camillone, N.; Bernasek, S.; Scoles, G.; Ramanarayanan, T. A.; Liang, K. S. Structure of CH 3 (CH 2) 17 SH Self-Assembled on the Ag(111) Surface: An Incommensurate Monolayer. *Langmuir* **1991**, *7* (10), 2013–2016. https://doi.org/10.1021/la00058a008.

(37) Leong, K.; Chen, Y.; Masiello, D. J.; Zin, M. T.; Hnilova, M.; Ma, H.; Tamerler, C.; Sarikaya, M.; Ginger, D. S.; Jen, A. K. Y. Cooperative Near-Field Surface Plasmon Enhanced Quantum Dot Nanoarrays. *Adv. Funct. Mater.* **2010**, *20* (16), 2675–2682. https://doi.org/10.1002/adfm.201000424.

(38) Porter, M. D.; Bright, T. B.; Allara, D. L.; Chidsey, C. E. Spontaneously Organized Molecular Assemblies. 4. Structural Characterization of n-Alkyl Thiol Monolayers on Gold by Optical Ellipsometry, Infrared Spectroscopy, and Electrochemistry. *J. Am. Chem. Soc.* **1987**, *109* (12), 3559–3568. https://doi.org/10.1021/ja00246a011.

(39) Sarikaya, M.; Aksay, I. A. *Biomimetics : Design and Processing of Materials*; AIP Press: Woodbury, N.Y, 1995.

(40) So, C. R.; Hayamizu, Y.; Yazici, H.; Gresswell, C.; Khatayevich, D.; Tamerler, C.; Sarikaya, M. Controlling Self-Assembly of Engineered Peptides on Graphite by Rational Mutation. *ACS Nano* **2012**, *6* (2), 1648–1656. https://doi.org/10.1021/nn204631x.

(41) Akdim, B.; Pachter, R.; Kim, S. S.; Naik, R. R.; Walsh, T. R.; Trohalaki, S.; Hong, G.; Kuang, Z.; Farmer, B. L. Electronic Properties of a Graphene Device with Peptide Adsorption: Insight from Simulation. *ACS Appl. Mater. Interfaces* **2013**, *5* (15), 7470–7477. https://doi.org/10.1021/am401731c.

(42) Sarikaya, M.; Tamerler, C.; Jen, A. K.; Schulten, K.; Baneyx, F. Molecular Biomimetics-Nanotechnology through Biology. *Nat. Mater.* **2003**, *2*, 577–585.

(43) Tamerler, C.; Khatayevich, D.; Gungormus, M.; Kacar, T.; Oren, E. E.; Hnilova, M.; Sarikaya, M. Molecular Biomimetics: GEPI-Based Biological Routes to Technology. *Biopolymers* **2010**, *94* (1), 78–94. https://doi.org/10.1002/bip.21368.

(44) Evans, J. S.; Samudrala, R.; Walsh, T. R.; Oren, E. E.; Tamerler, C. Molecular Design of

Inorganic-Binding Polypeptides. *MRS Bull.* **2008**, *33* (5), 514–518. https://doi.org/10.1557/mrs2008.103.

(45) Hnilova, M.; Karaca, B. T.; Park, J.; Jia, C.; Wilson, B. R.; Sarikaya, M.; Tamerler, C. Fabrication of Hierarchical Hybrid Structures Using Bio-Enabled Layer-by-Layer Self-Assembly. *Biotechnol. Bioeng.* **2012**, *109* (5), 1120–1130. https://doi.org/10.1002/bit.24405.

(46) Hnilova, M.; So, C. R.; Oren, E. E.; Wilson, B. R.; Kacar, T.; Tamerler, C.; Sarikaya, M. Peptide-Directed Co-Assembly of Nanoprobes on Multimaterial Patterned Solid Surfaces. *Soft Matter* **2012**, *8* (16), 4327–4334. https://doi.org/10.1039/c2sm06426j.

(47) Hnilova, M.; Liu, X.; Yuca, E.; Jia, C.; Wilson, B.; Karatas, A. Y.; Gresswell, C.; Ohuchi, F.; Kitamura, K.; Tamerler, C. Multifunctional Protein-Enabled Patterning on Arrayed Ferroelectric Materials. *ACS Appl. Mater. Interfaces* **2012**, *4* (4), 1865–1871. https://doi.org/10.1021/am300177t.

(48) Hu, Y.; Mitchell, K. M.; Albahadily, F. N.; Michaelis, E. K.; Wilson, G. S. Direct Measurement of Glutamate Release in the Brain Using a Dual Enzyme-Based Electrochemical Sensor. *Brain Res.* **1994**, *659* (1–2), 117–125. https://doi.org/10.1016/0006-8993(94)90870-2.

(49) Wilson, G. S.; Gifford, R. Biosensors for Real-Time in Vivo Measurements. *Biosens. Bioelectron.* **2005**, *20* (12), 2388–2403. https://doi.org/10.1016/j.bios.2004.12.003.

(50) Wilson, G. S.; Hu, Y. Enzyme-Based Biosensors for in Vivo Measurements. *Chem. Rev.* **2000**, *100* (7), 2693–2704. https://doi.org/10.1021/cr990003y.

(51) Karaca, B. T.; Hnilova, M.; Tamerler, C. *Addressable Biological Functionalization of Inorganics: Materials-Selective Fusion Proteins in Bio-Nanotechnology*; 2004.

(52) VanOosten, S. K.; Yuca, E.; Karaca, B. T.; Boone, K.; Snead, M. L.; Spencer, P.; Tamerler, C. Biosilver Nanoparticle Interface Offers Improved Cell Viability. *Surf. Innov.* **2017**, No. 3, 139–148. https://doi.org/10.1016/j.physbeh.2017.03.040.

(53) Yuca, E.; Karatas, A. Y.; Seker, U. O. S.; Gungormus, M.; Dinler-Doganay, G.; Sarikaya, M.; Tamerler, C. In Vitro Labeling of Hydroxyapatite Minerals by an Engineered Protein. *Biotechnol. Bioeng.* **2011**, *108* (5), 1021–1030. https://doi.org/10.1002/bit.23041.

(54) Yucesoy, D. T.; Karaca, B. T.; Cetinel, S.; Caliskan, H. B.; Adali, E.; Gul-Karaguler, N.; Tamerler, C. Direct Bioelectrocatalysis at the Interfaces by Genetically Engineered Dehydrogenase. Thomas Telford.

(55) Zhang, S.; Karaca, B. T.; Vanoosten, S. K.; Yuca, E.; Mahalingam, S.; Edirisinghe, M.; Tamerler, C. Coupling Infusion and Gyration for the Nanoscale Assembly of Functional Polymer Nanofibers Integrated with Genetically Engineered Proteins. *Macromol. Rapid Commun.* **2015**, *36* (14), 1322–1328. https://doi.org/10.1002/marc.201500174.

(56) Tropea, J. E.; Cherry, S.; Waugh, D. S. Expression and Purification of Soluble His(6)-Tagged TEV Protease. *Methods Mol. Biol.* **2009**, *498*, 297–307.

(57) Hegner, M.; Wagner, P.; Semenza, G. Ultralarge Atomically Flat Template-Stripped Au Surfaces for Scanning Probe Microscopy. *Surf. Sci.* **1993**, *291* (1–2), 39–46. https://doi.org/10.1016/0039-6028(93)91474-4.

(58) Hu, J.; Qin, H.; Cross, T. A. A Systematic Assessment of Mature MBP in Membrane Protein Production: Overexpression, Membrane Targeting and Purification. *Protein Expr Purif* **2011**, *80* (1), 34–40.

(59) Mishin, V.; Gray, P. J.; Heck, D. E.; Laskin, D. L.; Laskin, J. D. Application of the Amplex Red/Horseradish Peroxidase Assay to Measure Hydrogen Peroxide Generation by

Recombinant Microsomal Enzymes. *Free Radic. Biol. Med.* **2014**, *48* (11), 1485–1491. https://doi.org/10.1037/a0032811.Child.

(60) Zhou, M.; Diwu, Z.; Panchuk-Voloshina, N.; Haugland, R. P. A Stable Nonfluorescent Derivative of Resorufin for the Fluorometric Determination of Trace Hydrogen Peroxide: Applications in Detecting the Activity of Phagocyte NADPH Oxidase and Other Oxidases. *Anal. Biochem.* **1997**, *253* (2), 162–168. https://doi.org/10.1006/abio.1997.2391.

Chapter 4: Investigation of the Selectivity of binding of Putrescine Oxidase through Genetically Engineered Gold Binding Peptide Tags

This project is carried out with the collaboration of Dwight O. Deay III,[1] Rachel T. Lietz,[2] Steve Seibold,[1] James Meyer,[2] Brandon Tomas,[1,2] Banu Taktak Karaca,[2] Mark Richter,[1] and Candan Tamerler[2,3] ([1]Department of Molecular Biosciences; [2]Department of Mechanical Engineering; [3]Bioengineering Research Center (BERC) & Bioengineering Program, University of Kansas). *The tentative title of the manuscript is "Investigation of the Selectivity of binding of Putrescine Oxidase through Genetically Engineered Gold Binding Peptide Tags." Some of the data presented here collected by Tyler Nguyen and Talisa Hughes, who worked as undergraduate students in Berrie Lab.*

4.1 Abstract

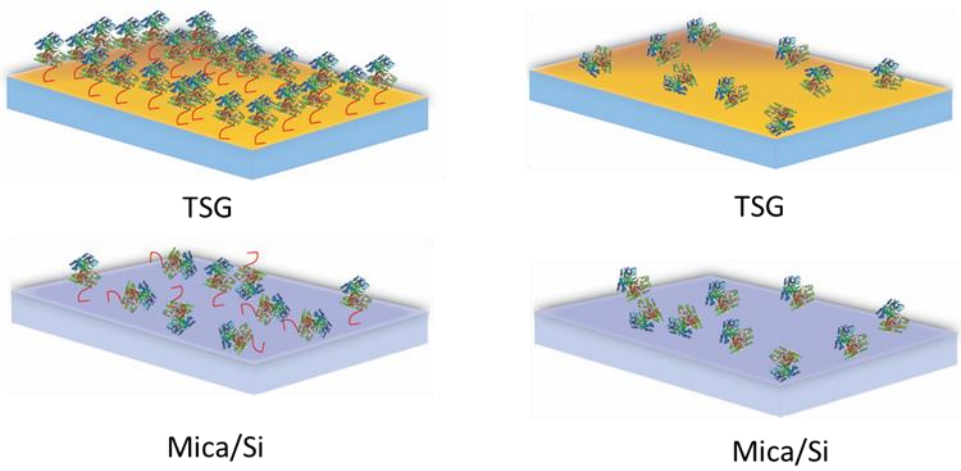

Adsorption and self-assembly of biological molecules onto surfaces play critical roles in a large range of novel applications from biosensors to chemical reactors. These applications require immobilization of proteins in such a way that the molecules remain functionally active on the surface, often with precise spatial arrangement. For this purpose, development of affinity peptide sequences towards different metal substrates have been developed for materials such as gold, silver

and silicon surfaces. The peptide sequence recognizes specific inorganic materials and can be used as molecular building blocks for novel applications. Gold binding peptide sequences have been incorporated with putrescine oxidase (PutOx) enzymes and their binding to a variety of surfaces was studied using AFM. To be useful in protein based biosensing, the orientation and conformation of the protein on surfaces must be controlled so that the active site can be accessible. Here we report the behavior of wild-type (PutOx) and gold binding peptide tagged putrescine oxidase (PutOx-AuBP) enzymes on template-stripped gold (TSG), mica, Si(111), Octadecyltrichlorosilane on Silicon (OTS-Si-SAM), Graphite, Carboxyl self-assembled monolayers on TSG (COOH-TSG-SAM), and hydroxyl-terminated self-assembled monolayers on TSG (OH-TSG-SAM). This allows selectivity to be investigated for a wide range of surface chemistries. When the protein adsorption was carried out on the TSG surface, AuBP tagged protein adsorbed preferentially on to the surface over wild type. The comparison of protein dimensions on TSG surface suggested that there is a significant difference in the height when PutOx-AuBP on the surface compared with the wild type (See *chapter 3*). On the mica and Si surfaces, the dimensions do not show significant difference suggesting that the binding occurs through nonspecific interactions with the protein on these surfaces, while there is significant involvement of the peptide sequence in binding to the gold surface. We observed protein aggregation and unfolding on hydrophobic surfaces such as graphite and OTS-Si-SAM due to the hydrophobic interaction between protein and surface. On hydrophilic surfaces such as Si, mica, COOH-TSG-SAM, and OH-TSG-SAM, the protein does not aggregate or unfold as extensively as on the hydrophobic surfaces. This study demonstrates how the surface chemistry affects the binding of the peptide-labeled protein, which will aid in the design of materials for the development of nanoscale bionanodevices which display a range of surface chemistries in the device.

4.2 Introduction

Controlling protein adsorption at solid surfaces is critical for a large variety of applications such as biocatalysis, biomedicine[1,2], food safety, and environmental monitoring. [3–5] Increasingly, the importance of the orientation and conformation of the protein at the surface has been recognized as key to successful implementation of such applications. A number of approaches have been taken to control the orientation of the protein on surfaces to obtain the desired biological activity or reactions including covalent and noncovalent coupling using a variety of functional groups.[6–9]

Investigations involving a specific protein interacting with a range of different surfaces will aid in the design of the most suitable platform for more sensitive applications in biosensing or biocompatible device formation, by allowing control of coverage and orientation of the protein. It is essential for the protein to remain functionally active upon adsorption to the surface.[10,11] The adsorption of molecules often proceeds through several steps: adsorption of the weakly bound precursor, diffusion, and finally the conformational changes which results in a stable and tightly bound configuration.[11,12] The amount adsorbed and the conformation of the protein on the surface depend strongly on the surface functionality. A variety of approaches have been taken to allow attachment of proteins to surfaces including nonspecific binding, covalent coupling through amino acid residues, or attachment of functional surface binding tags such as histidines, or thiols. Some of these approaches allow selective attachment of the protein through a specific site on the protein, allowing some hope of control of the orientation of the protein. One such approach is the use of genetically engineered peptide tags. This provides the control needed for the specific adsorption of desired molecules at the nanoscale. Atomic force microscopy (AFM) allows information regarding protein orientation and conformation to be obtained directly through imaging even at the single molecule level.[13,14]

4.2.1 Model Protein System: Putrescine Oxidase

Wild type putrescine oxidase (PutOx) and gold binding peptide labeled putrescine oxidase (PutOx-AuBP) have been investigated as a suitable model enzyme to represent redox enzymes which can be engineered to detect a variety of molecules ranging from cancer markers in blood to spoiled food. [15–18] Putrescine Oxidase is an enzyme that belongs to a family of Flavin-containing Amine Oxidases (FAO), which are involved in the oxidation of putrescine and other aliphatic diamines in the presence of oxygen and water (See **Scheme 1**). These biogenic amines are derived from free amino acids. Putrescine oxidase and other amine oxidase enzymes can be used for the detection of spoiled food[15–17] and cancer markers in blood.[18] In this study, we used putrescine oxidase from actinomycete *Rhodococcus erthropolis,* which is a homodimer of ~100 kDa molecular weight. The gold binding peptide sequence cpgWALRRSIRRQSYgpc is linked to PutOX via PGGG linker onto the N-terminal end of the protein. Both the wild type and the labeled enzyme are robust, relatively easily expressed in functionally active form, and have well-defined structures, making this particular enzyme an attractive protein for model studies of protein binding.

Scheme 1. *The reaction catalyzed by Putrescine oxidase enzyme.*

$$\textit{Putrescine (aq)} + O_2\,(g) + H_2O\,(l) \rightarrow \textit{4-aminobutanal (aq)} + NH_3\,(g) + H_2O_2\,(l)$$

4.2.2 Protein Immobilization Strategy: Affinity peptides

Affinity peptides are specific sequences of amino acids which have a high affinity for a specific material. While the amino acids are the fundamental units of proteins and peptides, they combine in specific sequences for advanced biological function. As an example, by using combinatorial biological techniques, researchers were able to select peptide sequences for controlling the nucleation of nanocrystals, inorganic nanoparticle assembly, and use as molecular linkers. Also,

researchers have utilized cell surface display[19] and phage display[20] to investigate the material specific affinity peptide sequences. Among those, gold binding peptide sequences,[21,22] silica binding peptide sequences,[23,24] and silver binding peptide sequences[25,26] have been studied as molecular tools for biotechnological and nanotechnological applications.[26] QCM and SPR studies have investigated the adsorption kinetics of an engineered gold binding peptide 3×MHGKTQATSGTIQS (3R-GBP2) sequence which was derived using cell surface display.[21] From the Langmuir model, they observed bi-exponential kinetics, which suggests two different processes of binding to gold. During the studies of the adsorption, diffusion, and self-assembly of the molecules on Au(111) surface, multiple stages of structural evolution were observed over time with the diffusion of 3R-GBP2 on the gold surface.[21,27] By utilizing the same affinity peptide sequence on the gold surface researchers have been able to immobilize streptavidin as a probe protein as confirmed by SPR and AFM studies.[28] Because of the selectivity of these affinity peptides, they have been utilized as linkers between surfaces such as Au and Si interfaces.[23,29] QCM and CV studies also show that the excess negative charge on the solid surfaces plays an important role in peptide binding on the gold surface.[30] In this study, a previously characterized AuBP: WALRRSIRRQSY sequence was used for the immobilization of putrescene oxidase on gold (see *Chapter 3* for detailed information).[31–33]

4.2.3 Protein on Surfaces

Controlling the orientation of proteins on surfaces is critical since the activity of protein molecules is required for biosensing. It is known that for some proteins, adsorption occurs differently on different surfaces.[8] As an example changes in conformation have been observed for fibrinogen upon addition to hydrophilic and hydrophobic surfaces.[34] Further on hydrophobic

surfaces, unfolding, aggregation, and clustering have been observed.[10] Surface coverage and the morphology of the adsorbed proteins on self-assembled monolayers such as carboxyl, methyl, and aldehyde terminated SAM on gold, depend on the pH and the surface functionality.[35] Also, at the isoelectric point, protein molecules adsorbed readily on to the surface, typically through hydrophobic interactions.[36,37] Further there are other methods such as immobilization of protein via covalent interactions to polymer surfaces.[38] In previous studies, researchers have shown that the oriented immobilization of protein can be done using affinity peptides towards the polystyrene surfaces.[39]

In this work, the behavior of an affinity peptide tagged model enzyme, putrescine oxidase (along with the wild type enzyme) on different surfaces has been investigated using atomic force microscopy. Wild-type (PutOx) and peptide tagged protein (PutOx-AuBP) were adsorbed onto hydrophilic, hydrophobic and SAMs, and several inorganic surfaces to investigate differences in adsorption related to the surface chemistry. The ability to assemble proteins for nanoscale devices requires specific recognition of the patterning material with low background absorption on the rest of the surface. Therefore, investigation of how the absorption varies with material is critical for design of such devices. In this work we use AFM to show that the molecules adsorption differently to gold when the peptide sequence is attached, and with greater affinity. In addition, the adsorption to all other surfaces shows very little difference between the native and the peptide tagged protein. Hydrophobic surfaces also show significant denaturation and aggregation of the protein. Hydrophilic surfaces including mica, carboxyl and hydroxyl-terminated SAM surfaces do not show extensive denaturation and result in minimal nonspecific binding. These may be ideal candidates for resist layers when immobilizing protein on patterned gold surfaces at the nanoscale.

Overall, these results investigate the specificity and selectivity of the AuBP tag in controlling protein-surface interactions with a variety of materials.

4.3 Materials and methods

Wild-type and the gold binding peptide tagged putrescine oxidase enzymes were obtained from the Mark Richter group, Department of Molecular Biosciences, University of Kansas, Lawrence, Kansas-66045. HOPG graphite samples were purchased from Veeco (digital instruments) and cleaved immediately before use. Mica was purchased from Lawrence Mica Company (New York, ruby muscovite mica), and cleaved before use. A standard phosphate buffer of pH=8.0 was obtained from Fisher Scientific. 11-mercapto-1-undecanol and 11-mercaptoundecanoic acid were purchased from Sigma-Aldrich. Octadecyltrichlorosilane (OTS, 95 %) was purchased from ACROS-Organics. Trifluoroacetic acid solution was purchased from Fisher Scientific. The single-side polished Silicon samples (Virginia Semiconductor) used in this experiment were cut from boron-doped Si(111) wafers (resistivity = 3.0-6.0 Ω. cm). Epoxy A and B solutions were purchased from Epoxy Technology, Billerica, MA. Milli-Q water (resistivity> 18.2 MΩ-cm) was used to clean the surfaces before and after protein incubation.

All surface topography images were taken with a Veeco multimode scanning probe microscope (Digital Instruments CA) using tapping mode. For the tapping mode images, diamond-like carbon coated (DLC) tap 300 probes from Budget sensors (spring constant 40 N/m and resonance frequency of 300 kHz) were used. For contact mode images, non-conductive silicon nitride cantilevers, with spring constants ranging from 0.12 to 0.06 N/m, were used (Veeco, Camarillo, CA). All AFM images were analyzed by NanoScope Analysis 1.5 software by Bruker Corporation.

4.3.1 Template Stripped Gold Surfaces Formation

a. Preparation of Gold Films

The gold thin films on mica were prepared using an Edwards 306A diffusion-pumped vacuum evaporator system. A tungsten wire basket was filled with commercial gold wire (99.999%, Alfa Aesar). Mica sheets were cleaved to expose fresh surfaces and were mounted on a rotatable heated sample holder. The samples were heated radiatively using a quartz lamp. After thoroughly degassing the chamber, metal source, and samples, the gold was evaporated onto the mica substrates by passing current through the wire basket. The evaporation is typically carried out at a rate of ~1-3 Å/s to a thickness of ~100-200 nm. Throughout the evaporation the temperature of the system circulates from 100-300 ˚C (monitored by thermocouple). The thickness and evaporation rate was monitored using a quartz crystal microbalance. Once the desired thickness of gold samples were coated, the current was slowly decreased and turned off and the shutter was replaced. Then, the gold was allowed to anneal for 1-3 hours with the lamp heating the system. Finally, lamp was then turned off, the system was allowed to cool, and vented to atmospheric pressure before opened.

b. Preparation of Gold for Template Stripping

Template stripped gold surface were prepared according to previous procedures.[40] Briefly, the gold evaporated mica surfaces were glued onto a ~1 × 1 cm^2 glass surface by using a mixture of 1:1 epoxy kit (EPO-TEK 377) part A and part B (Epoxy Technology). Then, the surfaces were cured at 80 °C for 4-24 hours. After cooling, the glass pieces were cleaved from mica immediately before use. This method produces surface with large single crystalline domains, that are quite flat.

4.3.2 Si Surfaces Preparation for Monolayer Formation and Protein Adsorption

Silicon wafers were cut into an approximate 1×1 cm^2 size, and the samples were piranha cleaned using 3:1 (by volume) solution of H_2SO_4 and H_2O_2 mixture, rinsed with MilliQ water and dried under a stream of nitrogen. (*NOTE: Piranha solution is an extremely corrosive, strong oxidizer. Avoid any contact with organic substances, do not store in a closed container, and handle with appropriate personal protective clothing.)*

4.3.3 Self-assembled Monolayer Formation

a. Thiol Monolayer Formation on Template-Stripped Gold (TSG) Surfaces

First, fresh template-stripped gold pieces were rinsed with ethanol to remove any impurities on the surface. Then, the samples were dried under N_2 stream, and the optical constants were obtained for each gold sample. Samples were placed in 0.1-5.0 mM ethanolic solutions of 11-mercapto-1-undecanol or 11-mercaptoundecanoic acid for 24 hours. To prevent multilayer formation of the carboxyl SAM surfaces, 2% trifluoroacetic acid (2 % TFA) solution was added to the thiol solution.[41] Next, the samples were taken out from the solutions, rinsed in ethanol, and dried under N_2 stream.

b. OTS-Monolayer Formation on Cleaned Si(111) Surface

Self-assembled monolayers were prepared using the method explained by Sung *et al*. for forming alkyl monolayers on silicon oxide substrates.[42] Piranha cleaned samples were placed in a 2.5 mM solution of OTS in toluene for 24 hours in airtight containers. After that, samples were taken out of solution and rinsed with toluene, chloroform, acetone, and ethanol respectively. Next, samples

were sonicated in toluene for 30 minutes, and these N_2 dried samples were characterized by ellipsometry, goniometry, and AFM imaging.

4.3.4 Characterization of the Monolayers

a. Ellipsometry

The film thicknesses were determined using an Auto EL III ellipsometer (Rudolph Research). The measurements were made with a HeNe laser at a wavelength of 632.4 nm and an angle of 70°. The optical constants for the gold films were determined independently for each sample from the measurement on the freshly cleaned bare gold sample. These optical constants were used as input for the substrate properties in the determination of the thickness of the adsorbed organic layer. For the organic thin film, a refractive index of 1.45[43,44] was assumed. Measurements were recorded at five different spots on the sample, and the reported thicknesses are an average of the measurements over each of those spots along with the standard deviation of the measurement.

b. Contact angle measurements

Static contact angles were obtained on a Rame´-Hart 100-00 NRL goniometer using the sessile drop technique. Measurements were made with Milli-Q water (droplet size ~2 μL) on at least three to five spots per sample.

c. Atomic Force Microscope (AFM) Measurements

AFM experiments were carried out with a Digital Instruments Nanoscope IIIA Multimode system in tapping mode with typical scan rates of 1-3 Hz. The measurements were performed in tapping mode using diamond-like carbon coating silicon cantilevers with resonance frequencies from 300 to 400 kHz (Budget sensors). For the analysis done for the protein, most of the images are 1.00×1.00 μm in size.

4.3.5 Protein Adsorption Studies

The surfaces were washed with pH (8.0) adjusted Milipure water for 30 seconds and rinsed with pH 8.0 phosphate buffer solution for 30 seconds before protein adsorption. Then, 100 µL of 5.0 µg/mL solutions of enzymes were adsorbed for a specific time under ambient conditions. Next, surfaces were washed with pH 8.0 phosphate buffer and followed by washing with pH adjusted Milipure water to reduce salt formation. After drying with the stream of N_2, surfaces were imaged with Nanoscope IIIA Multimode AFM system in tapping mode with typical scan rates of 1 Hz.

To determine the time at which a monolayer of protein adsorbed on the surface, 5.0 µg/mL solution of 100 µL PutOX-AuBP solution was introduced to the TSG surfaces and incubated for different time intervals (2, 4, 30, 60, and 90 minutes). Time at which monolayer coverage was observed for the PutOX-AuBP on TSG surface was 45 approximately minutes. This was used as an estimate of the time that would be required for a resist layer to prevent protein adsorption. Protein adsorption was carried out on a variety of different surfaces under these conditions including graphite, mica, silicon, and hydrophobic and hydrophilic SAM films. After protein adsorption and rinsing, AFM tapping mode topography images were taken to compare the amount and shape of proteins adsorbed on each surface.

As model hydrophobic surfaces, graphite and OTS-Si-SAM were used in protein adsorption studies. To observe the behavior of the protein in the presence of higher concentrations of protein, 5.0 µg/mL solution was adsorbed for 2 hours following the same procedure mentioned above on the graphite surface. Then to isolate and observe single molecules on the surface, 0.3 µg/mL solution of protein was used with adsorption time of 30 minutes. To study the protein adsorption on the OTS-SAM surfaces, 5.0 µg/mL protein solution was placed on the surface for 2 hours.

Piranha cleaned Si(111) surfaces were used to study the adsorption of protein molecules, and 5.0 μg/mL solutions of wild-type and gold binding peptide tagged protein was adsorbed for 2 hours following the same procedure mentioned above. For the mica samples, 5.0 μg/mL protein solutions were absorbed for 2.0 hours. In each of these cases, the dimensions and the surface density of the protein were analyzed by Nanoscope Analysis 1.5 software (Bruker Corporation).

4.4 Results and Discussion

In this study, adsorption of PutOx-AuBP and the wild-type enzyme on different surfaces were compared using atomic force microscopy. The surfaces investigated in this study were TSG, OH-SAM-TSG, COOH-SAM-TSG, Graphite, OTS-Si-SAM, Si(111), and Mica.

The engineered peptide used has been demonstrated to bind selectively to the Au(111) surface with high affinity.[31–33] [32] Template stripped gold surfaces were used here because they exhibit large terraces of flat, Au(111) grains (Fig 4.1a). To determine the time at which a monolayer coverage of protein was observed for the PutOx-AuBP molecules on the template-stripped gold surface, 100 μL of 5.0 μg/mL solution was adsorbed on to the surface for different time intervals and the surface density (number of molecules per square micrometer) with respect to time was plotted. For some of the time points, relevant AFM images are shown in *Figure 4.1a* (next to the data points). It was observed that for a 5.0 μg/mL solution, 30 to 45 minutes of incubation gives roughly monolayer coverage, with the coverage increasing more slowly beyond this time point. Once monolayer formation occurred, stacking of the next layer on top of the first layer can be seen. When wild type protein adsorbed on to the surface, there were a significantly smaller number of molecules observed on the surface with compared to the peptide tagged protein on the surface (*see Figure 4.1c and 4.1d*).

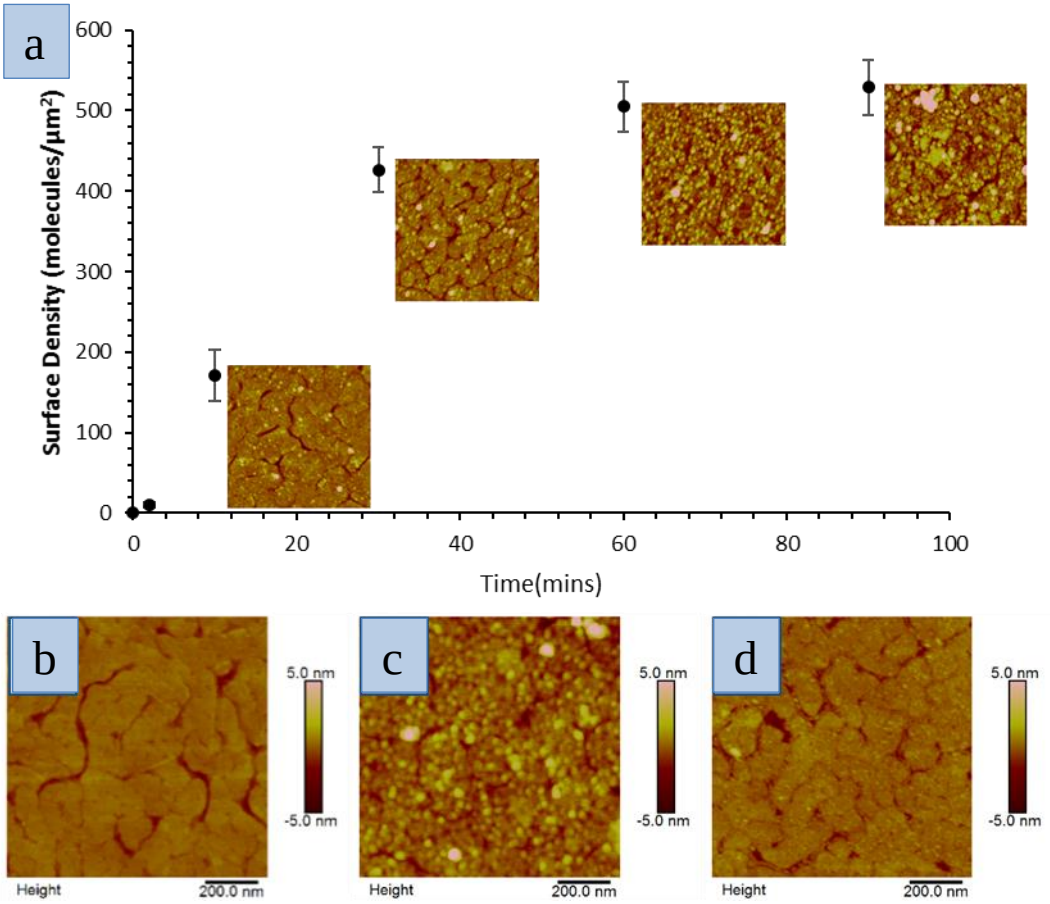

Figure 4. 1: *Comparison of the bare surface of TSG with the protein adsorbed surfaces. a) The plot on the top shows the surface coverage change with respect to time of PutOx-AuBP protein incubation. The AFM images next to the plot show the coverage at relevant data points. The bottom panel represents AFM images for b) bare gold surface before protein incubation, c) after adsorption of 5.0 µg/mL PutOx-AuBP for 45 minutes and d) after adsorption of 5.0 µg/mL PutOx for 45 minutes. The images are in 1.0×1.0 µm in size and 10 nm in height (color scale on the left).*

Since 100 µL of 5.0 µg/mL solution of PutOx-AuBP for 45 minutes of incubation gives a monolayer of protein on the surface, these conditions were used to investigate a resist layer which will be used to develop metal-based nanostructures for biosensing. To investigate the interactions of the wild-type and the peptide tagged enzyme on SAM covered surfaces, OH and COOH terminated SAMs on TSG were studied and compared with the TSG surface. For the TSG-SAM-COOH surfaces, the monolayer thickness obtained was 15.4±2.6 Å, and the contact angle was

30.0°±2.3°. For the TSG-SAM-OH surfaces, the monolayer thickness obtained was 16.1±3.3 Å, and the contact angle was 32.2°±2.0°.

Images show that when the functionality on the surface changes, the density of protein on the surface also changes. From the AFM topography images shown in *Figure 4.2*, regardless of the type of surface, nonspecific protein adsorption on the surfaces can be observed. But, compared with the bare gold surfaces for the same concentration and the same adsorption time, the gold-binding peptide tagged putrescine oxidase enzyme show the highest affinity towards the gold and least affinity towards to the TSG-OH-SAM surface *(Figure 4 2)*. Wild type enzyme also shows less affinity towards the gold. This indicates that the surface functionality plays a significant role in the adsorption process and this is important to maintain the activity of the protein while attached to the surface.

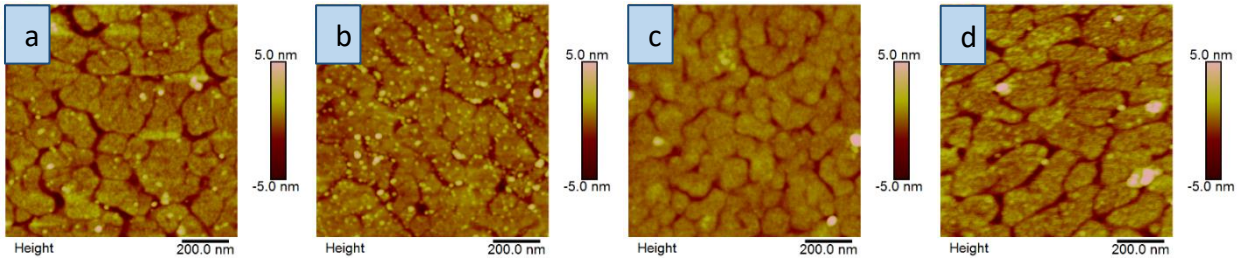

Figure 4. 2: *AFM topography images for the comparison of 5.0 µg/mL protein adsorbed for 45 minutes. a. PutOX-AuBP on COOH SAM, b. Wild type enzyme on TSG on COOH SAM, c. PutOx-AuBP on OH-SAM and d. Wild type enzyme on OH-SAM. The images are in 1.0×1.0 µm in size and 10 nm in height (color scale in left).*

Both hydrophobic surfaces investigated (graphite, and OTS-SAM) are flat and uniform. When the wild type or the peptide tagged protein adsorbed, due to the hydrophobic interactions, aggregation and clustering of molecules were observed with or without the AuBP tag. *Figure 4.3* shows the behavior of the wild type and peptide tagged protein on the graphite surface. When 5.0 µg/mL solution was adsorbed on to the surface for 45 minutes, molecules tend to unfold and

aggregate on the surface. Next, the second layer builds on the unfolded molecules with less denaturation.

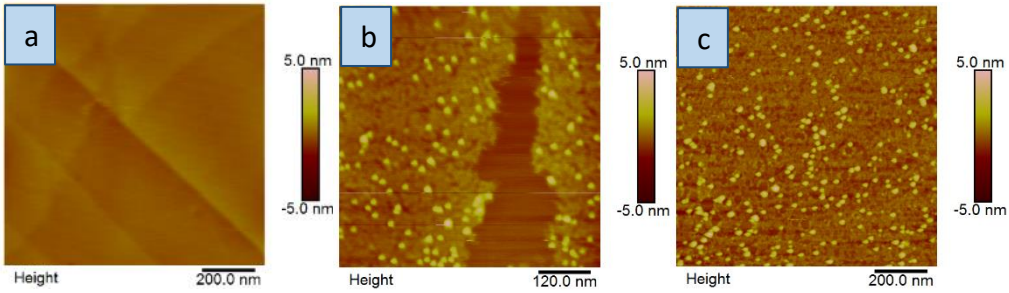

Figure 4. 3: *AFM images of a) bare surface of graphite, b) 5.0 µg/mL PutOX-AuBP adsorbed on graphite for 45 minutes, and c) wild type 5.0 µg/mL PutOX adsorbed on to graphite for 45 minutes. Both molecules behave in the same way on the graphite surface which forms unfolded first layer and a second layer with sphere-like molecules. The images are in 1.0×1.0 µm in size and 10 nm in height (color scale in left).*

To study the single molecule behavior, the concentration of the solution was dropped down to 0.3 µg/mL, and adsorption time was decreased to 30 minutes to reduce the coverage (*see Figure 4.4a*). Regardless of whether the wild type or peptide tagged protein adsorbed on to the surface, protein adsorption is often observed near the step edges, and molecules have the same behavior. Because of this AFM images were shown only for the PutOx-AuBP adsorption. From the AFM images, single molecules (partially unfolded and aggregated) and small clusters were isolated (*Figure 4.4b*). Overall, both protein types prefer the step edges of the graphite surface due to a combination of energetic, surface chemistry, and steric considerations, as previously observed in other protein systems.[10] One of the unfolded dimer on the graphite surface is shown in *Figure 4.4c*. The molecule has a length of 47.1 nm, the width of 45.5 nm and height of 0.8 nm. The molecules analyzed on the graphite surface consistently appear to have two partially unfolded units, which have single unit dimensions of 25.993 nm × 25.971 nm × 0.831 nm.

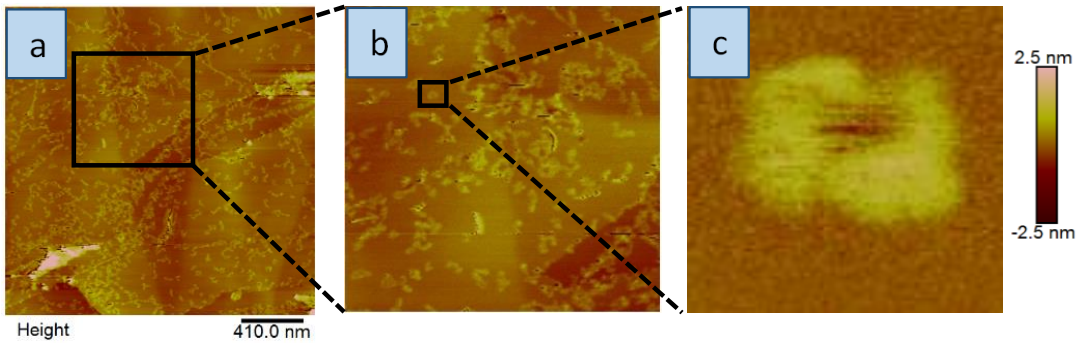

Figure 4. 4: *a) Adsorption of 0.3 µg/mL PutOX-AuBP on to graphite surface for 30 minutes and showing molecules on the step edges,* ***b)*** *Zoomed image of clustered molecules and* ***c)*** *a partially unfolded isolated molecule. The images are 5 nm in height (color scale in left).*

The OTS-SAM surface has a well-packed methyl terminated self-assembled monolayer of octadecyltrichlorsilane (C_{18}). The surface does not have step edges and is relatively smooth. Regardless of the type of putrescine oxidase introduced, aggregation and unfolding of the protein are observed on this hydrophobic surface as well. On the surface, branch-like structures have been observed, and they appear to be clustered and aggregated on the surface (see *Figure 4.5*).

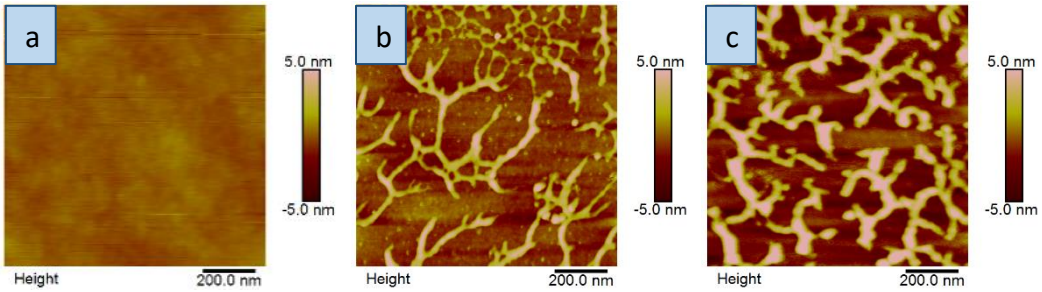

Figure 4. 5: *AFM images of a) methyl terminated, hydrophobic SAM film, and (b, c) aggregated and unfolded molecules of b) PutOx-AuBP, and c) PutOx on OTS-SAM surfaces. These molecules again appear clustered as in the case of the graphite surfaces. The images are in 1.0×1.0 µm in size and 10 nm in height (color scale in left).*

On the other hand, hydrophilic surfaces such as Si(111), mica, TSG-COOH, and TSG-OH surfaces have weaker interactions with the protein molecules, as the protein does not tend to

aggregate or unfold on the surface. When comparing the protein binding on hydrophilic surface with the hydrophobic surfaces, isolated single molecules were commonly observed on the hydrophilic surfaces (see *figure 4.2*), the surfaces of hydrophobic materials contained larger clusters and aggregates of protein molecules (see *Figures 4.3-4.5*). Also, hydrophilic surfaces show low coverage of molecules while hydrophobic surfaces give higher coverage under the same conditions. This suggests weaker binding to the hydrophilic SAMs with respect to hydrophobic SAMs.

As the model hydrophilic surfaces, silicon and mica surfaces were used for the protein adsorption studies. The Si(111) surface has a SiO_2 layer, which was used for the adsorption of enzyme and the adsorption concentrations were 5.0 µg/mL for 2 hours. There was no significant difference between wild-type and the peptide tagged protein. This suggests the nonspecific binding of the enzyme on the Si(111) surface (*see Figure 4. 6*). The dimensions of isolated single molecules were analyzed using AFM software. *Table 4.1* shows the average putrescine oxidase dimensions from the cross-sectional measurements of individual molecules on Si(111) surfaces.

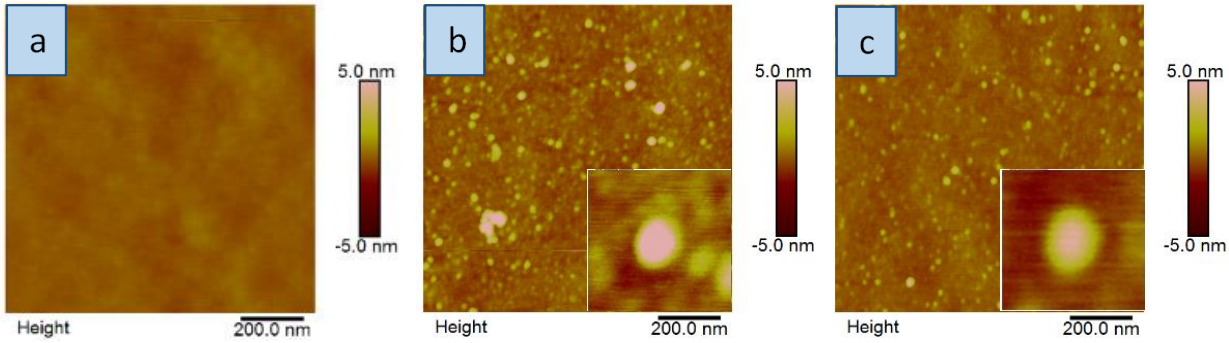

Figure 4. 6: *AFM topography images of the a) Bare Si surface, after adsorption of 5.0 µg/mL b) PutOx-AuBP (isolated single molecule on the right), and c) PutOX (isolated single molecule on the right) for 2 hours. The images are 1.0×1.0 µm in size and 10 nm in height (color scale in left).*

Table 4. 1: *Average putrescine oxidase dimensions obtained from cross-sectional measurements of individual molecules on Si(111) surfaces (n=50).*

Protein type	Length (nm)	Width (nm)	Height (nm)
PutOX	19.6±1.1	18.1±0.5	2.6±0.2
PutOX-AuBP	19.5±1.3	17.6±0.9	2.6±0.3

The measurements suggested that the enzyme molecules were randomly oriented on the surface regardless of having an additional peptide sequence or not. Also, compared with the hydrophobic surfaces mentioned above, molecules do not aggregate, and they had spherical shape once adsorbed on to the surface.

In addition to Si(111) surface, the other hydrophilic surface studied was mica, and the concentration studied on the mica surface was 5.0 μg/mL. Regardless of the type of the protein, there was no significant difference between the adsorbed amount of wild-type and the peptide tagged protein on the Mica surface *(see Figure 4.7)*. This suggests the nonspecific binding of the enzyme on the mica surface. Also, single molecules isolation and dimension analysis were carried out using AFM software. *Table 4.2* shows the average dimensions of putrescine oxidase from the cross-sectional measurements of individual molecules on Mica Surfaces. Dimensional analysis was not carried out on the hydrophobic surfaces due to unfolding and aggregation which led to clusters of molecules on the surface.

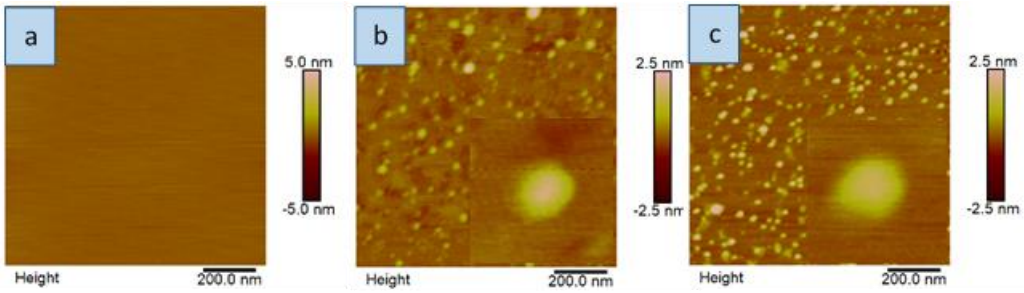

Figure 4. 7: *AFM topography images of the a) bare mica surface, after adsorption of 5.0 µg/mL b) PutOx-AuBP (isolated single molecule on the right), and c) PutOX (isolated single molecule on the right) for 2 hours. The images are in 1.0×1.0 µm in size and 5 nm in height (color scale in left).*

Table 4. 2: *Average putrescine oxidase dimensions obtained from cross-sectional measurements of individual molecules on mica surfaces (n=50).*

Protein type	Length (nm)	Width (nm)	Height (nm)
PutOx	21.6±2.2	18.6±1.8	2.1±0.3
PutOx-Aubp	22.3±2.0	20.3±1.4	2.1±0.3

The observed dimensions of the molecules suggest that the enzyme molecules are randomly oriented on the surface regardless of having an additional peptide sequence or not. Also, compared with the hydrophobic surfaces mentioned above, proteins do not aggregate, and they have a spherical shape once adsorbed on to the surface. The wild type enzyme on the TSG surface has average dimensions of 19.5±1.5, 17.3±1.1, and 2.3±0.2 (*See Chapter 5*). These values are not significantly different than the wild type enzyme on mica and silicon surfaces (*see Table 4.1 and 4.2*) suggesting that the adsorption in these cases is nonspecific. On the other hand, the dimensions determined for the PutOx-AuBP were 20.0±1.2, 17.8±1.2, and 3.2±0.4 (*See Chapter 3*). This suggests that there is a significant difference in the height of the adsorbed molecules on TSG when comparing the WT and peptide tagged protein, due to the specific binding through the AuBP. Also,

when comparing the dimensions of peptide tagged PutOx on TSG with the protein on mica and silicon, still there is a significant difference in height. This strongly suggests that there is a significant impact of the peptide tag on the binding to the gold surface, and we suggest that the protein molecules behind through the AuBP tag on the gold surface, allowing the protein to sit farther from the surface, while retaining activity and shape. On the hydrophilic surfaces, the protein shows no sign of aggregation, unfolding, or the clustering since there is less favorable interactions with protein molecules and silicon, mica, and TSG surfaces.

Since hydrophobic surfaces tend to aggregate and unfold the proteins that adsorbed on to the surface, there is a need of an alternative resist layer which prevents protein adsorption/aggregation while only the gold surface binds protein molecules for biosensor development (see *Figures 4.3-4.5*). We had developed gold nanowires and nanodot arrays on OTS monolayers (s*ee Chapters 6 and 7*) and show that this isn't the best approach to this protein system due to unfolding and aggregation of protein molecules on hydrophobic monolayers. To further investigate this, a variety of surfaces were studied and found that hydroxyl terminated SAM was the best surface to be used as a resist layer.

From the comparison of adsorption on a variety of surfaces, it is clear that the PutOx binding is significantly influenced by the surface chemistry, the AuBP tag only has a significant effect on the gold surface. This is to be expected since the AuBP was designed for high affinity for this surface. Importantly, the nonspecific interactions with other surfaces result in reduced binding but can result in unfolding and aggregation of the protein. If engineered peptide tags are to use in the self-assembly of complex hierarchical structures, the influence of the interactions with areas of the surface outside the desired protein pattern must be considered.

4.5 Conclusion

In this study report the behavior of PutOX and PutOX-AuBP enzymes on TSG, mica, Si(111), OTS-Si-SAM, Graphite, COOH-TSG-SAM, and OH-TSG-SAM. These molecules adsorbed differently on different surfaces. On hydrophilic surfaces, PutOx and PutOx-AuBP showed decreased adsorption compared to the hydrophobic surfaces. The PutOx showed aggregation, unfolding clustering, and mobility towards the step edges on hydrophobic surfaces. When comparing the TSG surfaces, WT had less affinity towards gold showing nonspecific binding, while PutOX-AuBP showed higher affinity towards the gold highlighting the involvement of the affinity peptide tag in binding on the gold surface. Little difference was observed between the molecular dimensions of molecules adsorbed nonspecifically on gold and the hydrophilic SAM surfaces. The coverage and distribution of both the PutOx and PutOx-AuBP depend strongly on the surface chemistry of the substrate, showing the importance of both the selectivity and specificity of binding the peptide tagged protein in the design of complex self-assembled hybrid materials.

4.6 References

(1) Maduraiveeran, G.; Sasidharan, M.; Ganesan, V. Biosensors and Bioelectronics Electrochemical Sensor and Biosensor Platforms Based on Advanced Nanomaterials for Biological and Biomedical Applications. *Biosens. Bioelectron.* **2018**, *103* (October 2017), 113–129. https://doi.org/10.1016/j.bios.2017.12.031.

(2) Erol, O.; Uyan, I.; Hatip, M.; Yilmaz, C. Recent Advances in Bioactive 1D and 2D Carbon Nanomaterials for Biomedical Applications. *Nanomedicine Nanotechnology, Biol. Med.* **2018**, *14* (7), 2433–2454. https://doi.org/10.1016/j.nano.2017.03.021.

(3) Justino, C.; Duarte, A.; Rocha-Santos, T. Recent Progress in Biosensors for Environmental Monitoring: A Review. *Sensors* **2017**, *17* (12), 1–25. https://doi.org/10.3390/s17122918.

(4) Lang, Q.; Han, L.; Hou, C.; Wang, F.; Liu, A. A Sensitive Acetylcholinesterase Biosensor Based on Gold Nanorods Modified Electrode for Detection of Organophosphate Pesticide. *Talanta* **2016**, *156–157*, 34–41. https://doi.org/10.1016/j.talanta.2016.05.002.

(5) Soh, N.; Tokuda, T.; Watanabe, T.; Mishima, K. A Surface Plasmon Resonance Immunosensor for Detecting a Dioxin Precursor Using a Gold Binding Polypeptide. **2003**, *60*, 733–745. https://doi.org/10.1016/S0039-9140(03)00139-5.

(6) Hitaishi, V.; Clement, R.; Bourassin, N.; Baaden, M.; de Poulpiquet, A.; Sacquin-Mora, S.; Ciaccafava, A.; Lojou, E. Controlling Redox Enzyme Orientation at Planar Electrodes. *Catalysts* **2018**, *8* (5), 192. https://doi.org/10.3390/catal8050192.

(7) Johnson, D. L.; Martin, L. L. Controlling Protein Orientation at Interfaces Using Histidine Tags: An Alternative to Ni/NTA. *J. Am. Chem. Soc.* **2005**, *127* (7), 2018–2019. https://doi.org/10.1021/ja045084g.

(8) Lin, W.; Insley, T.; Tuttle, M. D.; Zhu, L.; Berthold, D. A.; Král, P.; Rienstra, C. M.; Murphy, C. J. Control of Protein Orientation on Gold Nanoparticles. *J. Phys. Chem. C* **2015**, *119* (36), 21035–21043. https://doi.org/10.1021/acs.jpcc.5b07701.

(9) Wasserberg, D.; Cabanas-Danés, J.; Prangsma, J.; O'Mahony, S.; Cazade, P. A.; Tromp, E.; Blum, C.; Thompson, D.; Huskens, J.; Subramaniam, V.; et al. Controlling Protein Surface Orientation by Strategic Placement of Oligo-Histidine Tags. *ACS Nano* **2017**, *11* (9), 9068–9083. https://doi.org/10.1021/acsnano.7b03717.

(10) Marchin, K. L.; Phung, S.; Berrie, C. L. Evidence for Fibrinogen Mobility on Hydrophobic Surfaces. *e-Journal Surf. Sci. Nanotechnol.* **2005**, *3*, 173–178. https://doi.org/10.1380/ejssnt.2005.173.

(11) Horbett, T. A.; Brash, J. L. Proteins at Interfaces: Current Issues and Future Prospects. In *Proteins at Interfaces: Physicochemical and Biochemical Studies*; 1987; pp 1–33. https://doi.org/10.1021/bk-1987-0343.ch001.

(12) Horbett, T. A.; Brash, J. L.; Chemistry., A. C. S. D. of C. and S.; 12-06-12, A. C. S. M. C. N.-S. S. Q. U. 55 P. 1995 D. U. E. Proteins at Interfaces II : Fundamentals and Applications. *ACS Symp. Ser.* **1995**, xiv, 561 p. https://doi.org/10.1080/01932699708943757.

(13) Hansma, H. G.; Hoh, J. H. Biomolecular Imaging With the Atomic Force Microscope. *Annu. Rev. Biophys. Biomol. Struct.* **1994**, *23*, 115–139.

(14) Gaczynska, M.; Osmulski, P. AFM of Biological Complexes: What Can We Learn? *Curr Opin Colloid Interface Sci.* **2008**, *13* (5), 351–367. https://doi.org/10.1016/j.cocis.2008.01.004.

(15) Lee, J. I.; Jang, J. H.; Yu, M. J.; Kim, Y. W. Construction of a Bifunctional Enzyme Fusion for the Combined Determination of Biogenic Amines in Foods. *J. Agric. Food Chem.* **2013**,

61 (38), 9118–9124. https://doi.org/10.1021/jf403044m.

(16) Kopacz, M. M.; Heuts, D. P. H. M.; Fraaije, M. W. Kinetic Mechanism of Putrescine Oxidase from Rhodococcus Erythropolis. *FEBS J.* **2014**, *281* (19), 4384–4393. https://doi.org/10.1111/febs.12945.

(17) Bóka, B.; Adányi, N.; Szamos, J.; Virág, D.; Kiss, A. Putrescine Biosensor Based on Putrescine Oxidase from Kocuria Rosea. *Enzyme Microb. Technol.* **2012**, *51* (5), 258–262. https://doi.org/10.1016/j.enzmictec.2012.07.006.

(18) Nagy, L.; Nagy, G.; Gyurcsányi, R. E.; Neuman, M. R.; Lindner, E. Development and Study of an Amperometric Biosensor for the in Vitro Measurement of Low Concentration of Putrescine in Blood. *J. Biochem. Biophys. Methods* **2002**, *53* (1–3), 165–175. https://doi.org/10.1016/S0165-022X(02)00105-7.

(19) Wittrup, K. D. Protein Engineering by Cell-Surface Display. *Curr. Opin. Biotechnol.* **2001**, *12* (4), 395–399. https://doi.org/10.1016/S0958-1669(00)00233-0.

(20) Smith, G. P. Filamentous Phage Fusion: Novel Expression Vectors That Display Cloned Antigens on the Surface of the Virion Surface. *Science (80-.).* **1985**, *228* (1984), 1315–1317.

(21) Tamerler, C.; Oren, E. E.; Duman, M.; Venkatasubramanian, E.; Sarikaya, M. Adsorption Kinetics of an Engineered Gold Binding Peptide by Surface Plasmon Resonance Spectroscopy and a Quartz Crystal Microbalance. *Langmuir* **2006**, *22* (18), 7712–7718. https://doi.org/10.1021/la0606897.

(22) So, C. R.; Tamerler, C.; Sarikaya, M. Adsorption, Diffusion, and Self-Assembly of an Engineered Goldbinding Peptide on Au(111) Investigated by Atomic Force Microscopy. *Angew. Chemie - Int. Ed.* **2009**, *48* (28), 5174–5177. https://doi.org/10.1002/anie.200805259.

(23) Hnilova, M.; So, C. R.; Oren, E. E.; Wilson, B. R.; Kacar, T.; Tamerler, C.; Sarikaya, M. Peptide-Directed Co-Assembly of Nanoprobes on Multimaterial Patterned Solid Surfaces. *Soft Matter* **2012**, *8* (16), 4327–4334. https://doi.org/10.1039/c2sm06426j.

(24) Ramakrishnan, S. K.; Jebors, S.; Martin, M.; Cloitre, T.; Agarwal, V.; Mehdi, A.; Martinez, J.; Subra, G.; Gergely, C. Engineered Adhesion Peptides for Improved Silicon Adsorption. *Langmuir* **2015**, *31* (43), 11868–11874. https://doi.org/10.1021/acs.langmuir.5b02857.

(25) Naik, R. R.; Jones, S. E.; Murray, C. J.; McAuliffe, J. C.; Vaia, R. A.; Stone, M. O. Peptide Templates for Nanoparticle Synthesis Derived from Polymerase Chain Reaction-Driven Phage Display. *Adv. Funct. Mater.* **2004**, *14* (1), 25–30. https://doi.org/10.1002/adfm.200304501.

(26) Eckhardt, S.; Brunetto, P. S.; Gagnon, J.; Priebe, M.; Giese, B.; Fromm, K. M. Nanobio Silver: Its Interactions with Peptides and Bacteria, and Its Uses in Medicine. *Chem. Rev.* **2013**, *113* (7), 4708–4754. https://doi.org/10.1021/cr300288v.

(27) Tamerler, C.; Duman, M.; Oren, E. E.; Gungormus, M.; Xiong, X.; Kacar, T.; Parviz, B. A.; Sarikaya, M. Materials Specificity and Directed Assembly of a Gold-Binding Peptide. *Small* **2006**, *2* (11), 1372–1378. https://doi.org/10.1002/smll.200600070.

(28) Zareie, H. M.; Sarikaya, M. Assembly of Gold-Binding Proteins for Biomolecular Recognition. *Austin J. Biosens. Bioelectron.* **2015**, *1* (1), 1–4.

(29) Hnilova, M.; Khatayevich, D.; Carlson, A.; Oren, E. E.; Gresswell, C.; Zheng, S.; Ohuchi, F.; Sarikaya, M.; Tamerler, C. Single-Step Fabrication of Patterned Gold Film Array by an Engineered Multi-Functional Peptide. *J. Colloid Interface Sci.* **2012**, *365* (1), 97–102. https://doi.org/10.1016/j.jcis.2011.09.006.

(30) Donatan, S.; Sarikaya, M.; Tamerler, C.; Urgen, M. Effect of Solid Surface Charge on the Binding Behaviour of a Metal-Binding Peptide. *J. R. Soc. Interface* **2012**, *9* (75), 2688–2695. https://doi.org/10.1098/rsif.2012.0060.

(31) Akdim, B.; Pachter, R.; Kim, S. S.; Naik, R. R.; Walsh, T. R.; Trohalaki, S.; Hong, G.; Kuang, Z.; Farmer, B. L. Electronic Properties of a Graphene Device with Peptide Adsorption: Insight from Simulation. *ACS Appl. Mater. Interfaces* **2013**, *5* (15), 7470–7477. https://doi.org/10.1021/am401731c.

(32) Van Hellemond, E. W.; Van Dijk, M.; Heuts, D. P. H. M.; Janssen, D. B.; Fraaije, M. W. Discovery and Characterization of a Putrescine Oxidase from Rhodococcus Erythropolis NCIMB 11540. *Appl. Microbiol. Biotechnol.* **2008**, *78* (3), 455–463. https://doi.org/10.1007/s00253-007-1310-4.

(33) Sarikaya, M.; Aksay, I. A. *Biomimetics : Design and Processing of Materials*; AIP Press: Woodbury, N.Y, 1995.

(34) Marchin, K. L.; Berrie, C. L. Conformational Changes in the Plasma Protein Fibrinogen upon Adsorption to Graphite and Mica Investigated by Atomic Force Microscopy. *Langmuir* **2003**, *19* (23), 9883–9888. https://doi.org/10.1021/la035127r.

(35) Topoglidis, E.; J. Campbell, C.; E. G. Cass, A.; R. Durrant, J. Factors That Affect Protein Adsorption on Nanostructured Titania Films. A Novel Spectroelectrochemical Application to Sensing. *Langmuir* **2001**, *17* (25), 7899–7906. https://doi.org/10.1021/la010309b.

(36) Wadu-Mesthrige, K.; Amro, N. A.; Liu, G.-Y. Immobilization of Proteins on Self-Assembled Monolayers. *Scanning* **2006**, *22* (6), 380–388. https://doi.org/10.1002/sca.4950220607.

(37) Ortega-Vinuesa, J. .; Tengvall, P.; Lundström, I. Molecular Packing of HSA, IgG, and Fibrinogen Adsorbed on Silicon by AFM Imaging. *Thin Solid Films* **1998**, *324* (1–2), 257–273. https://doi.org/10.1016/S0040-6090(98)00363-0.

(38) Shen, L.; Cheng, K. C. K.; Schroeder, M.; Yang, P.; Marsh, E. N. G.; Lahann, J.; Chen, Z. Immobilization of Enzyme on a Polymer Surface. *Surf. Sci.* **2016**, *648*, 53–59. https://doi.org/10.1016/j.susc.2015.10.046.

(39) Kumada, Y.; Tokunaga, Y.; Imanaka, H.; Imamura, K.; Sakiyama, T.; Katoh, S.; Nakanishi, K. Screening and Characterization of Affinity Peptide Tags Specific to Polystyrene Supports for the Orientated Immobilization of Proteins. *Biotechnol. Prog.* **2006**, *22* (2), 401–405. https://doi.org/10.1021/bp050331l.

(40) Vogel, N.; Zieleniecki, J.; Köper, I. As Flat as It Gets: Ultrasmooth Surfaces from Template-Stripping Procedures. *Nanoscale*. 2012, pp 3820–3832. https://doi.org/10.1039/c2nr30434a.

(41) Wang, H.; Chen, S.; Li, L.; Jiang, S. Improved Method for the Preparation of Carboxylic Acid and Amine Terminated Self-Assembled Monolayers of Alkanethiolates. *Langmuir* **2005**, *21* (7), 2633–2636. https://doi.org/10.1021/la046810w.

(42) Kluth, G. J.; Sung, M. M.; Maboudian, R. Thermal Behavior of Alkylsiloxane Self-Assembled Monolayers on the Oxidized Si (100) Surface. **1997**, *7463* (100), 3775–3780. https://doi.org/10.1021/la970135r.

(43) Rezaee, A.; Wong, K. K. H.; Manifar, T.; Mittler, S. Octadecyltrichlorosilane (OTS): A Resist for OMCVD Gold Nanoparticle Growth. *Surf. Interface Anal.* **2009**, *41* (7), 615–623. https://doi.org/10.1002/sia.3073.

(44) Peters, R. D.; Nealey, P. F.; Crain, J. N.; Himpsel, F. J. A near Edge X-Ray Absorption Fine Structure Spectroscopy Investigation of the Structure of Self-Assembled Films of

Octadecyltrichlorosilane. *Langmuir* **2002**, *18* (4), 1250–1256. https://doi.org/10.1021/la011198j.

Chapter 5: Controlled Electroless Deposition of Noble Metals on Silicon Substrates Using Self-Assembled Monolayers as Molecular Resists to Generate Nanopatterned Surfaces for Electronics and Plasmonics

The content in this chapter belongs to a manuscript titled "Controlled Electroless Deposition of Noble Metals on Silicon Substrates Using Self-Assembled Monolayers as Molecular Resists to Generate Nanopatterned Surfaces for Electronics and Plasmonics," ACS Appl. Nano Mater. ***2019****, 2 (12), 7114–7125. In my part of the study, I was working towards the development of gold nanodot arrays by utilizing the mythology developed by Sasanka B. Ulapane. The content is being reprinted here with the permission of all authors.*

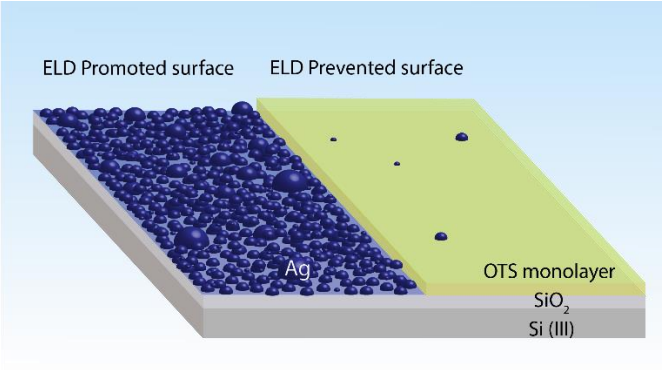

5.1 Abstract

Electroless deposition of noble metals on silicon (Si) has applications in a wide range of fields including electronic circuitry, metal plating industry, lithography, and other fabrication techniques. In addition, studies using self-assembled monolayers (SAM) as resists for electroless deposition for controlled deposition have significant potential for aiding advancement in the fields of nano electronics, sensing applications, and fundamental studies. Herein, we discuss the development of appropriate plating solutions for controlled deposition of metallic gold and silver on Si(111) surfaces in the presence of an organic silane monolayer acting as a resist film for

directed metal deposition to produce metal-monolayer hybrid surfaces while investigating microscopic plating trends. For this, plating solutions were optimized to deposit metal on bare Si surfaces while avoiding deposition on the SAM protected areas. Trends in the electroless deposition of gold on a Si(111) surface as a function of concentration of metal ion, NH_4F, citric acid, sodium citrate, polyvinylpyrrolidone (PVP) and deposition time have been monitored under ambient conditions. The resulting surfaces were characterized using atomic force microscopy (AFM) and the stability of plating solutions was investigated by UV-Vis spectroscopy. We observed an increase in metal deposition when the concentration of NH_4F, citric acid, and deposition time increased. The addition of PVP and the pH of the solution were also shown to have a significant effect on the metal deposition. The octadecyltrichlorosilane (OTS) SAM films act as effective nanoscale resists when the NH_4F concentration is reduced from typical plating conditions. In particular, NH_4F concentrations from 0.02-0.50 M and gold ion concentrations from 0.001-0.012 M were found to allow deposition of metal nanostructures on a bare Si surface while preserving OTS protected areas.

5.2 Introduction

Electroless deposition of metals at interfaces is a relatively straight-forward deposition method that is receiving significant attention recently due to rapid developments in the electronics, semiconductor, magnetic materials, biomedical, and nanofabrication industries.[1–7] The combination of electroless deposition with organic thin films to generate hybrid materials could potentially enhance applications of electroless metal deposition. Recent development of hybrid materials such as peptide-functionalized graphene moieties, metal organic frameworks, biological ligands capped nanoparticles, and other organometallic structures have attracted a lot of attention

and promise in both commercial and fundamental applications.[8–10] Selective metal deposition on Si substrates allows fabrication of a new class of hybrid materials with potential applications in nanoscale electronic components, high performance optoelectronic devices, highly sensitive detectors, and platforms to study biological systems.[11–13] Nevertheless, challenges in combining different materials have imposed a significant delay in the development of such devices.

Applying electroless metal deposition in combination with self-assembled monolayers as a means to provide selective metal deposition is an ideal cost-effective technique for manufacturing metal organic hybrid surfaces that has been relatively unexplored.[14–18] Electroless (*i.e.,* galvanic) deposition, is a process that does not require an application of an external current since the substrate is acting as an electron donor while metal ions in the plating solution undergo spontaneous reduction on the oxidizable surface. This occurs when the difference in reduction potentials between the substrate and solution phase metal ions are compatible (*i.e.,* the free energy change for the process is negative).[19–21] Based on their reduction potentials, electroless deposition of metal ions including (but not limited to) Au^{3+}, Ag^{+} and Cu^{2+} on Si(111) surfaces is feasible.[5,6,22] Self-assembled monolayer formation allows surface chemistry modification of surfaces such as glass, SiO_2, Al_2O_3, TiO_2 or mica[23–25] using organosilanes, or metallic surfaces such as Au or Ag using organothiols.[26] Among these, Si substrates are of particular interest here due to their many potential applications, but also because they can be functionalized with silane monolayers such as octadecyltrichlorisilane (OTS) via hydration of the trichlorosilane followed by condensation with the surface hydroxyl groups. This type of protective coating can act as a resist by protecting the native oxide layer on the Si surface from being etched in a plating solution. In regions which lack the silane modification, the oxide can be etched, allowing the underlying Si to be oxidized in electroless metal deposition.[20,24] Once the Si surface is functionalized with OTS, plating solution

components such as NH_4F and metal ions will no longer have access to the substrate surface, hence OTS provides a resist film preventing metal deposition on the surface. Selective removal of OTS coverage would allow controlled metal deposition on desired locations on the surface.

Most of the studies based on metal electroless deposition in the literature provide conditions for industrial scale macroscopic plating, which involves complex mixtures of components at high concentrations.[27–30] Common compositions of plating solutions include additives such as complexing agents, pH regulators, weak acids, stabilization or capping agents, etc.[1] Rapid nucleation and fast growth associated with these solution conditions tend to produce microscopically non-uniform, thick metal films. Therefore, such conditions are not easily transferred to the deposition of nanoscale features with controlled dimensions. Furthermore, high concentration plating baths often compromise fragile molecular resist films by depositing metal on defect sites of the monolayer.[31] To obtain nanoscale-structured metallic films with reduced local roughness while preserving organic monolayers in the presence of plating solutions requires significantly different plating solution conditions which must be optimized for such applications. Specifically, conditions are required which will allow the deposition of uniform metal films with nanoscale thickness, with precise positional control on the surface. In order to achieve this, the local roughness of the films must be reduced by controlling the growth and coalescence of the metal nuclei on the surface. AFM provides an ideal tool for observing such changes in the local structure of the surface as the deposition conditions are changed.

Among the metals which can potentially be deposited electrolessly on Si surfaces, gold is of specific interest due to their wide range of applications and chemical inertness. Gold is one of the least reactive metals and shows excellent catalytic properties in the form of nanoparticles. Since

it is a good conductor of heat and electricity there are wide range of applications[2] in optoelectronics,[29,32,33] biosensors,[34] SERS platforms,[20,35,36] and in cancer treatment.[32,37]

In this study, we have used noble metal salts of gold ($HAuCl_4 \bullet 3H_2O$) with ammonium fluoride (NH_4F) to plate corresponding metals on bare Si(111) substrates using electroless deposition while demonstrating the ability of an octadecyltrichlorosilane SAM on the Si(111) surface to successfully resist metal deposition under the same plating conditions. To achieve this, we have developed and optimized an appropriate plating solution that plates metallic gold on bare Si substrates yet prevents any metal deposition over areas protected by organosilane monolayers. First, we investigated the effect of change in concentration of typical electroless plating solution components including metal ions, ammonium fluoride, citric acid, trisodium citrate, PVP, pH and deposition time for the electroless deposition of gold on the Si(111) surface. Root mean square average of height deviations taken from the mean image plane were investigated as a function of the deposition parameters. Deposition on bare Si(111) and OTS coated Si(111) were then compared, in order to assess the effectiveness of the OTS monolayer as a resist coating under optimized deposition conditions. AFM images show very few metal nanoparticles deposited on the OTS coated Si surface under the same conditions which allow a bare Si surface to be fully coated with metal.

5.3 Materials and Methods

Certified ACS grade 30% (w/w) hydrogen peroxide, 96.5% (w/w) sulfuric acid, 37.4% (w/w) hydrochloric acid, nitric acid, sodium hydroxide, 99% sodium citrate ($Na_3C_6H_5O_7 \cdot 2H_2O$), 99.3% ammonium fluoride (NH_4F), and 99.5% citric acid anhydrous ($C_6H_8O_7$), were purchased from Fisher Chemical Industries. $(C_6H_9NO)_n$, Polyvinylpyrrolidone (PVP, F.W. 40,000 g/mol),

and 99% tetrachloroauric(III) acid trihydrate ($HAuCl_4 \cdot 3H_2O$) were purchased from Sigma-Aldrich. All chemicals were used without further purification. Single-side polished boron-doped Si(111) wafers (resistivity = 3.0-6.0 Ω.cm) from Virginia Semiconductor (Fredericksburg, VA) were used. Milli-Q water (resistivity> 18.2 MΩ) was used to rinse the substrates and make plating solutions.

All surface topography images were taken with a multimode scanning probe microscope (Nanoscope IIIA, Digital Instruments CA) using tapping mode and contact mode. For tapping mode images, diamond like carbon coated (DLC) Tap 300 probes (spring constant of 40 N/m) from Budget sensors were used. For contact mode images, non-conductive Si nitride cantilevers, with spring constants ranging from 0.12 to 0.06 N/m, were used from Veeco (Camarillo, CA). All AFM images were analyzed using NanoScope Analysis 1.5 software by Bruker Corporation.

5.3.1 Preparation of Surfaces for the Electroless Deposition

Si(111) wafers were cut into approximately 1×1 cm^2 pieces using a diamond tipped scribe and cleaned using a 3:7 hydrogen peroxide to sulfuric acid (V/V) piranha solution. *Piranha solution is an extremely corrosive, strong oxidizer. Avoid any contact with organic substances, do not store in a closed container, and handle with appropriate personal protective clothing. Piranha solutions should be made immediately prior to use, never stored in a closed container, and be neutralized immediately following use.* Si substrates were cleaned by submerging in hot piranha solution for approximately 20 min, followed by rinsing with copious amounts of Milli-Q water. Finally, the substrates were dried under a stream of N_2 gas before use.

5.3.2 Self-assembled Monolayer Formation on Si(111)

Piranha cleaned Si pieces were submerged in 2.5 mM OTS solution in toluene to facilitate the self-assembly. Samples were removed from the silane solution after 24 hours and sonicated in

toluene for 30 minutes to remove physisorbed OTS molecules. The resulting samples were rinsed with toluene, chloroform, acetone and ethanol, respectively, and dried under a stream of N_2 gas. Then, the monolayers were characterized using ellipsometry, goniometry and AFM imaging. These samples were subjected to same plating conditions as the bare Si samples, to test the monolayer's robustness.

5.3.3 Electroless Deposition of Gold on Si(111) Surface

Tables 5.1 and 5.2 provide the details of the experiments carried out in sections (a)-(g) below. These experiments explore the effect of the concentration of a particular solution component and its effect on the metal deposition. Metal electroless deposition was accomplished by placing a drop of plating solution on the freshly piranha cleaned Si surface. Plating solutions as described in *Table 5.1 (Sections a-d) and 5.2 (Sections e-g)* were prepared immediately prior to the start of the deposition experiments. All trials were performed by placing a 100 µL drop of plating solution on the surface at room temperature under ambient conditions and rinsed with Milli-Q water after the time indicated in *Tables 5.1 and 5.2*, followed by drying under a stream of N_2 gas. During the plating time, metal ions are being reduced at the surface to form a nanoscale metal coating on the substrate. At the short deposition times used here, experiments suggest that the metal ions in solution are not depleted. The pH of all the plating solutions was recorded before the plating. AFM images were collected from two different samples at four different spots of every surface. All images were collected using contact mode AFM unless specified otherwise. Root mean square average of height deviation (Rq image roughness) was calculated over 10 × 10 µm images (average of 3 from each surface) using nano scope analysis 1.5 software. The plating solution parameters and the conditions used in each study are summarized in *Table 5.1*. Sections (a)-(d) (*Table 5.1*) involve varying the keys components of the plating solutions for Au deposition

including time (a), metal ion concentration (b), NH_4F concentration (c) and pH (d). Sections (e)-(g) (*Table 5.2*) investigate the role of several common additives in the plating process including trisodium citrate concentration (e), citric acid concentration (f), and PVP concentration (g). The general procedure for deposition is as described above (with specific concentrations and times specified within the sections which follow).

5.3.3a. Time dependence growth of metal on Si(111) surface in the presence of metal ion and NH_4F.

The growth of metal on the surface with respect to time was monitored for both gold plating solutions. Deposition times ranged from 5 to 480 seconds keeping [NH_4F] = 100 mM, [$HAuCl_4 \bullet 3H_2O$] = 1 mM *(Table 5.1a)*.

5.3.3b. Metal ion concentration dependence

To study the effect of metal ion concentration, [$HAuCl_4 \bullet 3H_2O$] was changed from 10 mM to 100 mM while keeping [NH_4F] at 50 mM *(Table 5.1b)*. The electroless deposition was carried out for 30 seconds for gold.

5.3.3c. NH_4F concentration

The effect of [NH_4F] on electroless deposition was studied by varying its concentration from 10 mM to 1000 mM while keeping the [$HAuCl_4 \bullet 3H_2O$] at 12 mM *(Table 5.1c)*. The electroless deposition was carried out for 2 minutes for gold.

5.3.3d. Effect of pH on metal plating

To study the effect of pH, plating solutions with 1 mM [$HAuCl_4 \bullet 3H_2O$] and 100 mM [NH_4F] were made and the final pH was adjusted to 1.0, 4.0, 7.0, and 10.0 by adding either hydrochloric acid or sodium hydroxide (*Table 5.1d).* The electroless deposition was carried out for two minutes for gold.

5.3.3e. Effect of sodium citrate

The effects of the addition of sodium citrate ($Na_3C_6H_5O_7 \bullet 2H_2O$) were investigated by varying its concentration from 0.00 mM to 300 mM while keeping [$HAuCl_4 \bullet 3H_2O$] and [NH_4F] at 12 mM and 400 mM respectively *(Table 5.2e)*. The electroless deposition was carried out for 2 minutes for gold.

5.3.3f. Effect of citric acid

To study the effects of citric acid ($C_6H_8O_7$), [$C_6H_8O_7$] in the gold plating solution was varied from 0.00 mM to 300 mM while keeping the [$HAuCl_4 \bullet 3H_2O$]at 1 mM and [NH_4F] at 90 mM *(Table 5.2f)*. The electroless deposition was carried out for two minutes for gold.

5.3.3g. effect of PVP

To study the effects of PVP, 0.000 to 0.005 g/mL of PVP was used while keeping the [$HAuCl_4 \bullet 3H_2O$] and [NH_4F] at 1 mM and 170 mM respectively *(Table 5.2g)*. The electroless deposition was carried out for two minutes for gold.

Table 5. 1: *Plating solution compositions for Au deposition trials on Si(111) with different concentrations of key plating components.*

$HAuCl_4 \cdot 3H_2O$ (mM)	NH_4F (mM)	Time(s)	pH
(a) Plating conditions for time dependence growth			
1	100	5	4.5
1	100	15	4.5
1	100	30	4.5
1	100	60	4.5
1	100	90	4.5
1	100	120	4.5
1	100	180	4.5
1	100	240	4.5
1	100	480	4.5
(b) Plating conditions and measured pH for $HAuCl_4 \cdot 3H_2O$ and $AgNO_3$ dependent studies			
10	50	30	3.0
20	50	30	2.5
50	50	30	2.5
100	50	30	2.0
(c) Plating conditions and measured pH for NH_4F dependent studies			
12	10	120	1.5
12	20	120	1.5
12	50	120	2.0
12	100	120	2.5
12	500	120	4.0
12	1000	120	4.5
(d) Plating conditions for pH dependence studies			
1	100	120	1.0
1	100	120	4.0
1	100	120	7.0
1	100	120	10

Table 5. 2: *Plating solution compositions for Au and Ag deposition trials on Si(111) with different concentrations of various additives.*

$HAuCl_4 \cdot 3H_2O$ (mM)	NH_4F (mM)	Time (s)	Additive	Additive concentration	pH
(e) Plating conditions and measured pH for $C_6H_8O_7$ dependent studies					
1	90	120	$C_6H_8O_7$ ($x10^{-1}$ M)	0	4.5
1	90	120		100	3
1	90	120		200	2.5
1	90	120		300	2
(f) Plating conditions and measured pH for PVP dependent studies					
1	170	120	PVP ($x10^{-3}$ g/mL)	0	4.5
1	170	120		1	4.5
1	170	120		3	4.5
1	170	120		5	4.5
(g) Plating conditions and measured pH for Citrate ($Na_3C_6H_5O_7 \cdot 2H_2O$) dependent studies					
12	400	120	$Na_3C_6H_5O_7 \cdot 2H_2O$ (mM) ($x10^{-3}$ g/mL)	0	4.5
12	400	120		50	5.0
12	400	120		100	5.5
12	400	120		150	6.0
12	400	120		200	6.0
12	400	120		250	6.0
12	400	120		300	6.0

5.3.4 Stability of Plating Solutions

To investigate the stability of plating solutions, UV-Vis absorption spectroscopy measurements were carried out for all plating solutions. To obtain absorption measurements in the linear region of the instrument, necessary dilutions were carried out immediately before the measurements. Measurements were taken for the solution combinations of gold/NH_4F *(Figures 5.1)*, gold/NH_4F/citric acid *(Figures 5.2)*, and gold/NH_4F/PVP (*Figure5.3)* were prepared fresh

immediately prior to each plating experiment. The Au solutions were found to be stable for extended periods of time, as long as the citric acid and PVP are not added at the range of NH_4F concentrations studied Therefore, the solutions can be used over a period of several days, as long as the PVP or citric acid was added immediately prior to deposition. Under these conditions, we see no changes in color which would indicate solution-phase nanoparticle formation. *Figure 5.1* Shows the UV-Vis spectra for the $HAuCl_4 \bullet 3H_2O/NH_4F$ plating solution taken at different time intervals. Notice that the solution was stable for few weeks and there were no noticeable changes in the spectra for the time interval that studied. In *Figure 5.2* UV-Vis spectra for the $HAuCl_4 \bullet 3H_2O/NH_4F$/citric acid plating solution shown ($HAuCl_4 \bullet 3H_2O$ /NH_4F solution used as a blank for this study). After few minutes of mixing, color of the solution changed, different peaks as shown in the wavelength ranges of 300- 400 nm and 500-600 nm of appears and the maximum absorbance wavelength shift to higher wavelengths (from 450 to550 nm) with the time. UV-Vis spectra for the $HAuCl_4 \bullet 3H_2O/NH_4F$/PVP plating solution taken at different time intervals shown in *Figure 5.3.* Soon after mixing color of the solution changes and UV-Visible spectra indicates appearance of new peaks (400-500 nm) and shifting of maximum absorbance to higher wavelengths (from 415 to 425 nm). These continuously growing peaks in visible region suggest that the solution phase nanoparticle formation in $HAuCl_4 \bullet 3H_2O/NH_4F$/citric acid and $HAuCl_4 \bullet 3H_2O/NH_4F$/PVP solutions.

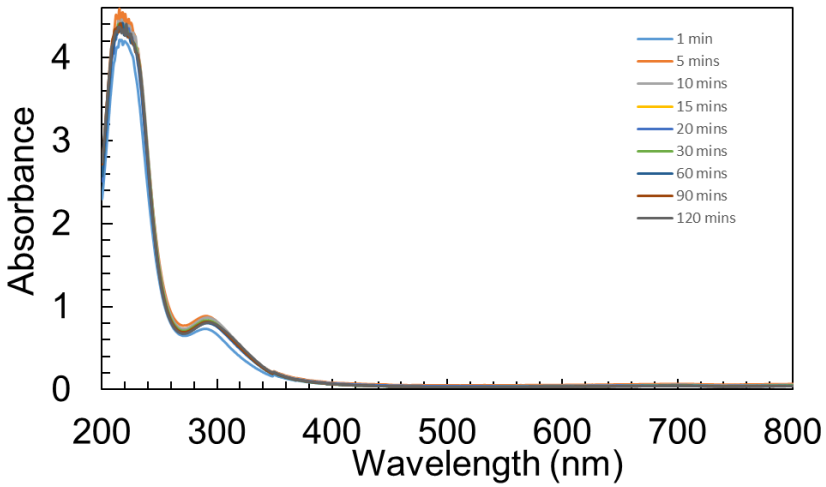

Figure 5. 1: *UV-Vis spectra for the $HAuCl_4 \cdot 3H_2O/NH_4F$ plating solution taken at different time intervals. Notice that the solution was stable for few weeks and there were no noticeable changes in the spectra for the time interval that studied.*

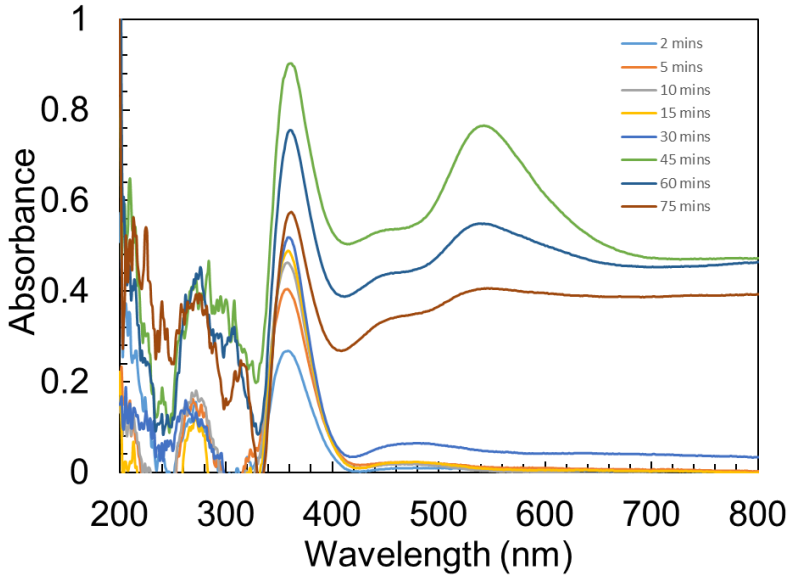

Figure 5. 2: *UV-Vis spectra for the $HAuCl_4 \cdot 3H_2O/NH_4F$/citric acid plating solution taken at different time intervals ($HAuCl_4 \cdot 3H_2O /NH_4F$ solution used as a blank for this study). After few minutes of mixing, color of the solution changed, different peaks as shown in the figure above appears and the maximum absorbance wavelength shift to higher wavelengths.*

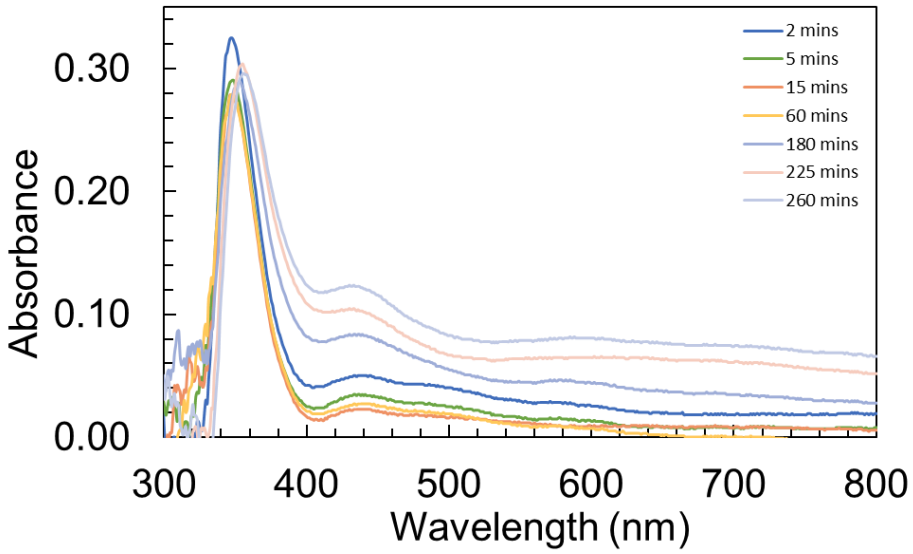

Figure 5. 3: *UV-Vis spectra for the $HAuCl_4 \cdot 3H_2O/NH_4F$/PVP plating solution taken at different time intervals. Soon after mixing color of the solution changes and UV--Visible spectra indicates appearance of new peaks and shifting of maximum absorbance to higher wavelength.*

5.4 Results and Discussion

In this work, we investigated the effects of concentration of metal ions, ammonium fluoride, citric acid, sodium citrate, PVP, pH, and plating time for the electroless deposition of gold on Si(111) surfaces. Further, we investigate and optimize plating conditions to sustain OTS self-assembled surfaces in similar plating solutions while a thin and uniform metal coating is chemically reduced on bare Si(111) surfaces to make metal-monolayer hybrid surfaces. This allows creation of hybrid nanomaterials using OTS SAMs as the resist layer during the fabrication. The concentrations for each plating solution component were varied independently to observe the effect of the component on the metal deposition. The deposition was monitored using AFM. Original concentrations for electroless silver deposition reported by Ye et al.[38] were investigated initially and modified later after observing the OTS protected surface had metal deposited after a very short immersion period in that plating solution, implying that the OTS SAM was being compromised in a short time under these conditions. Our initial trials indicated that there is a

significant metal deposition over OTS protected surfaces at higher NH_4F concentrations and longer plating times *(see Figure 5.4 (A-C))* Such undesirable metal deposition on the OTS SAM film could initiate from defect sites in the protective OTS monolayer where the etching solution can penetrate to the Si oxide beneath the OTS layer, allowing etching and exposure of the underlying Si. It is also possible that degradation of the OTS SAM itself could occur in harsh plating solutions. When an OTS coated Si(111) surface is exposed to a 0.2 M NH_4F solution for 20 minutes no changes in the contact angle or ellipsometry were observed, but for a 2.0 M NH_4F solution, the contact angle drops by at least 10° and the thickness changes are observed by 20 minutes of exposure. This suggests that the OTS film may degrade over time at high NH_4F concentrations. The density of defect sites in an OTS SAM has been investigated by Jalali et al.[31] in previous work. Deposition of metal on such defect sites therefore should be prevented to succeed in achieving selective deposition by optimizing deposition conditions. When using concentrated plating solutions, monolayers could still be susceptible to the metal deposition which will not allow clean nanofabrication using this method. The concentration of ammonium fluoride was decreased several orders of magnitudes before OTS showed resistance to metal deposition as desired (*See Figure 5.4 C*). Similar conditions were used as a starting point for fine-tuning gold deposition.

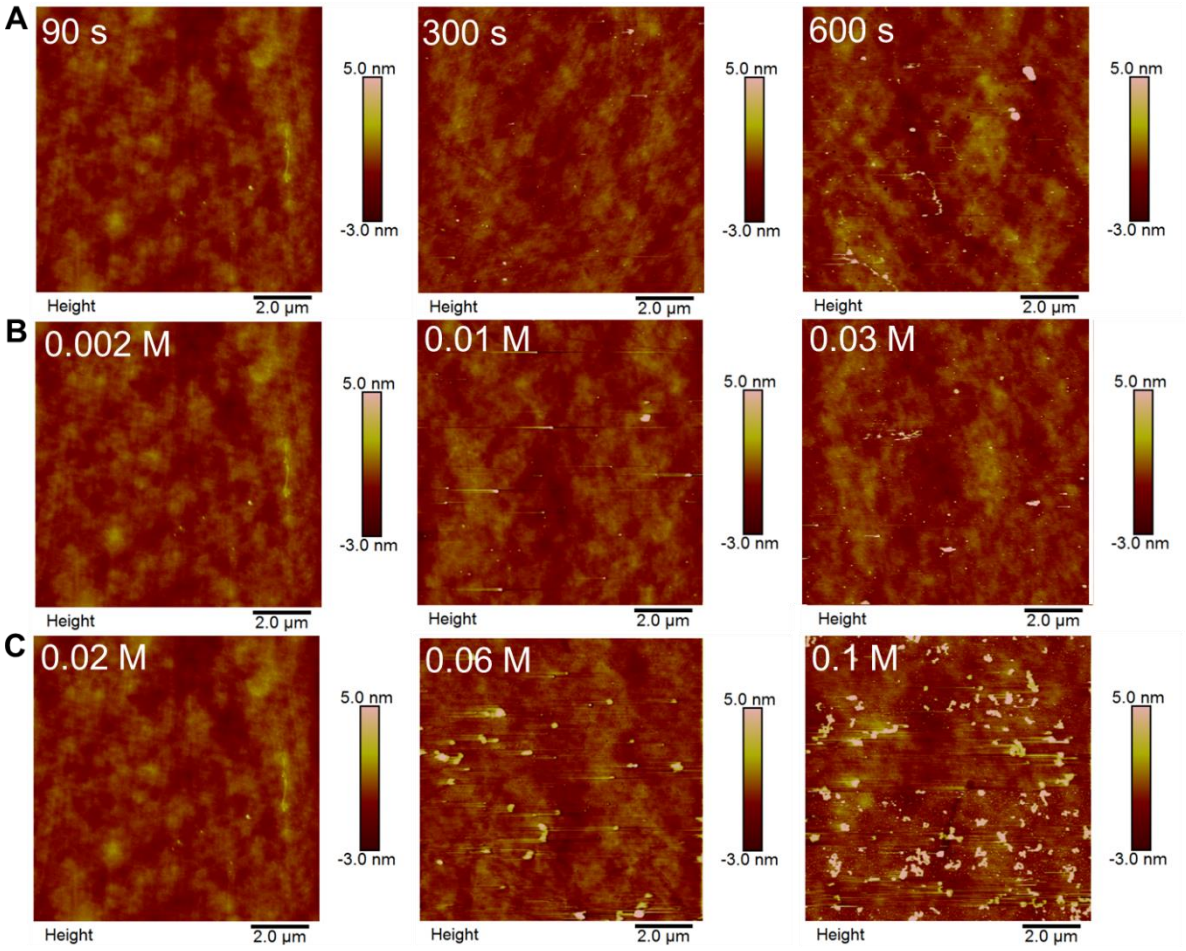

Figure 5. 4: *(A) Shows the comparison of OTS surfaces after changing the time of electroless deposition A. for gold deposition while keeping [$HAuCl_4$•$3H_2O$] = 0.002 M and [NH_4F] = 0.020 M, (B) shows the comparison of OTS surfaces after changing the metal ion concentration for gold deposition while keeping [NH_4F] = 0.02 M, and time of deposition at 90 s, (C) shows the comparison of OTS surfaces after changing the [NH_4F] A. for gold deposition while keeping [$HAuCl_4$•$3H_2O$] =0.002 M and time of deposition at 90 s. All the AFM images are 10.0 ×10.0 µm in size and the height scale are shown next to each image.*

To carry out electroless deposition on Si surfaces, an etching agent is required to remove the ~ 15 Å thick native oxide layer on Si and expose the underlying Si. Once the Si is exposed, spontaneous redox chemistry will result in local metal reduction on the surface. In principle, any Si surface could be used for the metal reduction, but in this case, doped Si(111) surfaces were used. It is possible that the doping plays a role in the deposition, since the doping type and level would influence the availability and mobility of electrons on the surface; however, all experiments were performed with the same doped Si(111), and this effect was not investigated. The most

widely used etching agent for removal of the oxide is hydrogen fluoride (HF), despite its high toxicity upon contact with skin.[19,39–41] HF is a weak acid and dissociates partially when dissolved in water with a dissociation constant of (K_a) 6.8×10^{-4} at 25 °C.[42] In this study, we have used NH_4F as an alternative etching agent with significantly reduced toxicity,[43] and to produce atomically flat Si(111)-H surfaces.[41] Furthermore, the concentration of HF in the plating solution can be consistently maintained using the NH_4F dissociation equilibrium by altering the pH and NH_4F concentration (see reaction scheme 1-5).

$$NH_4F(aq) + H_2O(l) \leftrightharpoons NH_4^+(aq) + F^-(aq) \quad (1)$$

$$F^-(aq) + H_3O^+(aq) \leftrightharpoons HF(aq) + H_2O(l) \quad (2)$$

$$SiO_2(s) + 6HF(aq) \rightarrow 2H^+(aq) + SiF_6^{2-}(aq) + 2H_2O(l) \quad (3)$$

$$Si(s) + 6F^-(aq) \rightarrow SiF_6^{2-}(aq) + 4e^- \quad (4)$$

$$AuCl_4^- 4^{n+}(aq) + 3e^-(aq) \rightarrow Au(s) + 4Cl^- \quad (5)$$

Balanced chemical equations 1 and 2 show the tunability of the dissociation upon altering the pH of the solution as well as the chemical dissolution of SiO_2 (Equation 3) when reacted with HF produced. Reactions 4 and 5 refer to the spontaneous oxidation and reduction half reactions of the Si atoms exposed on the surface and the metal ions in solution respectively. While equation 3 serves the purpose of this discussion and models a simplistic version of the ongoing complex reaction, it is likely that the etching process is significantly more complex, occurring in multiple steps with a variety of species involved.[44] The simplified illustration in *Figure 5.5* shows the initiation of etching, metal electroless deposition and progression steps with the oxidation and reduction half reactions of surface and metal ions respectively (Equation 4 and 5).

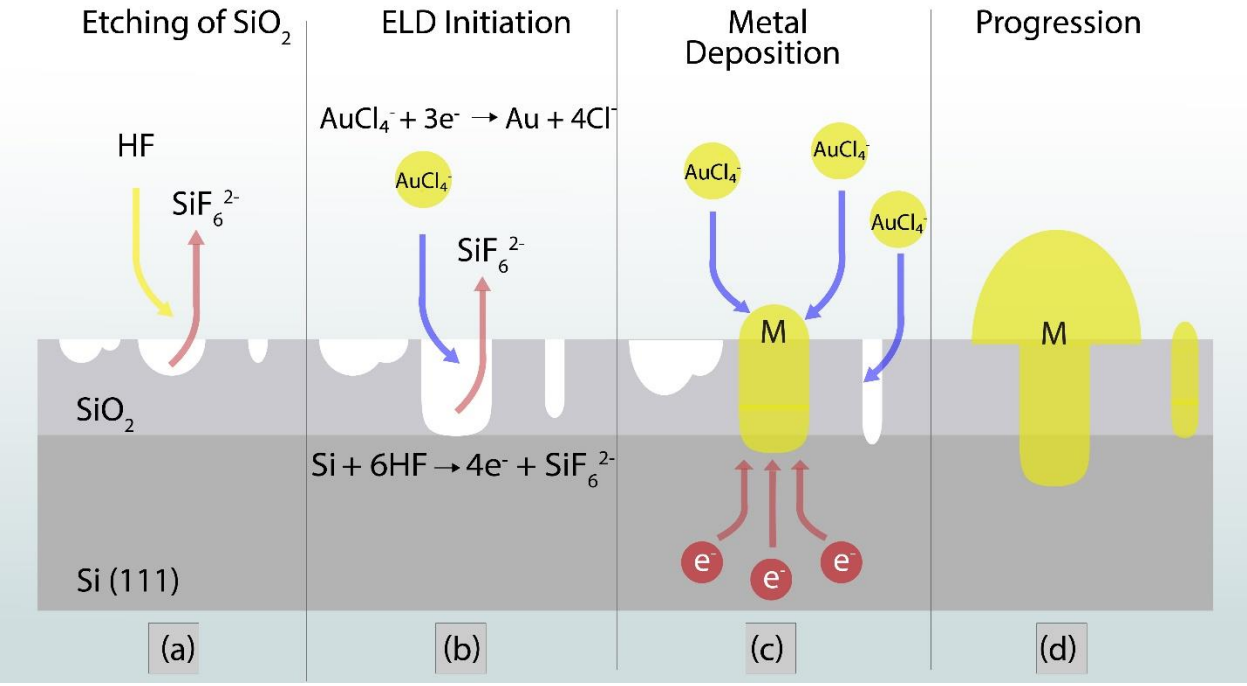

Figure 5. 5: *Key steps of the gold electroless deposition process. (a) Etching and removal of the native oxide layer of Si, (b) Initiation of electroless deposition by electron exchange between Si surface and solution phase gold ions via anodic and cathodic half reactions, (c) nucleation and gold deposition, (d) progression.*

This portion of the study is dedicated to observing microscopic changes and understanding the underlying trends of electroless deposition upon small variations of plating conditions. Plating conditions were optimized by looking at metal coverage on bare Si surfaces at different time points with different NH_4F concentrations, metal ions concentrations, and chelating agent concentrations. It is important to note that the temperature can significantly affect the kinetics of electroless deposition reactions. Therefore, all experiments were carried out at ambient temperature throughout this work as stated in the experimental section. Conventional industrial plating is often performed by submerging samples in a plating bath. Due to the nature of this study, it was found that placing a droplet of solution over the samples is more practical, while saving plating solution and minimizing halogenated waste generation. Further, our investigations have shown similar

effects on both submerging a sample in solution as well as drop casting a fixed amount of solution, suggesting no depletion of metal ion concentration over the time intervals tested.

5.4.1a Time Dependent Growth of Metal on Si(111) Surface in the Presence of Metal Ion and NH_4F

When plating time is increased, the amount of gold deposited on the surface increased (*Figure 5.6*). Immediate deposition of metal nanoparticles on surfaces was observed even at time durations as short as 5 seconds with given plating conditions in *Table 5.1a*. More nucleation sites appear after the first 30 s, thus increasing roughness and surface coverage can be seen at latter time points. For gold surfaces, the roughness (Rq) changed from 0.5 ± 0.1 nm to 27.8 ± 4.9 nm, as the deposition time increased. Previous studies have been done for gold by Bhuwana et al.,[39] Rossiter et al.[40] and Warren et al.[43] on H terminated Si. Similar trends were observed in this study, with an initial linear increase in roughness as a function of deposition time, which remained relatively constant at higher time points for gold.

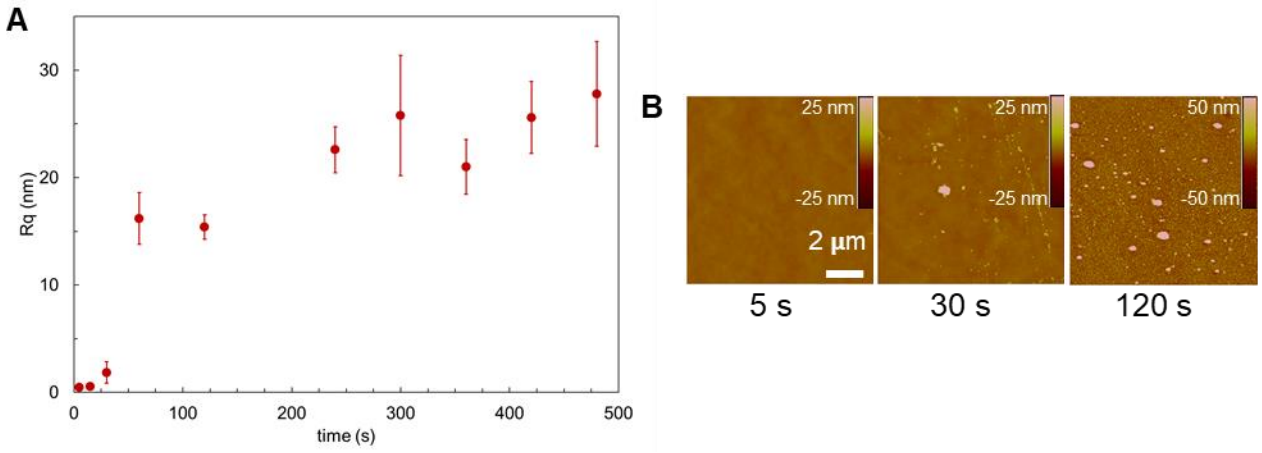

Figure 5. 6: *The observations associated with electroless deposition with time.* ***A)*** *Change in Rq roughness with time for gold for conditions in Table 5.1a. (Bars represent standard deviation of measurement).* ***B)*** *AFM topography images for selected data points of gold deposition on Si(111) surface. AFM images are 10 × 10 µm in size (length scale shown on first image).*

Observed consistent roughness at longer times may be due to the eventual completion of full coverage of the Si surface with the metal, and subsequent conformal coating of metal on Si. Forming a metal thin film by filling gaps between larger particles grown at earlier times contributes to smaller roughness changes, although metal deposition continues to occur. This observation is consistent with previous studies by the Buriak group that had shown similar growth patterns of Au on Germanium surfaces following a Volmer−Weber growth mechanism.[5]

5.4.1b Metal ion Concentration

The reduction of Au^{3+} to Au is a three-electron process. We have compared Rq roughness alongside with particle diameter, height, and density to observe similar trends in growth patterns, suggesting Rq roughness provides a reasonable metric for monitoring growth (*see Figure 5.7*). As expected, from the AFM images, density, as well as the size of particles grow as the concentration of the metal ion is increased due to increasing the Au^{3+} availability in solution.

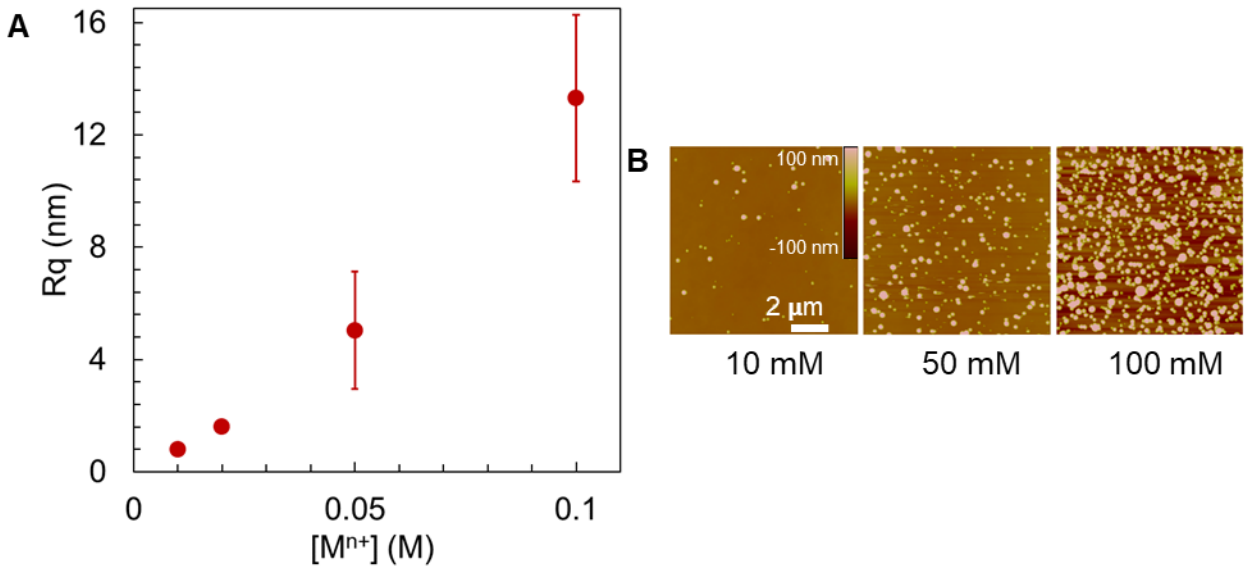

Figure 5. 7: *The changes associated with metal ion concentration for the electroless deposition discussed in Table 5.1b.* ***A)*** *Change in Rq roughness with metal ions concentration for gold metal. (Bars represent standard deviations of the measurements.)* ***B)*** *AFM topography images for selected concentrations of gold with* $[NH_4F]$ *= 50 mM. AFM images are 10 × 10 µm in size and height scales are 200 nm.*

5.4.1c NH_4F Concentration

Increasing the amount of ammonium fluoride resulted in an increase in pH for gold plating solutions (*Table 5.1c*). This increase is caused by the removal of H^+ ions in media (from the $HAuCl_4$) to form HF. AFM images indicate that the surface coverage of metal increases when increasing the NH_4F concentration while adding more nucleation sites on the surface. Increasing the NH_4F concentrations elevates the F^- ion concentration, hence increasing the effective HF concentration in the plating solution. This will accelerate the removal of native oxide of Si, increasing the rate of deposition of metal (see equations 1-5). An increase in vertical growth of nanostructures also contributes to the rise in RMS roughness. For gold, surface roughness (Rq) changed from 0.6 ± 0.1 nm to 140±8 nm when NH_4F concentration increased from 10 mM to 1000 mM. Particle diameter on the surface increased with increasing NH_4F concentration within the range of concentrations studied (*Figure 5.8*).

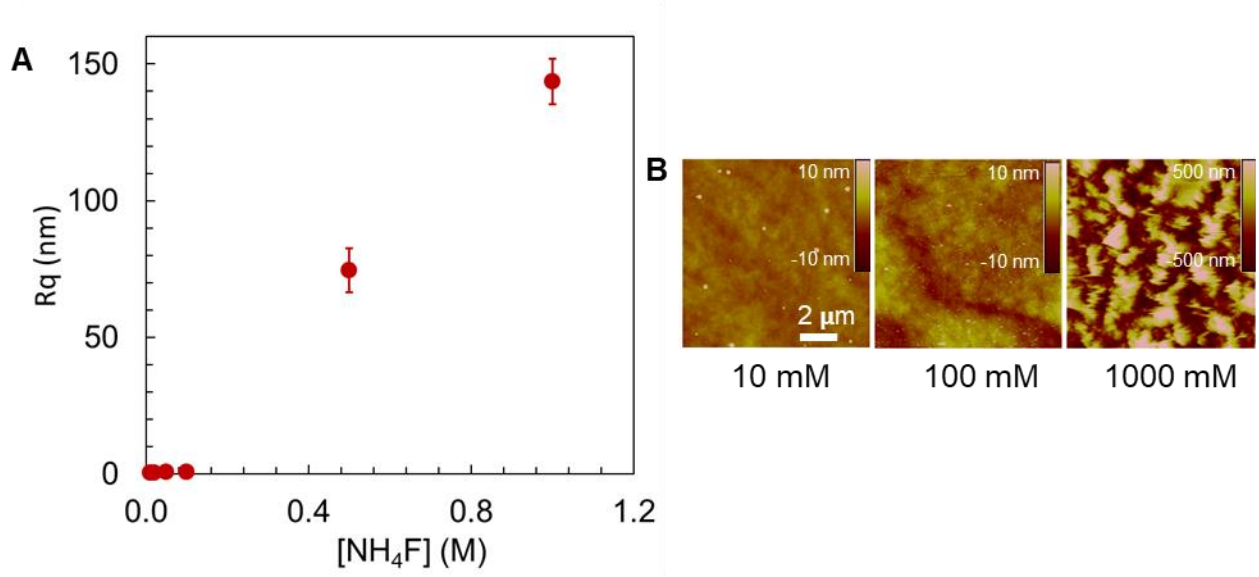

Figure 5. 8: *Changes associated with the variation of [NH_4F] discussed in Table 5.1c, with metal ion concentration kept at [$HAuCl_4 \cdot 3H_2O$] =12 mM, (Bars represent standard deviation of measurements).* ***A)*** *Rq roughness change with the increase of [NH_4F] for gold electroless deposition.* ***B)*** *AFM topography images for the electroless deposition of gold for selected [NH_4F] AFM images are 10 × 10 µm in size.*

5.4.1d Effect of pH in the Presence of NH_4F and the Metal Ion

The amount of gold deposited decreased as pH of the plating solution increased *(Figure 5.9)*. We suggest this may be due to the depletion of HF which facilitates removal of the native oxide layer on Si surface which is the first and rate limiting step of the electroless deposition process. At lower pH, higher amounts of HF are produced by driving reaction (2) towards products according to Le Chatelier's principle. Therefore, controlling the pH is an effective way to control the surface density of deposited metal, without changing any of the constituents of the plating solution.

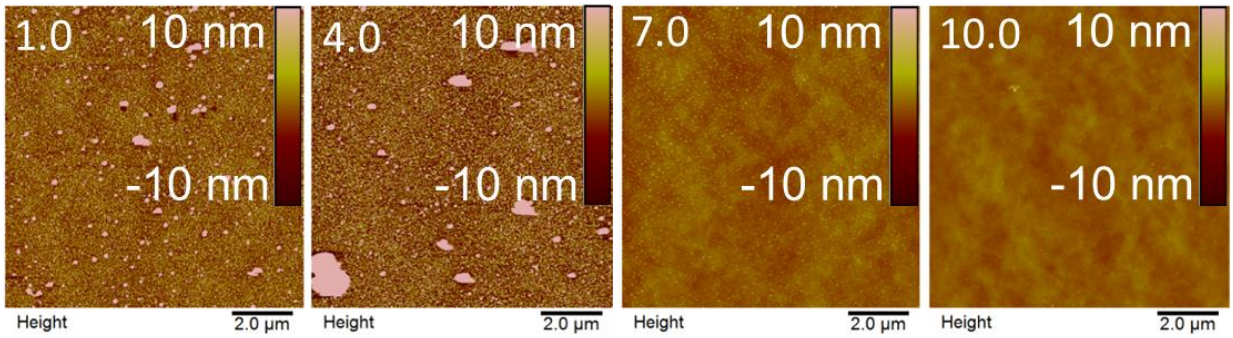

Figure 5. 9: *AFM topography images associated with the variation of pH discussed in Table 5.1d, while keeping [$HAuCl_4 \cdot 3H_2O$] = 1 mM and [NH_4F] = 100 mM.. All the AFM images are 10 × 10 µm in size and the height scales are shown on the images. pH of the plating solutions is indicated on top left.*

5.4.1e Effect of sodium citrate and citric acid in the presence of NH_4F and the metal ion

Electroless deposition of metals has been studied extensively and a large variety of additives have been included in the plating solutions for a variety of reasons including solution stabilization, pH regulation, chelating metal ions.[1] Among them, trisodium citrate is a popular additive for electroless deposition.[45,46] Theoretical and experimental evidence suggest the usage of citrate as a capping agent helps to control the shape and size of nanoparticles.[47–49] On the other

hand, some studies have shown that citrate acts as a reducing agent for the gold nanoparticle formation.[50]

When the concentration of trisodium citrate was increased *(Figure 5.10 A-B*), the pH of the plating solution increases. As a result, the amount of gold plated on Si(111) surface was decreased. Because the amount of HF in plating solution is reduced at higher pH, the etching rate decreases and less metal is deposited. Furthermore, solution phase chelating and reduction become prominent under these conditions, which results in the formation of nanoparticles. For a deposition time of 120 seconds (*Figure 5.10 A*), the surface roughness decreased from 18.7 ± 3.3 nm to 0.7 ± 0.1 nm as the citrate concentration increased from 0.0 to 250 mM, suggesting a decrease in metal deposition rate. During washing and contact mode AFM imaging, poor adhesion of gold on the Si surface was observed (F*igure 5.10 B*). This may be caused by deposition of nanoparticles formed in the solution phase, which are moved by the AFM tip. The plating solution showed signs of nanoparticle formation within 10-20 minutes after preparation and was observed via absorbance measurements *(see Figure 5.2)*.

For the considered plating solutions, electroless deposition increases when citric acid concentration increases *(Figure 5.10C)*. For a gold surface, the roughness (Rq) changed from 0.5 ± 0.1 nm to 8.7 ± 0.3 nm, when citric acid concentration increased, indicating particle growth acceleration on respective surfaces. The increased metal deposition can be explained using two possible mechanisms. First, reduction of metal ions in solution phase to produce a thin film of nanoparticles over the surface that increases with increasing concentration of citric acid, or second, a decrease in pH that promotes the formation of HF in the reaction media, accelerating the etching limited deposition process.

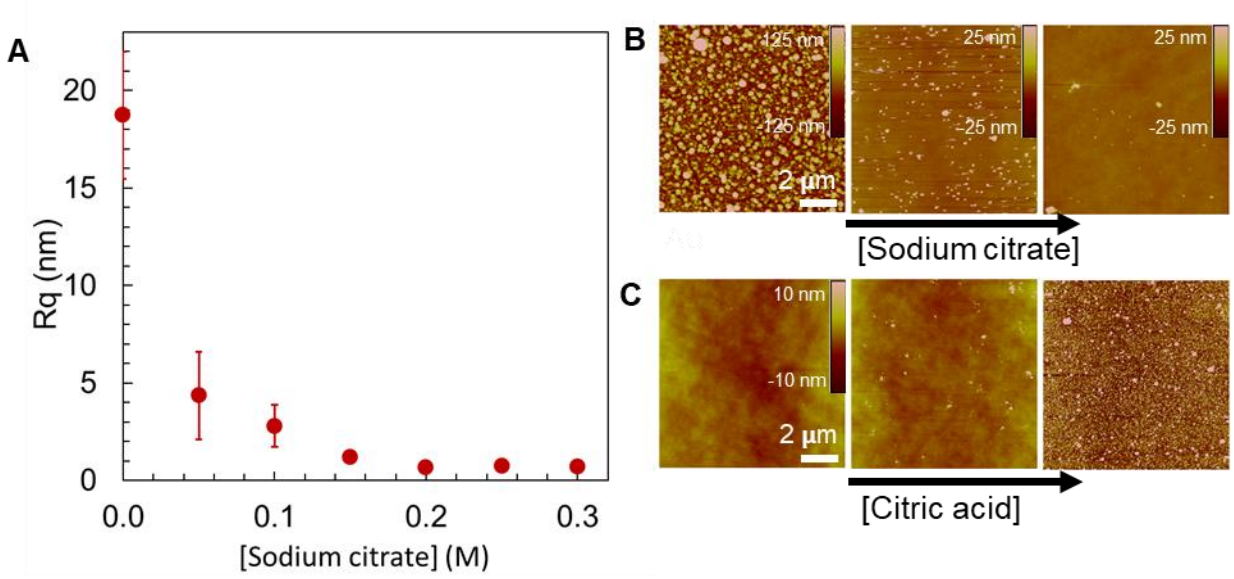

Figure 5. 10: *The effects of sodium citrate and citric acid for the metal electroless deposition (Table 5.2).* ***A)*** *Rq roughness change with respect to [sodium citrate] for gold plating solution.* ***B)*** *AFM topography images of selected data points for change of sodium citrate in the presence of [$HAuCl_4 \cdot 3H_2O$] = 12 mM and [NH_4F] = 400 mM,* ***C)*** *AFM topography images of selected data points for change of citric acid in the presence of [$HAuCl_4 \cdot 3H_2O$] = 12 mM and [NH_4F] = 90 mM. All the AFM images are 10×10 µm in size and height scales are shown on each figure.*

The pH dependent studies (*Figure 5.9*) suggest that the addition of citric acid may increase the etch rate by decreasing the pH. We observed similar trends when acetic acid is gradually added to plating solutions. UV-Vis spectra of the gold plating solution also show a peak at λ_{max} = 476 nm which shifts over time to λ_{max} = 543, due to the formation of nanoparticles in solution (*Figure 5.2*). From the pKa values of citric acid (pKa_1=3.15, pKa_2=4.77, pKa_3=6.40), most of the citrate ions are in triprotic and diprotic states at the pH of the plating solutions.[51] This may indicate that not only the pH of the solution but also the protonation state of chelating agent has effects on the rate of the electroless deposition. This also indicates that the state of the citric acid determines the chelating or the reducing ability of the citrate ion in the plating solution. Tyagi et al[52] discussed the influence of pH and protonation state of citric acid/sodium citrate for gold nanoparticle synthesis. In brief, when the pH is below the first pKa of citric acid, most of the citrate ions are protonated. This prevents the oxidation of citrate, limiting its electron donating ability to reduce

metal ions. Although decreasing pH with the addition of citric acid diminishes reducing capabilities of citrates, lower pH values promote faster etching rates resulting in favorable electroless deposition conditions. Similarly, high pH gold plating solutions will decrease electroless deposition ability while accelerating the nanoparticle formation in the solution phase.

5.4.1f Effect of PVP

When the electroless deposition was carried for 2.0 minutes on the Si(111) surface in the presence of PVP, metal deposition drastically decreased (*Figure 5.11*). For gold, a decrease in surface roughness (Rq) was observed from 3.2 ± 0.3 nm to 0.4 ± 0.1 nm. PVP establishes an equilibrium between free and bound metal ions by chelating metal ions, depleting effective metal ion concentration in solution, and allowing more control over the slow release of metal ions to plating reaction on the surface. Also, PVP containing gold plating solutions tend to show evidence of nanoparticle formation within 3-4 hours, leading to a purple color UV-Vis spectroscopy data indicates nanoparticle formation in the solution phase for gold plating solutions (*see Figure 5.3*). Researchers have used PVP often as a shape-directing agent, stabilizing agent, and reducing agent for nano particle synthesis.[53] The PVP to metal ion ratio and the molar mass of PVP are known to play a role in controlling the shape and size of the nanostructures. [54–56] During this work, no preferential growth was observed during surface reactions carried out during time intervals investigated.

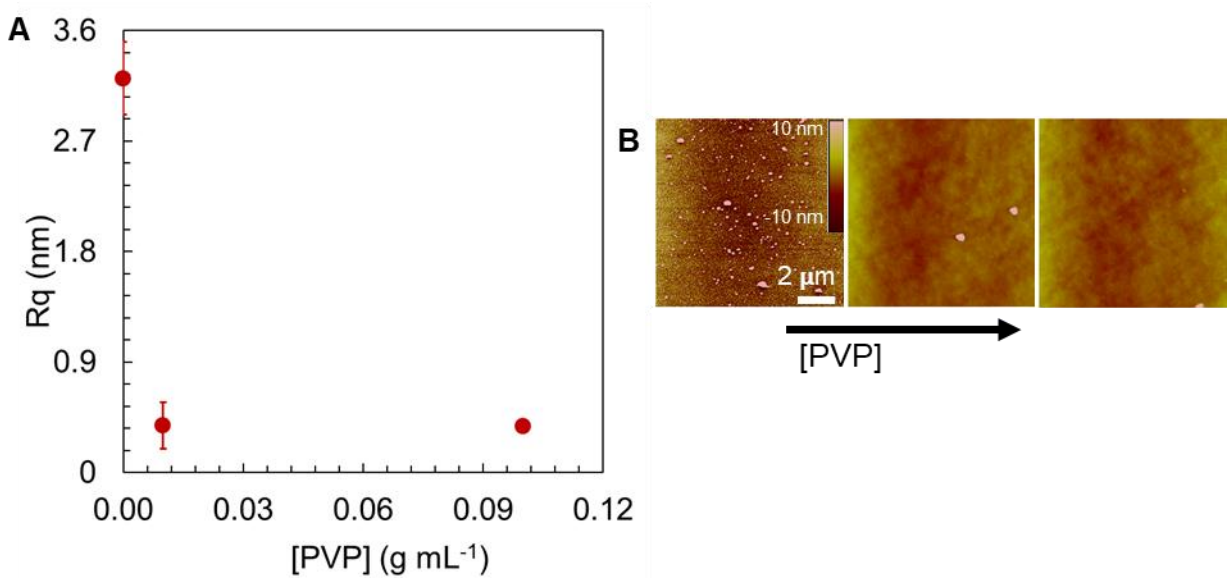

Figure 5. 11: *Effects of PVP in the plating solutions for gold and silver.* ***A)*** *Rq roughness change with respect to [PVP] for both plating solutions. (Bars represent standard deviations of measurements.)* ***B)*** *AFM topography images of selected data points for gold plating solutions with [$HAuCl_4 \cdot 3H_2O$] = 1 mM and [NH_4F] = 170 mM. All the AFM images are 10×10 µm in size and 20 nm in height. PVP amounts used can be found in table 5.2f.*

5.4.2 Plating Solution Optimization to Sustain OTS Self-assembled on Si Surfaces to Resist Electroless Deposition

While a close-packed monolayer would be expected to be robust and prevent the underlying substrate from being exposed to the plating solution, in practice the presence of defects in the film can lead to metal deposition within the SAM film itself. Hence, even when a Si substrate with a uniformly packed monolayer is exposed to a plating solution, the etching occurs at defects sites facilitating electroless deposition on the surface (see *Figure 5.4*). In this part of the work, we compare how plating solutions were applied on both bare Si surfaces and Si surfaces with monolayer resists. The goal is to achieve metal deposition on bare Si surfaces while monolayer protected surfaces are free from any metal deposition at optimized plating conditions. According to the literature, the rate-limiting step in an electroless deposition reaction is the removal of the native Si dioxide film through etching by NH_4F.[57] Therefore, the plating solutions were

strategically designed to have lower amounts of NH_4F than previously reported to further decrease the deposition rate. With a reduction in the NH_4F concentration, it is less likely the NH_4F will penetrate the defect sites and etch there during the deposition time required to plate the metal on the exposed Si surface. These initial nucleation sites act as a seed layer for rapid reduction for solution phase metal ions on the bare Si surface yielding high coverage in short deposition times. However, reducing the concentration of NH_4F too much decreases the number of nucleation sites on the surface, resulting in poor adhesion between the surface and the metal film deposited. Optimal nanoscale metal film formation was observed for NH_4F concentrations between 0.020 M and 0.500 M and metal ion concentration between 0.001 M and 0.200 M. Under these conditions, we observed uniform metal films on bare Si substrates with minimal metal deposition on OTS modified surfaces (*see Figure 5.12*). While typical plating durations range from 30–300 s for given concentrations, deposition times had to be decreased to prevent the monolayer from being compromised when [NH_4F] concentration is towards the upper limit. Moreover, all metal films produced except ones made with plating solution containing citrates showed good adhesion to the Si surface. The films survived extensive washing and repeated contact mode AFM imaging but were subject to damage under extensive sonication.

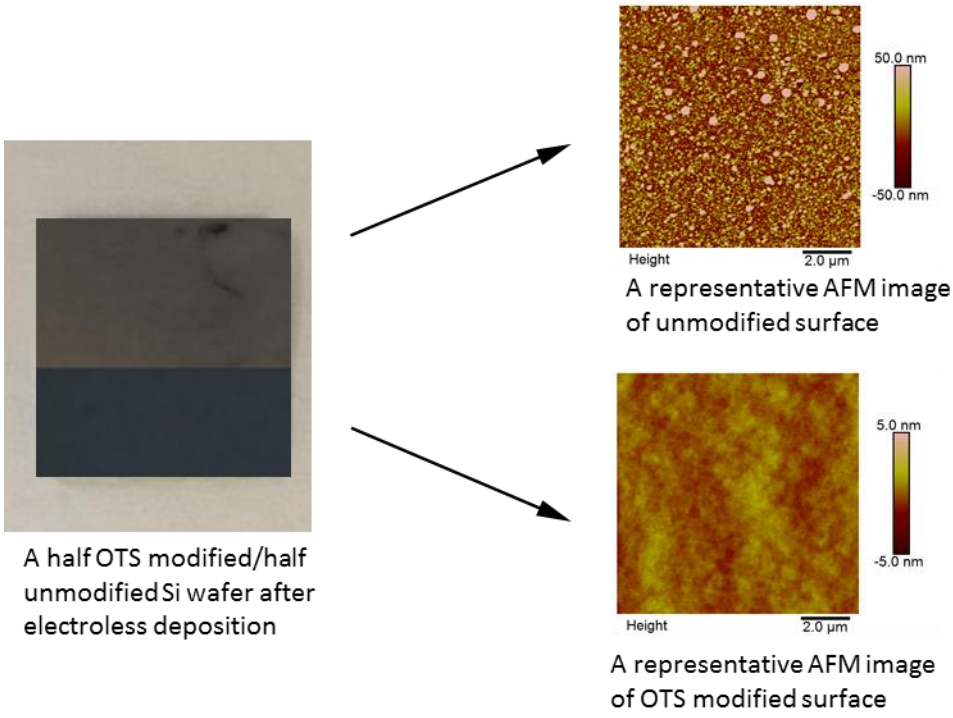

Figure 5. 12*: Using OTS SAM as a resist film to control electroless metal deposition. A Si substrate half bare and half OTS modified submerged in a gold plating solution (0.02 M NH_4F and 0.001 M $HAuCl_4 \cdot 3H_2O$ for 300 s) displaying selective gold deposition on bare Si surface with AFM images of OTS modified and bare areas after metal deposition*

5.5 Conclusion

In this work, we explore microscopic trends in an electroless deposition for two noble metal, gold, on Si surfaces. Further, we investigate the possibility of using self-assembled monolayers as a resist film for electroless deposition. Metal plating solutions for gold were optimized and studied in the range where the OTS monolayer can withstand exposure to the plating solution for adequate durations without showing evidence of metal deposition, while bare Si substrates were completely covered with reduced metal from plating solutions. Deposition trends with increasing concentrations of plating solution components including NH_4F and deposition time were investigated resulting in an increase in metal deposition. Increasing [$HAuCl_4 \cdot 3H_2O$] increased surface roughness while Decreasing pH with citric acid or mineral acids also increased

surface deposited metal amounts, while citrate ions demonstrated chelating ability at higher pH for gold ions. PVP acted as a chelating agent for both metals by reducing availability of metal ions in plating solution decreasing electroless metal deposition while demonstrating some reducing ability on Au^{3+} ions. OTS monolayer surfaces successfully resisted metal deposition in the modified plating solutions under NH_4F concentrations less than 0.50 M. For plating times less than 300 s, metal ion concentrations between 0.001-0.02 M, and NH_4F concentrations lower than 0.02 M successful deposition of metal films was achieved on bare Si(111) while the OTS coated surface remained uncoated. This modified plating solution has the potential to be used in lithography processes such as AFM based static plowing lithography, e-beam lithography, and nanosphere lithography to deposit noble metal on nanoscale patterns for applications such as plasmonics, electronics, and biosensing.

5.6 References

(1) Shacham-Diamand, Y.; Osaka, T.; Okinaka, Y.; Sugiyama, A.; Dubin, V. 30 Years of Electroless Plating for Semiconductor and Polymer Micro-Systems. *Microelectron. Eng.* **2015**, *132*, 35–45.

(2) Lahiri, A.; Kobayashi, S. Electroless Deposition of Gold on Silicon and Its Potential Applications : Review. *Surf. Eng.* **2015**, *32* (5), 321–337.

(3) Gray, J. E.; Norton, P. R.; Alnouno, R.; Marolda, C. L.; Valvano, M. A.; Griffiths, K. Biological Efficacy of Electroless-Deposited Silver on Plasma Activated Polyurethane. *Biomaterials* **2003**, *24* (16), 2759–2765.

(4) Osaka, T. Co-Based Soft Magnetic Films Produced by Electroless Deposition. *J. Electrochem. Soc.* **2006**, *139* (5), 1311.

(5) Porter, L. A.; Choi, H. C.; Ribbe, A. E.; Buriak, J. M. Controlled Electroless Deposition of Noble Metal Nanoparticle Films on Germanium Surfaces. *Nano Lett.* **2002**, *2* (10), 1067–1071.

(6) Khoperia, T. N. Electroless Deposition in Nanotechnology and ULSI. *Microelectron. Eng.* **2003**, *69*, 384–390.

(7) Osaka, T.; Takano, N.; Yokoshima, T. Microfabrication of Electro- and Electroless-Deposition and Its Application in the Electronic Field. *Surf. Coatings Technol.* **2003**, *169–170*, 1–7.

(8) Slocik, J. M.; Zabinski, J. S.; Phillips, D. M.; Naik, R. R. Colorimetric Response of Peptide-Functionalized Gold Nanoparticles to Metal Ions. *Small* **2008**, *4* (5), 548–551.

(9) Lu, C. H.; Li, J.; Zhang, X. L.; Zheng, A. X.; Yang, H. H.; Chen, X.; Chen, G. N. General Approach for Monitoring Peptide-Protein Interactions Based on Graphene-Peptide Complex. *Anal. Chem.* **2011**, *83* (19), 7276–7282.

(10) Zhou, H.-C.; Long, J. R.; Yaghi, O. M. Introduction to Metal–Organic Frameworks. *Chem. Rev.* **2012**, *112* (2), 673–674.

(11) Bontempi, N.; Chong, K. E.; Orton, H. W.; Staude, I.; Choi, D. Y.; Alessandri, I.; Kivshar, Y. S.; Neshev, D. N. Highly Sensitive Biosensors Based on All-Dielectric Nanoresonators. *Nanoscale* **2017**, *9* (15), 4972–4980.

(12) Liu, Y.; Zhao, L.; Li, X.; Zeng, Z.; Wang, P.; Zhang, L. Investigation of Plasmon Properties of Silver Microsphere Array Demonstrated Experimentally by Tip-Enhanced Raman Spectroscopy. *Appl. Surf. Sci.* **2018**, *428*, 900–905.

(13) Ahn, W.; Roper, D. K. Periodic Nanotemplating by Selective Deposition of Electroless Gold Island Films on Particle-Lithographed Dimethyldichlorosilane Layers. *ACS Nano* **2010**, *4* (7), 4181–4189.

(14) Porter, L. A.; Ribbe, A. E.; Buriak, J. M. Metallic Nanostructures via Static Plowing Lithography. *Nano Lett.* **2003**, *3* (8), 1043–1047.

(15) Garno, J. C.; Zangmeister, C. D.; Batteas, J. D. Directed Electroless Growth of Metal Nanostructures on Patterned Self-Assembled Monolayers. *Langmuir* **2007**, *23* (14), 7874–7879.

(16) Lu, P.; Shi, Z.; Walker, A. V. Selective Electroless Deposition of Copper on Organic Thin Films with Improved Morphology. *Langmuir* **2011**, *27* (21), 13022–13028.

(17) Saavedra, H. M.; Mullen, T. J.; Zhang, P.; Dewey, D. C.; Claridge, S. A.; Weiss, P. S. Hybrid Strategies in Nanolithography. *Reports Prog. Phys.* **2010**, *73* (3), 1–40.

(18) Zabetakis, D.; Dressick, W. J. Selective Electroless Metallization of Patterned Polymeric

Films for Lithography Applications. *ACS Appl. Mater. Interfaces* **2009**, *1* (1), 4–25.
(19) Nagahara, L. A.; Ohmori, T.; Hashimoto, K.; Fujishima, A. Effects of HF Solution in the Electroless Deposition Process on Silicon Surfaces. *J. Vac. Sci. Technol. A Vacuum, Surfaces, Film.* **1993**, *11* (4), 763–767.
(20) Miyake, H.; Ye, S.; Osawa, M. Electroless Deposition of Gold Thin Films on Silicon for Surface-Enhanced Infrared Spectroelectrochemistry. *Electrochem. commun.* **2002**, *4* (12), 973–977.
(21) Chen, W. W. pdf.; Sun, X. H.; Wang, S. D.; Lee, S. T.; Teo, B. K. Etching Behavior of Silicon Nanowires with HF and NH4F and Surface Characterization by Attenuated Total Reflection Fourier Transform Infrared Spectroscopy: Similarities and Differences between One-Dimensional and Two-Dimensional Silicon Surfaces. *J. Phys. Chem. B* **2005**, *109* (21), 10871–10879.
(22) Okinaka, Y.; Kato, M. Electroless Deposition of Gold. In *Modern Electroplating*; Schlesinger, M., Paunovic, M., Eds.; John Wiley and Sons, 2011; pp 483–498.
(23) Ulman, A. Formation and Structure of Self-Assembled Monolayers. *Chem. Rev.* **1996**, *96* (4), 1533–1554.
(24) Woodward, J. T.; Ulman, A.; Schwartz, D. K. Self-Assembled Monolayer Growth of Octadecylphosphonic Acid on Mica. *Langmuir* **2002**, *12* (15), 3626–3629.
(25) Liao, S.; Yang, G.; Jordan, R.; Ulman, A.; Liu, G.; Kang, J. F. Self-Assembled Rigid Monolayers of 4‘-Substituted-4-Mercaptobiphenyls on Gold and Silver Surfaces. *Langmuir* **2002**, *17* (1), 95–106.
(26) Schoenfisch, M. H.; Pemberton, J. E. Air Stability of Alkanethiol Self-Assembled Monolayers on Silver and Gold Surfaces. *J. Am. Chem. Soc.* **1998**, *120* (18), 4502–5413.
(27) Sullivan, A. M.; Kohl, P. A. The Autocatalytic Deposition of Gold in Nonalkaline, Gold Thiosulfate Electroless Bath. *J. Electrochem. Soc.* **1995**, *142* (7), 2250–2255.
(28) Kato, M.; Yazawa, Y.; Okinaka, Y. Electroless Gold Plating Bath Using Ascorbic Acid as Reducing Agent - Recent Improvements. *Lancet* **1979**, *1* (8116), 615.
(29) Osaka, T.; Okinaka, Y.; Sasano, J.; Kato, M. Development of New Electrolytic and Electroless Gold Plating Processes for Electronics Applications. *Science and Technology of Advanced Materials.* 2006, pp 425–437.
(30) Ali, H. O.; Christie, I. R. A. A Review of Electroless Gold Deposition Processes. *Circuit World* **1984**, *17* (4), 118–127.
(31) Jalali, H.; Gates, B. D. Monitoring and Mapping Imperfections in Silane-Based Self-Assembled Monolayers by Chemical Amplification. *Langmuir* **2009**, *25* (16), 9078–9084.
(32) Huang, X.; El-Sayed, M. A. Gold Nanoparticles: Optical Properties and Implementations in Cancer Diagnosis and Photothermal Therapy. *J. Adv. Res.* **2010**, *1* (1), 13–28.
(33) Green, T. A. Gold Electrodeposition for Microelectronic, Optoelectronic and Microsystem Applications. *Gold Bull.* **2007**, *40* (2), 105–114.
(34) Zeng, S.; Yong, K.-T.; Roy, I.; Dinh, X.-Q.; Yu, X.; Luan, F. A Review on Functionalized Gold Nanoparticles for Biosensing Applications. *Plasmonics* **2011**, *6* (3), 491–506.
(35) Lahiri, A.; Wen, R.; Kuimalee, S.; Chowdhury, A.; Kobayashi, S. I.; Zhang, L.; Wang, P.; Fang, Y. Photo-Assisted Control of Gold and Silver Nanostructures on Silicon and Its SERRS Effect. *J. Phys. D. Appl. Phys.* **2013**, *46* (27), 1–7.
(36) Brejna, P. R.; Griffiths, P. R. Electroless Deposition of Silver onto Silicon as a Method of Preparation of Reproducible Surface-Enhanced Raman Spectroscopy Substrates and Tip-Enhanced Raman Spectroscopy Tips. *Appl. Spectrosc.* **2010**, *64* (5), 493–499.

(37) Jain, S.; Hirst, D. G.; O'Sullivan, J. M. Gold Nanoparticles as Novel Agents for Cancer Therapy. *Br. J. Radiol.* **2012**, *85*, 101–113.
(38) Ye, W.; Shen, C.; Tian, J.; Wang, C.; Bao, L.; Gao, H. Self-Assembled Synthesis of SERS-Active Silver Dendrites and Photoluminescence Properties of a Thin Porous Silicon Layer. *Electrochem. commun.* **2008**, *10* (4), 625–629.
(39) Bhuvana; Kulkarni, G. U. Optimizing Growth Conditions for Electroless Deposition of Au Films on Si(111) Substrates. *Bull. Mater. Sci.* **2006**, *29* (5), 505–511.
(40) Rossiter, C.; Suni, I. I. Atomic Force Microscopy of Au Deposition from Aqueous HF onto Si(111). *Surf. Sci.* **1999**, *430* (1), L553–L557.
(41) Dumas, P.; Chabal, Y. J.; Gunther, R.; Ibrahimi, A. T.; Petroff, Y. Vibrational Characterization and Electronic Properties of Long Range-Ordered, Ideally Hydrogen-Terminated Si(111). *Prog. Surf. Sci.* **1995**, *48* (1–4), 313–324.
(42) Gilbert, T. R.; Kriss, R. V.; Foster, N.; Davis, G. *Chemistry: The Science in Context*, 4th ed.; Fahlgren, E., Ed.; W.W. Norton & company, Inc, 2015.
(43) Warren, S.; Reitzle, A.; Kazimirov, A.; Ziegler, J. C.; Bunk, O.; Cao, L. X.; Renner, F. U.; Kolb, D. M.; Bedzyk, M. J.; Zegenhagen, J. A Structure Study of the Electroless Deposition of Au on Si(111):H. *Surf. Sci.* **2002**, *496* (3), 287–298.
(44) Hoshino, T.; Nishioka, Y. Etching Process of SiO2 by HF Molecules. *J. Chem. Phys.* **1999**, *111* (5), 2109–2114.
(45) Ha, T. H.; Koo, H. J.; Chung, B. H. Shape-Controlled Syntheses of Gold Nanoprisms and Nanorods Influenced by Specific Adsorption of Halide Ions. *J. Phys. Chem. C* **2007**, *111* (3), 1123–1130.
(46) Nehl, C. L.; Hafner, J. H. Shape-Dependent Plasmon Resonances of Gold Nanoparticles. *J. Mater. Chem.* **2008**, *18* (21), 2415–2419.
(47) Park, J. W.; Shumaker-Parry, J. S. Structural Study of Citrate Layers on Gold Nanoparticles: Role of Intermolecular Interactions in Stabilizing Nanoparticles. *J. Am. Chem. Soc.* **2014**, *136* (5), 1907–1921.
(48) Grzelczak, M.; Pérez-Juste, J.; Mulvaney, P.; Liz-Marzán, L. M. Shape Control in Gold Nanoparticle Synthesis. *Chemical Society Reviews*. 2008, pp 1783–1791.
(49) Ji, X.; Song, X.; Li, J.; Bai, Y.; Yang, W.; Peng, X. Size Control of Gold Nanocrystals in Citrate Reduction: The Third Role of Citrate. *J. Am. Chem. Soc.* **2007**, *129* (45), 13939–13948.
(50) Kumar, S.; Gandhi, K. S.; Kumar, R. Modeling of Formation of Gold Nanoparticles by Citrate Method. *Ind. Eng. Chem. Res.* **2007**, *46* (10), 3128–3136.
(51) Wang, H. L.; Liu, L. Y.; Jiang, W. F. Effect of Novel Ternary Ligand System on Acidic Electroless Ni-P Plating on AZ91D Magnesium Alloy. *Trans. Nonferrous Met. Soc. China* **2014**, *24* (9), 3014–3022.
(52) Tyagi, H.; Kushwaha, A.; Kumar, A.; Aslam, M. A Facile PH Controlled Citrate-Based Reduction Method for Gold Nanoparticle Synthesis at Room Temperature. *Nanoscale Res. Lett.* **2016**, *11* (362), 1–11.
(53) Koczkur, K. M.; Mourdikoudis, S.; Polavarapu, L.; Skrabalak, S. E. Polyvinylpyrrolidone (PVP) in Nanoparticle Synthesis. *Dalt. Trans.* **2015**, *44* (41), 17883–17905.
(54) Lin, J. Y.; Hsueh, Y. L.; Huang, J. J. The Concentration Effect of Capping Agent for Synthesis of Silver Nanowire by Using the Polyol Method. *J. Solid State Chem.* **2014**, *214*, 2–6.
(55) Lin, J. Y.; Hsueh, Y. L.; Huang, J. J.; Wu, J. R. Effect of Silver Nitrate Concentration of

Silver Nanowires Synthesized Using a Polyol Method and Their Application as Transparent Conductive Films. *Thin Solid Films* **2015**, *584*, 243–247.

(56) Zeng, X.; Zhou, B.; Gao, Y.; Wang, C.; Li, S.; Yeung, C. Y.; Wen, W. J. Structural Dependence of Silver Nanowires on Polyvinyl Pyrrolidone (PVP) Chain Length. *Nanotechnology* **2014**, *25*, 1–6.

(57) Smith, Z. R.; Smith, R. L.; Collins, S. D. Mechanism of Nanowire Formation in Metal Assisted Chemical Etching. *Electrochim. Acta* **2013**, *92*, 139–147.

Chapter 6: Fabrication of metallic nanostructures via electroless deposition on nano shaved self-assembled monolayers on Si(111) surfaces.

6.1 Abstract

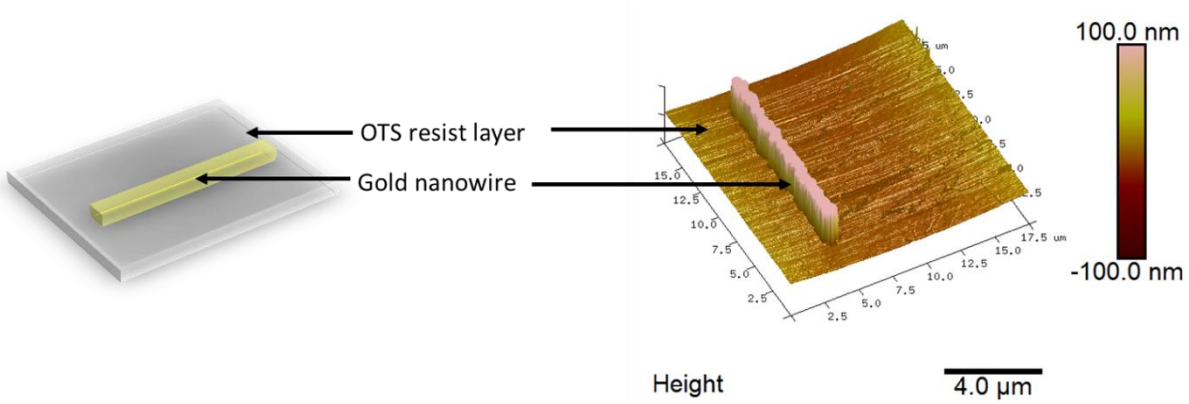

The electroless deposition of metals in selective areas of surfaces is useful for a large range of applications such as nanosensors, nanobiodevices, electronics, and optoelectronics. The optimization of the gold plating conditions for selective deposition is not trivial but achievable. In this study, we focus on an atomic force microscopic (AFM)-based method to remove a nanoscale area from the self-assembled monolayer surface and selectively deposit gold. Octadecyl trichlorosilane (OTS) based monolayers were used as a matrix self-assembled monolayer (SAM) and nanoscale regions of the SAM were removed selectively under the force of the AFM tip. After that, the optimized electroless plating solution, composed of ammonium fluoride (NH_4F), sodium citrate ($Na_3C_6H_5O_7 \cdot 2H_2O$) and gold chloride ($HAuCl_4 \cdot 3H_2O$), was used to deposit a gold nanowire in the patterned region of the surface. Redox reactions between gold ions and a bare silicon surface initiate the deposition of gold on the nanopatterned areas. We have demonstrated the ability to fabricate gold nanowires of various sizes using this technique. In the future, gold binding peptide conjugated putrescine oxidase enzyme, will be used to show selective binding of protein on the gold deposited areas of the silicon-OTS sample.

6.2 Introduction

In general, nanofabrication has gained a lot of attention due to the large range of applications such as biosensing, transparent electronics,[1–3] energy storage,[4] solar cells,[4,5] nanocircuits,[6] and optoelectronics. The ability to selectively fabricate precise metal nanostructures with nanoscale dimensions are important for the above applications. Researchers have developed 0D (all the dimensions are confined below 100 nm), 1D (two dimensions confined under 100 nm), and 2D (only one dimension is confined to the nanoscale) nanomaterials on different surfaces with the use of different materials for a vast variety of applications. In particular, there is a high demand for the metallic structures with reduced dimensions due to the miniaturization of electronic devices. Researchers have developed different metallic structures such as nanowires,[7] nanorods,[8,9] nanostars,[10] quantum dot structures[11] using solution-phase reactions. These nanostructures can be used for applications such as drug delivery,[12,13] protein adsorption,[14] and surface-enhanced Raman spectroscopy.[10,15] Most of the above mention strategies make solution-phase nanoparticles and they have tunability or the size and shape controllability by changing the temperature, pH or reactant concentration.[9,16,17]

Some of the existing methods for nanowire formation on surfaces are electron beam lithography (using a beam of electrons),[18–20] photolithography (using light),[21,22] and nanoimprint lithography (using a mold or a stamp).[23,24] Most of these methods utilize patterning of polymer or resist coated surfaces and deposit the metal of interest by utilizing different strategies. After development of scanning probe techniques, AFM-based patterning techniques have also been developed. These AFM-based surface patterning methods include dip-pen lithography (using coated AFM tips with material to be locally deposited),[25,26] oxidative lithography (using conductive AFM tips and an applied potential to initiate local redox chemistry),[27,28]

thermochemical nanolithography (utilizing the control of temperature on AFM tip)[29] and AFM nanoshaving (using AFM tip to locally remove the surface resist coating).[30,31]

Metals such as Au,[23,32–34] Ag,[35–38] Cu,[2] Fe,[39,40] Ni,[41–44] and Co[45–48] have been used to synthesize nanowires on different surfaces or in solution phase. Gold nanowires have applications within the fields of biosensing, cancer treatment and surface-enhanced Raman scattering.[32,33] Fe nanowires have been used as tunable magnetic wires for biomedical applications such as cancer treatment. Fe nanowires are magnetic and they can be used at high temperature without losing the magnetic properties since the oxide layer protects the underlying iron metal.[40]Ag nanowires are mainly prepared using electrochemical methods and polyol methods. Ag nanowires are often utilized in conductive materials such as semiconductors, transparent conductive films, and hybrid with carbon nanotubes, polymers, and graphene.[35,37] Co nanowires are ferromagnetic in nature and have applications in high-density magnetic storage media, immunomagnetic separation, and as a target drug carrier.[45,47,48] Nickel also is magnetic metal and have applications in optical devices, sensors, biotechnology, and microelectronics.[41–44]

In this study, we make gold nanowires by using AFM-based nanoshaving or static plowing lithography which utilize a stiff AFM cantilever to apply enough force to selectively remove part of the protective coating on surface and deposit metal using electroless deposition. Once the nanoshaving has been completed, the exposed substrate (often either silicon or germanium) can be modified further with different functional molecules or metals.[31]Research has demonstrated the potential of electroless deposition to introduce metals to nanoshaved areas.[31,49] AFM nanoshaving has a number of advantages including substrate flexibility (such as Si, Ge), ability to achieve nanometer scale structures, and the ability to control the position and the shape of nanostructure.[50,51]

Most of the time, the resist layer is either polymeric material or self-assembled monolayers. Among these, we are more interested in SAM surfaces due to the fact that the terminal group of the SAM molecule can be modified to obtain different functionality. The terminal group can be modified into hydrophilic or hydrophobic functionality in order to improve compatibility to the application. In our studies we utilize silane SAM on silicon surfaces since silanes are capable of forming uniform and well-packed monolayers on silicon surfaces which can act as resistive layers for the electroless deposition. Overall our fabrication process starts with the optimization of the OTS SAM coating on silicon. Then, the AFM-based fabrication process is employed to create nanoscale shaved areas. Finally, gold electroless deposition is used to deposit metal nanostructures in the patterns which can be used as platforms for different applications such as protein biosensing, nanoelectronics and optoelectronics. This method has advantages such as ability to change the functionality of the resist layer, ability of utilizing different metals, ability of formation of nanostructures with different sizes and shapes, and more importantly being able to control the placement of the nanostructure.

6.3 Materials and Methods

Certified ACS grade 30% (w/w) hydrogen peroxide, 96.5% (w/w) sulfuric acid, 37.4% (w/w) hydrochloric acid, nitric acid, sodium hydroxide, 99% sodium citrate ($Na_3C_6H_5O_7 \cdot 2H_2O$), and 99.3% ammonium fluoride (NH_4F) were purchased from Fisher Chemical Industries. Tetrachloroauric(111) acid trihydrate 99% ($HAuCl_4 \cdot 3H_2O$) were purchased from Sigma-Aldrich. All chemicals were used without further purification. Single-side polished boron-doped Si(111) wafers (resistivity 3.0-6.0 Ω.cm) from Virginia Semiconductor (Fredericksburg, VA) were used.

Milli-Q water (resistivity> 18.2 MΩ.cm) was used to rinse the substrates and make plating solutions.

All surface topography images were taken with a multimode scanning probe microscope (Nanoscope IIIA, Digital Instruments CA) using contact mode. For AFM nanoshaving, diamond-like carbon-coated (DLC) Tap 300 probes (spring constant of 40 N/m) from Budget sensors were used. For imaging, the surface after nano shaving, non-conductive silicon nitride cantilevers, with spring constants ranging from 0.12 to 0.06 N/m, were used from Veeco (Camarillo, CA). All AFM images were analyzed using NanoScope Analysis 1.5 software by Bruker Corporation. The contact angles were obtained with a Ramé-Hart, Inc. NRL C.A. Goniometer and the monolayer thickness were obtained from Rudolph Auto EL III ellipsometer.

6.3.1 Preparation of Surfaces for the SAM Formation

Pieces (~1.0 × 1.0 cm^2) of silicon chips were cut from wafers and cleaned using a 3:7 hydrogen peroxide to sulfuric acid (V/V) piranha solution. *This solution is strong oxidizer and also corrosive. Should avoid any contact with organic substances, do not store in a closed container, and handle with appropriate personal protective clothing.* Silicon substrates were cleaned by submerging in hot piranha solution for approximately 15 to 20 min, followed by rinsing with Milli-Q water. Finally, the substrates were dried under a stream of N_2 gas before use.

6.3.2 Self-Assembled Monolayer Formation on Si(111)

The cleaned silicon surfaces were kept in a solution of 2.5 mM OTS in toluene for 24 hours. Then the samples were taken out and sonicated in toluene for 30 minutes to remove physiosorbed OTS molecules. Then the samples were rinsed with toluene, chloroform, acetone and ethanol, respectively, and dried under a stream of N_2 gas. Then, the monolayers were characterized using ellipsometry, goniometry and AFM imaging.

6.3.3 AFM Nanoshaving of the OTS-SAM

For nano-shaving, diamond-like carbon coated probes (DLC Tap 300, k=40 N/m, Budget Sensors) were used. These cantilevers have a more durable DLC coating, as well as a higher spring constant than normal contact mode imaging probes. By using higher force than normal contact mode force, it can penetrate through the monolayer to the oxide layer. Two diagonal locating marks were made using a diamond tipped scribe prior to AFM-based fabrication to allow the pattern locations to be located after each step in the process. The AFM tip and the alignment marks on the surface are mapped on to a transparent film over the optical image shown in LCD screen to allow tip-surface alignment. (See *Figure 6.1)* The AFM was used in contact mode to create the pattern ans image the pattern. For this, higher deflection setpoints were utilized. To obtain wire-like structures AFM patterned line widths were controlled by changing the aspects ratios. *Figure 6.2* illustrates the overall method for the nanowire formation process. The force applied by the AFM tip on surface while patterning is given by the following Equation 1.[52]

$$F_n = k_n S_n I_n \quad (1)$$

Where, F_n is the normal force applied by the tip on the surface, k_n is the force constant of cantilever (40 N/ m DLC tips used in this study), S_n is the deflection sensitivity and the I_n is the photodiode response signal or the deflection set point.

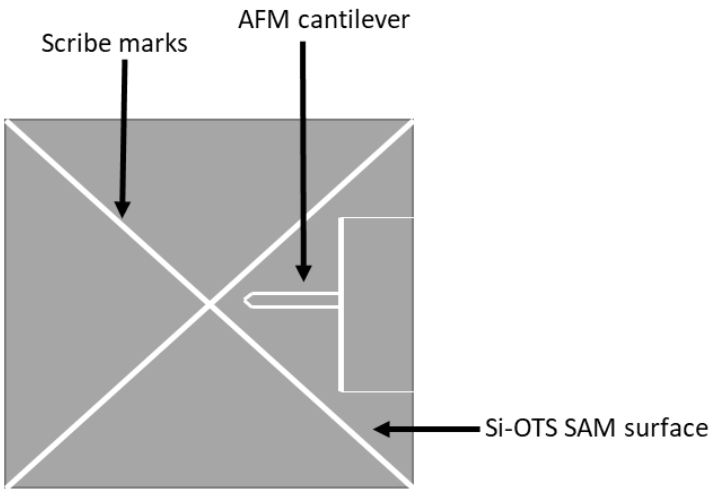

Figure 6. 1: *Image showing the diagonal markings of the Si-OTS surface and positioning of the AFM cantilever for the nano shaving.*

It is extremely difficult to go back and locate the nanoshaved area without the alignment strategy, since the patterns are too small to be located even under the optical microscope. Once the nanoshaving is complete the sample was re-imaged with a larger scan area to locate the shaved area using non-conductive silicon nitride cantilevers with lower deflection setpoint. The nanoshaved areas were characterized using the cross sections along the patterned areas to ensure the removal of the 2-3 nm thick monolayer.

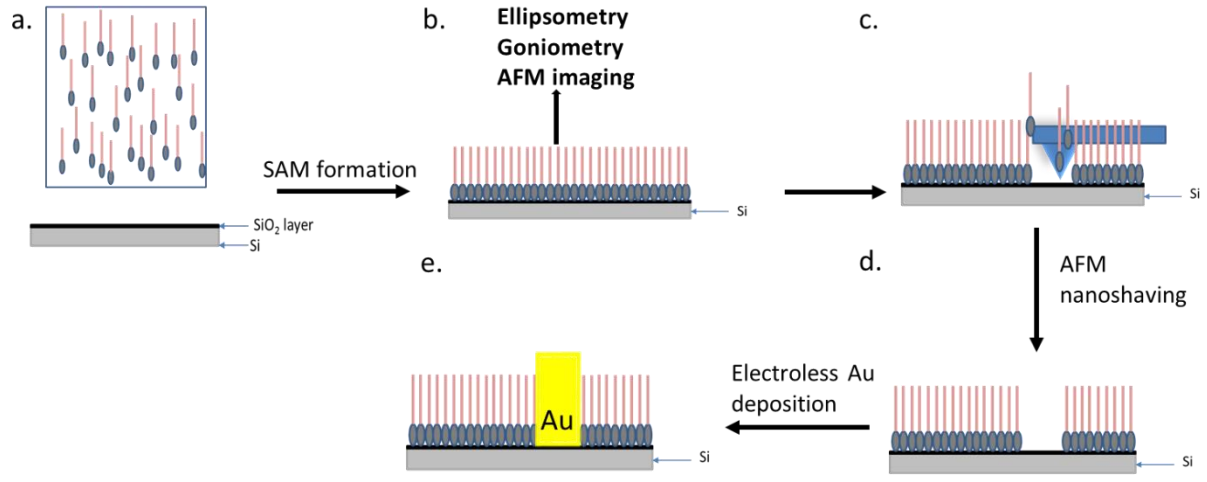

Figure 6. 2: *Method for the nanowire fabrication on Si-OTS nano shaved areas. (a) dried and piranha cleaned Si chip and OTS in toluene, (b) OTS self-assembly and characterization, (c) AFM nanoshaving of the OTS, (d) AFM imaging after nano shaving and (e) gold electroless deposition on nanoshaved areas.*

6.3.4 Electroless deposition of gold on Si-OTS-SAM modified surface

After patterning the OTS SAM surface, electroless deposition was accomplished by placing a drop of plating solution on the nanoshaved OTS surface. A 100 µL drop of plating solution was dropped onto the surface and rinsed with Milli-Q water after a set amount of time, followed by drying under a stream of N_2 gas. The pH of all the plating solutions was recorded before the plating. AFM images were collected from the pre-marked areas of surface with the nanowires.

Table 6.1 shows the optimized plating solutions that were used for the electroless deposition on the nanoshaved areas. Details about the optimization and the process of Au electroless deposition can be found in the *Chapter 5*. Solution 1 with a chelating agent can be used to prepare nanowires within shorter time periods, but the plating solution is unstable due to solution phase nanoparticle formation. Solution 2 contains no chelating agents and was stable for a longer time. The plating solution 2 plates metal slower than the plating solution 1 due to having lower concentrations of metal and NH_4F.

Table 6. 1: *The optimized plating solution concentrations and the deposition times that used for the nanowire formation.*

	Solution 1	Solution 2
$HAuCl_4 \cdot 3H_2O$/M	0.012	0.001
NH_4F/M	0.625	0.02
$Na_3C_6H_5O_7 \cdot 2H_2O$/M	0.100	N/A
Time/s	30	30-300

6.3.5 Variation of Depth of the Nanoshaved Area for the Electroless Deposition of Gold

To investigate the effect of the depth of the nanoshaved feature on the metal nanostructure formation, nanoshaved areas were fabricated with different applied force, leading to features of different depths. For that, adjacent nanoshaved areas were made and the respective depth obtained were 0.5 nm (less than a monolayer), 4 nm (roughly a monolayer) and 12 nm (penetrated into the silicon surface). This was done by increasing the deflection setpoint applied. After that electroless deposition was carried out using the plating solution 1 (see *Table 6.1*) and imaged under contact mode AFM using NPS cantilevers.

6.4 Results and Discussion

In this study, we report a methodology to fabricate different size and shaped gold nanowires using a combination of AFM nanoshaving and electroless deposition (see *Figure 6.2*). The process starts with the piranha cleaning of the surface to remove the organic residuals on the surface. Then the self-assembly of an OTS layer was carried out. To obtain desired outcome, the surface should be completely covered with monolayer showing minimum defect sites. If not, when the electroless deposition carried out, it will deposit metal on the entire surface. Next, the nanoshaving is carried out by using DLC coated AFM tips, by scanning over the desired patterning area with high applied force in contact mode. Then a drop of metal plating solution is introduced on to the surface for predetermined time to grow the nanowire. After cleaning the surface, contact mode AFM images of the resulting nanowires were recorded in contact mode. The next sections contain detailed descriptions of each step of the fabrication process.

6.4.1 OTS Self-Assembly Monolayer Formation on Si Surfaces

To obtain a good nanowire from electroless gold deposition requires a good resist layer that covers the Si surface uniformly with minimal defect sites. This will prevent the metal deposition on the areas that have resist layers while the nanoshaved areas allow gold deposition. Also, these resist films should be capable of removal by the AFM nanoshaving. Previous studies have shown OTS monolayers on Si surfaces are good candidates for nanoshaving and electroless deposition since possible to and also can be made with low defect density.[53,54]

Unwanted organic matter on the Si surface can be removed by using piranha cleaning. The topmost layer of the silicon surface will contain silicon hydroxide and silicon oxide species. In the presence of a trace amount of water, the Cl functional groups will be substituted by the hydroxyl groups and release hydrogen chloride molecules. Then, through a condensation reaction the polymerization of the molecules on the surface will occur to obtain continuous monolayer. The complete reaction mechanism of OTS monolayer formation on a cleaned silicon surface is explained step by step in *Chapter 2, Section 3.*

The monolayers of OTS were characterized by ellipsometry, goniometry, and AFM imaging to make sure that they were well-formed. A uniform, tightly packed monolayer is very important for the OTS layer to provide resistance against electroless deposition. This also prevents the penetration of the metal ions to the underlying silicon surface, which could promote metal deposition which leads to creation of more defect sites. The average contact angle for OTS-SAM was 108.7±0.9° This indicates the hydrophobic nature of the surface. To measure the thickness, the value for the refractive index of OTS was used as n=1.45, and the assumed value for the thickness of native oxide film on silicon was 15 Å.[55] Average monolayer thickness obtained for the OTS monolayer was 28.5±1.5 Å. The above mentioned values are comparable with the values

reported in the literature.[55,56] *Figure 6.3(a, c)* shows the AFM topography images of the piranha cleaned Si(111) surface and the silicon surface with OTS SAM. The images are 10.0 ×10.0 μm in size and the height scales are shown in the AFM images. The AFM cross sectional profiles show that both surfaces are flat and uniform. The respective Rq roughness values over 10.0 × 10.0 μm^2 areas are 0.471±0.02 nm for Si(111) surface and 0.717±0.01nm for the OTS surfaces.

6.4.2 Selectivity of Electroless Deposition

To determine the selectivity, optimized plating solution 2 was placed on bare silicon surfaces and also on OTS protected SAM for 2 minutes (see *Table 6.1*). The resulting surface image, AFM topography images, and the cross-sectional profiles are shown in *Figure 6.3(b, d)* for the Si(111) and the OTS protected SAM after exposure to the gold plating solution. Before exposure to the plating solution, the cross-sectional profiles of Silicon (111) and Si-OTS surfaces are flat and uniform. The topography of bare silicon surface was drastically changed after exposure to the plating solution while OTS protected surface shows little change. Due to this, the roughness of the bare silicon surface after metal deposition was changed from 0.471±0.02 nm to 29±1 nm. The macroscopic images of the bare silicon and Au plated surfaces exhibited drastic color change (from reflective mirror like finish of the silicon surface to gold) while the OTS protected surface remained unchanged throughout the process.

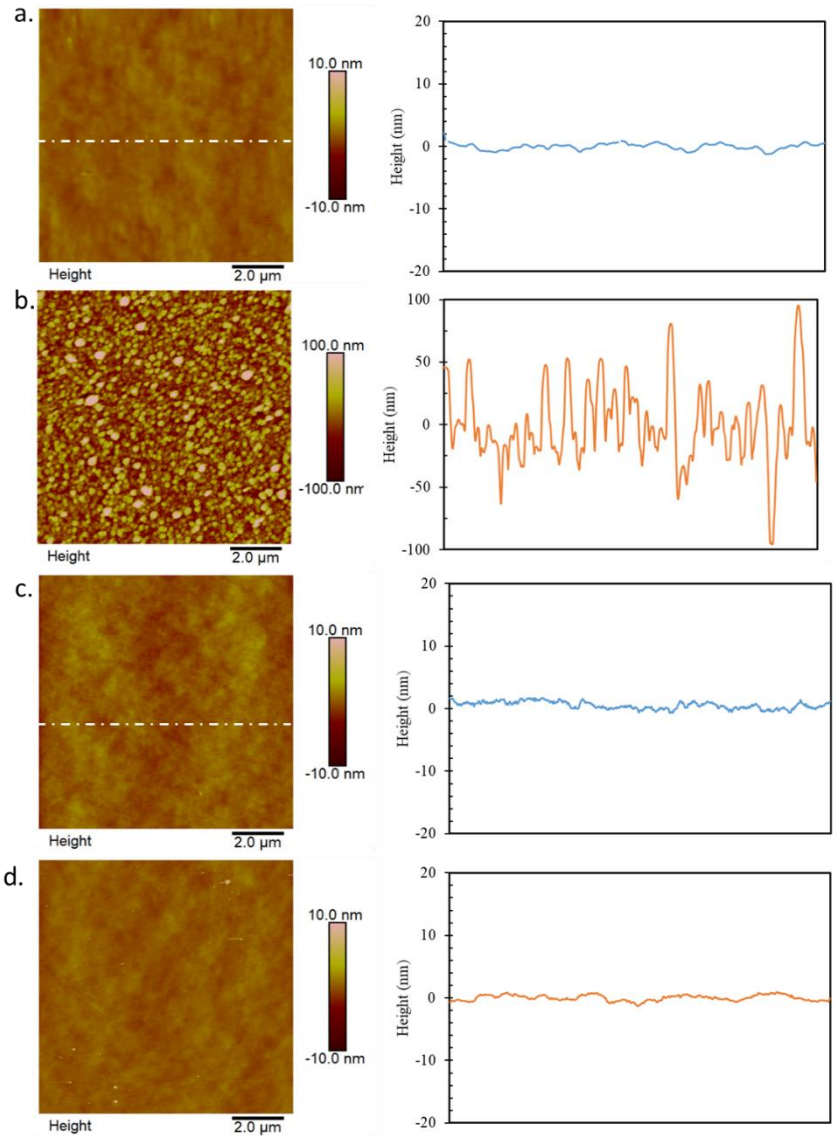

Figure 6. 3: *Shows the AFM images (a) bare Si(111) and (b) surface after gold ELD, (c) bare OTS, and (d) OTS surface after gold ELD. Cross-sectional profiles for each surface are shown next to each AFM image. All the AFM images are 10×10 µm* ^{2} *in size and height scales are shown next to images.*

6.4.3: Nanoshaving and variation of depth of shaved area by changing the setpoint

Once the uniformity and the selectivity of the surfaces are confirmed, freshly prepared OTS samples were utilized for the AFM nanoshaving. For this, a stiffer tip was used, and selective area of the monolayer was removed by using contact mode AFM by using different deflection set points (applied force). With larger applied forces, the depth of the features patterned increased, and in

some cases exceeded the thickness of the OTS coating. *Figure 6.4a* shows an OTS surface with different depth profiles that were made by varying the deflection set point. Also, by changing the aspect ratio and the scan size, the shape and size of the nanoshaved areas can be changed accordingly.

The first pattern in *Figure 6.4a* was made by nano shaving is approximately 15 nm in depth by using a deflection set point of 6.00 V, so the tip penetrates through OTS, SiO_2 and some of the Si layers. To make the second nanopattern with a 4 nm depth, a deflection set point of 3.50 V was used OTS the resulting thickness is consistent with removing primarily the OTS monolayer. Finally, due to using low deflection set point of 1 V, the tip was unable to penetrate through the monolayer, so a uniform nanoshaved area was not achieved (see *Figure 6.4*). The average depth of the feature created under these conditions was 0.5 nm (see *Figure 6.4a*). These nanoshaved expose the underlying substrate and the patterned areas can be modified by introducing a differently functionalized 2^{nd} monolayer or by introducing metal onto it.[57,58]

6.4.4: Electroless deposition of gold on nanoshaved areas.

Once the nanoshaving has been carried out, the next step is to carry out the electroless deposition. Optimized conditions for the electroless plating have been discussed in previous chapters. In summary, the industrial plating conditions were significantly altered to carryout mild plating on organic thin film modified surfaces.[59] *Figure 6.5* shows the complete process of electroless deposition on OTS modified surface with the nanoshaved areas. The mechanism of electroless deposition is discussed in detail in *Chapter 2* and *Chapter 5*.

In our studies, several optimized plating solutions have been utilized and *Table 6.1* shows the composition of the optimized plating solutions. Nanoshaved areas shown in *Figure 6.4a* were

subjected to electroless deposition under optimized plating solution 1 and the image after deposition is shown in *Figure 6.5b*. If the depth of the nanoshaved area is high, the time taken to complete the wire is long. This will lead to issues such as metal deposition on defect sites and damaging the OTS surface. Also, if the AFM tip is unable to penetrate through the OTS layer, there will be minimum metal deposition. Depth of nanoshaved area around 2-5 nm is the ideal depth which indicates the removal of organic thin film that prevent metal deposition. *Figure 6.4b*. shows the AFM image after gold ELD on the nanoshaved areas and the 4.0 nm deep wire in the middle has the maximum metal deposition and is the most complete.

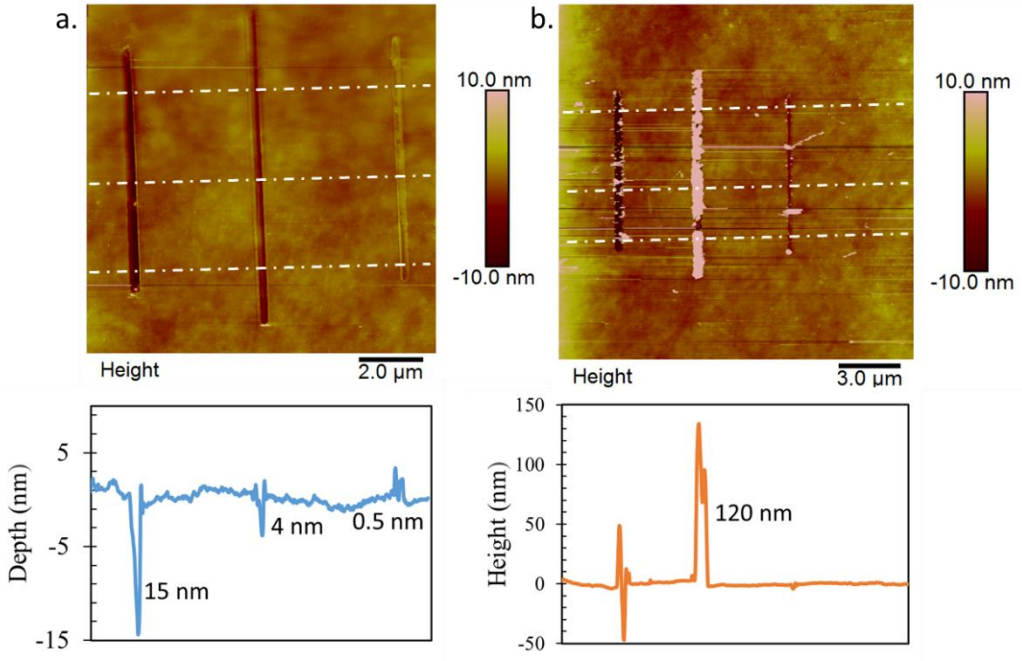

Figure 6. 4: *Nano shaving and electroless deposition. (a) AFM nanoshaved areas using 6 V, 3.5 V and 1 V of deflection set points, (b) Cross sectional profiles after electroless deposition using plating solution 1. AFM images shows three different nano shaved areas that have different depths. Depth profile across three different places are shown underneath.*

It is very important to control the depth of the nano shaved area to obtain a uniform coverage of metal deposition. So, the ideal depth of the nano shaved area is 3-5 nm in depth to make sure to obtain uniform, continuous nanowires. If the depth of the nano shaved area is high,

it will take more time to fill the pattern, and access to the bottom of the feature by the metal ions in solution may be inhibited on the nanoshaved area.

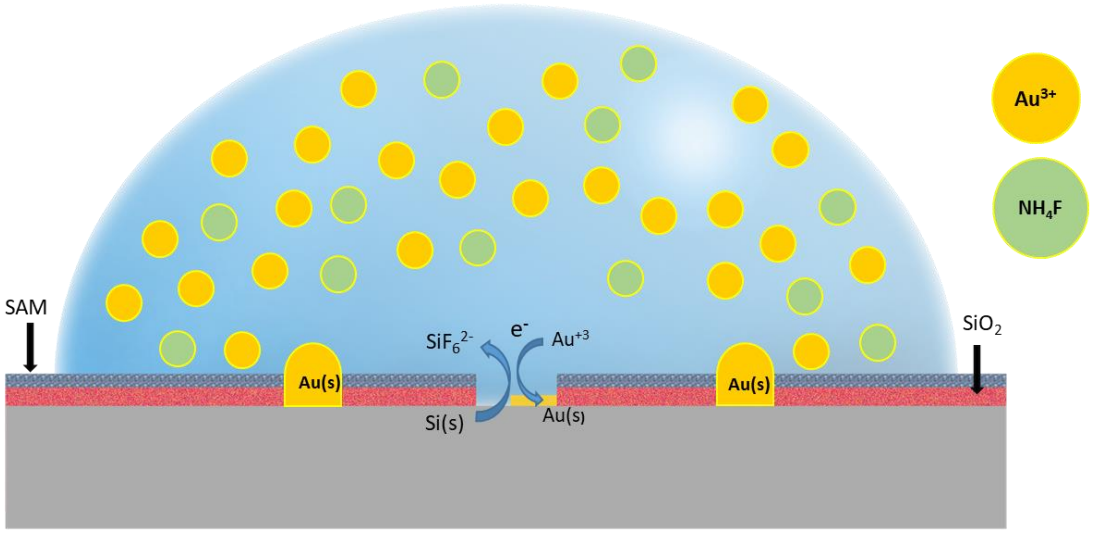

Figure 6. 5: *Electroless metal deposition on AFM nanoshaved areas of OTS protected surface.*

6.4.5: Effect of chelating agent for the electroless deposition of gold

In our previous studies and literature, it was demonstrated that the introduction of additives such as sodium citrate can act as either chelating agents or reducing agents for the metal.[16,59] *Figure 6.6 (A-C)* shows metal deposition on nanoshaved areas with varying concentrations of sodium citrate. When the concentration of additives was increased, more uniform nanowires were obtained and less metal was deposited on OTS monolayer. When the amount of sodium citrate was decreased, the OTS surface was damaged quickly. This shows the usefulness of the external additives, but on the other hand the stability of the plating solution decreases drastically due to the reducing ability of additive (see *Chapter 5* for more details).

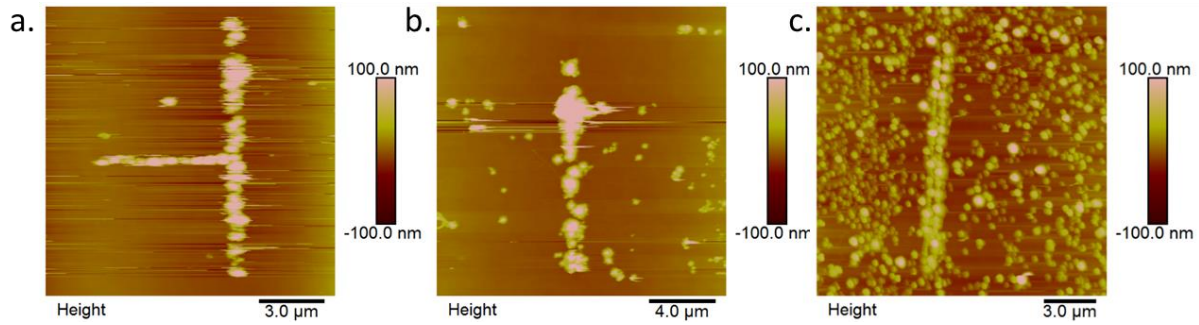

Figure 6. 6: *Nanowire fabrication using 0.625 M NH_4F and 0.012 M $HAuCl_4 \cdot 3H_2O$ using the plating time of 30 s while changing the concentration of sodium citrate (a) 0.090 M, (b) 0.080 M, and (c) 0.040 M. The size and the height scales of each image are shown in each image.*

6.4.6: Nanowire fabrication using different optimized plating solutions.

There is a possibility of developing different optimized combinations of plating solutions for the electroless deposition of gold. *Table 6.1* shows two different optimized plating solutions for gold. While developing the plating solutions the time of deposition, pH, and concentration of each additive should be optimized. *Figure 6.7* shows a continuous gold structure obtained from plating solution 1 in *Table 6* with the plating time of 30 seconds. These features have an average length of ~15 µm, width of ~1.2 µm and height of ~250 nm. There were a couple of problems associated with the plating solution 1. Plating solution 1 contains sodium citrate, which can act as a reducing agent for the metal ions in the plating solution.[16,60] The plating solution crashes out within minutes after preparation (see *Chapter 5*). Also, during a short period of time, the average height of the feature obtained was 250 nm. So, there is a need for stabilizing the plating solution and reducing the height under 100 nm.

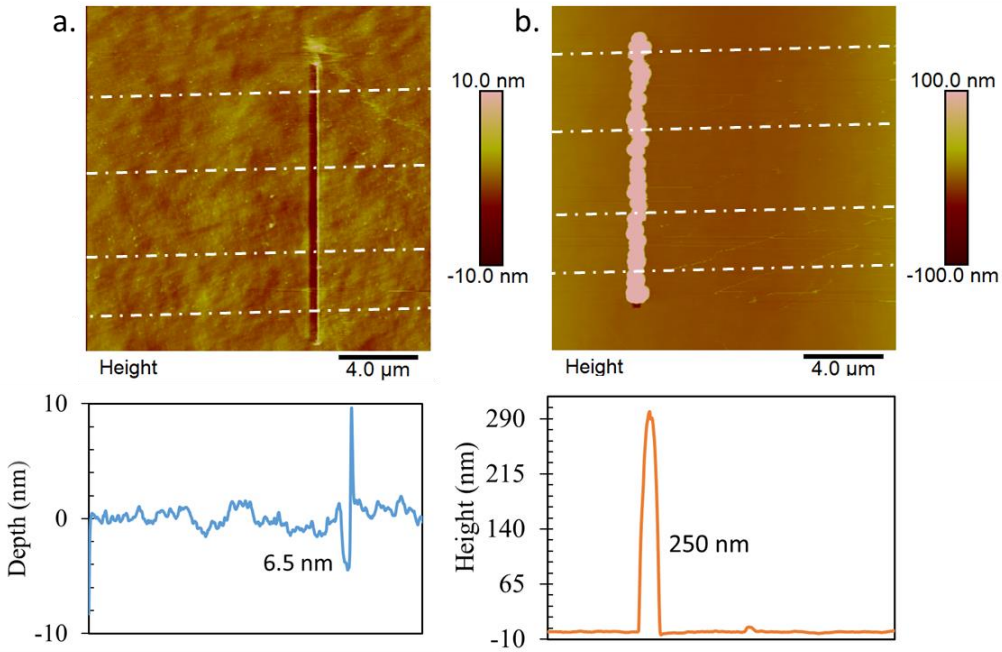

Figure 6. 7: *(a)Nano shaved areas made on OTS using AFM nanoshaving, (b) after subjected to the plating solution 1 (Table 6.1). Relevant cross-sectional profiles are shown under each AFM image.*

To overcome these issues, the plating solution was modified by removing the additive and also dropping concentration of other components significantly. The concentration of NH_4F was dropped from 0.625 M to 0.02 M to slow the etching process and the concentration of gold was dropped from 0.012 M to 0.001 M to lower the metal ion deposition rate (see *Table 6.1*). The OTS surface can withstand exposure to this plating solution without noticeable metal deposition for more than 5 minutes. *Figure 6.8* shows a nanostructure which was obtained from plating solution 2 and has length of ~3.0 µm, width of ~400 nm and height of ~65 nm.

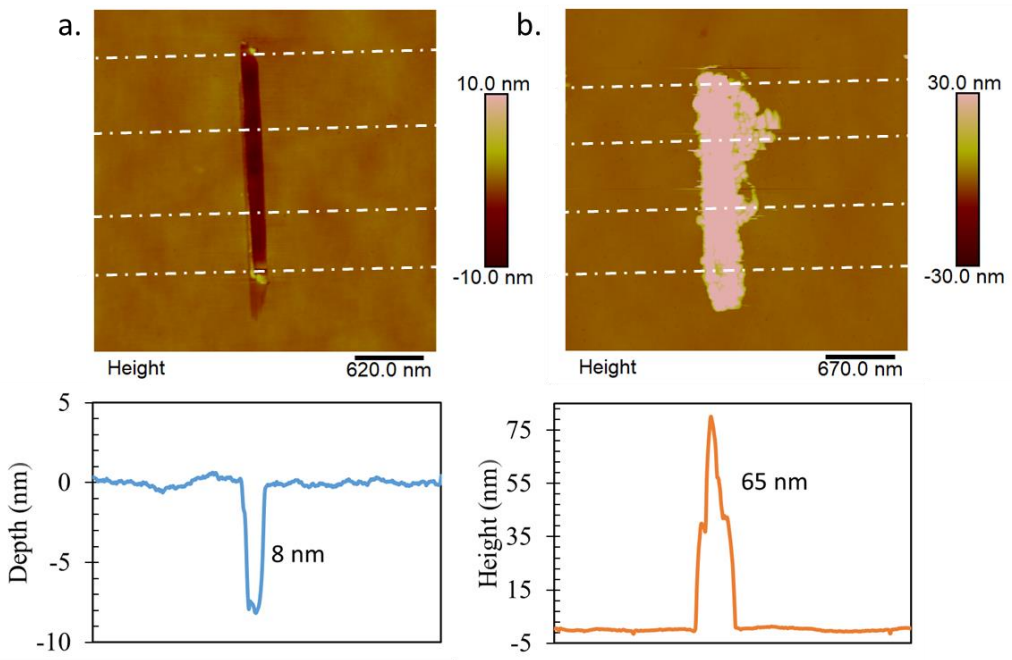

Figure 6. 8: *(a)Nano shaved areas made on OTS using AFM nanoshaving, (b) after subjected to the paling solution 2 showed in table 6.1. Relevant cross-sectional profiles are shown under each AFM image.*

In this study we discussed AFM based nanoshaving method followed by electroless deposition to obtain gold nanostructures on OTS modified silicon surfaces. We have shown successful fabrication of nano structures by using Au, Ag and Cu following above-described method. For silver plating, $AgNO_3$ and NH_4F plating solution was utilized.[61] For Cu plating solution containing NH_4F, $Cu_2(SO_4)$, sodium tartrate ($Na_2C_4H_4O_6$), and ascorbic acid ($C_6H_8O_6$) were used.[62] This approach can be used to develop nano wires of metal ions that demonstrate the same redox chemistry with Si, including Ni, Pb, Cd, Fe, and Pt.[63] To optimize the conditions further for the electroless deposition of Au, approaches such as usage of different chelating agents (ascorbic acid, PVP and citric acid) can be used in plating solution optimization. Also, for the already optimized plating solutions, modification of pH, and changing of temperature can be used to make the solutions even better plating solutions. These nanostructures have the advantage of precise control of positioning alone with the shape and size. Also, being able to modify the

functionality of the surface or the organic thin film will open up to variety of applications such as selective protein adsorption, and biosensing.

6.5 Conclusion

In this chapter, we discussed an AFM-based technique combined with electroless deposition to fabricate gold nanowires on OTS-SAM modified surfaces. Using the optimization and development of plating solutions that has been discussed in *Chapter 5*, and we selected two plating solutions that can be utilized to fabricate nanostructures on AFM nanoshaved areas. The first solution (solution 1) contains 0.625 M NH_4F, 0.012 M $HAuCl_4 \bullet 3H_2O$ and 0.100 M sodium citrate. The fabrication process is rapid and a complete nanowire with average height of 250 nm can be obtained within 30 seconds. We noticed the instability of plating solution after 15 minutes of preparation, so this will not be ideal solution for stability and storage of the plating solution. The second plating solution (solution 2) contains only 0.02 M NH_4F and 0.001 M HAuCl4$\bullet 3H_2O$. This solution had significantly lower concentrations of each of the components and wires with average height of ~65 nm in height can be obtained after 2 minutes of fabrication. The width and the length of the nanostructures can be controlled by changing imaging parameters during the nanoshaving process. The OTS monolayer acts as a good resist layer for gold electroless deposition giving minimum metal deposition outside the nanoshaved area. This method provides the control of the precise positioning of gold nanostructure on surfaces with organic resist films which can potentially be used in fundamental applications such as studying cell signaling pathways or controlled protein binding via affinity peptides.

6.6 References

(1) Hu, L.; Wu, H.; Cui, Y. Metal Nanogrids, Nanowires, and Nanofibers for Transparent Electrodes. *MRS Bull.* **2011**, *36* (10), 760–765. https://doi.org/10.1557/mrs.2011.234.

(2) Nam, V.; Lee, D. Copper Nanowires and Their Applications for Flexible, Transparent Conducting Films: A Review. *Nanomaterials* **2016**, *6* (3), 1–17. https://doi.org/10.3390/nano6030047.

(3) Chen, D.; Liu, Z.; Liang, B.; Wang, X.; Shen, G. Transparent Metal Oxide Nanowire Transistors. *Nanoscale* **2012**, *4* (10), 3001–3012. https://doi.org/10.1039/c2nr30445g.

(4) Goktas, N. I.; Wilson, P.; Ghukasyan, A.; Wagner, D.; McNamee, S.; LaPierre, R. R. Nanowires for Energy: A Review. *Appl. Phys. Rev.* **2018**, *5* (4), 041305-1-041305–041321. https://doi.org/10.1063/1.5054842.

(5) Wang, C. C. D.; Choy, W. C. H.; Duan, C.; Fung, D. D. S.; Sha, W. E. I.; Xie, F.-X.; Huang, F.; Cao, Y. Optical and Electrical Effects of Gold Nanoparticles in the Active Layer of Polymer Solar Cells. *J. Mater. Chem.* **2012**, *22* (3), 1206. https://doi.org/10.1039/c1jm14150c.

(6) Wang, D.; Jakobson, H. P.; Kou, R.; Tang, J.; Fineman, R. Z.; Yu, D.; Lu, Y. Metal and Semiconductor Nanowire Network Thin Films with Hierarchical Pore Structures. *Chem. Mater.* **2006**, *18* (18), 4231–4237. https://doi.org/10.1021/cm052216b.

(7) Haussmann, A.; Milde, P.; Erler, C.; Eng, L. M. Ferroelectric Lithography: Bottom-up Assembly and Electrical Performance of a Single Metallic Nanowire. *Nano Lett.* **2009**, *9* (2), 763–768. https://doi.org/10.1021/n18033784.

(8) Kittler, S.; Greulich, C.; Köller, M.; Epple, M. Synthesis of PVP-Coated Silver Nanoparticles and Their Biological Activity towards Human Mesenchymal Stem Cells. *Mater. Sci. Eng. Technol.* **2009**, *40* (4), 258–264. https://doi.org/10.1002/mawe.200800437.

(9) Xu, X.; Caswell, K. K.; Tucker, E.; Kabisatpathy, S.; Brodhacker, K. L.; Scrivens, W. A. Size and Shape Separation of Gold Nanoparticles with Preparative Gel Electrophoresis. *J. Chromatogr. A* **2007**, *1167* (1), 35–41. https://doi.org/10.1016/j.chroma.2007.07.056.

(10) Khoury, C. G.; Tuan, V.-D. Gold Nanostars For Surface-Enhanced Raman Scattering: Synthesis, Characterization and Optimization. *J Phys Chem C Nanomater Interfaces* **2008**, *23* (1), 1–7. https://doi.org/10.1038/jid.2014.371.

(11) Leong, K.; Chen, Y.; Masiello, D. J.; Zin, M. T.; Hnilova, M.; Ma, H.; Tamerler, C.; Sarikaya, M.; Ginger, D. S.; Jen, A. K. Y. Cooperative Near-Field Surface Plasmon Enhanced Quantum Dot Nanoarrays. *Adv. Funct. Mater.* **2010**, *20* (16), 2675–2682. https://doi.org/10.1002/adfm.201000424.

(12) Wang, L.; Liu, Y.; Li, W.; Jiang, X.; Ji, Y.; Wu, X.; Xu, L.; Qiu, Y.; Zhao, K.; Wei, T.; et al. Selective Targeting of Gold Nanorods at the Mitochondria of Cancer Cells: Implications for Cancer Therapy. *Nano Lett* **2011**, *11* (2), 772–780. https://doi.org/10.1021/nl103992v.

(13) Jain, S.; Hirst, D. G.; O'Sullivan, J. M. Gold Nanoparticles as Novel Agents for Cancer Therapy. *Br. J. Radiol.* **2012**, *85*, 101–113. https://doi.org/10.1259/bjr/59448833.

(14) Lin, W.; Insley, T.; Tuttle, M. D.; Zhu, L.; Berthold, D. A.; Král, P.; Rienstra, C. M.; Murphy, C. J. Control of Protein Orientation on Gold Nanoparticles. *J. Phys. Chem.* **2015**, *119* (36), 21035–21043. https://doi.org/10.1021/acs.jpcc.5b07701.

(15) Nie, S.; Emory, S. R. Probing Single Molecules and Single Nanoparticles by Surface Enhanced Raman Scattering. *Science (80-.).* **1997**, *275* (December), 1102–1106. https://doi.org/10.1126/science.275.5303.1102.

(16) Ji, X.; Song, X.; Li, J.; Bai, Y.; Yang, W.; Peng, X. Size Control of Gold Nanocrystals in Citrate Reduction: The Third Role of Citrate. *J. Am. Chem. Soc.* **2007**, *129* (45), 13939–13948. https://doi.org/10.1021/ja074447k.

(17) Liu, F.-K.; Ko, F.-H.; Huang, P.-W.; Wu, C.-H.; Chu, T.-C. Studying the Size/Shape Separation and Optical Properties of Silver Nanoparticles by Capillary Electrophoresis. *J. Chromatogr. A* **2005**, *1062* (1), 139–145. https://doi.org/10.1016/j.chroma.2004.11.010.

(18) Contreras, A. M.; Grunes, J.; Yan, X. M.; Liddle, A.; Somorjai, G. A. Fabrication of Platinum Nanoparticles and Nanowires by Electron Beam Lithography (EBL) and Nanoimprint Lithography (NIL): Comparison of Ethylene Hydrogenation Kinetics. *Catal. Letters* **2005**, *100* (3–4), 115–124. https://doi.org/10.1007/s10562-004-3436-7.

(19) Juhasz, R.; Elfström, N.; Linnros, J. Controlled Fabrication of Silicon Nanowires by Electron Beam Lithography and Electrochemical Size Reduction. *Nano Lett.* **2005**, *5* (2), 275–280. https://doi.org/10.1021/nl0481573.

(20) Montemagno, C.; Bachand, G. Constructing Nanomechanical Devices Powered by Biomolecular Motors. *Nanotechnology* **1999**, *10* (3), 225–231. https://doi.org/10.1088/0957-4484/10/3/301.

(21) Doan, N. M.; Qiang, L.; Li, Z.; Vaddiraju, S.; Bishop, G. W.; Rusling, J. F.; Papadimitrakopoulos, F. Low-Cost Photolithographic Fabrication of Nanowires and Microfilters for Advanced Bioassay Devices. *Sensors (Switzerland)* **2015**, *15* (3), 6091–6104. https://doi.org/10.3390/s150306091.

(22) Porter, L. A.; Choi, H. C.; Schmeltzer, J. M.; Ribbe, A. E.; Elliott, L. C. C.; Buriak, J. M. Electroless Nanoparticle Film Deposition Compatible with Photolithography, Microcontact Printing, and Dip-Pen Nanolithography Patterning Technologies. *Nano Lett.* **2002**, *2* (12), 1369–1372. https://doi.org/10.1021/nl025790k.

(23) Mårtensson, T.; Carlberg, P.; Borgström, M.; Montelius, L.; Seifert, W.; Samuelson, L. Nanowire Arrays Defined by Nanoimprint Lithography. *Nano Lett.* **2004**, *4* (4), 699–702. https://doi.org/10.1021/nl035100s.

(24) Zhao, L.; Jin, Y.; Li, J.; Deng, H.; Li, H.; Huang, K.; Cui, L.; Zheng, D. Fabrication of Nb Superconducting Nanowires by Nanoimprint Lithography. *IEEE Trans. Appl. Supercond.* **2015**, *25* (3), 1–5. https://doi.org/10.1109/TASC.2014.2382976.

(25) Salaita, K.; Wang, Y.; Mirkin, C. A. Applications of Dip-Pen Nanolithography. *Nat. Nanotechnol.* **2007**, *2* (1), 145–155.

(26) Basnar, B.; Weizmann, Y.; Cheglakov, Z.; Willner, I. Synthesis of Nanowires Using Dip-Pen Nanolithography and Biocatalytic Inks. *Adv. Mater.* **2006**, *18* (6), 713–718. https://doi.org/10.1002/adma.200502320.

(27) Masubuchi, S.; Arai, M.; MacHida, T. Atomic Force Microscopy Based Tunable Local Anodic Oxidation of Graphene. *Nano Lett.* **2011**, *11* (11), 4542–4546. https://doi.org/10.1021/nl201448q.

(28) Held, R.; Heinzel, T.; Studerus, P.; Ensslin, K. Nanolithography by Local Anodic Oxidation of Metal Films Using an Atomic Force Microscope. *Phys. E Low-Dimensional Syst. Nanostructures* **1998**, *2* (1–4), 748–752. https://doi.org/10.1016/S1386-9477(98)00153-2.

(29) Albisetti, E.; Carroll, K. M.; Lu, X.; Curtis, J. E.; Petti, D.; Bertacco, R.; Riedo, E. Thermochemical Scanning Probe Lithography of Protein Gradients at the Nanoscale. *Nanotechnology* **2016**, *27* (31), 315302 (6pp). https://doi.org/10.1088/0957-4484/27/31/315302.

(30) Xu, S.; Liu, G. Nanometer-Scale Fabrication by Simultaneous Nanoshaving and Molecular

Self-Assembly. *Langmuir* **2002**, *13* (2), 127–129. https://doi.org/10.1021/la962029f.

(31) Porter, L. A.; Ribbe, A. E.; Buriak, J. M. Metallic Nanostructures via Static Plowing Lithography. *Nano Lett.* **2003**, *3* (8), 1043–1047. https://doi.org/10.1021/nl034328c.

(32) Wang, Q.; Min, F.; Zhu, J. Preparation of Gold Nanowires and Its Application in Glucose Biosensing. *Mater. Lett.* **2013**, *91*, 9–11. https://doi.org/10.1016/j.matlet.2012.09.080.

(33) Feng, H.; Yang, Y.; You, Y.; Li, G.; Guo, J.; Yu, T.; Shen, Z.; Wu, T.; Xing, B. Simple and Rapid Synthesis of Ultrathin Gold Nanowires, Their Self-Assembly and Application in Surface-Enhanced Raman Scattering. *Chem. Commun.* **2009**, No. 15, 1984. https://doi.org/10.1039/b822507a.

(34) Huang, T.-K.; Chen, Y.-C.; Ko, H.-C.; Huang, H.-W.; Wang, C.-H.; Lin, H.-K.; Chen, F.-R.; Kai, J.-J.; Lee, C.-Y.; Chiu, H.-T. Growth of High-Aspect-Ratio Gold Nanowires on Silicon by Surfactant-Assisted Galvanic Reductions. *Langmuir* **2008**, *24* (11), 5647–5649. https://doi.org/10.1021/la8000575.

(35) Zhang, P.; Wyman, I.; Hu, J.; Lin, S.; Zhong, Z.; Tu, Y.; Huang, Z.; Wei, Y. Silver Nanowires: Synthesis Technologies, Growth Mechanism and Multifunctional Applications. *Mater. Sci. Eng. B Solid-State Mater. Adv. Technol.* **2017**, *223*, 1–23. https://doi.org/10.1016/j.mseb.2017.05.002.

(36) Peng, P.; Huang, H.; Hu, A.; Gerlich, A. P.; Zhou, Y. N. Functionalization of Silver Nanowire Surfaces with Copper Oxide for Surface-Enhanced Raman Spectroscopic Bio-Sensing. *J. Mater. Chem.* **2012**, *22* (31), 15495–15499. https://doi.org/10.1039/c2jm33158f.

(37) Lin, J. Y.; Hsueh, Y. L.; Huang, J. J. The Concentration Effect of Capping Agent for Synthesis of Silver Nanowire by Using the Polyol Method. *J. Solid State Chem.* **2014**, *214*, 2–6. https://doi.org/10.1016/j.jssc.2013.12.017.

(38) Smith, Z. R.; Smith, R. L.; Collins, S. D. Mechanism of Nanowire Formation in Metal Assisted Chemical Etching. *Electrochim. Acta* **2013**, *92*, 139–147. https://doi.org/10.1016/j.electacta.2012.12.075.

(39) Shi, J. Bin; Chen, Y. J.; Lin, Y. T.; Wu, C.; Chen, C. J.; Lin, J. Y. Synthesis and Characteristics of Fe Nanowires. *Jpn. J. Appl. Phys.* **2006**, *45* (12), 9075–9077. https://doi.org/10.1143/JJAP.45.9075.

(40) Ivanov, Y. P.; Alfadhel, A.; Alnassar, M.; Perez, J. E.; Vazquez, M.; Chuvilin, A.; Kosel, J. Tunable Magnetic Nanowires for Biomedical and Harsh Environment Applications. *Sci. Rep.* **2016**, *6* (January), 1–10. https://doi.org/10.1038/srep24189.

(41) García, M.; Escarpa, A. Disposable Electrochemical Detectors Based on Nickel Nanowires for Carbohydrate Sensing. *Biosens. Bioelectron.* **2011**, *26* (5), 2527–2533. https://doi.org/10.1016/j.bios.2010.10.049.

(42) Wang, J.; Wei, L.; Zhang, L.; Jiang, C.; Siu-Wai Kong, E.; Zhang, Y. Preparation of High Aspect Ratio Nickel Oxide Nanowires and Their Gas Sensing Devices with Fast Response and High Sensitivity. *J. Mater. Chem.* **2012**, *22* (17), 8327–8335. https://doi.org/10.1039/c2jm16934g.

(43) Liu, P.; Li, Z.; Zhao, B.; Yadian, B.; Zhang, Y. Template-Free Synthesis of Nickel Nanowires by Magnetic Field. *Mater. Lett.* **2009**, *63* (20), 1650–1652. https://doi.org/10.1016/j.matlet.2009.04.031.

(44) Kuruppu Arachchige, N. M. K.; Chambers, P. C.; Taylor, A. M.; Highland, Z. L.; Garno, J. C. Nickel Nanofilms Electrolessly Deposited on Organosilane Nanorings and Characterized by Contact Mode AFM Combined with Magnetic Sample Modulation. *ACS Appl. Nano Mater.* **2019**, *2* (4), 2193–2203. https://doi.org/10.1021/acsanm.9b00153.

(45) Saini, D.; Chauhan, R. P.; Kumar, S. Effects of Annealing on Structural and Magnetic Properties of Template Synthesized Cobalt Nanowires Useful as Data Storage and Nano Devices. *J. Mater. Sci. Mater. Electron.* **2014**, *25* (1), 124–127. https://doi.org/10.1007/s10854-013-1560-0.

(46) Ciuculescu, D.; Dumestre, F.; Comesaña-Hermo, M.; Chaudret, B.; Spasova, M.; Farle, M.; Amiens, C. Single-Crystalline Co Nanowires: Synthesis, Thermal Stability, and Carbon Coating. *Chem. Mater.* **2009**, *21* (17), 3987–3995. https://doi.org/10.1021/cm901349y.

(47) Hultgren, A.; Tanase, M.; Chen, C. S.; Reich, D. H. High-Yield Cell Separations Using Magnetic Nanowires. *IEEE Trans. Magn.* **2004**, *40* (4), 2988–2990. https://doi.org/10.1109/TMAG.2004.830406.

(48) Gao, W.; Wang, J. Synthetic Micro/Nanomotors in Drug Delivery. *Nanoscale* **2014**, *6* (18), 10486–10494. https://doi.org/10.1039/c4nr03124e.

(49) Lu, P.; Shi, Z.; Walker, A. V. Selective Electroless Deposition of Copper on Organic Thin Films with Improved Morphology. *Langmuir* **2011**, *27* (21), 13022–13028. https://doi.org/10.1021/la202839z.

(50) Cappella, B.; Sturm, H.; Weidner, S. M. Breaking Polymer Chains by Dynamic Plowing Lithography. *Polymer (Guildf).* **2002**, *43* (16), 4461–4466. https://doi.org/10.1016/S0032-3861(02)00285-9.

(51) Heyde, M.; Rademann, K.; Cappella, B.; Geuss, M.; Sturm, H.; Spangenberg, T.; Niehus, H. Dynamic Plowing Nanolithography on Polymethylmethacrylate Using an Atomic Force Microscope. *Rev. Sci. Instrum.* **2001**, *72* (1 I), 136–141. https://doi.org/10.1063/1.1326053.

(52) Liu, W.; Bonin, K.; Guthold, M. Easy and Direct Method for Calibrating Atomic Force Microscopy Lateral Force Measurements. *Rev Sci Instrum.* **2007**, *78* (6), 1–7. https://doi.org/10.1038/jid.2014.371.

(53) Rezaee, A.; Wong, K. K. H.; Manifar, T.; Mittler, S. Octadecyltrichlorosilane (OTS): A Resist for OMCVD Gold Nanoparticle Growth. *Surf. Interface Anal.* **2009**, *41* (7), 615–623. https://doi.org/10.1002/sia.3073.

(54) Wang, M.; Liechti, K. M.; Wang, Q.; White, J. M. Self-Assembled Silane Monolayers: Fabrication with Nanoscale Uniformity. *Langmuir* **2005**, *21* (5), 1848–1857. https://doi.org/10.1021/la048483y.

(55) Prunici, P.; Hess, P. Ellipsometric in Situ Measurement of Oxidation Kinetics and Thickness of (C2–C20) Alkylsilyl (Sub)Monolayers. *J. Appl. Phys.* **2008**, *103* (2), 024312. https://doi.org/10.1063/1.2832439.

(56) Wasserman, S. R.; Whitesides, G. M.; Tidswell, I. M.; Ocko, B. M.; Pershan, P. S.; Axe, J. D. The Structure of Self-Assembled Monolayers of Alkylsiloxanes on Silicon: A Comparison of Results from Ellipsometry and Low-Angle X-Ray Reflectivity. *J. Am. Chem. Soc.* **1989**, *111* (15), 5852–5861. https://doi.org/10.1021/ja00197a054.

(57) Saavedra, H. M.; Mullen, T. J.; Zhang, P.; Dewey, D. C.; Claridge, S. A.; Weiss, P. S. Hybrid Strategies in Nanolithography. *Reports Prog. Phys.* **2010**, *73* (3), 1–40. https://doi.org/10.1088/0034-4885/73/3/036501.

(58) Headrick, J. E.; Armstrong, M.; Cratty, J.; Hammond, S.; Sheriff, B. A.; Berrie, C. L. Nanoscale Patterning of Alkyl Monolayers on Silicon Using the Atomic Force Microscope. *Langmuir* **2005**, *21* (9), 4117–4122. https://doi.org/10.1021/la0481905.

(59) Porter, L. A.; Choi, H. C.; Ribbe, A. E.; Buriak, J. M. Controlled Electroless Deposition of Noble Metal Nanoparticle Films on Germanium Surfaces. *Nano Lett.* **2002**, *2* (10), 1067–1071. https://doi.org/10.1021/nl025677u.

(60) Ojea-Jiménez, I.; Bastús, N. G.; Puntes, V. Influence of the Sequence of the Reagents Addition in the Citrate-Mediated Synthesis of Gold Nanoparticles. *J. Phys. Chem. C* **2011**, *115* (32), 15752–15757. https://doi.org/10.1021/jp2017242.

(61) Ulapane, S. B.; Kamathewatta, N. J. B.; Ashberry, H. M.; Berrie, C. L. Controlled Electroless Deposition of Noble Metals on Silicon Substrates Using Self-Assembled Monolayers as Molecular Resists to Generate Nanopatterned Surfaces for Electronics and Plasmonics. *ACS Appl. Nano Mater.* **2019**, *2* (12), 7114–7125. https://doi.org/10.1021/acsanm.9b01641.

(62) Edwards, C. M. Fabrication and Manipulation of Metallic Nanofeatures and CVD Graphene through Nanopatterning and Templating, 2004.

(63) Shacham-Diamand, Y.; Osaka, T.; Okinaka, Y.; Sugiyama, A.; Dubin, V. 30 Years of Electroless Plating for Semiconductor and Polymer Micro-Systems. *Microelectron. Eng.* **2015**, *132*, 35–45. https://doi.org/10.1016/j.mee.2014.09.003.

Chapter 7: Periodic Gold Nanodot Array Fabrication on Particle Lithography-Based Nanopore patterns Using Electroless Deposition

The content in this chapter belongs to a manuscript submitted recently by Sasanka B. Ulapane, Nilan J. B. Kamathewatta, Ashley K. Borkowski, Samuel J. Steuart, and Cindy L. Berrie, titled as Periodic Silver and Gold Nanodot Array Fabrication on Particle Lithography-Based Nanopore patterns Using Electroless Deposition ***ACS Applied Nano Materials 2019****. In my part of the study, I was working towards the development of gold nanodot arrays by utilizing the mythology developed by Sasanka B. Ulapane. The content is being reprinted here with permission of all authors.*

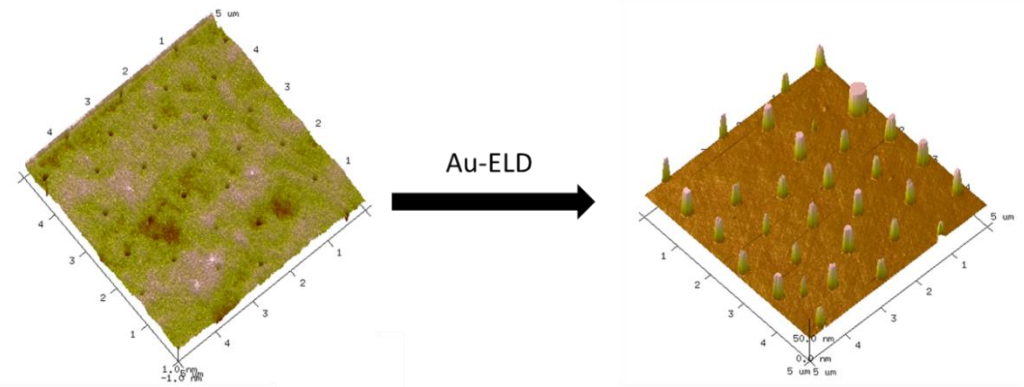

7.1 Abstract

Precision controlled fabrication of metallic nanostructures attracts great interest in fields of sensing, optoelectronics, surface enhanced Raman scattering, and high capacity storage devices. However, the expense and throughput of current methods limit the applicability of metal nanodot arrays for many of these applications. In this study, hexagonal arrays of gold nanodots were fabricated on silicon (111) surfaces via a particle lithography-based approach followed by electroless deposition. Silicon surfaces with hexagonally packed nanospheres were reacted with octadecyltrichlorosilane to form a self-assembled monolayer resist over the substrate, which leads

to a nanopore pattern upon removal of the spheres. Plating solutions for gold were introduced onto the nanopore surfaces to selectively deposit metal in the nanopores, resulting in metal nanodots grown where the nanospheres were in contact with the substrate. Nanodot heights were effectively controlled from 20-100 nm by varying plating time and the composition of the plating solution. Atomic force microscopy was used to characterize the height and diameter of the nanopore and nanodot arrays. This approach demonstrates the ability to fabricate nanodots of two different noble metals, for potential application in sensing, surface enhanced Raman spectroscopy, and optoelectronics. This method provides control over the spacing between nanodots and their size by changing nanosphere diameter and varying plating duration (or solution composition) with high reproducibility.

7.2 Introduction

Advances in technology and increased demand on depleting resources have created a push towards miniaturizing high tech devices,[1,2] leading to nanoscale electronics,[3] storage devices,[2] memory circuits,[4,5] optical components,[6] and sensory and detection systems.[7–9] Metal nanodot arrays spaced at regular intervals have shown remarkable properties in these applications due to enhanced surface plasmon resonance and strong electromagnetic wave coupling on the surfaces.[10–13] Attempts have been made to design regularly spaced metal nanodot arrays with precise separation and size control from various metals;[14–18] however, the ability to maintain good reproducibility, allow high throughput, low cost production, and easily adapt to different metals with minimal use of high tech equipment are ongoing challenges for fabrication of such metal nanodot arrays.

The two most commonly used classifications for surface patterning techniques are “top down” and “bottom up” approaches.[1] Traditional top down approaches, such as electron or ion beam lithography,[19,20] reactive ion bombardment,[17] and nano imprint techniques, often employ expensive equipment or have limited throughput.[14] Contemporary, yet costly, technological developments have allowed high resolution patterning with advanced electron beam and photo lithography equipment that costs millions of dollars.[19] Scanning probe techniques such as dip pen nanolithography have demonstrated remarkable precision as a direct writing tool; however, they lack the throughput required for routine production of large arrays.[21,22] In contrast, recently developed microcontact printing techniques show considerable promise in scalability, but they work best for making patterns over 100 nm in size.[14] Bottom up processes use spontaneous self-assembly of materials to fabricate functionally organized surfaces from molecular to nanoscale features. [23] These processes are generally inexpensive and approachable, but they are limited in applicability by the materials properties. Investigations are ongoing regarding how bottom up processes can be fully developed into techniques useful for fast and reliable metallic nanoarray fabrication. Bottom up strategies, including nanosphere lithography, can be combined with further functionalization using organosilane thiols, metals or proteins for various applications. [24] Block copolymer micellar nanolithography has also been combined with metal evaporation for metal nanoarray fabrication to form periodic metallic nanodot arrays. [15,25] Thiol-coupled biomolecule immobilization on these metal nanoparticles could further extend the utility for biological applications.[26,27]

History of particle lithography date back to 1982, when it was known as “natural lithography”.[24] Particle or nanosphere lithography was further developed in the mid 1990’s by the Van Duyne research group, and it has found applications in modern nanofabrication to make

regularly spaced plasmonic nanoarrays.[28,29] These plasmonic nanodot arrays have shown remarkable biosensing properties with femtomolar detection limits and have demonstrated use in the investigation of binding kinetics.[16,26] Similar approaches have been used to make functionalized nanoarrays with regularly ordered ligand structures on surfaces by the Liu[30] and Garno[24] groups. This approach uses the sphere as a contact mask in contrast to the Van Duyne approach, where the spheres are used as a shadow mask to deposit metal between the spheres via evaporation. In this approach, monodispersed nanospheres in water are drop cast on a glass/silica substrate, allowing the surface tension of water to produce a uniformly packed hexagonal array of spheres covering the substrate. Using a glass or Si substrate, organosilanes can be self-assembled from solution[31,32] or the vapor phase[33,34] onto the sphere coated substrate to modify the surface chemistry[24] and leave the contact areas between the spheres and the substrate unmodified. Upon removal of the spheres, arrays of periodic holes in the monolayer resist, commensurate with the hexagonal sphere packing, are revealed. Similar approaches have been used to couple biomolecules in the nanoscale arrays for applications in sensory systems and investigation of cell signaling pathways.[35] Sub-micron level precision in placement of biological functional groups allows triggering of targeted cell membrane receptors,[36] separated on comparable length scales, allowing researchers to broaden the understanding of multivalent interactions in signaling and cell-cell interactions. Development of platforms with metal nanodot arrays using nanosphere lithography has been accomplished by either secondary modifications using thiol functionalized organosilane self-assembly on exposed nanopores to bind Au nanoparticles,[37] or using electroless deposition onto a seed layer of one or more precursor metal layers on the Si surface.[19,38] Electroless deposition (ELD) is an easy benchtop approach that allows metal deposition on a Si substrate by utilizing the redox potential difference between the metal and the Si substrate, which would allow

fast, inexpensive formation of metal nanostructures when used in combination with particle lithography. Previously reported techniques using particle lithography-based metal nanodot array fabrication require extra chemical modification steps on the exposed Si surface through nanoholes to grow metal nanopatterns,[19,37] adding extra time and complexity to the process. The method described here has three advantages: 1) it avoids potential issues from the seed layer of a different metal that adds contamination to the nanodots, 2) it provides better adhesion to the substrate by avoiding the use of thiol coupling and 3) add enhanced electrical conductivity.

In this report, we demonstrate a technique to selectively deposit metal on particle lithography-based nanopore arrays made on Si substrates using octadecyltrichlorosilane (OTS) as a monolayer resist. The method generates regularly placed hexagonal arrays of metallic nanodot arrays using the redox potential difference between metal ions of interest in solution phase and the Si substrate. This general approach allows deposition of numerous metal ions that demonstrate spontaneity in redox chemistry with Si, including Ag, Au, Cu, Ni, Pb, Cd, Fe, and Pt.[39] We have studied and optimized plating conditions to fabricate Au nanodot arrays with nanoscale control over sizes (both height and width) by changing the plating duration. Spacing of the array elements was varied by using nanospheres with different diameters during the particle lithography. The plating process takes only minutes to form nanodot arrays once the nanopore arrays are made using particle lithography, and the OTS monolayer shows improved resistance to electroless deposition over other silanes,[16] enabling a simple, low cost, high throughput approach that allows control of metal nanodot spacing and size over large areas of the substrate.

7.3 Materials and Methods

Certified ACS grade 30% hydrogen peroxide, sulfuric acid and toluene were purchased from Fisher Chemical Industries. 200-proof ethanol from Decon Labs was used for sonication and washing Si substrates after nanopore formation. Octadecyltrichlorosilane (OTS) was purchased from Acros Organics in New Jersey. Tetrachloroauric(III) acid trihydrate ($HAuCl_4 \bullet 3H_2O$) was purchased from Sigma-Aldrich. All chemicals were used without further purification. Polished Si wafers (Si(111)) wafers doped with phosphorous (<1 Ω.cm) were purchased from Virginia Semiconductor (Fredericksburg, VA). 500 and 1000 nm Duke standards silica microspheres was purchased from Thermo scientific.

All surface topography images were taken with a multimode Nanoscope IIIA scanning probe microscope (Digital Instruments, CA). Non-conductive silicon nitride (Si_3N_4) cantilevers, with spring constants of 0.12 to 0.06 N/m, were used from Bruker (Camarillo, CA) for all contact mode images. Tapping mode images were taken using DLC tap 300 probes (spring constant 40 N/m and resonance frequency of 300 kHz) with a diamond like carbon coating from Budget sensors. AFM images were analyzed using NanoScope Analysis 1.5 by Bruker Corporation (Billerica, MA)

7.3.1 Formation of Organosilane Nanopatterns

Si wafers were cut to approximately 1 cm^2 pieces and cleaned using a 3:7 hydrogen peroxide to sulfuric acid (V/V) piranha solution. *Piranha solution is extremely corrosive and reacts violently with organic compounds. It must be handled with appropriate personal protective clothing and must be neutralized immediately after use.* Clean Si substrates were washed with copious amounts of deionized water and dried under a stream of N_2. To remove surfactants, an aliquot of silica microspheres was diluted with equal volume of deionized water, vortexed for one

minute, and centrifuged for five minutes at 5000 rpm. A set volume of the supernatant was removed and diluted again to original volume by adding deionized water followed by another vortexing step. This process was executed three times before fixing the volume of spheres to bring to 1:1 diluted nanosphere solution. A 20 µL of the nanosphere solution was dropcast on freshly piranha-cleaned Si substrates. Si substrates with the nanosphere solution were dried in ambient conditions (~22°C and ~22% relative humidity) for 30 minutes before oven dried at 100 ℃ for 1 hr. Samples were placed in a homemade glove bag maintained at 22°C and approximately 60-70% relative humidity by bubbling N_2 through water. Samples were kept in this controlled environment for an hour and submerged in 2.50 mM OTS solution in toluene to facilitate the self-assembly of the monolayer. Samples were removed from the silane solution after 24 hours and sonicated in ethanol for 45 minutes to remove the silica nanospheres. The resulting samples were washed with ethanol and dried using N_2.

7.3.2 Characterization of the Nanopore Arrays

Nanopore arrays were characterized by surface imaging using AFM. Five to ten 5x5 μm^2 AFM images were taken on various locations of the surface of three sample made in three different batches. Pore diameter, depth, and pore separation was recorded (n>50 for each sphere size) and recorded with standard deviations.

7.3.3 Electroless Deposition of Metal to Produce Metal Nanoarrays

Metal electroless deposition was accomplished by a placing a drop of plating solution on the nanopore array for a certain time duration after a pre-etching step lasted a fixed 30 s. A pre-etching solution was prepared by dissolving 5% NH_4F (W/W) in deionized water. Standard plating solution was made containing 0.002 M $HAuCl_4 \cdot 3H_2O$ and 0.02 M NH_4F for Au nanodot arrays. 100 µL of pre-etching solution was dropped on a silica substrate containing an OTS monolayer

with nanopore arrays and removed after 30 seconds by blowing with N_2. Immediately after, another 100 µL of the plating solution was placed on the surface and left for another set duration of time before being washed under a gentle stream of deionized water and dried under N_2.

7.3.4 Characterization of the Nanodot Arrays

Nanodots were characterized similarly to nanopores using AFM images. Nanodot height, diameter at base, and separation was recorded (n>50) for each type of spheres used along with standard deviations.

7.4 Results and Discussion

In this study, large scale arrays of Au nanodots were fabricated by making nanopore arrays in OTS monolayers, the pores where then filled with Au in an electroless deposition step (or by ELD method). *Figure 7.1* outlines the steps for fabrication of metal nanostructures using electroless deposition on nanopore arrays made using particle lithography. A dilute monodispersed nanosphere solution was drop-cast onto a piranha cleaned Si surface to create a hexagonally packed nanosphere array on the surface (*Figure 7.1a*). The substrates with the spheres were exposed to an OTS solution to self-assemble a monolayer over the substrate. The periodically packed nanospheres prevent any surface modifications on nanosphere contact points with the surface (*Figure 7.1b*). Next, the nanospheres were removed by sonication, exposing the unmodified nanopore patterns on the substrate and revealing the native oxide layer on the Si (*Figure 7.1c*). Finally, the two step electroless deposition of gold on nanopores was carried out (*Figure 7.1d*).

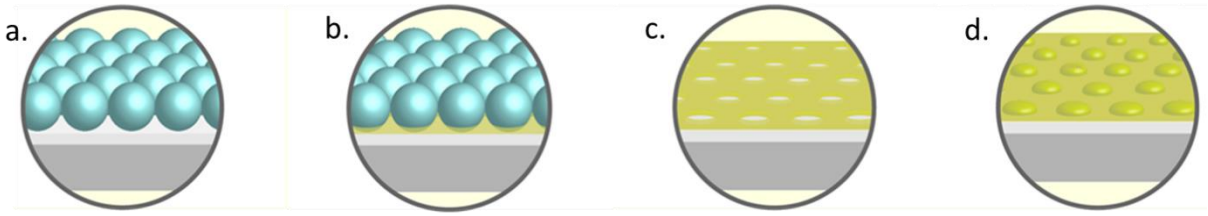

Figure 7. 1: *Process outline for metal nanodot array fabrication using particle lithography. (a) Monodispersed nanospheres arranged on the surface as repeating hexagonal units. (b) OTS self-assembly on Si substrate while nanospheres effectively mask their contact points with the substrate from chemical modification. (c) Nanopore arrays commensurate with hexagonal packing arrangement of nanospheres after the removal of nanospheres by sonication. (d) Repeating hexagonal arrays of metal nanodots formed on OTS self-assembled Si scaffolds after electroless deposition of metal.*

A solution of nanospheres was prepared by diluting the stock nanosphere solution 1:1 with water to generate a monolayer of nanospheres on the Si substrate. Surfactant from the nanospheres solution was washed off by vortexing and centrifugation to promote inter-sphere interactions as previously reported.[32,34] Spheres tend to pack well on the surface in a repeating hexagonal arrangement due to inter-sphere interactions and capillary forces created by residual water, where the bottom of each sphere comes into contact with the substrate. The contact points of spheres with the substrate effectively mask self-assembly of OTS on those areas, creating nanopores at the contact points once the spheres are removed.

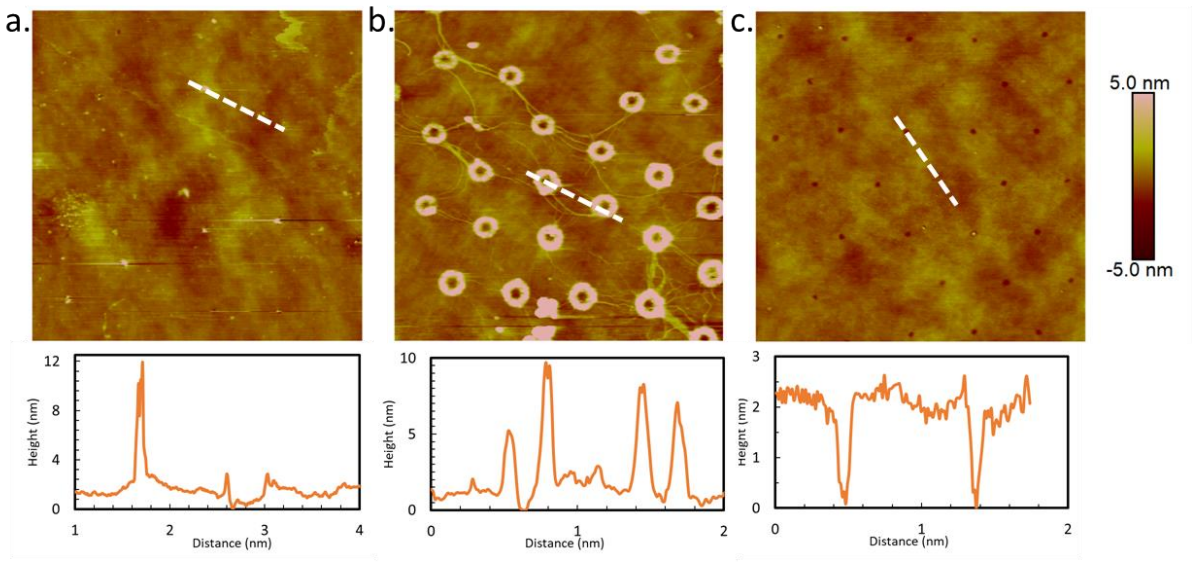

Figure 7. 2: *Effects of drying time before self-assembly on monolayer formation. 1000 nm nanosphere arrays dried under different conditions before self-assembled with OTS on underlaying Si substrates using 2.5 mM OTS in toluene. (a) Sample surface after drying under 20% humidity for 2 hr, (b) after drying under 40% humidity for 20 minutes and (c) After oven drying the surface for 1 hr and re-hydrating at 70% humidity for 1 hr using a glove bag to bubble N_2 through water Cross sectional profiles are shown under each image which took along the dotted lines shown in AFM images.*

Residual water on the SiO_2 surface plays a critical role in the monolayer formation process and, consequently, in this fabrication approach.[40] The formation of the OTS monolayer also depends highly on the water content, water being necessary for the exchange of chloro groups on OTS for hydroxyls. To investigate the effect of water, substrates were dried under different humidity conditions. Garno *et. al.* [37] previously demonstrated[32] that the relative humidity at which the samples are dried prior to monolayer formation effects the quality, packing, and thickness of the monolayer formed on the SiO_2 surface.[37] Here, three different drying conditions were explored as shown in *Figure 7.2*. Low humidity with 2 hours drying and medium humidity with 20 minutes drying did not yield any nano patterns as expected. Monolayer formation at 70% relative humidity after oven drying reproducibly resulted in a pore depth consistent with literature values[31,41] of monolayer thickness, without obvious polymerization on the surface. This suggests the lack of water on the surface inhibits silanization on surface (*Figure 7.2a*). Shorter drying durations left traces of pores and ring like structures (*Figure 7.2b*) that correlate with the nanosphere packing.

This was previously reported[24,33,41] to be a result of trapped residual water on the edges of nanosphere contact points, creating a water meniscus between the substrate and nanosphere. Formation of a well-packed OTS monolayer on the exposed area of the SiO_2 requires a uniformly adsorbed residual water layer. This was achieved by completely drying substrates in an oven and rehydrating at 70% relative humidity in a glovebox afterward (F*igure 7.2b*). Controlling the relative humidity establishes an equilibrium between surface adsorbed and gas phase water at a given temperature. Relative humidity in the glove bag was controlled by adjusting the rate of N_2 bubbled through a temperature-controlled water container into the glove bag. The substrates were equilibrated at controlled humidity for approximately one hour. The process outline for the OTS monolayer formation over the native oxide layer on Si is discussed in *Chapters 2 and 5*.

Optical properties of the substrate show a clear change before and after the nanosphere removal as observed visually. This provides a good indication of when the nanospheres are removed from the surface. Multiple layers of spheres allows more extensive cross linking of the spheres, making them more difficult to remove. It also may prevent access of the OTS to the substrate surface. This is largely due to OTS cross polymerization between the spheres. Previous work on organosilane monolayer formation with the combination of particle lithography has provided evidence of well packed monolayer formation even in the presence of multiple layers of nanospheres on the surface.[31] Importantly, OTS monolayers are quite robust, and they can withstand long durations of sonication needed to remove spheres.

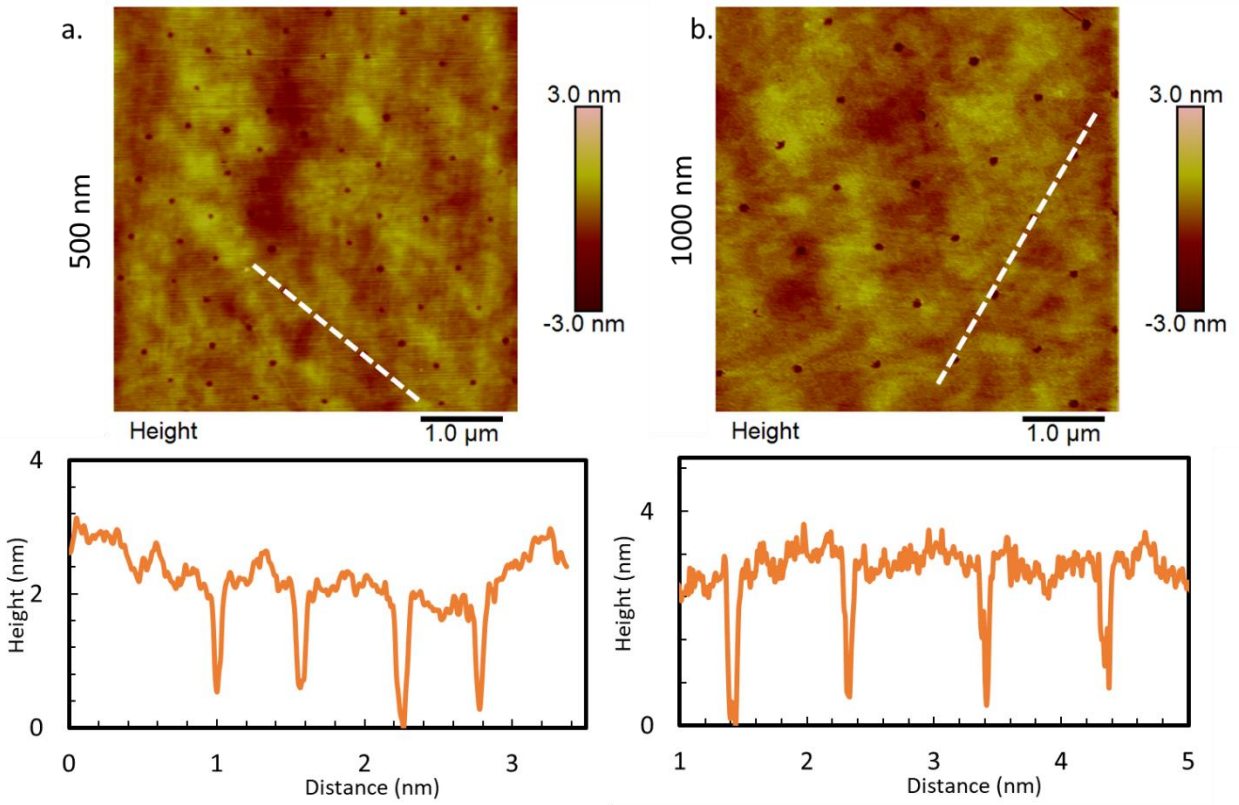

Figure 7. 3: *AFM images of nanopore arrays and their cross sections along the respective dotted lines. (a) 500 nm nanopore arrays. (b) 1000 nm nanopore arrays. Cross sectional profiles are shown under each image taken along the dotted lines shown in AFM images.*

AFM images collected after the removal of nanospheres from the substrate indicated where the nanospheres were seated on the surfaces. *Figure 7.3* shows AFM images collected on 500 and 1000 nm nanopore arrays before metal deposition and their cross-sections. The pore depth, diameter and pore separation profiles of the nanopore structures were analyzed and their values were consistent with previous reports.[31] Nanopore depths were measured to be 1.6 ± 0.3 nm and 1.5 ± 0.2 nm for nanopore structures fabricated using 500 nm and 1000 nm nanospheres, respectively (*Figure 7.4a*). Previous work has also pointed out this difference in comparison to monolayer thicknesses on bare Si/SiO_2 substrates (2.2-2.8 nm) and nanopore scaffolds.[31,42] Unlike in fully packed monolayers, nanopore surfaces will have empty spaces that the monolayer can tilt into, when pressure is applied upon the SAM film. We suggest the decrease in thickness compared

to a fully formed monolayer is due to this tilt upon contact mode imaging. The average diameter of the nanopores obtained for 500 nm and 1000 nm spheres were 125 ± 21 nm and 147 ± 22 nm respectively. Nanopore diameters have been shown to vary with drying conditions including humidity, drying time, and parameters such as solvent system used during self-assembly.[31] *Figure 7.4c* shows the inter-pore distance for 500 and 1000 nm nanospheres. By changing the size of the spheres used (50 nm, 200 nm 500 nm and 1000 nm), distance between nanoholes can be further reduced or increased (we have used 500 nm and 1000 nm to demonstrate this).

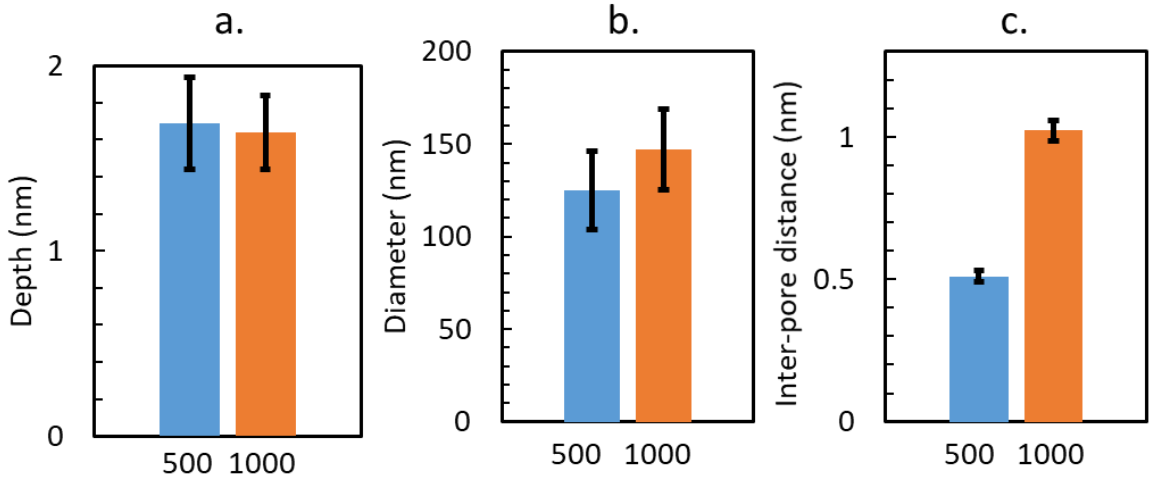

Figure 7. 4: *(a) Nanopore depth for 500 (blue) and1000 nm (orange) particle lithographed surfaces. (b) Nanopore diameter for 500 (blue) and1000 nm (red) particle lithographed surfaces, and (c) the inter-pore distance for 500 (blue) and1000 nm (red) surfaces. The error bars indicate the standard deviations.*

7.4.1 Electroless Deposition of Metal on Nanopores

Electroless deposition is a spontaneously driven process due to redox potential difference between two species. Here the ELD process occurs between solution phase metal ions and a Si surface. This redox chemistry has been used to plate metal from various metal cations, on a Si surface, without the need of an applied external potential. Solution phase metal ions undergo a reduction from their cationic form to form solid metal, while Si from the substrate is oxidized,

providing necessary electrons for the process (see *Figure 7.5*). However, the 1.5 nm thick native oxide present on top of bulk Si must be removed by chemical etching before the bulk Si underneath can be oxidized to deposit the metal.

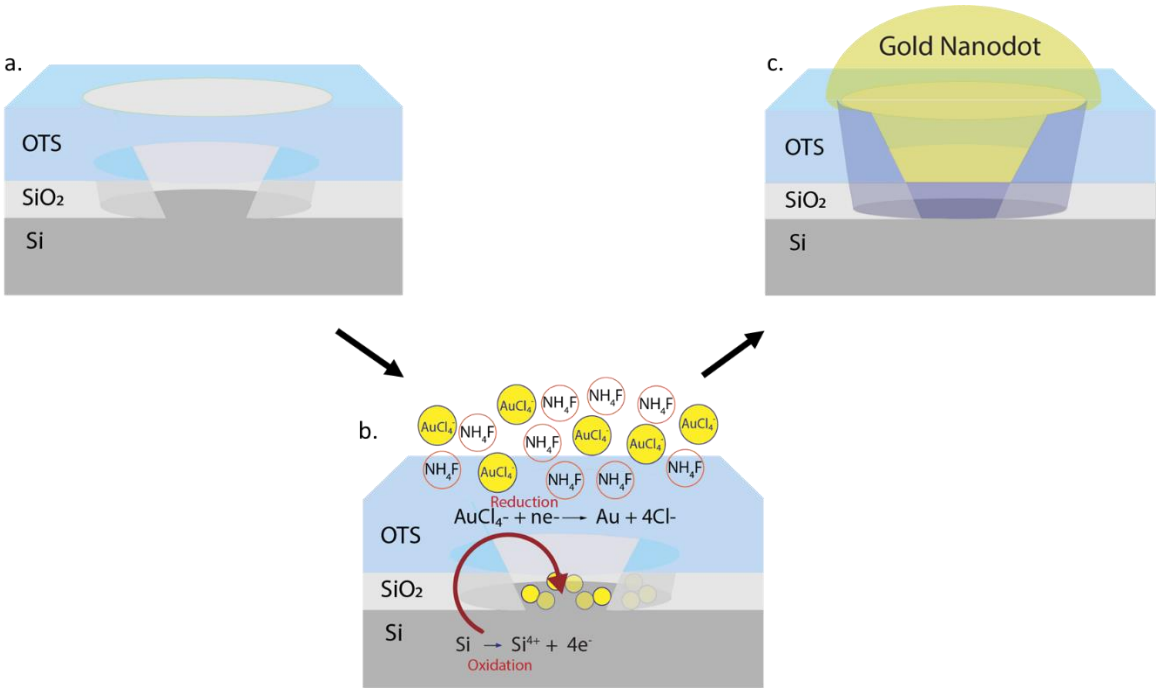

Figure 7. 5: *Redox reactions between gold ions in the plating solution and Si substrate. (a) Nanopore formed during the partial lithography process before the pre-etching to remove the native oxide. (b) Gold deposition process through redox reactions between Si surface and gold ions in solution after oxide is removed via pre-etching. (c) Nanodot grown on the pore after metal deposition is complete.*

Etching of SiO_2 to facilitate redox reactions can be achieved by using solution such as HF or NH_4F. In this work, NH_4F was utilized for etching in place of HF as it provides increased safety Further, we have demonstrated that NH_4F provides mild etching conditions, without compromising the OTS monolayer resist on the surface and provides a more uniformly etched surface.[43] *Figure 7.5* illustrates the key steps during oxide removal and metal deposition during electroless redox reactions. Etching occurs through a complex series of reactions, resulting in formation of SiF_x species.[44] The chemical reactions involved in the proposed etching process are included in *Chapter 5*. Once the oxide is fully removed, redox chemistry between the surface and

the solution phase gold ions is possible. We have found that pre-etching of the nanopores results in more uniform metal growth on the surface with narrower height and width distributions.[45] This is because pre-etching removes the oxide on Si and leaving a uniform, bare Si surface for the metal deposition. Also, it is important that the concentration of NH_4F in the plating solution be much smaller than that of the pre-etching solution to prevent excessive damage to the OTS monolayer. The optimum time of pre-etching was found to be 30 s for gold.

Most importantly, electroless deposition is facilitated only where the silicon substrate is exposed to the plating solution, *i.e.* where the nanospheres were seated on the substrate while the rest of the surface is protected by an OTS resist layer. The etching solution only removes the oxide and exposes the underlying Si in the regions of the nanopores, where the OTS layer is not covering the surface. ELD could also occur where the monolayer has defects; however, the tested conditions were previously optimized to minimize the amount of multilayer formation or defect sites on the monolayer film, resulting a hexagonal array of Au dots. Our previous work extensively investigated the plating solution components and their role in electroless Au deposition on Si, in presence of an organic monolayer as a resist film.[43] During this work, we investigated the electroless deposition time dependence on growth of metal nanodot arrays while other plating parameters, such as concentrations of plating solution components, were held constant. Conditions such as NH_4F concentration, metal ion concentration, the addition of chelating agents, pre-etching duration, bath temperature, and pH were previously shown to have effects towards electroless deposition; however, they were held constant in this work for the simplicity. [39,46,47] Modifications of these parameters could affect growth rate, size, and shape of the nanostructures on the surface because they would impact the kinetics of metal deposition.

7.4.2 Controlling the Height of Nanodots

We previously optimized conditions for mild plating solutions that can be used in the presence of organic thin films. In this study, OTS on SiO_2 were utilized as resist layers, where the organic monolayer prevents any metal deposition on the Si surface during electroless metal deposition. Further, we concluded that a decrease in pH and an increase in electroless plating duration both increase the amount of metal deposited on Si surface, while increasing NH_4F concentration increased both the rate of metal deposition and nucleation density of metal ions. Plating solutions optimized for Au deposition were derived from this study.

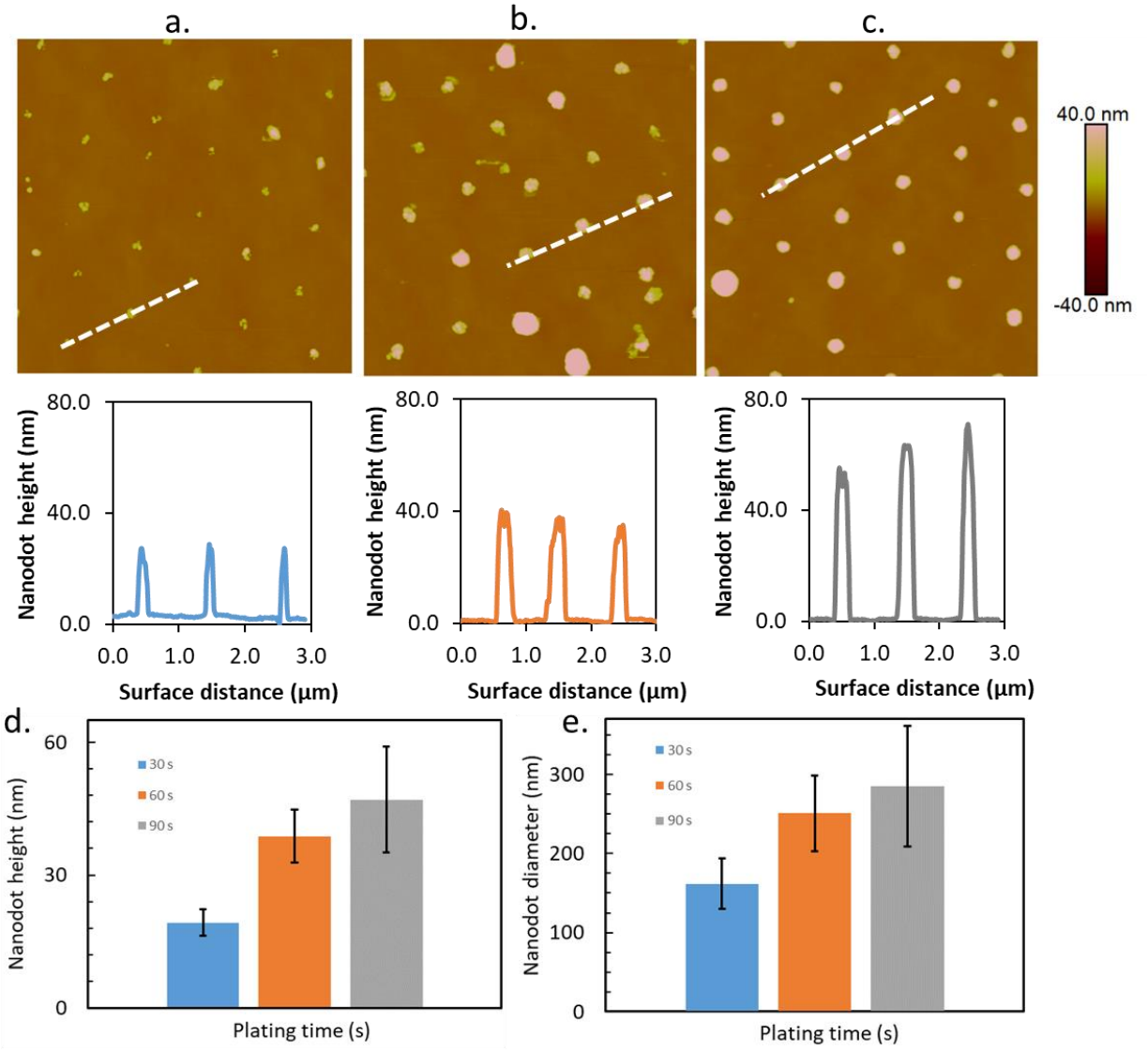

Figure 7. 6: *Au nanodots grown in nanopore arrays spaced 1000 nm apart for (a) 30, (b) 60, (c) 90 s in 0.002 M $HAuCl_4$•$3H_2O$.and 0.02 M NH_4F gold plating solution after a 30s pre etching step in 5% NH_4F. Under each image cross-section profiles are shown along the dotted lines on AFM images Nanodot height and diameter averages for 1000 nm images are shown in figure (d) and (e). The error bars denoted are standard deviations.*

Electroless deposition times were varied between 30 and 90 s for Au plating, demonstrating effective control over sizes for Au nanodots, in both height and diameter. *Figure 7.6 (a-c)* shows size variations for Au nanodots as a function of time for 1000 nm sphere samples. Au nanodots were grown to heights ranging from approximately 20 to 40 nm with diameters from 150 to 270

nm in the reported 30 to 90 s time intervals (*Figure 7.6 d, and e*). As shown in *Figure 7.6a* the cross-sectional profile indicates a collection of smaller Au particles rather than an individual structure. This phenomenon is likely due to particle nucleation kinetics, where-in Au particles are formed initially and over time merge together to form the uniform hemispherical structures (nanodots) As growth continues, there are fewer available reaction sites for the metal ions to be reduced, and the deposition rate may slow.

Figure 7.7 shows size variations for Au nanodots as a function of time for 500 nm sphere samples. Au nanodots were grown to heights ranging from approximately 6 to 30 nm with diameters from 70 to 150 nm in the reported 60 to 90 s time intervals (*Figure 7.7 c, and d*). The AFM images shows inconsistent filling of the nanoholes at shorter time of metal deposition. Also, some of the metal nanostructures show poor adhesion on to the surface by seeing the streaking pattern as the metal dots are pushed by the movement of the AFM tip while scanning in contact mode.

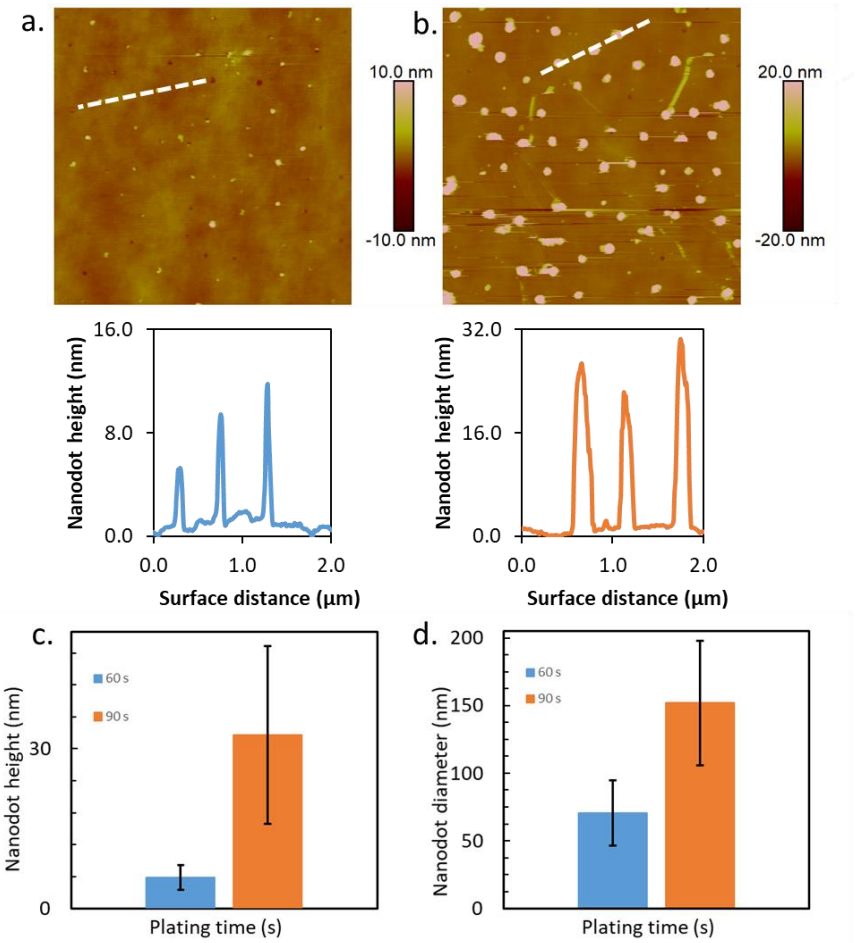

Figure 7. 7: *Au nanodots grown in nanopore arrays spaced 500 nm apart for (a) 60, (b) 90 s in 0.002 M $HAuCl_4$•3H_2O.and 0.02 M NH_4F gold plating solution after a 30s pre etching step in 5% NH_4F. Under each image, cross-section profiles are shown along the dotted lines on AFM images nanodot height and diameter averages for 500 nm images are shown in figure (d) and (e). The error bars denoted are standard deviations.*

Looking at the cross-sectional profiles, the dots appear hemispherical, which should allow simple modeling of properties. This control over shape and size is important for a variety of applications such as plasmonic materials, as the localized surface plasmon resonance (LSPR) wavelength can be tuned as a function of size and shape of nanoparticles.[28] This is an attractive property for biosensing applications, as the tunability of these structures can potentially be used to shift the resonance wavelength. For instance, the UV-Vis region is more desirable than IR wavelengths considering simplicity in sensing measurements. Further, the hemispherical geometry

of these nanodots ideally would have optimal mass transport properties for electrochemical applications.[48,49] Although parameters such as plating duration, NH_4F concentration, and pH play a role during electroless deposition and contribute towards particle formation and growth on surface, we chose to vary the metal plating duration to avoid having to make different plating solutions to obtain features with different sizes.

7.5 Conclusion

In this work, particle lithography-based nanosphere arrays were used to generate arrays of oriented nanopores on Si substrates using self-assembled OTS monolayers as a resist and selectively deposited metal thorough electroless deposition on nanopores to produce periodic metallic nanodots. The process was found to be an affordable and reproducible method to grow regularly spaced Au nanostructures with control over the particle height and diameter. The particle size primarily was controlled by varying the electroless deposition duration, but it was also shown to be affected by eliminating pre-etching step or changing plating solution component concentrations. Nanostructures of approximately 60 nm tall were grown with no signs of undesirable metal growth on monolayer. The tunability of these structures could lead to possible applications including plasmonic biosensing arrays. Additionally, the flexibility in metal ions further widens the range of potential applications.

7.6 References

(1) Barth, J. V; Costantini, G.; Kern, K. Engineering Atomic and Molecular Nanostructures at Surfaces. *Nature*. September 28, 2005, pp 671–679. https://doi.org/10.1038/nature04166.

(2) Aricò, A. S.; Bruce, P.; Scrosati, B.; Tarascon, J.; Schalkwijk, W. V. A. N.; Picardie, U. De; Verne, J.; Umr-, C. Nanostructured Materials for Advanced Energy Conversion and Storage Devices. *Nature* **2005**, *4*, 366–377.

(3) Vogel, E. M. Technology and Metrology of New Electronic Materials and Devices. *Nature* **2007**, *2*, 25–32.

(4) Jeon, J. H.; Joo, H.-Y.; Kim, Y.-M.; Lee, D. H.; Kim, J.-S.; Kim, Y. S.; Choi, T.; Park, B. H. Selector-Free Resistive Switching Memory Cell Based on BiFeO3 Nano-Island Showing High Resistance Ratio and Nonlinearity Factor. *Sci. Rep.* **2016**, *6* (1), 1–10. https://doi.org/10.1038/srep23299.

(5) Hong, A. J.; Liu, C.; Wang, Y.; Kim, J.; Xiu, F.; Ji, S.; Zou, J.; Nealey, P. F.; Wang, K. L. Metal Nanodot Memory by Self-Assembled Block Copolymer Lift-Off. *Nano Lett.* **2010**, *10*, 224–229. https://doi.org/10.1021/nl903340a.

(6) Tracey, J. I.; Carroll, D. M. O. Short-Wavelength Lasing-Spasing and Random Spasing with Deeply Subwavelength Thin-Film Gain Media. *Adv. Funct. Mater.* **2018**, *28* (39), 1–9. https://doi.org/10.1002/adfm.201802630.

(7) Fabris, L.; Dante, M.; Braun, G.; Lee, S. J.; Reich, N. O.; Moskovits, M.; Nguyen, T.; Bazan, G. C. A Heterogeneous PNA-Based SERS Method for DNA Detection. *J. Am. Ceram. Soc.* **2007**, *129*, 6086–6087. https://doi.org/10.1021/ja0705184.

(8) Zhang, J.; Atay, T.; Nurmikko, A. V. Optical Detection of Brain Cell Activity Using Plasmonic Gold Nanoparticles. *Nano Lett.* **2009**, *9* (2), 519–524.

(9) Kim, S. A.; Byun, K. M.; Kim, K.; Jang, S. M.; Ma, K.; Oh, Y.; Kim, D.; Kim, S. G.; Shuler, M. L.; Kim, S. J. Surface-Enhanced Localized Surface Plasmon Resonance Biosensing of Avian Influenza DNA Hybridization Using Subwavelength Metallic Nanoarrays. *Nanotechnology* **2011**, *22* (28), 289501 (1pp). https://doi.org/10.1088/0957-4484/22/28/289501.

(10) Zou, S.; Schatz, G. C. Silver Nanoparticle Array Structures That Produce Giant Enhancements in Electromagnetic Fields. *Chem. Phys. Lett.* **2005**, *403*, 62–67. https://doi.org/10.1016/j.cplett.2004.12.107.

(11) Zhou, Y.; Butun, S.; Chen, P.; Schatz, G. C.; Dravid, V. P. Strong Coupling between Plasmonic Gap Modes and Photonic Lattice Modes in DNA-Assembled Gold Nanocube Arrays. *Nano Lett.* **2015**, *15* (7), 4699–4703. https://doi.org/10.1021/acs.nanolett.5b01548.

(12) Wang, W.; Ramezani, M.; Väkeväinen, A. I.; Törmä, P.; Rivas, J. G.; Odom, T. W. The Rich Photonic World of Plasmonic Nanoparticle Arrays. *Mater. Today* **2018**, *21* (3), 303–314.

(13) Indrasekara, A. S. D. S.; Thomas, R.; Fabris, L. Plasmonic Properties of Regiospecific Core–Satellite Assemblies of Gold Nanostars and Nanospheres. *Phys. Chem. Chem. Phys.* **2015**, *17*, 21133–21142. https://doi.org/10.1039/c4cp04517c.

(14) Perl, A.; Reinhoudt, D. N.; Huskens, J. Microcontact Printing : Limitations and Achievements. *Adv. Mater.* **2009**, *21*, 2257–2268. https://doi.org/10.1002/adma.200801864.

(15) Kim, H.; Park, S.; Hinsberg, W. D. Block Copolymer Based Nanostructures : Materials , Processes , and Applications to Electronics. *Chem. Rev.* **2010**, *110* (1), 146–177.

(16) Vazquez-Mena, O.; Sannomiya, T.; Villanueva, L. G.; Voros, J.; Brugger, J. Metallic Nanodot Arrays by Stencil Lithography for Plasmonic Biosensing Applications. *ACS Nano* **2011**, *5* (2), 844–853. https://doi.org/10.1021/nn1019253.

(17) Mori, T.; Mori, T.; Tanaka, Y.; Suzaki, Y.; Yamaguchi, K. Fabrication of Single-Crystalline Plasmonic Nanostructures on Transparent and Flexible Amorphous Substrates. *Sci. Rep.* **2017**, *7*, 1–7. https://doi.org/10.1038/srep42859.

(18) Kabashin, A. V; Delapore, P.; Pereira, A.; Grojo, D.; Torres, R.; Sentis, M. Nanofabrication with Pulsed Lasers. *Nanoscale Res Lett* **2010**, *5*, 454–463. https://doi.org/10.1007/s11671-010-9543-z.

(19) Ahn, W.; Roper, D. K. Periodic Nanotemplating by Selective Deposition of Electroless Gold Island Films on Particle-Lithographed Dimethyldichlorosilane Layers. *ACS Nano* **2010**, *4* (7), 4181–4189. https://doi.org/10.1021/nn100338f.

(20) Blake, P.; Ahn, W.; Roper, D. K. Enhanced Uniformity in Arrays of Electroless Plated Spherical Gold Nanoparticles Using Tin Presensitization. *Langmuir* **2010**, *26* (3), 1533–1538. https://doi.org/10.1021/la903985m.

(21) Salaita, K.; Wang, Y.; Mirkin, C. A. Applications of Dip-Pen Nanolithography. *Nat. Nanotechnol.* **2007**, *2* (1), 145–155.

(22) Garcia, R.; Knoll, A. W.; Riedo, E. Advanced Scanning Probe Lithography. *Nat. Nanotechnol.* **2014**, *9* (8), 577–587. https://doi.org/10.1038/nnano.2014.157.

(23) Grzelczak, M.; Vermant, J.; Furst, E. M.; Liz-marza, L. M. Directed Self-Assembly of Nanoparticles. *ACS Nano* **2010**, *4* (7), 3591–3605.

(24) Saner, C. K.; Lu, L.; Zhang, D.; Garno, J. C. Chemical Approaches for Nanoscale Patterning Based on Particle Lithography with Proteins and Organic Thin Films. *Nanotechnol Rev* **2015**, *4* (2), 129–143. https://doi.org/10.1515/ntrev-2015-0002.

(25) Bang, B. J.; Jeong, U.; Ryu, D. Y.; Russell, T. P.; Hawker, C. J. Block Copolymer Nanolithography : Translation of Molecular Level Control to Nanoscale Patterns. *Adv. Mater.* **2009**, *21*, 4769–4792. https://doi.org/10.1002/adma.200803302.

(26) Haes, A. J.; Duyne, R. P. Van. A Nanoscale Optical Biosensor : Sensitivity and Selectivity of an Approach Based on the Localized Surface Plasmon Resonance Spectroscopy of Triangular Silver Nanoparticles. *J. Am. Ceram. Soc.* **2002**, *124* (7), 10596–10604. https://doi.org/10.1021/ja020393x.

(27) Shin, D. O.; Jeong, J.; Han, H.; Koo, M.; Park, H.; Lim, T.; Ouk, S. A Plasmonic Biosensor Array by Block Copolymer Lithography. *J. Mater. Chem.* **2010**, *20*, 7241–7247. https://doi.org/10.1039/c0jm01319f.

(28) Anker, J. N.; Hall, W. P.; Lyandres, O.; Shah, N. C.; Zhao, J.; Duyne, R. P. Van. Biosensing with Plasmonic Nanosensors. *Nature* **2008**, *7*, 442–453.

(29) Willets, K. A.; Van Duyne, R. P. Localized Surface Plasmon Resonance Spectroscopy and Sensing. *Annu. Rev. Phys. Chem.* **2007**, *58*, 267–297. https://doi.org/10.1146/annurev.physchem.58.032806.104607.

(30) Garno, J. C.; Amro, N. A.; Wadu-mesthrige, K.; Liu, G.-Y. Production of Periodic Arrays of Protein Nanostructures Using Particle Lithography. *Langmuir* **2002**, *18* (21), 8186–8192. https://doi.org/10.1021/la020518b.

(31) Brownfield, A. L.; Causey, C. P.; Mullen, T. J. Influence of Solvent on Octadecyltrichlorosilane Nanostructures Fabricated Using Particle Lithography. *J. Phys. Chem. C* **2015**, *119* (22), 12455–12463. https://doi.org/10.1021/acs.jpcc.5b02576.

(32) Highland, Z. L.; Saner, C. K.; Garno, J. C. Preparation of Octadecyltrichlorosilane

Nanopatterns Using Particle Lithography: An Atomic Force Microscopy Laboratory. *J. Chem. Educ.* **2018**, *95*, 320–325. https://doi.org/10.1021/acs.jchemed.7b00158.

(33) Kulkarni, S. A.; Lyles, V. D.; Serem, W. K.; Lu, L.; Kumar, R.; Garno, J. C. Solvent-Responsive Properties of Octadecyltrichlorosiloxane Nanostructures Investigated Using Atomic Force Microscopy in Liquid. *Langmuir* **2014**, *30*, 5466–5473.

(34) Li, J.; Garno, J. C. Elucidating the Role of Surface Hydrolysis in Preparing Organosilane Nanostructures via Particle Lithography. *Nano Lett.* **2008**, *8* (7), 1916–1922.

(35) Zhu, M.; Baffou, G.; Meyerbro, N.; Polleux, J. Micropatterning Thermoplasmonic Gold Nanoarrays To Manipulate Cell Adhesion. *ACS Nano* **2012**, *6* (8), 7227–7233. https://doi.org/10.1021/nn302329c.

(36) Wang, M.; Mi, G.; Shi, D.; Bassous, N.; Hickey, D.; Webster, T. J. Nanotechnology and Nanomaterials for Improving Neural Interfaces. *Advanced Functional Materials*. March 2018, p 1700905. https://doi.org/10.1002/adfm.201700905.

(37) Li, J.; Lusker, K. L.; Yu, J.; Garno, J. C. Engineering the Spatial Selectivity of Surfaces at the Nanoscale Using Particle Lithography Combined with Vapor Deposition of Organosilanes. *ACS Nano* **2009**, *3* (7), 2023–2035.

(38) Komiyama, H.; Iyoda, T.; Sanji, T. Metal Nanodot Arrays Fabricated via Seed-Mediated Electroless Plating with Block Copolymer Thin Film Scaffolding. *Nanotechnology* **2015**, *26* (39), 1–7. https://doi.org/10.1088/0957-4484/26/39/395302.

(39) Shacham-Diamand, Y.; Osaka, T.; Okinaka, Y.; Sugiyama, A.; Dubin, V. 30 Years of Electroless Plating for Semiconductor and Polymer Micro-Systems. *Microelectron. Eng.* **2015**, *132*, 35–45. https://doi.org/10.1016/j.mee.2014.09.003.

(40) Desbief, S.; Patrone, L.; Goguenheim, D.; Guerin, D.; Vuillaume, D. Impact of Chain Length , Temperature , and Humidity on the Growth of Long Alkyltrichlorosilane Self-Assembled Monolayers W. *Phys. Chem. Chem. Phys.* **2011**, *13*, 2870–2879. https://doi.org/10.1039/c0cp01382j.

(41) Brown, A. L.; Causey, C. P.; Mullen, T. J. Effects of Surface Water on Organosilane Nanostructure Fabrication Using Particle Lithography. *Thin Solid Films* **2015**, *594*, 184–191. https://doi.org/10.1016/j.tsf.2015.10.029.

(42) Wang, Y.; Lieberman, M. Growth of Ultrasmooth Octadecyltrichlorosilane Self-Assembled Monolayers on SiO2. *Langmuir* **2003**, *19* (4), 1159–1167. https://doi.org/10.1021/la020697x.

(43) Ulapane, S. B.; Kamathewatta, N. J. B.; Ashberry, H. M.; Berrie, C. L. Controlled Electroless Deposition of Noble Metals on Silicon Substrates Using Self-Assembled Monolayers as Molecular Resists to Generate Nanopatterned Surfaces for Electronics and Plasmonics. *ACS Appl. Nano Mater.* **2019**, *2* (12), 7114–7125. https://doi.org/10.1021/acsanm.9b01641.

(44) Hoshino, T.; Nishioka, Y. Etching Process of SiO2 by HF Molecules. *J. Chem. Phys.* **1999**, *111* (5), 2109–2114. https://doi.org/10.1063/1.479480.

(45) Ulapane, S. B. Harnessing the Control of Metallic Nanostructures on Interfaces Towards Biosensing, Plasmonics and More, 2019.

(46) Smith, Z. R.; Smith, R. L.; Collins, S. D. Mechanism of Nanowire Formation in Metal Assisted Chemical Etching. *Electrochim. Acta* **2013**, *92*, 139–147. https://doi.org/10.1016/j.electacta.2012.12.075.

(47) Sullivan, A. M.; Kohl, P. A. The Autocatalytic Deposition of Gold in Nonalkaline, Gold Thiosulfate Electroless Bath. *J. Electrochem. Soc.* **1995**, *142* (7), 2250–2255.

https://doi.org/10.1149/1.2044282.

(48) Squires, T. M.; Messinger, R. J.; Manalis, S. R. Making It Stick : Convection , Reaction and Diffusion in Surface-Based Biosensors. *Nat. Biotechnol.* **2008**, *26* (4), 417–426. https://doi.org/10.1038/nbt1388.

(49) Sheehan, P. E.; Whitman, L. J. Detection Limits for Nanoscale Biosensors. *Nano Lett.* **2005**, *5* (4), 803–807. https://doi.org/10.1021/nl050298x.

Chapter 8: Conclusions and Future Directions

8.1 Overview

In this study, we examined the utilization of gold affinity peptide tags attached to proteins to study selectivity and specificity for gold surfaces. We studied both wild type and gold-binding peptide tagged putrescine oxidase (PutOx-AuBP) as a model enzyme. It was been found that the AuBP-tagged protein has a higher affinity and stability on gold surfaces than wild type enzyme. It wasobserved that both of these proteins unfold and aggregate on hydrophobic surfaces, such as and OTS-SAM on silicon and graphite. Therefore, hydrophilic surfaces have been explored as potential resist layer for protein immobilization on gold nanostructures. From these studies, the best candidate for the protein resist layer was found to be hydroxyl-terminated SAM. Once the specificity and the selectivity of the protein towards the gold was confirmed, this study was extended to develop nanostructures of gold using AFM nanoshaving and particle lithography-based techniques. This straight-forward, cost effective method allows fabrication of gold nanopatterns with the ability to control the size, shape and spacing at the nanoscale with-high throughput over large areas.

Our research involves interface studies, which involve self-assembled monolayers, thin films of gold on Si surfaces, electroless deposition, protein surface interactions, and the manipulation of protein orientation on gold surfaces, affinity peptides, atomic force microscopy and other surface characterization techniques. Dimensional analysis, molecule thickness, contact angle and surface topography were frequently utilized to understand surface modifications. These studies have applications in the fields of plasmonics, biosensing, optoelectronics, nanoelectronics, catalysts and more. *Chapter 3 and 4 discuss* the development and analysis of affinity peptide tagged proteins regarding their selectivity and sensitivity to gold surfaces. There is a brief

introduction to potential future applications of gold electroless deposition in *Chapter 5*, fabrication of metallic nanowires using AFM nanoshaving of OTS in *Chapter 6*, and periodic metallic nanodot formation using nanosphere lithography in *Chapter 7*.

8.2 Functional Self Assembly of Putrescine Oxidase Genetically Engineered with a Peptide Tag for Gold Surface Attachment

There are several ways to control the orientation of protein/biomolecules on a desired surface. Some of them are direct adsorption, chemical crosslinking, enzymatic immobilization, protein modification, affinity proteins and affinity peptides.[1] To be applicable in biosensing devices, protein bound to the surface must be active once introduced to the surface. Using genetically engineered peptide sequences has gained interest due to the ability of having a single-step bio-assembly process with the control of orientation and placement. In this study, affinity peptides for specific metal were used, such as those that are specific to surfaces like Au, Ag, and silica. There are few studies for the combination of protein and affinity peptides in the field of biosensing.

In this study, we investigated a model enzyme, putrescene oxidase, which belongs to the family of Flavin oxidases. Both wild type and AuBP-tagged proteins were used in binding studies, activity assays and AFM investigation. We observed the stronger interactions resulting in higher coverage along with greater thermal stability for AuBP tagged protein over wild type protein on to gold surface. This has been demonstrated using a combination of QCM, activity assays, and AFM investigations of coverage and shape of individual molecules in this study.

One of the other areas that can extend this study is electrochemical measurement of protein activity using cyclic voltammetry studies. Electrochemical sensors typically low limits of detection and high sensitivity and are therefore popular for development of biosensors.[2] Control of the

orientation of the protein at the interface can potentially enhance the electron transfer and activity of surface bound redox proteins.[3,4] Also, expressing different proteins with the same peptide sequence with fluorescence proteins such as GFP or DsRed to determine specificity and selectivity via fluorescence measurements will enhance the applicability towards specific immobilization of protein on surfaces. This will help to determine conformation and validation of the AFM-based studies and quantitation of the binding.

In addition to gold, this study can be applied to Ag affinity peptides or other metal affinity peptides as well. This will be useful for applications in multicomponent metal nanostructures for binding multiple proteins to the surface with a specific arrangement for investigations of multivalency and coupled enzyme systems. This includes selective material specific assembly of multiple proteins in multimetallic nonpatterns. Despite the current limitation of only being able to selectively bind and control the orientation of one protein, there are many applications which require the selective immobilization of multiple protein components in a precise structure, including protein micro/nanoarrays, and cell signaling investigations.

8.3 Investigation of the Selectivity of Binding of Putrescine Oxidase Through Genetically Engineered Gold Binding Peptide Tags

Most biosensing applications require immobilization of biomolecules in such a way that molecules remain functionally active on the surface. It is very important to study the effect of different surfaces on protein immobilization. Here we report the behavior of wild-type (PutOx) and gold binding peptide tagged putrescine oxidase (PutOx-AuBP) enzymes on template-stripped gold (TSG), mica, Si(111), Octadecyltrichlorosilane on Si (OTS-Si-SAM), Graphite, Carboxyl self-assembled monolayers on TSG (COOH-TSG-SAM), and hydroxyl-terminated self-assembled

monolayers on TSG (OH-TSG-SAM) allowing us to determine the selectivity of binding. In order to be applicable in the nanostructures developed on organic thin films, a proper protein resist layer should be identified that will not produce large amounts of nonspecific interactions with proteins.

Our study demonstrates that hydrophobic surfaces show significant denaturation and aggregation of the protein. Hydrophilic surfaces including mica, carboxyl and hydroxyl-terminated SAM surfaces do not show extensive denaturation and result in minimal nonspecific binding. Carboxyl and hydroxyl surfaces can be used as resist layers when immobilizing protein on Au nano wires and nano dot arrays developed on Si surfaces.

This study can be used to develop different functionalized monolayers on Si surfaces. As a starting point, we have developed and studied protein adsorption on hydroxyl and carboxyl terminated SAM on Au surfaces using previous research.[5] Since there are no available trichlorosilanes for carboxyl and hydroxyl SAM molecules, surface reactions must be employed to create these surfaces. Researchers have attempted a surface reactions on alkene silanes via oxidation using $KMNO_4$ to obtain carboxyl SAM on Si.[6] Some of these methods require many steps, result in incomplete reaction or leave residue on the surface. In our approach we utilize esterified versions of silanes (10-carboxymethoxydecyltrichlorosilane and 11-acetoxyundecyltrichlorosilane), which will lead to single-step functionalization process involved a hydrolysis reaction to modify the terminal function group. Development of Au nanowires and nanodots on these surfaces will drive this research towards the biosensing applications. Being able to develop protein resistive organic thin film and also nanostructures of gold on the same surface will continue the advancement towards the goal of using these structures a well-defined model system for fundamental investigations of biosensing, coupled enzyme reactions, and cell signaling pathways.

8.4 Controlled Electroless Deposition of Noble Metals on Silicon Substrates Using Self-Assembled Monolayers as Molecular Resists to Generate Nanopatterned Surfaces for Electronics and Plasmonics

In electroless deposition, no external current or potential is required, and this method has more control over the other methods like electroplating. This is a rapid and easy way to selectively deposit gold thin lines on Si-OTS nanoshaved areas. When using a Si surface, no reducing agent is needed due to sacrificing semiconductor surface in the presence of HF or NH_4F (etching agent). The contact between metal and the semiconductor surface is a potential barrier. Most of the studies related to electroless plating provide conditions for industrial plating. They are complex in nature and have high concentrations. This includes complexing agents, pH regulators, weak acids, chelating agents. In nanoscale studies, direct utilization of the above plating solutions is limited. This is due to lacking long term stability, the complex nature of the solution, and an inapplicability in nanoscale applications.

Previous research has not utilized the selectivity of metal ELD with an organic film as a protective layer on the Si surface. We developed mild plating solutions to perform electroless deposition on Si exposed areas while preventing metal plating on the areas which have organic thin-film coating. Selective deposition of gold was achieved by significant modification of the previously reported solutions. The optimized solutions contain 1) $HAuCl_4 \cdot 3H_2O$ = 0.012 M, $Na_3C_6H_5O_7 \cdot 2H_2O$ =0.100 M and NH_4F = 0.625 M solution 2) $HAuCl_4 \cdot 3H_2O$ = 0.001 M, and NH_4F = 0.02 M. To obtain these optimized solutions, several trend studies have been performed, such as ELD duration, solution pH, NH4F concentration, metal ions, PVP and citrate ions.

Electroless deposition on nanoshaved organic thin films has been performed for Cu and Ag by our previous research group members. Thin films of Cu have large variety of applications

in the field of electronics. Our previous studies have shown that the developed thin films of Cu have tendency of areal oxidation. On the other hand, metallic Ag is relatively inert, which makes it hard to oxidize in ambient air. Since Ag is a good thermal and electrical conductor, it can be used in electrical and energy applications. In this study, Au electroless plating solutions have been developed. Au thin films have large variety of applications ranging from electronics to biosensing. In our studies, we have investigated protein immobilization with the usage of Au affinity peptides. This will open up new paths to develop highly selective biosensing devices.

Development of electroless plating solutions for metals with magnetic properties, such as Ni, Fe, and Co, can enhance the applicability of metals in the fields of catalysis and storage devices. Ni electroless deposition is widely used in printed circuits and hydrogen storage, and hybrid electronics.[7–9] Fe electroless deposition is also useful in biomedical applications,[10] and cobalt is used as catalyst in organic reactions.[11] Studying the selective growth of metals such as Ni, Fe, and Co under the influence of a magnetic field will be useful in future research. There have been very few investigations done to determine elemental characterization at metal-semiconductor interfaces. This will help to determine composition, at interfaces and binding chemistry of Au on to Si surface. Also, this study can be extended to the characterization of elements at the gold-silicon interfaces. Some research has shown the exchange in elements at these interfaces while carrying out the electroless deposition. Finally, we have seen poor adhesion of metal to the Si surface when chelating agents such as citric acid added to the plating solution. More studies can be carried out to determine the mechanism of chelation and solving the adhesion issue

8.5 Fabrication of Metallic Nanostructures Via Electroless Deposition on Nanoshaved Self-assembly Monolayers on Si(111) Surfaces.

This chapter is focused on developing gold nanowires on Si-OTS modified surfaces by using the combination of AFM nanoshaving and electroless deposition. This process includes the development of OTS SAM on the Si surface and selectively removing part of the monolayer by using an AFM probe and electroless gold deposition. This technique has advantages such as having control of the size, shape and the positioning of nanowires. This technique can be utilized to make nanowires for the metals such as Fe, Ni, Co, Ag, Au, and Cu.[12] By carrying out surface reactions surface functionality can be changed which will increase the applicability towards the biosensing. However, this process will require harder probes and also a single probe can only utilize 3-4 times for the patterning process.

Former group members Dr. Christina Edwards and Dr. Sasanka Ulapane have studied the development of Cu and Ag nanostructures on Si-OTS modified surfaces. For Cu and Ag, the components of the plating solutions are significantly different, which is discussed in *Chapter 6*. Results from the Cu nanostructures shows that the conductivity of formed nanowires is low compared to bulk Cu due to the oxidation of Cu into CuO/Cu_2O_3 species under ambient conditions. During studies regarding Ag nanowires, continuous nanowires were developed, and they have an average height of 78 nm. In this study, we have developed gold structures with the average heights of ~250 nm using plating solution 1 and average height of ~65 nm using plating solution 2. However, for both Au and Ag, further studies should be done to determine the conductivity of nanowires by using the four-point probe measurements.

Au is one of the most common metals used in biological applications, such as cancer treatment,[13] protein immobilization,[14] molecular electronics,[15] plasmonics[16] and biosensing.[17] The

developed gold nanostructures can be used to study the selective binding of proteins that are tagged with gold affinity peptides (*see Chapter 3 and 4*). Also, alternatively grown Au and Ag nanostructures in close distances will open up interesting applications in Raman scattering, cell signaling, plasmonics and electrodes. Our group has access to affinity peptide tagged proteins through collaboration with the Tamerlar lab in mechanical engineering at KU that target Au and Ag, which can be used to perform studies regarding the selective immobilization of proteins onto an environment that has gold and silver grown alternatively on the surface. Cell signaling is also an interesting phenomena which can be mimicked in an artificial environment by using such alternative positioning of the metal nanostructures in close distances.[18] Having developed nanostructures with different metals in close distances can lead to immobilize biological receptors that facilitate the binding of cell to the surfaces. This will help to understand fundamental sciences behind the disease related to cell signaling and more.[19]

8.6 Periodic Gold Nanodot Array Fabrication on Particle Lithography-Based Nanopore Patterns Using Electroless Deposition

The fabrication of metallic nanodot arrays on surfaces has a wide range of applications ranging from sensing, optoelectronics, surface-enhanced Raman scattering and high capacity storage devices.[20] There have been several studies regarding the arrayed structures formation using particle lithography.[21,22] In this study, we developed Au nanodot arrays with particle lithography and electroless deposition. The process starts with drop-casting the nanospheres onto the Si surface, then introducing SAM molecules. Removal of nanospheres by sonication to obtain nanohole arrays. Then, the electroless deposition carried out to obtain gold nanodot arrays. This approach has several advantages compared to the previously mentioned scanning probe

techniques. Even though scanning probe techniques have excellent control over size, shape and positioning, it is unable to make arrays of the metallic structures, which is more useful in industrial scale.

Making a template for electroless deposition is an easy process and the distance between nanoholes can be controlled by changing the size of the spheres. Overall, this process is inexpensive and easily reproducible. We have developed regular gold nanodot arrays with less than 100 nm height. We have demonstrated the ability of tuning this nanostructure height by varying the time of the electroless deposition. Our former member, Dr. Sasanka Ulapane, has developed Si nanodot arrays by this method which have height range of 20-100 nm and the diameter ranging from 100-300 nm.

Overall, this method facilitates making large arrays of metal on the organic thin film protected surface. To be more applicable, decreasing the distance of nanodot arrays must be performed. Our group is currently carrying out experiments using 200 nm and 50 nm spheres to reduce the gap further. Initial investigations show less packing efficiency and difficulty removing spheres from the surface. The capability of modifying the organic thin film by changing the SAM molecule also provides advantages in the biological applications. These nanodot arrays have applications in the field of localized surface plasmon resonance. Development and characterization of these structures will lead to studying protein binding events that will shift the plasmonic resonance frequency, which is related to the concentration of the molecule of interest. Also, as mentioned previously, these structures can be used to study the affinity peptide tagged proteins to study the selective binding towards a specific metal.

We have performed preliminary studies towards developing periodic silver nanodot arrays via electroless deposition and gold triangles via metal evaporation on organic, thin-film protected

surfaces. Making two different shaped structures of Au and Ag metals on the same surface will enhance the applicability of these nanostructures in the field of biosensing and plasmonics. Assembly of multiple different proteins with well-defined spatial relationships particularly at the nanoscale remains a significant challenge. As a starting point, development periodic gold nano and Ag structure arrays on the surface will be an interesting solution for this issue. Also, this study can be extended to magnetic metals such as Ni, which have applications in magnetic storage devices and memory circuits. Previous studies have shown that Ni have excellent magnetic properties and the development of nanostructures can be carried out in the presence of a magnetic field.[23]

8.7. Final Statement

This study shows the utilization of Au affinity peptides to control the protein orientation on Au surfaces. An extensive study has been carried out by using different surfaces for optimization of a resist film for development of metal nanostructure fabrication. The nanowire and nanodot development has been carried out on Si OTS modified surfaces. These studies address several important concepts towards modern-day research and industry. This includes orientation control of protein, precise placement of nanostructures and nanoarrays, modification of surface, ease of fabrication and low cost. We believe our study will be useful in the future development of biosensing and in the nanoscience field.

8.8. References

(1) Faccio, G. From Protein Features to Sensing Surfaces. *Sensors (Switzerland)* **2018**, *18* (4), 1–17. https://doi.org/10.3390/s18041204.

(2) Zhu, C.; Yang, G.; Li, H.; Du, D.; Lin, Y. Electrochemical Sensors and Biosensors Based on Nanomaterials and Nanostructures. *Anal. Chem.* **2015**, *87* (1), 230–249. https://doi.org/10.1021/ac5039863.

(3) Prabhulkar, S.; Tian, H.; Wang, X.; Zhu, J.-J.; Li, C.-Z. Engineered Proteins: Redox Properties and Their Applications. *Antioxid. Redox Signal.* **2012**, *17* (12), 1796–1822. https://doi.org/10.1089/ars.2011.4001.

(4) Hitaishi, V. P.; Clement, R.; Bourassin, N.; Baaden, M.; de Poulpiquet, A.; Sacquin-Mora, S.; Ciaccafava, A.; Lojou, E. Controlling Redox Enzyme Orientation at Planar Electrodes. *Catalysts*. 2018, pp 1–38. https://doi.org/10.3390/catal8050192.

(5) Wang, H.; Chen, S.; Li, L.; Jiang, S. Improved Method for the Preparation of Carboxylic Acid and Amine Terminated Self-Assembled Monolayers of Alkanethiolates. *Langmuir* **2005**, *21* (7), 2633–2636. https://doi.org/10.1021/la046810w.

(6) Jadhav, S. A. Self-Assembled Monolayers (SAMs) of Carboxylic Acids: An Overview. *Cent. Eur. J. Chem.* **2011**, *9* (3), 369–378. https://doi.org/10.2478/s11532-011-0024-8.

(7) Osaka, T.; Takano, N.; Kurokawa, T.; Kaneko, T.; Ueno, K. Electroless Nickel Ternary Alloy Deposition on SiO2 for Application to Diffusion Barrier Layer in Copper Interconnect Technology. *J. Electrochem. Soc.* **2002**, *149* (11), 573–578. https://doi.org/10.1149/1.1512669.

(8) Bak, S. M.; Kim, K. H.; Lee, C. W.; Kim, K. B. Mesoporous Nickel/Carbon Nanotube Hybrid Material Prepared by Electroless Deposition. *J. Mater. Chem.* **2011**, *21* (6), 1984–1990. https://doi.org/10.1039/c0jm00922a.

(9) Lin, K. Y.; Tsai, W. T.; Chang, J. K. Decorating Carbon Nanotubes with Ni Particles Using an Electroless Deposition Technique for Hydrogen Storage Applications. *Int. J. Hydrogen Energy* **2010**, *35* (14), 7555–7562. https://doi.org/10.1016/j.ijhydene.2010.04.145.

(10) Zhang, X.; Han, W.; Fan, D.; Zheng, Y. Electroless Iron Plating on Pure Magnesium for Biomedical Applications. *Mater. Lett.* **2014**, *130*, 154–156. https://doi.org/10.1016/j.matlet.2014.05.102.

(11) Michalek, F.; Lagunas, A.; Jimeno, C.; Pericàs, M. A. Synthesis of Functional Cobalt Nanoparticles for Catalytic Applications. Use in Asymmetric Transfer Hydrogenation of Ketones. *J. Mater. Chem.* **2008**, *18* (39), 4692–4697. https://doi.org/10.1039/b808383e.

(12) Ulapane, S. B.; Kamathewatta, N. J. B.; Ashberry, H. M.; Berrie, C. L. Controlled Electroless Deposition of Noble Metals on Silicon Substrates Using Self-Assembled Monolayers as Molecular Resists to Generate Nanopatterned Surfaces for Electronics and Plasmonics. *ACS Appl. Nano Mater.* **2019**, *2* (12), 7114–7125. https://doi.org/10.1021/acsanm.9b01641.

(13) Huang, X.; El-Sayed, M. A. Gold Nanoparticles: Optical Properties and Implementations in Cancer Diagnosis and Photothermal Therapy. *J. Adv. Res.* **2010**, *1* (1), 13–28. https://doi.org/10.1016/j.jare.2010.02.002.

(14) Tamerler, C.; Duman, M.; Oren, E. E.; Gungormus, M.; Xiong, X.; Kacar, T.; Parviz, B. A.; Sarikaya, M. Materials Specificity and Directed Assembly of a Gold-Binding Peptide. *Small* **2006**, *2* (11), 1372–1378. https://doi.org/10.1002/smll.200600070.

(15) Chen, D.; Liu, Z.; Liang, B.; Wang, X.; Shen, G. Transparent Metal Oxide Nanowire

Transistors. *Nanoscale* **2012**, *4* (10), 3001–3012. https://doi.org/10.1039/c2nr30445g.

(16) Willets, K. A.; Van Duyne, R. P. Localized Surface Plasmon Resonance Spectroscopy and Sensing. *Annu. Rev. Phys. Chem.* **2006**, *58* (1), 267–297. https://doi.org/10.1146/annurev.physchem.58.032806.104607.

(17) Zeng, S.; Yong, K.-T.; Roy, I.; Dinh, X.-Q.; Yu, X.; Luan, F. A Review on Functionalized Gold Nanoparticles for Biosensing Applications. *Plasmonics* **2011**, *6* (3), 491–506. https://doi.org/10.1007/s11468-011-9228-1.

(18) Schenk, F. C.; Boehm, H.; Spatz, J. P.; Wegner, S. V. Dual-Functionalized Nanostructured Biointerfaces by Click Chemistry. *Langmuir* **2014**, *30* (23), 6897–6905. https://doi.org/10.1021/la500766t.

(19) Mora-Garcia, P.; Sakamoto, K. M. Cell Signaling Defects and Human Disease. *Mol. Genet. Metab.* **1999**, *66* (3), 143–171. https://doi.org/10.1006/mgme.1998.2798.

(20) Aizpurua, J.; Bryant, G. W.; Richter, L. J.; García De Abajo, F. J.; Kelley, B. K.; Mallouk, T. Optical Properties of Coupled Metallic Nanorods for Field-Enhanced Spectroscopy. *Phys. Rev. B - Condens. Matter Mater. Phys.* **2005**, *71* (23), 1–13. https://doi.org/10.1103/PhysRevB.71.235420.

(21) Ahn, W.; Roper, D. K. Periodic Nanotemplating by Selective Deposition of Electroless Gold Island Films on Particle-Lithographed Dimethyldichlorosilane Layers. *ACS Nano* **2010**, *4* (7), 4181–4189. https://doi.org/10.1021/nn100338f.

(22) Li, J.; Garno, J. C. Elucidating the Role of Surface Hydrolysis in Preparing Organosilane Nanostructures via Particle Lithography. *Nano Lett.* **2008**, *8* (7), 1916–1922.

(23) Khomutov, G. B.; Gubin, S. P.; Khanin, V. V.; Koksharov, A. Y.; Obydenov, A. Y.; Shorokhov, V. V.; Soldatov, E. S.; Trifonov, A. S. Formation of Nanoparticles and One-Dimensional Nanostructures in Floating and Deposited Langmuir Monolayers under Applied Electric and Magnetic Fields. *Colloids Surfaces A Physicochem. Eng. Asp.* **2002**, *198–200*, 593–604. https://doi.org/10.1016/S0927-7757(01)00980-3.